January 2018

Microstructures And Nanomechanical Properties Of The Bakken Shale

Kouqi Liu

MICROSTRUCTURES AND NANOMECHANICAL PROPERTIES OF THE BAKKEN SHALE

by

Kouqi Liu

Bachelor of Science, China University of Petroleum (East China), 2011

Master of Science, China University of Petroleum (East China), 2014

A Dissertation

Submitted to the Graduate Faculty

of the

University of North Dakota

In partial fulfillment of the requirements

for the degree of

Doctor of Philosophy

Grand Forks, North Dakota

August
2018

This dissertation, submitted by Kouqi Liu in partial fulfillment of the requirements for the Degree of Philosophy from the University of North Dakota, has been read by the Faculty Advisory Committee under whom the work has been done and is hereby approved.

_____
Mehdi Ostadhassan, PhD

_____
Vamegh Rasouli, PhD

_____
Kegang Ling, PhD

_____
Thomas Gentzis, PhD

_____
Member At Large

This dissertation is being submitted by the appointed advisory committee as having met all of the requirements of the School of Graduate Studies at the University of North Dakota and is hereby approved.

_____
Grant McGimpsey Dean of the School of Graduate Studies

_____
Date

PERMISSION

Title Microstructures and Nanomechanical Properties of The Bakken Shale
Department Petroleum Engineering
Degree Doctor of Philosophy

In presenting this dissertation in partial fulfillment of the requirements for a graduate degree from the University of North Dakota, I agree that the library of this University shall make it freely available for inspection. I further agree that permission for extensive copying for scholarly purposes may be granted by the professor who supervised my dissertation work or, in his absence, by the Chairperson of the department or the dean of the School of Graduate Studies. It is understood that any copying or publication or other use of this dissertation or part thereof for financial gain shall not be allowed without my written permission. It is also understood that due recognition shall be given to me and to the University of North Dakota in any scholarly use which may be made of any material in my dissertation.

Kouqi Liu
03/19/2018

TABLE OF CONTENTS

LIST OF FIGURES

LIST OF TABLES

ACKNOWLEDGEMENTS

First and Foremost, I would like to thank my advisor, Dr. Mehdi Ostadhassan who gave me a chance to join his group and study at the University of North Dakota. I thank Dr. Mehdi Ostadhassan for his many great advices in my research, teaching me how to do the research in a scientific and efficient way, how to overcome the difficulties and how to write and improve the quality of my publications. I thank Dr. Ostadhassan for the great balance of guidance and freedom he has given me, for allowing me the time to dig in different research ideas. I would also like to thank Dr. Thomas Gentzis from Reservoir Geology Group at the Core Laboratories in Houston, TX. Dr. Thomas gave me so much support during my PhD. I thank him for guiding me to use different instruments, data analysis and improving my writing skills. I would like to extend our gratitude to Dr. Humberto Carvajal-Ortiz from Reservoir Geology Group at Core Laboratories in Houston TX, for great discussions and sample processing for geochemical analysis. I also thank Ms. Bailey Bubach and Dr. Vamegh Rasouli. I thank them who are always very kind to help me solve problems in both research and personal life matters. I will not forget all the fun times I spent with my colleagues in the office: Lingyun Kong, Chunxiao Li, Alexeyev Alan, and Seyedalireza Khatibi. Thanks for the great time we had together, and I am looking forward to our continued friendship. I appreciate the support from Dr. Xiaodong Hou, who helped me a lot in the Lab and Professor Reza Rezaee and his group members Jie Zou and Yujie Yuan from Curtin University to help to do some experiments and data analysis. Last but not least, I would like to thank NDGS, Core Library, the manager Mr. Jeff Bader and lab technician, Mr. Kent Holland for their generosity in providing us adequate number of samples from the Bakken Formation.

ABSTRACT

The focus of this thesis is to study the pore structures along with mechanical properties of the shale rocks from the Bakken Formation. The pore structures that are obtained from the SEM image analysis method showed that total surface porosity of the studied samples is less than 12% and that organic porosity is not the main contributor to total porosity for the samples analyzed. Clay minerals and feldspar have a positive influence on porosity while quartz, pyrite, and TOC has a negative impact. The results from the multifractal theory and lacunarity methods based on the segmented SEM images indicated that pores distribution and size in Bakken shale are heterogeneous.

Regarding gas adsorption analysis, the results showed that all range of pore sizes: micro (<2 nm), meso (2-50 nm) and macro-pores (>50 nm) exist in the Bakken shale samples. Meso-pores and macro-pores are the main contributors to the porosity for these samples. In comparison with the Middle Bakken, samples from the Upper and Lower Bakken exhibited more micro pore volumes. The deconvolution of the pore distribution function from the combination of N_2 and CO_2 adsorption results proved that five typical pore size families exist in the Bakken shale samples: one micro-pore, one macro-pore and three meso-pore size clusters. In order to analyze the heterogeneity of the pore structures from gas adsorption, multifractal method was applied to analyze adsorption isotherms (CO_2 and N_2).

The results explained that the generalized dimensions derived from CO_2 and the N_2 adsorption isotherms decrease as q increases, demonstrating a multifractal behavior. Samples from the Middle Bakken demonstrated the smallest average *H* value and largest average α_{10-}- α_{10+} for micropores

while samples from the Upper Bakken depicted the highest average α_{10-}- α_{10+} for the meso-macropores. This indicated that the Middle Bakken and the Upper Bakken have the largest micropore and meso-macropore heterogeneity, respectively. The impact of rock composition on pore structures showed that organic matter could increase the micropore connectivity and reduce micropore heterogeneity.

This study was followed by mechanical analysis of shale samples from the Bakken. Statistical grid nanoindentation method was applied to analyze mechanical properties of the Bakken. Then the Mori-Tanaka scheme was carried out to homogenize the elastic properties of the samples and upscale the nanoindentation data to the macroscale. The discrepancy between the macro-mechanical modulus from the homogenization and unconfined compression test was less than 15% which was found acceptable. The creep analysis of the samples describes that minerals with various mechanical properties exhibit different creep behavior. Under the same constant load and time conditions, the creep displacement of hard minerals would be smaller than the soft ones. On the contrary, the changes in mechanical properties (storage modulus, loss modulus, complex modulus, and hardness) of hard minerals are larger than soft minerals. The results from curve fitting led us to conclude that the changes in creep displacement, storage modulus, complex modulus and hardness with respect to the creep time would follow a logarithmic function.

CHAPTER 1

INTRODUCTION

1.1. Overview and Motivation

This thesis is focusing on characterizing different properties of shale rocks and is mainly composed of several published journal papers. Four chapters are dedicated to the pore structures using SEM image analysis and gas adsorption. The porosity and pore heterogeneity of shale rocks are quantified via these methods. The last three chapters present the results from mechanical properties (Young's modulus, Hardness and creep behavior) of the shale rocks using nanoindentation method.

The Bakken Formation which is one the major unconventional reservoirs in the nation is an Early Mississippian late Devonian organic-rich shale, located in the Williston Basin covering areas in the states of Montana, North Dakota and southern Saskatchewan in Canada (Pitman, 2001). The importance of this study is that previous studies have shown that shale oil formations have different characteristics compared to shale gas reservoirs and less studied. In terms of the TOC, most of shale gas reservoirs have 5% (Yang et al., 2017), whereas the Bakken has TOC more than 10% (Liu et al., 2016), but also its relationship with nanopores that exist within the organic matter becomes very complex (Liu, et al., 2016). This lack of correlation can be interpreted due to an inaccurate estimation of the pores, particularly the nanopore within the organic matter. In addition, so far most of the research that has been done to study the nanopore structures addressed the shale gas reservoirs while very few research articles can be found on the shale oils.

Pore structure and mechanical properties are two important parameters for the reservoir to be quantified. Pore structures can affect the reservoir quality such as the storage capacity and the mass transport potential of hydrocarbon (Anovitz and Cole, 2015) while mechanical properties can influence the wellbore stability and the design of the hydraulic fracturing (Kissinger et al., 2013) which is now one of the most widely used tools in the Bakken and other unconventional shale plays. Quantitative understanding of these two parameters can assist the companies to make better developing schedules and field operations, thus increasing the ultimate production and the economic profits.

1.2. Thesis Outline

This thesis covers two main topics through 7 chapters: quantifying the pore information from SEM image analysis (Chapter 2 and Chapter 3), pore information from gas adsorption (Chapter 4 and Chapter 5), studying the mechanical properties using nanoindentation (Chapter 6-8). Chapter 2 to chapter 8 are based on the published journal papers.

From Chapter 2, we start by analyzing the geochemical properties of the Bakken shales using Rock-Eval and vitrinite reflectance. This is followed by presenting field emission scanning electron microscope (FE-SEM) data to analyze the porosity. For this chapter, our attention was to understand the relationship between the geochemistry and pore structures of the Bakken shale. This was done to provide a better insight to the potential correlations between the rock compositions (minerals and organic matter) and porosity (Liu et al., 2018a).

In addition to porosity, pore heterogeneity is another parameter that affects the transport ability of the oil and gas shale formations. The heterogeneity of the pore structures from the SEM images

are described in Chapter 3. We used multifractal theory and lacunarity method to analyze the same shale samples and compare the results (Liu and Ostadhassan 2017).

Chapter 2 and Chapter 3 are based on the SEM image analysis mostly. However, due to the limitation of the SEM, pores within 9 nm are very hard to characterize. In order to get the pore information with pores less than 9 nm, gas adsorption is employed in Chapter 4 to quantify the pore structures. We calculated the pore volume, pore size distribution and pore size clusters of the Bakken shale using gas adsorption data. The comparison of pore structures of the Upper/Lower Bakken Formation and the Middle Bakken Formation based on gas adsorption data are also described in this chapter (Liu et al., 2017).

Following chapter 4, we addressed pore heterogeneity from gas adsorption data in chapter 5. We analyzed micropore and meso-macro pore heterogeneity, respectively. We compared the micropore heterogeneity and meso-macro pore heterogeneity of the Upper/Lower Bakken and the Middle Bakken. In addition, the influence of the rock compositions (minerals and organic matter) on micropore heterogeneity and meso-macro pore heterogeneity is also discussed in this chapter (Liu et al., 2018b).

Chapter 6 is focused on the mechanical properties of the Bakken shale samples in nanoscale using nanoindentation. In this chapter, we reported the typical nanoindentation curves and the mechanical information of the Bakken shale (Young's modulus and hardness). Based on the energy method, the fracture toughness of the samples is analyzed and the correlations between fracture toughness and Young's modulus is also described in this chapter (Liu et al., 2016).

Considering chapter 6, we realized that nanoindentation can measure the mechanical properties in nanoscale. However, whether nanoindentation data can be used to estimate the mechanical

properties of shale in macroscale is still unknown. In chapter 7, we applied the grid indentation method and attempted to upscale nano-micro scale mechanical data to estimate the macroscale properties. The comparison of the homogenized value and the data from the uniaxial compression tests are discussed in the chapter (Liu et al., 2018c).

Creep data which can represent the long-time behavior of the samples (shale cap rocks for example) can also be derived from nanoindentation testing. In chapter 8, we used nano-DMA to measure the changes in displacement with respect to mechanical properties by focusing on creep time during testing procedure (Liu et al., 2018d).

1.3. Reference

Anovitz, L.M. and Cole, D.R., 2015. Characterization and Analysis of Porosity and Pore Structures. Rev. Mineral Geochem. 80(1), 61-164.

Kissinger, A. et al., 2013. Hydraulic fracturing in unconventional gas reservoirs: risks in the geological system, part 2. Environ. Earth. Sci.70(8), 3855-3873.

Liu, K., Ostadhassan, M., Gentzis, T., 2016. Carvajal-Ortiz H, and Bubach B. Characterization of geochemical properties and microstructures of the Bakken Shale in North Dakota. 2016 Joint Meeting TSOP-AASP-ICCP.

Liu, K., Ostadhassan, M., Gentzis, T., et al. 2018a. Characterization of geochemical properties and microstructures of the Bakken Shale in North Dakota. Int. J. Coal Geol. 190,84-98.

Liu, K., Ostadhassan, M., 2017. Quantification of the microstructures of Bakken shale reservoirs using multi-fractal and lacunarity analysis. J. Nat. Gas Sci. Eng. 39, 62-71.

Liu, K., Ostadhassan, M., Zou, J., et al. 2018b. Multifractal analysis of gas adsorption isotherms for pore structure characterization of the Bakken Shale. Fuel. 219,296-311.

Liu, K., Ostadhassan, M., & Bubach, B., 2016. Applications of nano-indentation methods to estimate nanoscale mechanical properties of shale reservoir rocks. J. Nat. Gas Sci. Eng.35, 1310–1319

Liu, K., Ostadhassan, M., et al., 2018c. Statistical grid indentation analysis to estimate mechanical properties of Bakken Shale samples. J. Nat. Gas Sci. Eng. 53,181-190.

Liu, K., Ostadhassan, M., Bubach, B., et al. 2018d. Nano-Dynamic Mechanical Analysis (nano-DMA) of Creep Behavior of Shales: Bakken case study. J. Mater. Sci. 53(6), 4417-4432.

Pitman, J. K., Price, L. C., LeFever, J. A. 2001.Diagenesis and fracture development in the Bakken Formation, Williston Basin: Implications for reservoir quality in the middle member. U.S.G.S.Professional Paper 1653.

Yang, R., He, S., Hu, Q., Sun, M.,2017. Applying SANS technique to characterize nano-scale pore structure of Longmaxi shale, Sichuan Basin (China). Fuel.197, 91–99.

CHAPTER 2

CHARACTERIZATION OF GEOCHEMICAL PROPERTIES AND MICROSTRUCTURES OF THE BAKKEN SHALE

Abstract

Research on unconventional shale reservoirs has increased dramatically due to the decline of production from conventional reserves. Geochemical properties and pore microstructures are known to be important factors that affect the storage capacity and nano-mechanical properties of self-sourced organic- rich shales. In this study, eleven shale samples were collected from the Upper and Lower Members of the Bakken Formation for the analysis of mineralogy, geochemical properties, and pore structure. Bulk pyrolysis analysis was conducted using the default method and two modified methods, namely the reservoir and the shale reservoir methods. Although all three methods showed the Bakken samples to be organic-rich and to have considerable remaining hydrocarbon generating potential, it was the shale reservoir method that gave the highest hydrocarbons yield because it captured most of the lighter thermo-vaporizable hydrocarbons. Thus, the shale method is considered to be more appropriate for the geochemical analysis of the Bakken samples. This method also showed that most of the remaining potential is due to the cracking of heavy hydrocarbons, NSO compounds (Resins + Asphaltenes) and kerogen. The organic matter in the samples is mixed II/III type (oil and gas-prone), is thermally mature, and plots at the peak of the oil window. The VRo-eq values, based on solid bitumen Ro measurements and conversion, ranged from 0.85% to 0.98 %. The pore structures obtained from the image analysis method showed that total surface porosity of the samples ranged from 3.89% to 11.56%

and that organic porosity is not the main contributor of total porosity for the samples analyzed. The pore structures of the samples are heterogeneous due to differences in lacunarity values. Results of the impact of mineralogical composition on pore structures demonstrate that clay minerals and feldspar have a positive influence on porosity while quartz, pyrite, and that TOC has a negative impact.

2.1. Introduction

Since commercial production from shale-gas reservoirs began, research on shales has increased significantly. There is still much research needed in shale oil reservoirs, specifically on the topic of characterizing the nature of pore structures and geochemical properties (Loucks, et al., 2009). Pore structure properties analysis can assist in accurately understanding the storage and migration properties of the gas and oil while geochemical analysis can help to assess the quantity, quality, and thermal maturity of the sedimentary organic matter from the perspective of hydrocarbon generation, retention, and expulsion (Carvajal-Ortiz and Gentzis, 2015). Many researchers have studied shale gas reservoirs, including the Barnett shale (USA) (Loucks, et al., 2009, 2012), Marcellus shale (USA) (Marcon, et al., 2017; Gu et al., 2015), Longxi shale (China) (Shao et al., 2017; Jiao et al., 2014), a Toarcian shale (Germany) (Houben et al., 2016), Boom Clay(Belgium) (Hemes et al., 2015), and Posidonia Shale (Germany) (Klaver et al., 2016). In recent years, mercury intrusion porosimetry (MIP) (Mastalerz et al, 2013), nuclear magnetic resonance (NMR) (Karimi et al., 2015), gas adsorption (Shao et al., 2014), small angle neutron scattering (Clarkson et al., 2013) and SEM image analysis (Loucks, et al., 2009; Klaver et al., 2016; Curtis et al., 2012; Deng, et al., 2016) have been applied to characterize the pore structures of shales. Field emission SEM, which has a much higher resolution than conventional SEM, shows great ability in characterizing the nanopores in shale formations. Combined with the Ar ion beam milling which reduces artifacts from mechanical polishing (Bowker, 2003; Nelson, 2009), Focused Ion Beam

Scanning Electron Microscopes(FIB-SEM) and Broad Ion Beam Scanning Electron Microscopes (BIB-SEM) have been widely used as an acknowledged tool for the quantitative characterization of the pore structures (Loucks et al., 2009; Klaver et al., 2012, 2016). For geochemical analysis, open system programmed pyrolysis (Rock-Eval pyrolysis) and organic petrography (visual kerogen analysis and vitrinite reflectance) are the usual methods (Carvajal-Ortiz and Gentzis, 2015). These methods will be used here to analyze the pore structure and geochemical properties of the Bakken Formation, an organic-rich self-sourcing shale.

The Bakken oil field, as a typical unconventional reservoir, is one of the largest shale oil fields in the world. The Bakken Formation is composed of three different members. Most researchers focus on analyzing the properties of the Middle Bakken member only, which is the main production zone [i.e. mechanical properties (Sayers and Dasgupta, 2014; Havens and Batzle, 2011; Zeng and Jiang, 2009) and fracturing/ refracturing potential (Cheng and Wang, 2012; Ruhle, 2016; Wilson 2014)]. Studies on the Upper and Lower members, which are considered to be source rocks, is limited. The properties of the pore structures, the geochemical properties of these rocks and their correlations are still not fully understood. In this paper, we apply the Rock-Eval and organic petrology to analyze geochemical properties of the Upper/Lower Bakken shale samples while use SEM image analysis to characterize the pore structures. The objectives of this study are to: (1) derive the geochemical properties of the shales such as TOC, Ro; (2) characterize the pore structures of the Upper and Lower Bakken Shale Members, including porosity; (3) quantify the complexity and heterogeneity of the pores; and (4) determine if there is a relationship between porosity and geochemical properties.

2.2. Geological Setting

The Bakken Formation is a thin organic rich mudstone/sandstone unit, located in the Williston Basin (Fig. 2.1). The basin is intracratonic, elliptical, and underlies most of western North Dakota,

northeastern Montana and extends into Canada. It is separated into three distinct members, the Upper, Lower and Middle Bakken. The Bakken Formation only occurs in the subsurface and has no outcrop. The study area was located in North Dakota (Fig. 2.2), near the center of the Williston Basin.

The upper and lower members of the Bakken Formation have a high organic matter content (an average of 8% and 10% TOC, respectively), with a maximum in the upper member being 20% and in the lower member 30% (Smith and Bustin, 1995; Sonnonberg et al., 2011; Jin et al., 2015). The two members serve as both the source and seal for the generated hydrocarbons, while the Middle Bakken, composed of mixed carbonates and fine-grained clastics, is classified as an unconventional reservoir rock (Fig. 2.3) (Pitman et al., 2001). The Bakken Formation is broken into nine different lithofacies, with the upper and lower members characterized as a single lithofacies, named Mb. Lithofacies Mb is composed primarily of black clay and silt, with amorphous organic material and is thinly laminated. Authigenic pyrite and calcite are abundant in lithofacies Mb. The Middle Bakken is divided into eight lithofacies, which are further subdivided into three sub-units; A, B and C. Sub-unit A is a basal mudstone, sub-unit B is a mudstone/sandstone unit, and sub-unit C is an upper mudstone similar to sub-unit A (Pitman et al., 2001).

Deposition of the Bakken Formation occurred during the Late Devonian and Early Mississippian time periods. The formation is part of the Upper Kaskaskia Sequence, which was a cycle of rapid transgressions with slow, intermittent progradation. The Lower and Upper Bakken Members were deposited during a rapid sea-level rise and deposition was restricted to deeper portions of the basin (Gerhard et al., 1991). The rapid transgression created a deep marine distal setting, with deposition occurring below the storm wave base. The authigenic pyrite nodules present, in both the upper and

lower member, are evidence that the bottom water was anoxic with minimal interactions between the sediments and storm waves, creating a uniform black shale. The middle member was deposited following a rapid sea-level drop, causing an erosional boundary between it and the lower member. The environment of deposition was coastal marine, which varied from a cycle of offshore to lower shore face and transgressed into the deep marine environment of the Upper Bakken Shale (Smith and Bustin, 1995).

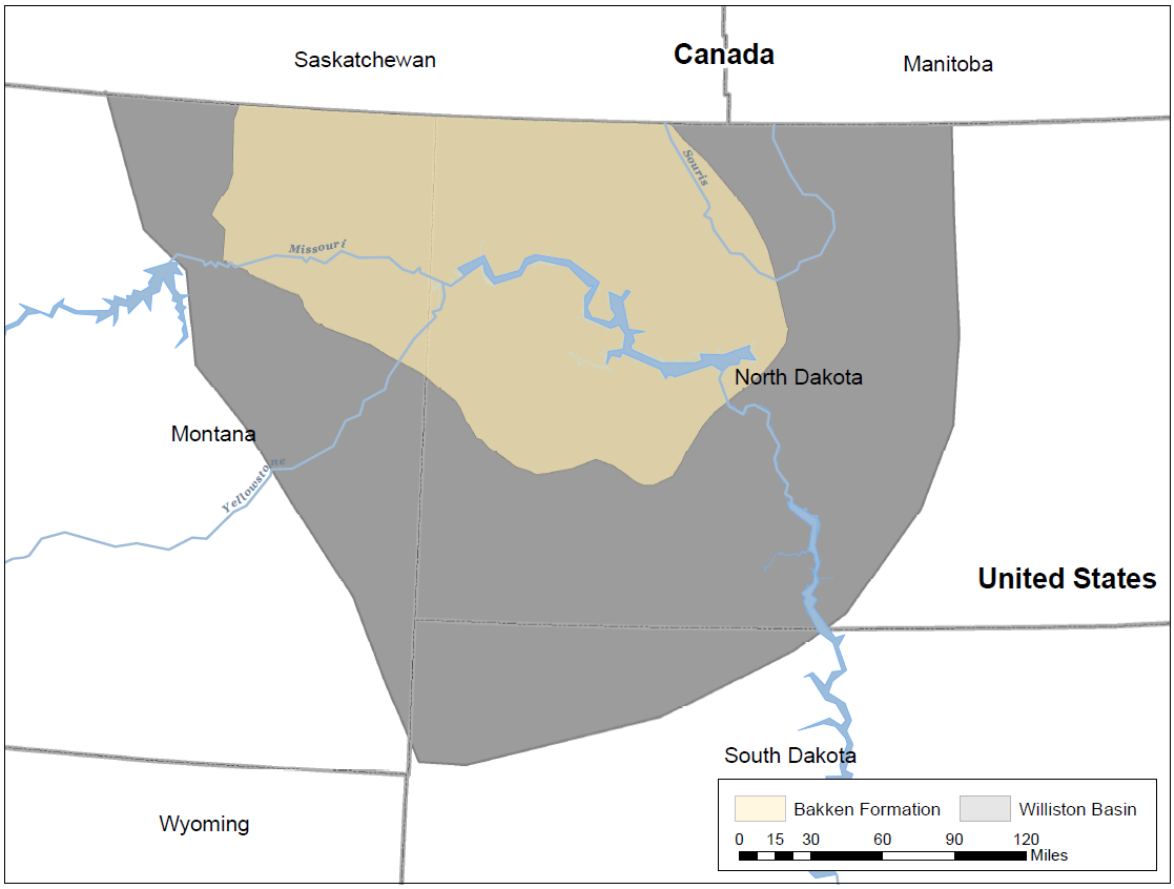

Fig. 2.1. Map of the Williston Basin and Bakken Formation extent in the United States.

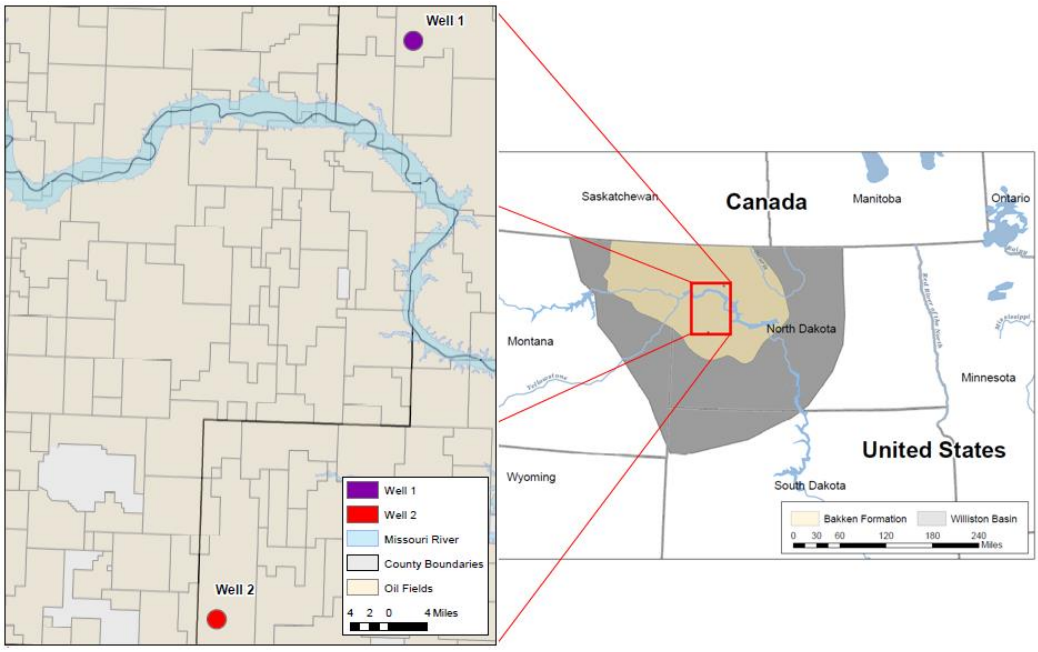

Fig. 2.2. Study area in the Williston Basin, North Dakota. The two wells studied are identified as Well #1 and Well #2.

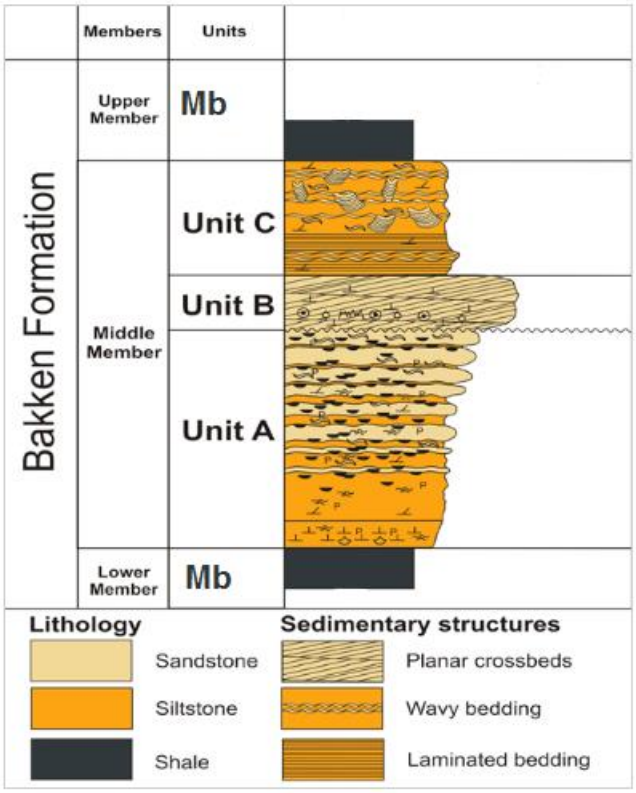

Fig. 2.3. Stratigraphic column of the Bakken Formation (after Pitman et al., 2001).

2.3. Samples and Methods

2.3.1. sample collection.

In order to select suitable Bakken shale samples for the various analyses, the North Dakota Industry Commission (NDIC) database was first searched to identify wells that have an economic production history (over the past 5 years). Information collected by reviewing numerous geophysical logs (e.g., sonic, density, gamma-ray, etc.) was also used in selecting the appropriate wells and drilling locations. TOC content, and thermal maturity maps available within the database were also reviewed. The two wells chosen (Fig. 2.2) were also selected based on the fact that Upper and Lower Bakken intervals are similar. For this study, the impact of maturity was not considered -- the samples analyzed have similar thermal maturity (i.e., in the oil generation window of the North Dakota portion of the basin) (Jin et al., 2015). Of the 11 samples analyzed from the two wells, six were from the Upper Bakken Shale and five were from the Lower Bakken Shale. Rock chips were taken from the Upper and Lower Bakken shale intervals and they were used to complete the analysis. The depth and description of the samples are shown in Table 2.1.

Table 2.1. Sample depth and description

	Sample	Formation/ Member	Depth (ft)	Sample description
Well #1	#1	Upper Bakken	10433	Shale: Black to dark brownish gray, firm, hard in part
	#2		10435.7	Shale: Dark brownish gray, black, firm, hard in part
	#3		10436.4	Shale: Dark brownish gray, black, firm, hard in part
	#4	Lower Bakken	10541	Shale: Black, dark brownish gray, hard, platy
	#5		10555	Shale: Black, dark brownish gray, hard, platy
Well #2	#6	Upper Bakken	11158	Shale: Gray Brown, dark gray in part, firm to hard
	#7		11159	Shale: Gray Brown, dark gray in part, firm to hard
	#8		11162	Shale: Gray Brown, dark gray in part, firm to hard
	#9	Lower Bakken	11201	Shale: Gray Brown, dark gray in part, firm to hard
	#10		11203	Shale: Gray Brown, dark gray in part, firm to hard
	#11		11205	Shale: Gray Brown, dark gray in part, firm to hard

2.3.2. geochemical properties analysis.

Bulk pyrolysis methods, such as Rock-Eval pyrolysis, have been used widely to characterize the organic matter type, maturity level, and source-rock potential of organic-rich rocks, and can also be used to quantify the total organic carbon (TOC) of the samples. In this study, approximately 60-70 mg per sample were used, and the detailed procedures outlined in Behar et al. (2001) were followed. The instrument used was the Rock-Eval 6 analyzer, commercialized by Vinci Technologies in France. Three different Rock-Eval methods were utilized and compared in this study: default method, reservoir method, and shale reservoir method. The difference between these three methods is based on their different temperature programs. Fig. 2.4 illustrates the schematic of the Rock-Eval temperature program of three different methods. For the default method, the sample was placed in the pyrolysis chamber and is heated at 300°C isothermally for 3 minutes, and then the temperature was increased to 650°C at a rate of 25°C/min. For the reservoir method, the temperature was kept at 150°C for 10 minutes (for calculating the S1r), then the temperature was increased to 650°C at 25°C/minute (for calculating the S2a and S2b). For the shale reservoir method, the initial temperature was 100°C, then the temperature was increased to 200°C at 25°C /min and held constant for 3 minutes (for the Sh0 calculation), then increased to 350°C at 25°C /min and held there for 3 minutes (for the Sh1 calculation), and, finally, to 650°C at 25°C /min (Romero-Sarmiento et al., 2015).

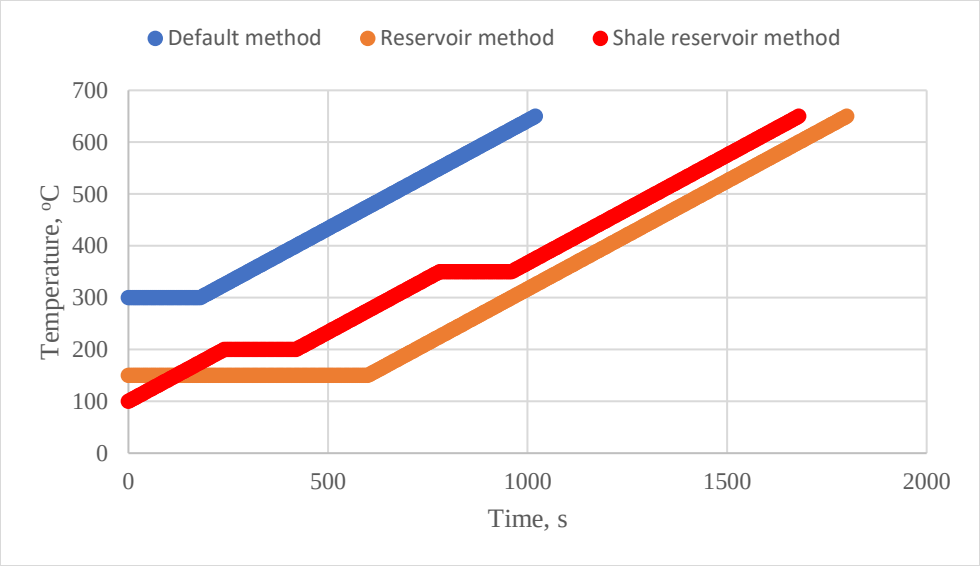

Fig. 2.4. Schematic of the Rock-Eval temperature program of three different methods (Romero-Sarmiento et al., 2015).

For vitrinite reflectance (R_o) analysis, the whole-rock samples were crushed to 20 mesh (850 μm) particles, mixed with the epoxy resin and hardener (ratio of 2:1) and left to harden under vacuum conditions for 24 hours (Hackley et al., 2015). The samples were polished to ensure the surface is scratch and relief free by using Buehler EcoMet/ AutoMet 250 automated polishing equipment. A Carl Zeiss Axio Imager A2m microscope, equipped with a white light source and a UV light to analyse the reflectance in oil (R_o) and fluorescence, was used for reflectance measurements and visual kerogen analysis.

2.3.3. SEM analysis.

The roughness of the surface from standard grinding and polishing methods can influence the quantitative pore structure analysis (Bowker, 2003; Nelson, 2009; Loucks et al., 2009). In order to avoid the irregularities caused by the mechanical polishing due to the differential hardness of components, the argon-milling method was used to derive a much flatter surface. Samples, which were taken parallel to the bedding, were trimmed down to a 0.5 cm square cube. Then, all faces of the cube were smoothed out by hand with a Buehler polishing wheel using 600-grit silicon carbide grinding paper. The samples were mounted to the ion mill sample holder and placed in the Leica

EM TIC 3X argon ion mill. After that, all samples were milled at an accelerating voltage of 8kV, with a gun current at 3mA for 8 hours. Finally, samples were removed from the ion mill's sample holder and mounted on a clean SEM stub using carbon paint. An FEI Quanta 650 FE-SEM instrument was applied to capture the surface of the prepared samples. All the images were taken under a low vacuum mode with 15 Kv voltage and 60 Pa pressure. The working distance is approximately 10 mm and the spot size is 3. Fig. 2.5 shows the surface prepared after the argon milling.

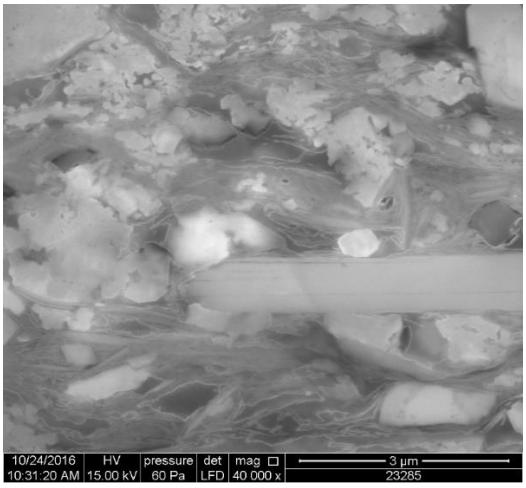

Fig. 2.5. Sample preparation for ion milling.

2.3.4. Mineral composition analysis.

The mineralogical composition was analyzed by X-ray diffraction (XRD). Sample powders with size less than 625 mesh were put in the Bruker D8 Advanced X-ray diffractometer. The scanning measurements were performed at the rate of 2°/min in the range of 3-90°. The relative mineral percentages were estimated by calculating the curve of the major peaks of each mineral with correction for Lorentz Polarization (Chen and Xiao, 2014).

2.3.5. Pore structure quantification analysis.

2.3.5.1. Image processing.

In order to investigate the pore structures from the gray scale SEM images, Image J, a very powerful commercial software widely applied in image analysis in other fields, was used (Liu and Ostadhassan, 2017; Chen et al., 2014). For the backscattering electron images (BSE) or the secondary images (SE) of shales, the pores have low gray scale values while the solid components have a high gray scale value. After selecting an appropriate threshold value, all of the images were segmented into the binary image where the black pixels (larger than the threshold value) represent the solid matrix and the white pixels (smaller than the threshold value) show the pores (Schneider et al., 2012). Fig. 2.6 shows the work flow of the imaging process for the shale sample. In this study, a critical overflow point technique was applied, which is related to the inflection of the cumulative brightness histogram. This was done in order to find the accurate upper threshold value to segment the images (Wong et al., 2006). Following this, porosity and pore size were quantified.

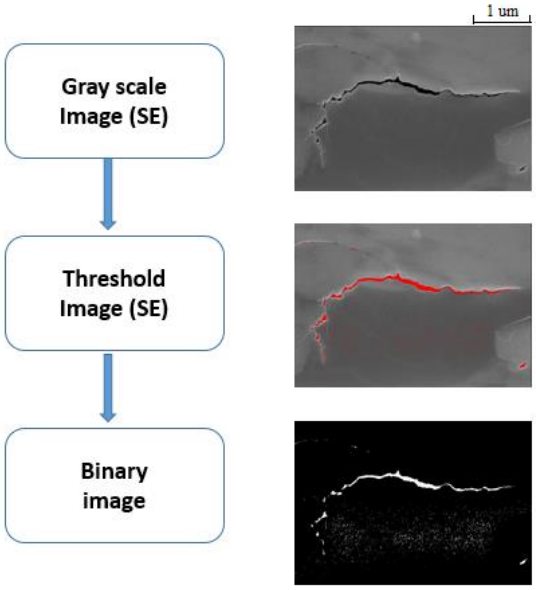

Fig. 2.6. Image process.

2.3.5.2. Fractal analysis.

Due to its strong ability to characterize the irregular or the fragmented shape of natural features as well as other complex objects that traditional Euclidean geometry fails to describe, fractal geometry has become a powerful tool to characterize pore structures. The box-counting method, defined by Russel et al. (1980), was applied to calculate the fractal dimension. This technique is used to obtain scaling properties of 2-D fractal objects by covering the 2-D image with a range of boxes of size ε and counting the number of boxes N. Each box contains at least one pixel representing the objects under study. This procedure is then repeated for a range of ε values. The different box counting numbers N covering the pore space at various grid sizes ε can thus be obtained. Finally, the following equation is used to calculate the fractal dimension:

$$D_0 = \lim_{\varepsilon \to 0} \frac{\log N_{(\varepsilon)}}{\log(1/\varepsilon)} \qquad (2\text{-}1)$$

2.4. Results and Discussions

2.4.1. Rock-Eval analysis.

Three pyrolysis temperature programs were applied to obtain the TOC and other parameters. Fig. 2.7 shows the pyrolysis program of Sample 1 using the three different methods. Fig. 2.7(a) represents the default method and shows that part of the low-molecular weight hydrocarbons is lost because the high starting temperature of this method – i.e., 300°C. Comparing the default method with the reservoir method that starts heating the sample at 150°C (Fig. 2.7b) and with the shale reservoir method that starts heating the sample at 100°C (Fig. 2.7c), it becomes obvious that the shale reservoir method can capture most of the lighter thermo-vaporizable hydrocarbons that are otherwise lost. To illustrate this, the "S1" equivalent (S1=S1r+S2a) from the reservoir method to the "S1" equivalent (S1=Sh0+Sh1) from the shale reservoir method and the S1 values from the default method was compared. The results (Fig. 2.8) show that the S1 equivalents from the shale reservoir method are the highest by <0.5 to almost 2 mg HC/g rock (average is about 1 mg HC/g

rock). This shows that the shale reservoir method is the best-suited for assessing the extractable hydrocarbon compounds in these unconventional shale reservoirs. For the Lower Bakken Formation, the reservoir method reports 26% higher S1 yield compared to the default method, and the shale reservoir method yields 45% higher S1 compared to the default method. For the Upper Bakken, the reservoir method yields 24% higher S1 than the default method while the shale reservoir method reports 37% higher S1 than the default method.

The results of the Tmax calculated from the three methods are shown in Fig. 2.9. The Tmax values derived from the three methods have a very narrow range, within 2°C, which is considered to be within our analytical error. Tmax values are largely invariant regardless of the pyrolysis method used. Based on our lengthy experience on tens of thousands of samples (with varying organofacies and thermal maturity) that we have analyzed worldwide, we have seen that Tmax is invariant when the S2 yields are much greater than the S1 values (i.e., when the S1 values contribute very little to the shape of the S2) (unpublished Core Laboratories data, 2016). Tmax is known to be affected, while using the Shale Play method, in samples where S1 is high (sometimes as high as) compared to the S2 (see Romero Sarmiento et al., 2015), thus significantly influencing the shape of the S2 (or Sh2) peak. Clearly, this is not the case in the Bakken samples used in this study because the S2 values are at least one order of magnitude greater than the S1 values. In our opinion, this is the reason why our Tmax values are relatively invariant (at least within the analytical error) regardless of the pyrolysis method used.

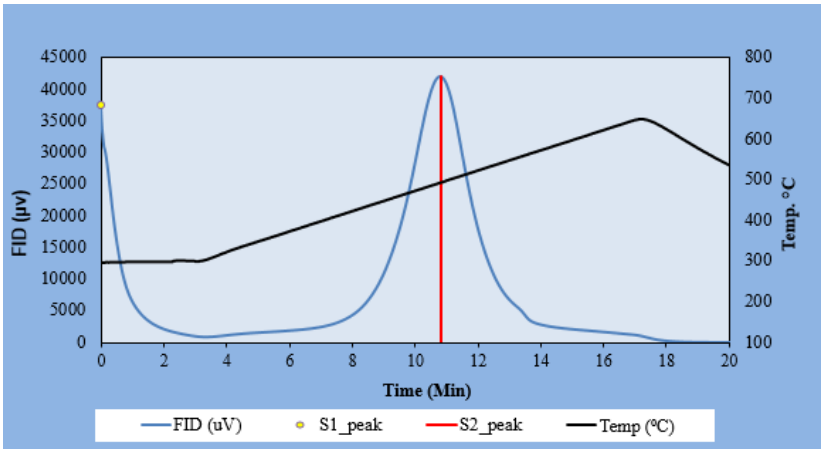

(a) Default Method.

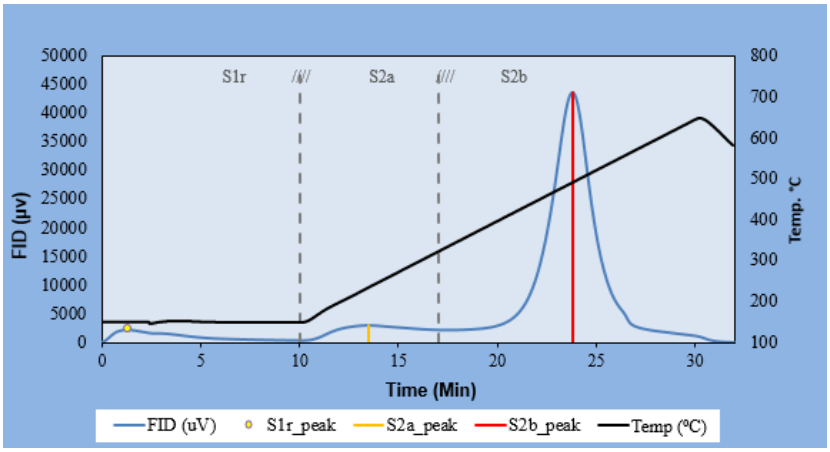

(b) Reservoir Method.

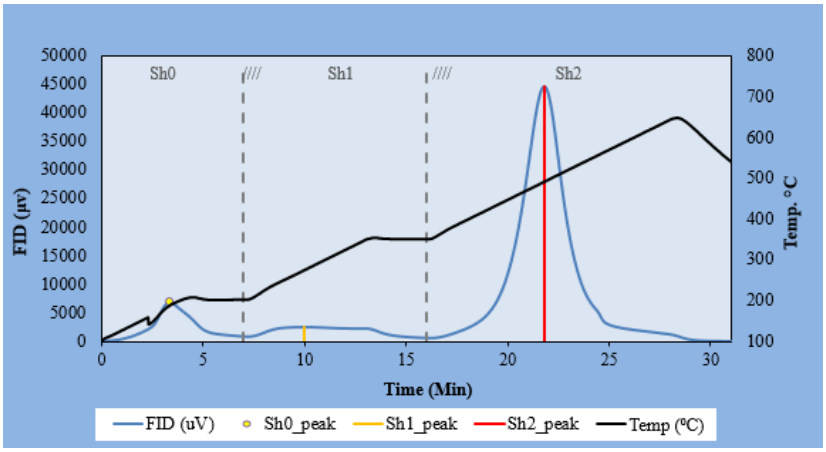

(c) Shale reservoir method.

Fig. 2.7. Rock-Eval data analysis programs of Sample 1 using the three different methods.

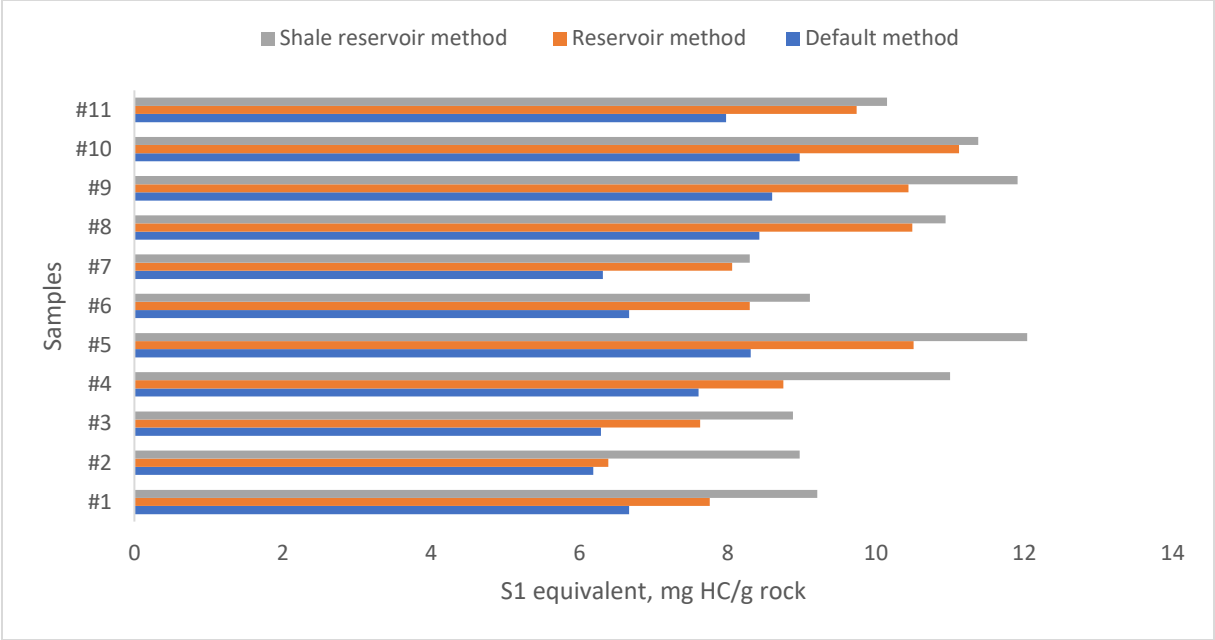

Fig. 2.8. Comparison of the S1 peak from default method and the S1 equivalent from the reservoir and shale reservoir methods.

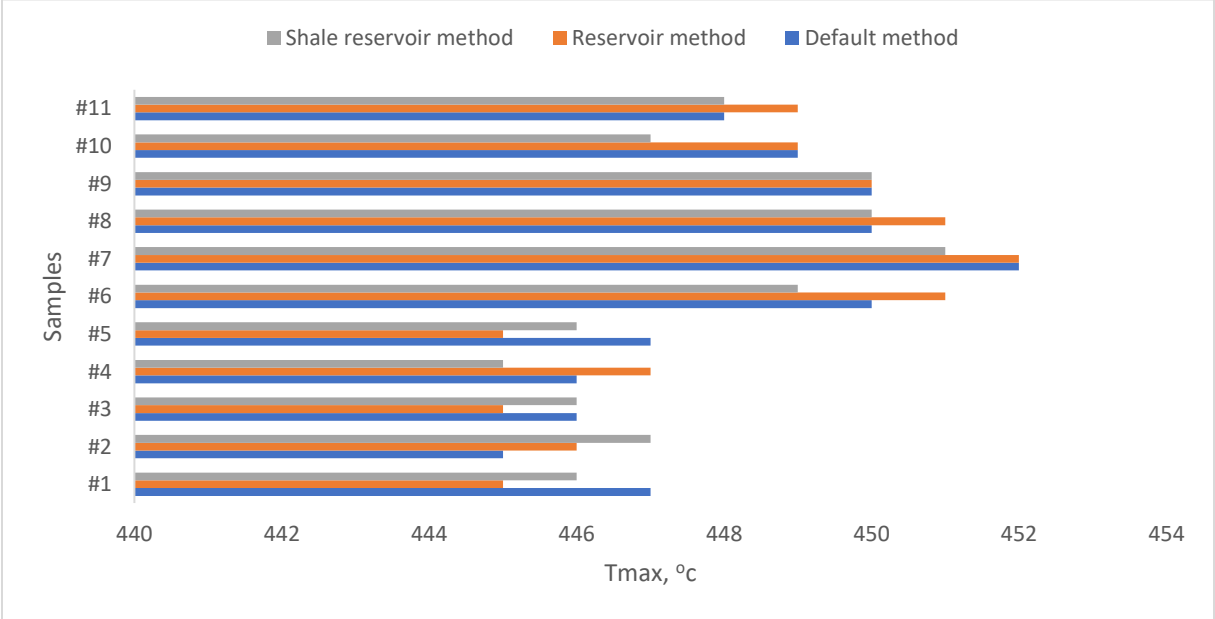

Fig. 2.9. Comparison of the Tmax derived from the three methods.

Based on the shale reservoir method, the geochemical analysis data for all 11 samples is shown in Table 2.2.

Table 2.2. Geochemical analysis results of the samples, using the shale reservoir method

Sample	TOC	*Oil in Rock	Light Oil%	Heavy Oil%	NSO or KERO%
	wt%	bbl oil/ac-ft	% TOC	% TOC	% TOC
#1	12.80	201.61	3.25	3.16	93.58
#2	16.83	196.35	1.95	2.80	95.25
#3	13.54	194.38	2.66	3.19	94.14
#4	12.30	240.79	3.61	4.36	92.02
#5	14.02	263.56	3.46	4.22	92.32
#6	13.06	199.42	2.75	3.49	93.76
#7	10.09	181.69	3.46	3.90	92.63
#8	11.46	239.48	3.95	4.60	91.45
#9	16.96	260.71	2.99	3.29	93.72
#10	10.21	249.11	5.16	4.81	90.02
#11	10.55	222.18	4.19	4.42	91.39

Note: bbl/ ac-ft means barrels per acre-foot. Explanations of these parameters can be seen in appendix

The data in Table 2.2 show that all Bakken Shale samples used in this study are organic-rich and have considerable remaining hydrocarbon generating potential. The thermo-vaporizable hydrocarbons are very low and most of the remaining potential is due to the cracking of heavy hydrocarbons, NSO (Resins + Asphaltenes) and kerogen. The organic matter plots in the mixed II/III type (oil and gas-prone) region and in the oil window zone (mature stage of hydrocarbon generation) are shown in Fig. 2.10. A positive intercept with the TOC axis in Fig. 2.10a indicates the possible existence of approximately 1.5wt% residual or 'dead' carbon in the Bakken Shale (e.g., Cornford et al, 1998). In addition, the samples from each well were plotted based on whether they came from the Upper or the Lower Bakken intervals (Fig. 2.10a). Samples from the Upper and Lower Bakken have almost identical S2 values in Well #2 whereas the Upper Bakken has slightly higher S2 values than the Lower Bakken in Well #1 over the same TOC range. The 'dogleg' trend seen in Fig. 2.10a suggests that these two Bakken intervals likely have different organofacies. The same reasoning was applied by Halpern and Cole (1994) to explain the trend

seen in their samples. Furthermore, organic petrologic evidence showed the Lower Bakken to be richer in marine alginite [mostly very long (>200 micrometers) *Leioshaeridia*, as shown in Fig. 2.11c] whereas the Upper Bakken contained less algal matter (mainly Prasinophytes) and of considerably smaller size (Fig. 2.11e-f). Thus, it is likely that two different organofacies are responsible for the S2 vs. TOC trend.

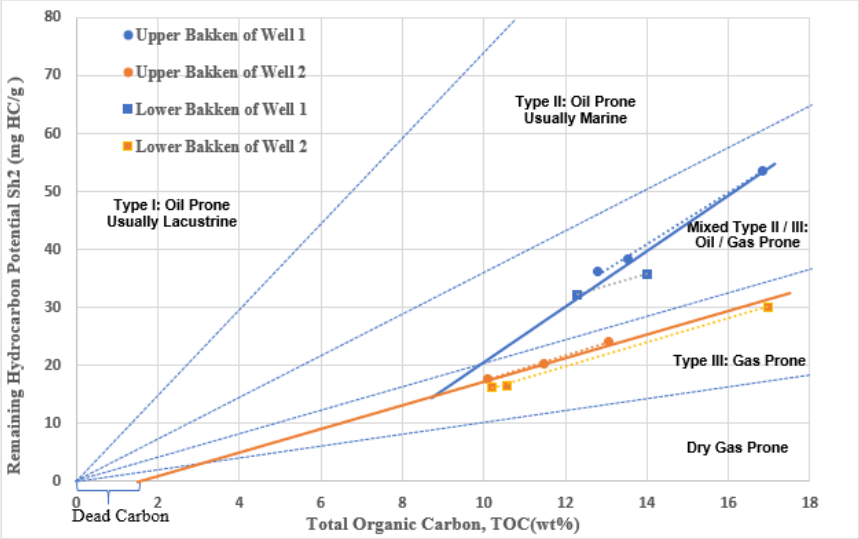

(a) Plot of S2 vs. TOC as a function of kerogen types

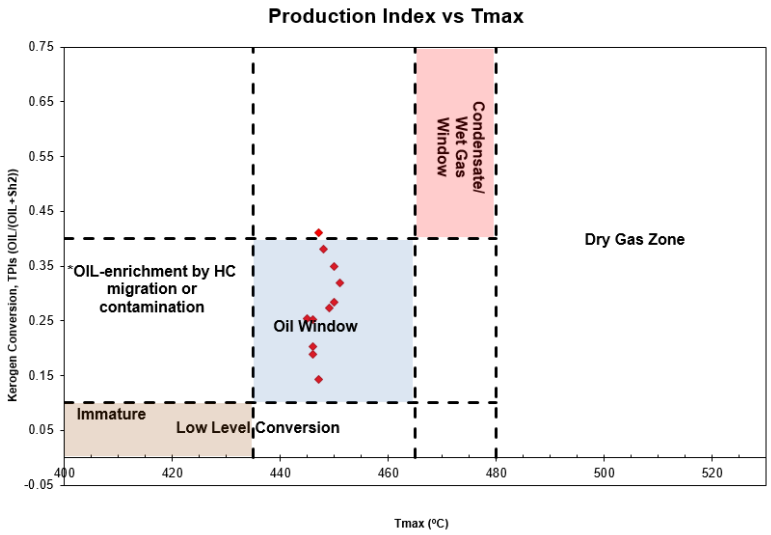

(b) Kerogen maturity analysis

Fig. 2.10. Kerogen type and maturity analysis.

2.4.2. Dispersed organic matter and Vitrinite reflectance.

Fig. 2.11 shows that the organic matter in those samples is comprised of two types of bitumen, a solid bitumen having light gray color in Sample #2 (Fig. 2.11a) and a low-reflecting bitumen having dark-grey color with internal orange reflections in Sample #5 (Fig. 2.11b). Also present is an oil-prone type of marine alginite (*Leiosphaeridia*-type) having mostly dull-yellow to orange or even light-brown fluorescence color under UV light excitation in Sample #4 (Fig. 2.11c) and diffuse hydrocarbons generated from algal matter in Sample # 5 (Fig. 2.11d). The fluorescence color of the alginite suggests that VRo is close to peak oil generation, i.e., at 0.90% (Mukhopadhyay, 1992). The samples are almost devoid of inertinite (type IV organic matter) and contain very little primary vitrinite (part of gas-prone type III organic matter). In the absence of reliable primary vitrinite particles, the vitrinite Ro-equivalent was calculated using the Jacob formula (Jacob, 1989) for all samples. In the sample from 10,435.7 ft, the depth at which the photomicrograph (Fig. 2.11a) was taken, the mean BRo is 0.77% and the mean VRo-eq is 0.88%. The VRo-eq calculated from the Tmax of the sample using the default Rock-Eval 6 pyrolysis method is 0.89% using the Barnett Shale model (Jarvie et al., 2001). Therefore, reflectance, fluorescence, and pyrolysis data all point to the dispersed organic matter being thermally mature and in the middle stage of the oil window (at or near peak oil generation). The remaining samples have VRo-eq values ranging from 0.85% to 0.98% (Fig. 2.12), thus confirming the mature stage of the organic matter.

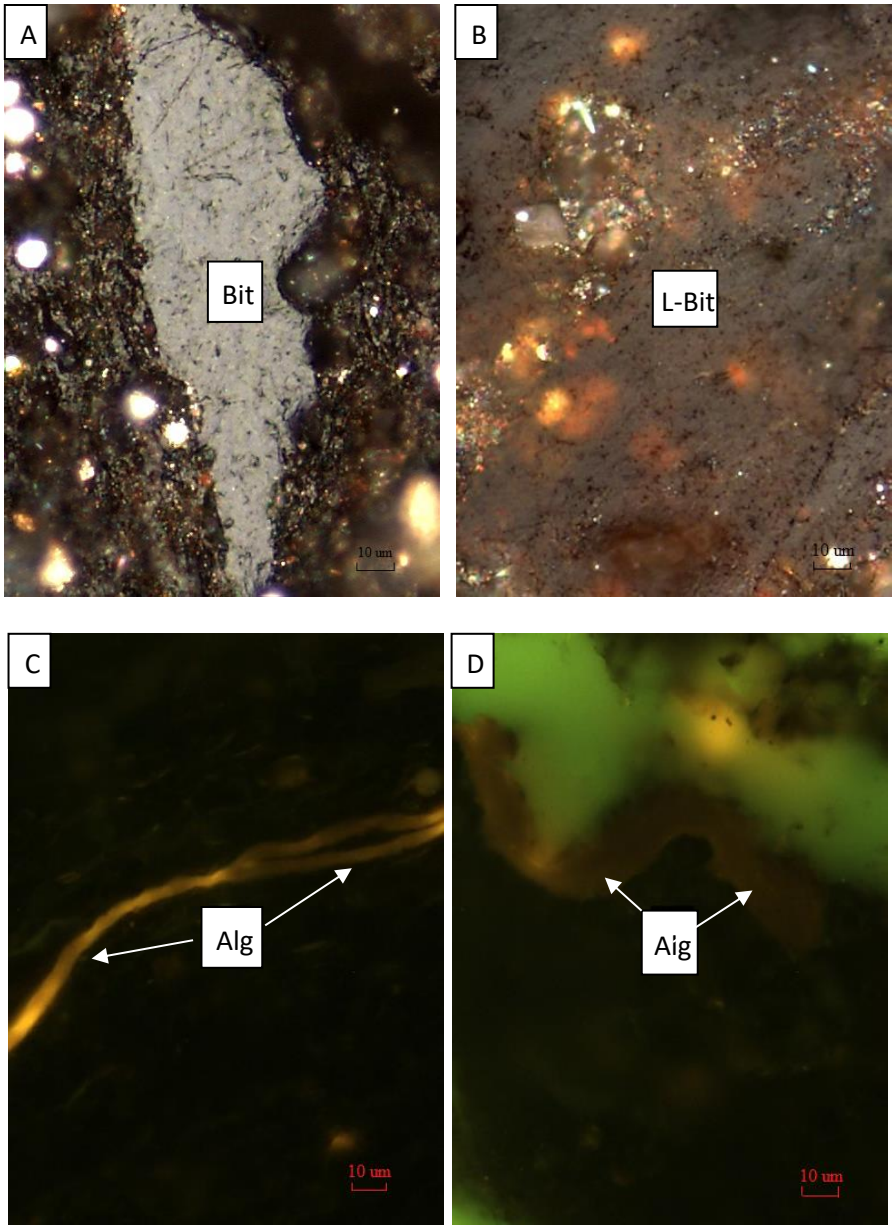
A
Bit
10 um
B
L-Bit
10 um
C
Alg
10 um
D
Aig
10 um

Fig. 2.11 cont

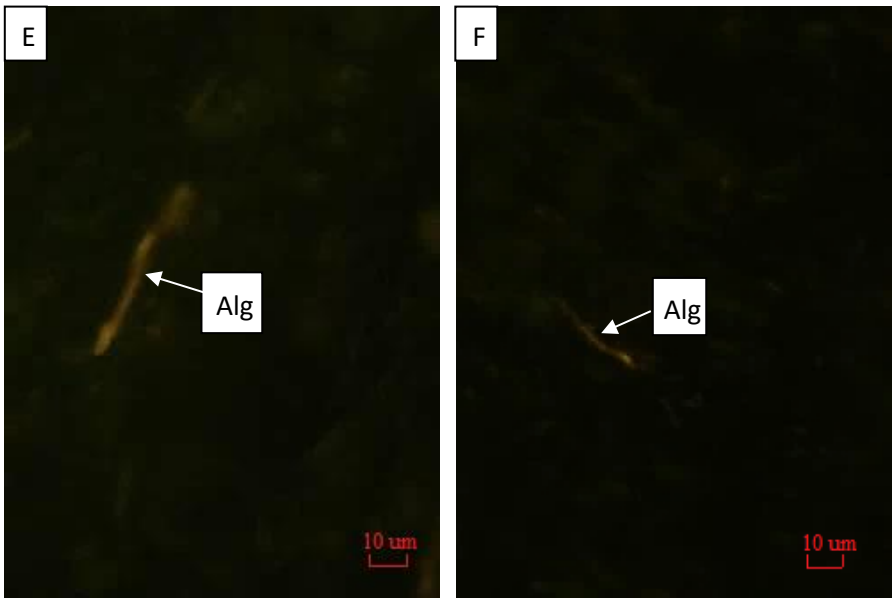

Fig. 2.11. Photomicrographs of Bakken Shale samples: (A) Well #1, Upper Bakken at 10435.7 ft, BRo=0.83% (VRo-eq=0.91%) showing primary bitumen (Bit) diffusing in the matrix; (B) Well #1, Lower Bakken at 10555 ft, BRo=0.29%, low-reflecting bitumen (L-Bit); (C) Well #1, Lower Bakken at 10541 ft, VRo-eq=0.90%, thin-walled *Leiosphaeridia* alginite (Alg) having dull-yellow fluoresce; and (D) Well #1, Lower Bakken at 10555 ft, dark greenish-brown weakly-fluorescing bitumen (Bit) generated from alginite; (E) and (F) Well #1, Upper Bakken at 10436.4 ft, showing small Prasinohyte algnite (Alg). Photos A and B were taken under white light, photos C-F were taken under UV light. Excitation filter is at 465 nm and combined beam splitter and barrier filter have a cut at 515 nm.

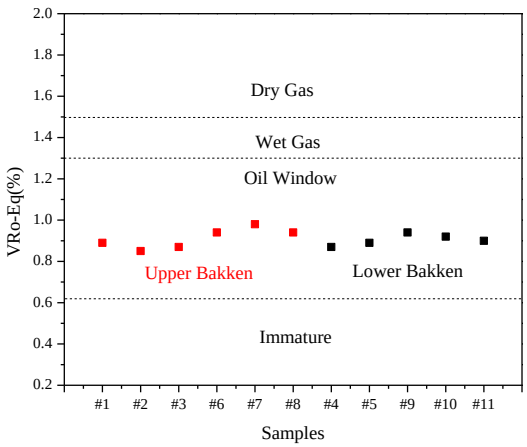

Fig. 2.12. Vitrinite reflectance of the 11 Bakken samples.

The plot of TOC vs. vitrinite reflectance-equivalent values is show in Fig. 2.13. The data illustrates that samples with high TOC do not have the highest VRo values. The reason there is no clear

relationship between TOC and VRo is that the maturity range of the 11 samples selected from the two wells varies very little (VRo-eq ranges from 0.85% to 0.98%). Within such a narrow thermal maturity range and with such high TOC samples, one would not expect to see a clear relationship between the two parameters.

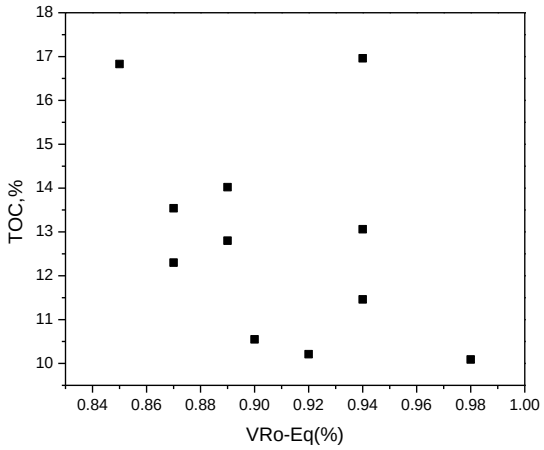

Fig. 2.13. The relationship between TOC and VRo-Eq.

2.4.3. Pore morphology.

Based on the results of Rock-Eval analysis, we picked the two samples (#2 and #9) with the highest TOC. Fig. 2.14 shows the SEM images of those two samples. Energy Dispersive X-ray Spectrometry (EDS) was applied to characterize the mineral compositions of the two samples. Quartz can be determined by the the presence of silicon and oxygen elements while K-feldspar can be characterized by the existence of potassium, silicon and oxygen and the trace of aluminum (Alstadt et al., 2016). The high concentrations of Fe (Iron)and S (Sulphur) can be used to indicate the pyrite mineral and the concentration of "Ca" can be used to study the presence of calcite. For the organic rich shale samples, the presence of organic matter can be identified by the large percentage of carbon atoms. (Abedi et al., 2016). Under low magnification, aligned mica flakes (mica) are visible and a discrete organic particle (op) belonging to a unicellular marine alginite is

noted. The bright white material is pyrite (py) and organic material appears black (Fig. 14a). Most of the fine to coarse silt-size grains are quartz (Q). Calcite (ca) noted in Sample 1 appears light gray in Fig. 2.14 a, while dolomite rhombs (d) are scattered across Sample 2 (Fig. 2.15a). No obvious pores can be found. Once the magnification was increased, pore-filling organic material (om) is seen intermixed within the siliceous and detrital clay matrix. A pyrite framboid (py), dolomite rhomb (d), and discrete organic particle (op) are noted (Fig. 2.14 b, Fig. 2.15b). For both samples, the organic particles are mostly non-porous. When the magnification is increased further, both samples have inter-particle pores along the edge of the organic matter and grain (Fig. 2.14c, Fig. 2.15c). Fig. 2.16 shows the representative EDS spectrum for each mineral in the shale samples.

Overall, in the 11 Bakken Shale samples analyzed, the organic matter is mostly non-porous. Inter-particle and intra-particle pores are the main pore types, which is quite different from the findings in many shale gas reservoirs where organic matter pores dominate the shale gas rock pore types (Milliken et al., 2013).

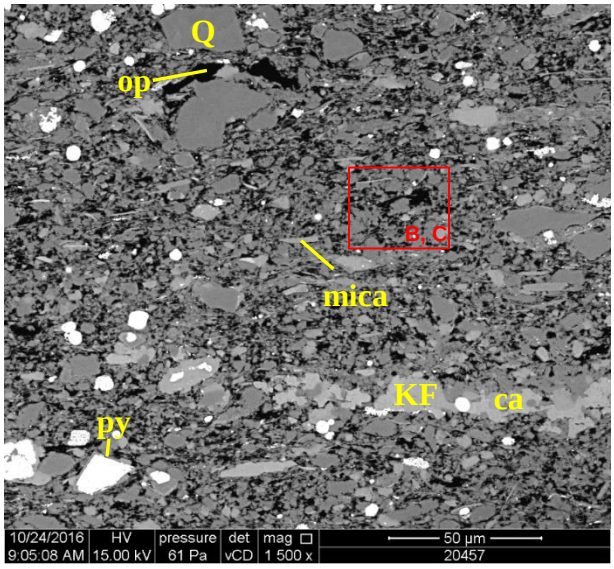

(a) Grain and pore morphology (BSE)

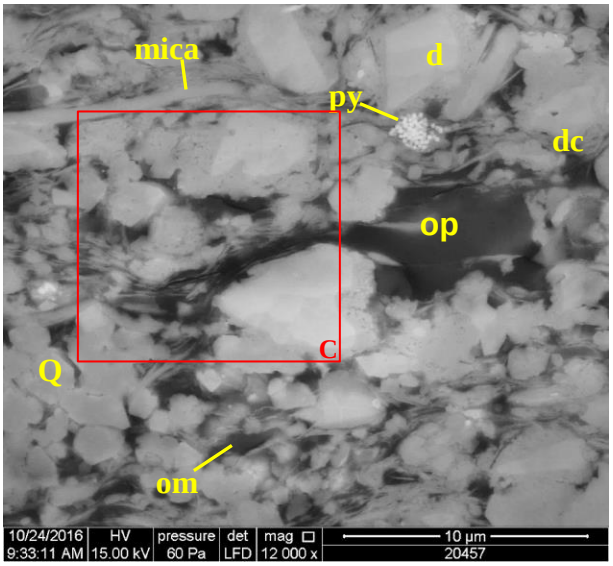

(b) Zoom in image of (a) (SE)

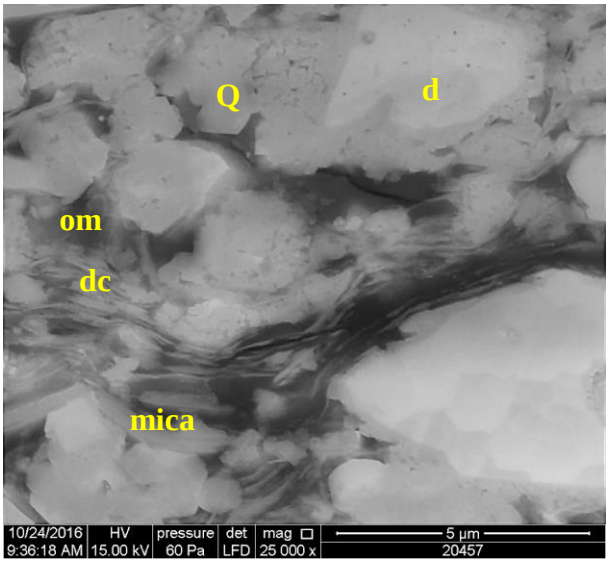

(c) Zoom in image of (b) (SE)

Fig. 2.14. Grain and pore morphology of Sample #2 (op donates discrete organic particle; py, d, dc, q, ca , KF and om represent pyrite, dolomite, detrital clay, quartz, calcite, potassium feldspar and pore-filling organic material, respectively).

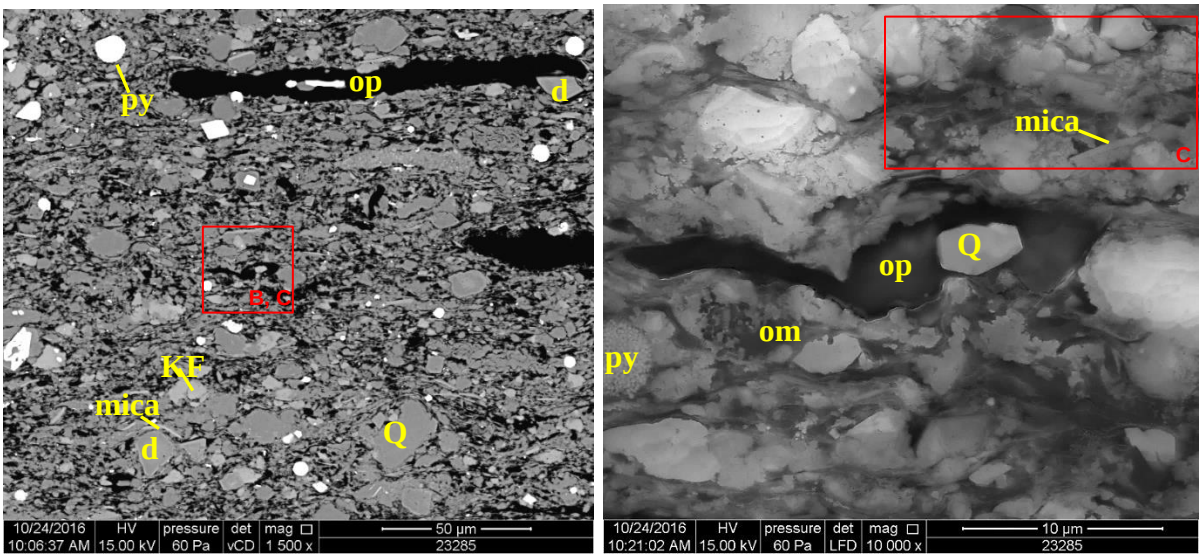

(a) Grain and pore morphology (BSE) (b) Zoom in image of (a) (SE)

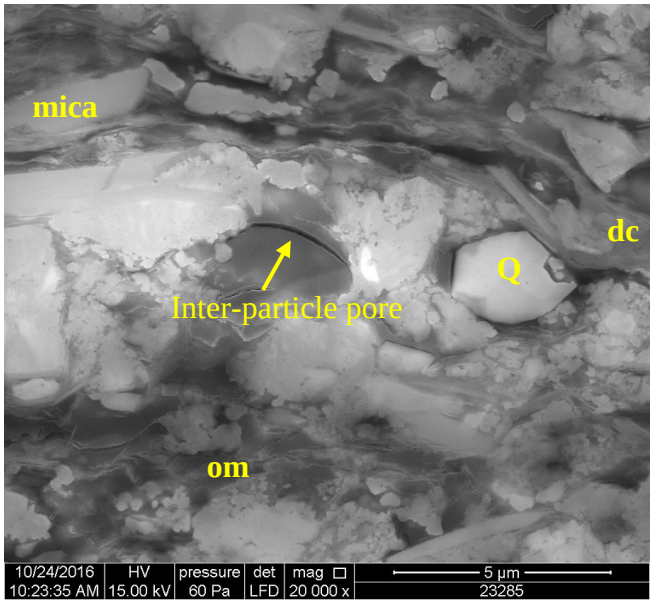

(c) Zoom in image of (b) (SE)

Fig. 2.15. Grain and pore morphology of Sample #9 (op donates discrete organic particle; py, d, dc, q, ca , KF and om represent pyrite, dolomite, detrital clay, quartz, calcite, potassium feldspar and pore-filling organic material, respectively).

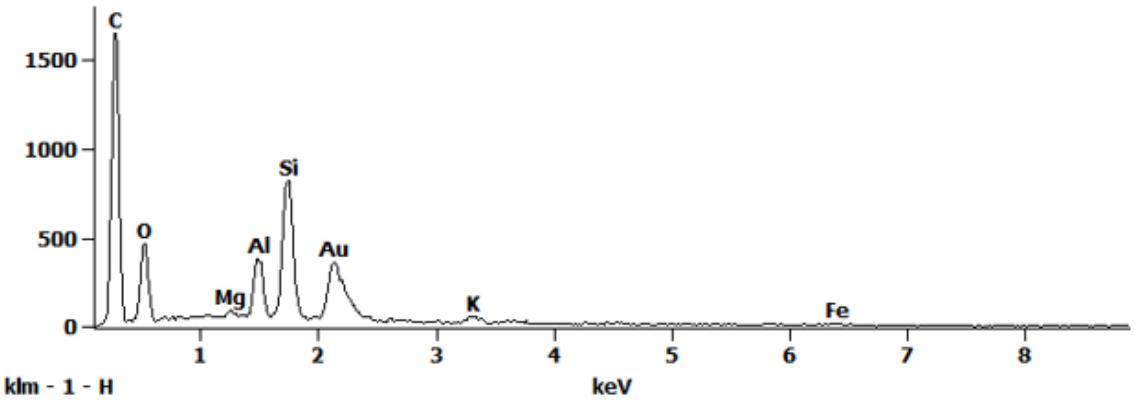

(a) Organic matter

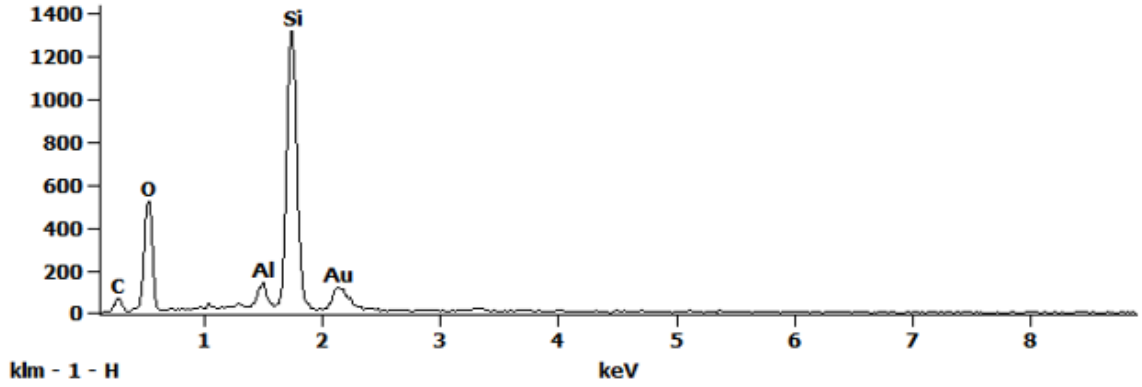

(b) Quartz

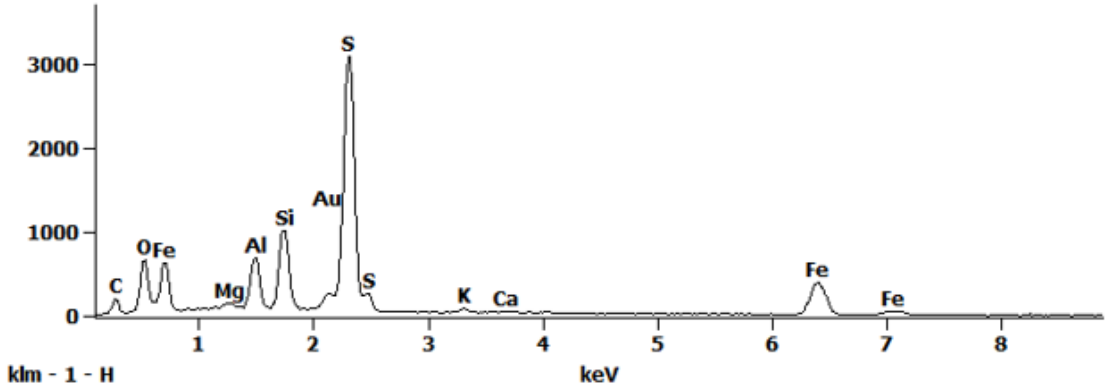

(c) Pyrite

Fig. 2.16 cont.

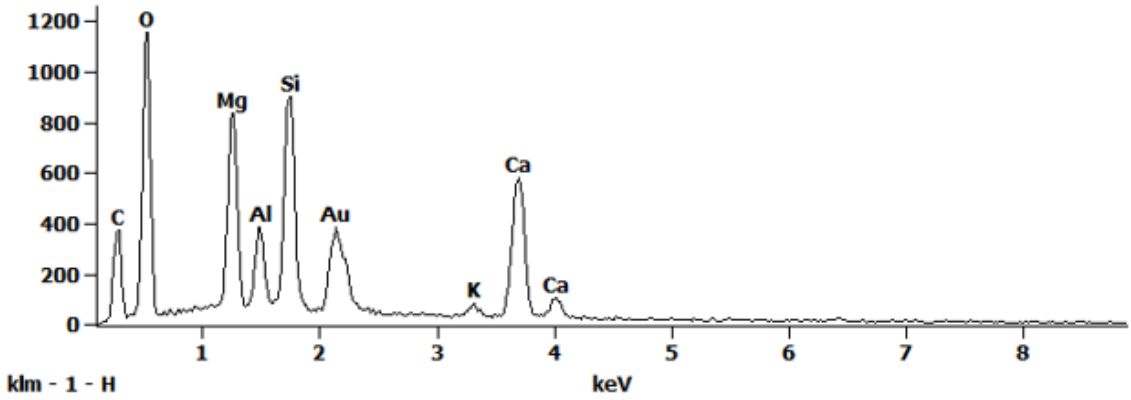

(d) Dolomite

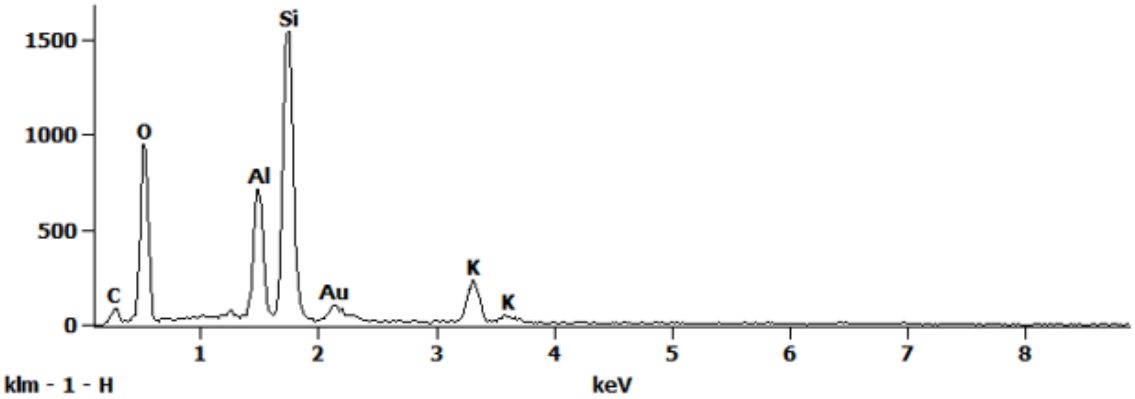

(e) K-feldspar

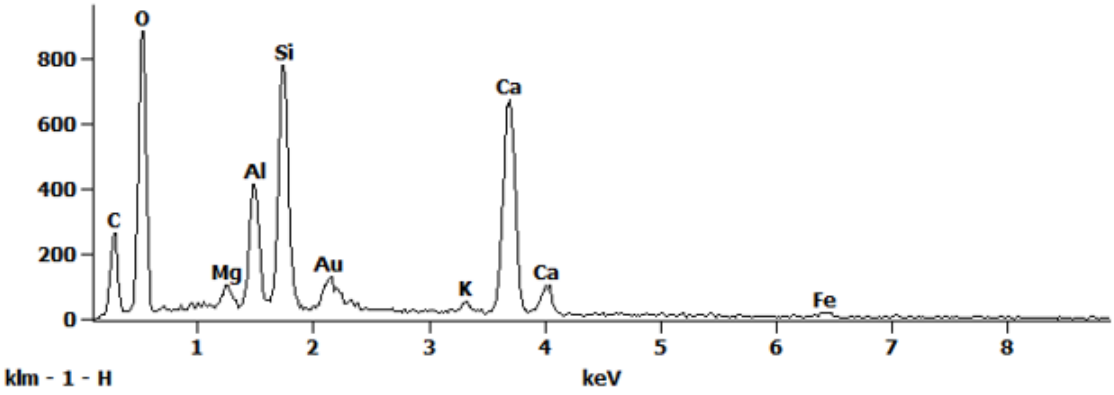

(f) Calcite

Fig. 2.16 cont.

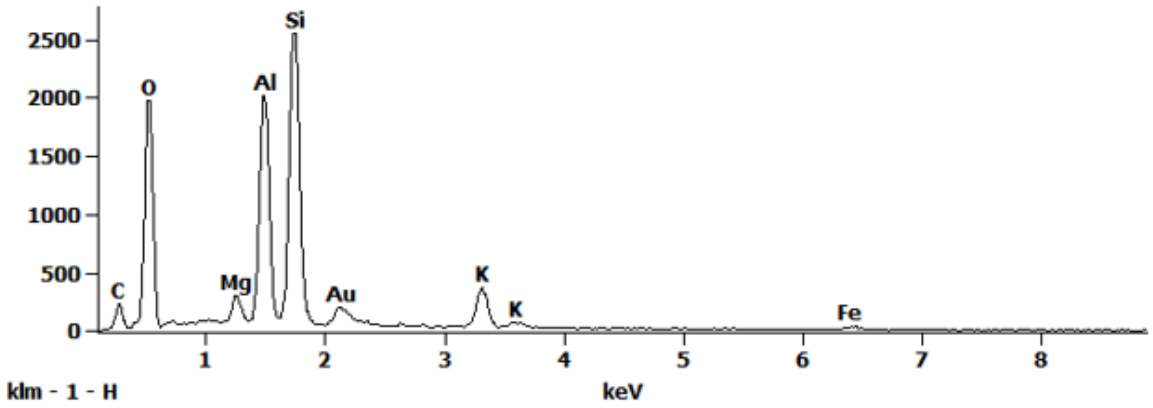

(g) Mica

Fig. 2.16. The representative EDS spectra for each mineral in samples #2 and #9 analyzed.

2.4.4. Quantitative pore structures analysis.

To quantitatively analyze the pore structures of the samples, the method of representative elementary area (REA) was used. REA for a porous medium has a minimum averaging area that will yield a value representative of the whole. The porosity indicator was used to determine the REA by analyzing the influence of the magnification on porosity (Saraji and Piri, 2015). For the samples studied, it was found that as the magnification was reduced (scan area increased), the porosity value oscillated until it remained steady under a critical magnification. The scan area under this critical magnification point was used as the REA. Fig. 2.17 shows the determination the REA of Sample #9 from Well #2, depth 11201 ft.

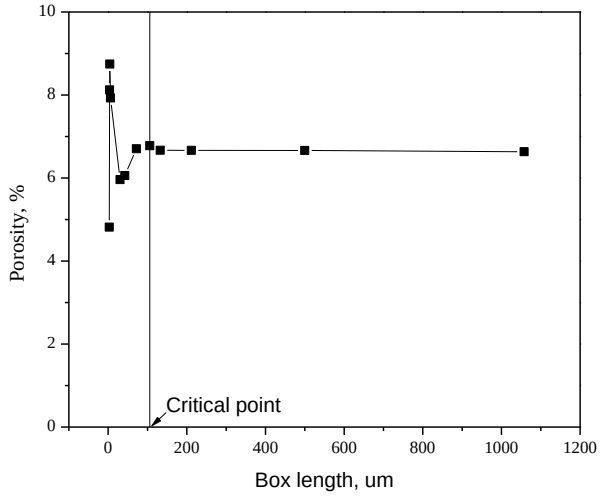

Fig. 2.17. The determination of the REA of Sample # 9 using a porosity indicator.

Based on determination of the REA, surface porosities of the samples were calculated. Table 2.3 shows that all the samples have abundant pore counts and most of the samples have very low porosity values (less than 10%). The data in Table 2.3 show that samples having high pore counts do not necessarily translate to also having high porosity values. This is because pore counts refer to the number of pores that exist in the samples while porosity refers to the ratio of the pore volume to the total sample volume. The study by Saraji and Piri (2015) shows that samples with large pore size and small pore counts can still have large porosity values. Thus, porosity should be determined by the combination of pore size and pore counts, not by pore counts alone. Pore counts were analyzed in this study because they can be used to analyze the fractal behavior of the pore structures, which will be discussed next.

Table 2.3. Porosities of the samples calculated from SEM images at their REA

Well	Sample	Bakken Location	Porosity, %	Pore counts
Well #1	#1	Upper Bakken	9.71	9823
	#2		8.58	14895
	#3		3.89	8968
	#4	Lower Bakken	9.59	21196
	#5		7.26	18443
Well #2	#6	Upper Bakken	9.97	5752
	#7		4.70	9818
	#8		9.63	12435
	#9	Lower Bakken	6.70	16837
	#10		7.67	10334
	#11		11.56	19495

The complexity properties of the pore structures were further studied by using fractal methods. Fig. 2.18 shows that the fractal dimensions are larger than 1.8 (dimensionless). By using the box counting method to calculate the fractal dimension in 2D, the fractal dimension value is expected to be in the range from 1 to 2 (dimensionless). When a value approaches or is close to 2, the pore structure is very complex (Liu et al., 2017). The D value of all the samples is above 1.8, which illustrates that all samples have very complicated pore structures.

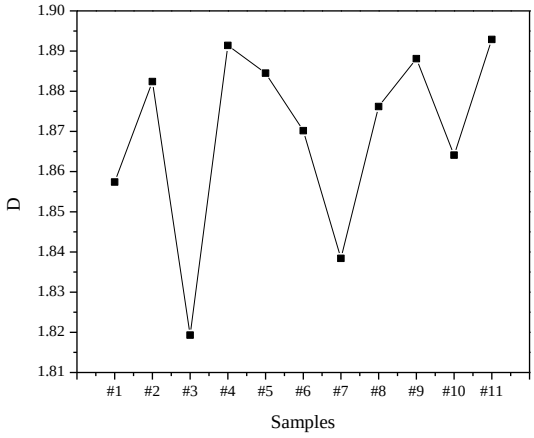

Fig. 2.18. The fractal dimension and lacunarity values of the samples.

The pore counts were plotted versus the fractal dimension, and a positive correlation was observed. The fractal dimension increases as the number of pores increase (Fig. 2.19). The positive relationship results from the fact that as the number of pores increases, the complexity of the pores also increases. This results in an overall increase in the fractal dimension and complexity of the pores (Dathe et al., 2001; Tang et al., 2012).

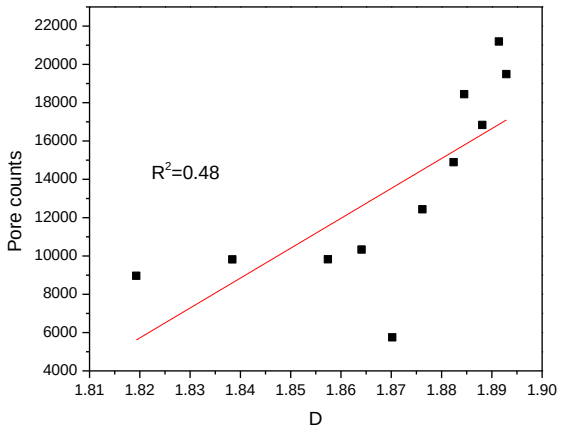

Fig. 2.19. The relationship between pore counts and fractal dimension.

The correlations between mineralogical composition and TOC content on one hand and the pore counts and porosity on the other were also investigated. The results are shown in Table 2.4. The data illustrate that the samples used in this study have the same minerals but in different weight ratios. In order not to eliminate the influence of one parameter on the other based on the bivariate plots, when in fact the parameter may exert a significant influence when it is joined by another independent parameter, PLS (partial least-squares regression) was applied. The composition of the samples (Quartz, Pyrite, Clay, Feldspar, and TOC) was treated as the independent parameter, and porosity and pore counts were used as the dependent variables. The fit parameters of the PLS model are shown in Table 2.5. The results show that for the porosity/pore counts, clays and feldspar have positive influence on the porosity/pore counts while quartz and pyrite has negative effects on

the porosity/pore counts. The increase of TOC can decrease the porosity/pore counts due to the extensive occurrence of non-porous organic matter. Among all components, TOC affects the porosity and pore count the most in this study.

We used the SEM quantitative analysis method to determine the pore parameters that could cause uncertainty due to resolution limitation. The minimum pore size we could analyze is 10 nm, which means that pores smaller than 10 nm that may exist in the shale samples cannot be detected by the SEM. Other methods, such as USANS (Ultra-Small-Angle Neutron Scattering) and gas adsorption, will be applied in a future study to analyze those pores smaller than 10nm and to study their impact on the pore parameters. A previous study (Liu and Ostadhassan, 2017) showed the presence of fractures and pores in Bakken Shale samples using the circularity index. The present study considers fractures as a special type of pores in the shale. It combined pores and fractures to analyze the impact of mineralogical composition on the pore structures (Deng et al., 2016). Our study did not consider whether the fractures are artifacts or real. Since our samples were prepared using the Argon ion milling method instead of standard mechanical polishing, it is expected that any artifacts will be fewer. However, one can still find artifacts between the different mechanical phases (i.e. solids and organic matter), which could be incorrectly interpreted as being inter-particle pores. One reliable way to distinguish whether a fracture is real or artificial is by using the EDX mapping method.

Table 2.4. Mineralogical composition of the samples (in wt%)

Samples	Quartz, %	Pyrite, %	Clays, %	Feldspar, %	TOC, %
#1	39.01	2.45	17.11	26.18	12.72
#2	47.88	2.15	18.82	8.42	17.45
#3	55.97	2.43	23.18	2.83	14.16
#4	41.30	5.01	29.88	9.67	12.12
#5	27.31	1.36	2.04	51.90	14.92
#6	39.92	2.30	39.23	3.33	14.71

#7	50.82	4.65	22.39	4.91	13.87
#8	52.14	5.30	26.97	2.25	10.10
#9	43.66	2.65	32.70	2.74	11.62
#10	36.20	4.28	27.15	5.43	17.73
#11	16.10	0.05	62.60	3.13	10.57

Table 2.5. PLS model fitting results

Variable	Porosity		Pore counts	
	Fit value	Standard deviation	Fit value	Standard deviation
Intercept	13.11	2.60	21894.92	3014.58
Quartz, %	-0.07	0.04	-113.50	45.95
Pyrite, %	-0.17	0.24	-295.43	470.20
Clays, %	0.03	0.03	44.93	65.11
Feldspar, %	0.01	0.02	19.23	69.33
TOC, %	-0.19	0.11	-316.77	165.71

2.5. Conclusions

The following conclusions are drawn from the analysis of the pore structures and geochemical properties of 11 Bakken Shale samples.

1) Of the three Rock-Eval analysis methods, the shale reservoir method is the best-suited method to characterize the geochemical properties of Bakken Shale, followed by the reservoir method. The shale reservoir method shows the Bakken to be organic-rich with considerable remaining hydrocarbon generating potential.

2) The thermo-vaporizable hydrocarbon content is very low; most of the remaining potential is due to the cracking of heavy hydrocarbons, NSO (Resins + Asphaltenes) and kerogen. The organic matter of the samples studied is mixed II/III type (oil and gas-prone) and plots in the oil window zone (mature stage of hydrocarbon generation).

3) Organic matter is dominated by solid bitumen. Two types of bitumen were identified. The low-Ro bitumen exhibits dull-yellow to light-brown fluorescence. Oil-prone marine alginite having

dull-yellow fluorescence was also identified. The vitrinite reflectance equivalent (based on the solid bitumen) ranges from 0.85% to 0.98%, indicating a level of maturity equivalent to peak oil generation.

4) Pores of various sizes (mostly in the nanoscale range) are widely distributed in the Upper and Lower Bakken samples. The majority of the organic matter is non-porous.

4) The porosity in the Bakken samples is low -- most of the samples have values less than 10%. Fractal dimension is a useful indicator and can reflect the complexity of the pore structures of the shale samples.

5) Clay minerals and feldspar have a positive influence on the porosity and pore counts while quartz, pyrite, and TOC have a negative influence. TOC affects the porosity and pore counts the most.

Appendix I. Definitions/formulae of the parameters from the Rock Eval method

For the Shale reservoir method:

- Oil in rock = 21.89 * (Sh0 + Sh1)
- Light oil, % = Sh0 (%)
- Heavy oil, % = Sh1 (%)
- Sh0 refers to the thermo-vaporizable light hydrocarbons (C1-C15)
- Sh1 refers to medium-heavy oil or thermo-vaporizable hydrocarbons (C15-C40)
- Sh2 refers to the cracking of the remaining heavy hydrocarbons, NSO and/or kerogen,
- NSO% = Resins + asphaltenes %; undefined if TPIs < 0.4 (TPI refers to Reservoir Production Index)
- Kerogen % = Kerogen %; undefined if TPIs > 0.4

- TPIs= Production index for this method (Sh0+Sh1/Sh0+Sh1+Sh2)

For the reservoir method:

- S1r = Thermo-vaporizable light hydrocarbons (C1-C15)
- S2a = Heavy oil or thermos-vaporizable hydrocarbons (C15-C40)
- S2b = Cracking of remaining heavy hydrocarbons, NSO and/or kerogen
- TPIr = Reservoir production index = (S1r+S2a/S1r+S2a+S2b)
- Tmaxb = Pyrolysis temperature S2b
- Oil in rock = Thermo-vaporizable light + heavy hydrocarbons (S1r + S2a). This is equivalent to the S1 parameter from the Standard Rock-Eval method (Bulk-Rock method used for source-rock analysis)

2.6. References

Abedi, S., Slim, M., Hofmann, R., Bryndzia, T. and Ulm, F.-J., 2016. Nanochemo-mechanical signature of organic-rich shales: a coupled indentation–EDX analysis. Acta Geotech. 11(3), 559-572.

Alstadt, K.N., Katti, K.S. and Katti, D.R., 2016. Nanoscale Morphology of Kerogen and In Situ Nanomechanical Properties of Green River Oil Shale. J. Nanomech. Micromech. 6(1), 04015003.

Behar, F., Beaumont, V., De B., Penteado, H.L., 2001. Rock-Eval 6 technology: performances and developments. Oil Gas Sci. Technol. 56, 111–134.

Bowker, K.A., 2003. Recent development of the Barnett Shale play, Fort Worth Basin: West Texas Geological Society. AAPG Bull. 42, 1–11.

Carvajal-Ortiz, H., Gentzis, T., 2015. Critical considerations when assessing hydrocarbon plays using Rock-Eval pyrolysis and organic petrology data: Data quality revisited. Int. J. Coal Geol. 152, 113–122.

Chen, J., Xiao, X., 2014. Evolution of nanoporosity in organic-rich shales during thermal maturation. Fuel. 129, 173–181.

Chen, S., Wang, X., 2012. Hydraulic Fracturing Design and Its Effects on Oil Recovery in Bakken Formation. SPE162186 presented at SPE Canadian Unconventional Resources Conference in Calgary, Alberta. 30 October-1 November.

Chen, Y., Mastalerz, M., Schimmelmann, A., 2014. Heterogeneity of shale documented by micro-FTIR and image analysis. J. Microsc. 256, 177–189.

Clarkson, C.R., Solano, N., Bustin, R.M., Bustin, A., Chalmers, G., He, L., Melnichenko, Y.B., Radlinski, A.P., Blach, T.P., 2013. Pore structure characterization of North American shale gas reservoirs using USANS/SANS, gas adsorption, and mercury intrusion. Fuel. 103, 606–616.

Cornford, C., Gardner, P., Burgess, C., 1998. Geochemical truths in large data sets. I: geochemical screening data. Org. Geochem. 29, 519–530.

Curtis, M.E., Sondergeld, C.H., Ambrose, R.J., Rai, C.S., 2012. Microstructural investigation of gas shales in two and three dimensions using nanometer-scale resolution imaging. AAPG Bull. 96, 665–677.

Dathe, A., Eins, S., Niemeyer, J., Gerold, G., 2001. The surface fractal dimension of the soil–pore interface as measured by image analysis. Geoderma. 103, 203-229.

Deng, H., Hu, X., Li, H., Luo, B., Wang, W., 2016. Improved pore-structure characterization in shale formations with FESEM technique. J. Nat. Gas Sci. Eng. 35, 309-319.

Gerhard, L.C., Anderson, S.B. and Fischer, D.W. 1990. Petroleum geology of the Williston Basin. Interior cratonic basins: AAPG Memoir. 51, 507-559.

Gu, X., Cole, D.R., Rother, G., Mildner, D.F.R., Brantley, S.L., 2015. Pores in Marcellus Shale: A Neutron Scattering and FIB-SEM Study. Energ Fuel. 29, 1295-1308.Hackley, P.C., Araujo, C.V., Borrego, A.G., Bouzinos, A., Cardott, B.J., Cook, A.C., Eble, C., Flores, D., Gentzis, T., Gonçalves, P.A., Mendonça Filho, J.G., Hámor-Vidó, M., Jelonek,I., Kommeren, K., Knowles, W., Kus, J., Mastalerz, M., Menezes, T.R., Newman, J., Oikonomopoulos, I.K., Pawlewicz, M., Pickel, W., Potter, J., Ranasinghe, P., Read, H.,Reyes, J., De La Rosa Rodriguez, G., Fernandes de Souza, I.V.A., Suárez-Ruiz, I., Sýkorová, I., Valentine, B.J., 2015. Standarization of reflectance measurements in dispersed organic matter: results of an exercise to improve interlaboratory agreement. Mar. Pet. Geol. 59, 22–34.

Halpern, H. I., Cole, G. A., 1994. An explanation for the positive organic carbon intercepts on Rock-Eval S2 versus TOC plots - an example from Saudi Arabia: Arabian J. Sci. Eng. 19, 299–307.

Havens, J.B., Batzle, M.L., 2011. Minimum horizontal stress in the Bakken formation. ARMA 11-322 presented at the 45th U.S. Rock Mechanics / Geomechanics Symposium in San Francisco, California. 26-29 June.

Hemes, S., Desbois, G., Urai, J.L., Schröppel, B., Schwarz, J.-O., 2015. Multi-scale characterization of porosity in Boom Clay (HADES-lever, Mol, Belgium) using a combination of X-ray μ-CT, 2D BIB-SEM and FIB-SEM tomography. Micropor Mesopor Mat. 208, 1–20.

Houben, M.E., Barnhoorn, A., Wasch, L., 2016. Microstructures of Early Jurassic (Toarcian) shales of Northern Europe. Int. J. Coal Geol. 165, 76–89.

Jacob, H., 1989. Classification, structure, genesis and practical importance of natural solid oil bitumen ("migra-bitumen"). Int. J. Coal Geol. 11, 65-79.

Jarvie, D.M., Claxton, B., Henk, B., Breyer, J., 2001. Oil and Shale Gas from Barnett Shale, Ft. Worth Basin, Texas. AAPG National Convention, Denver, CO. 3-6 June.

Jiao, K., Yao, S., Liu, C., Gao, Y., Wu, H., Li, M., Tang, Z., 2014. The characterization and quantitative analysis of nanopores in unconventional gas reservoirs utilizing FESEM–FIB and image processing: An example from the lower Silurian Longmaxi Shale, upper Yangtze region, China. Int. J. Coal Geol. 128–129, 1–11.

Jin, H., Sonnonberg, S.A., and Sarg, J.F., 2015. Source Rock Potential and Sequence Stratigraphy of Bakken Shales in the Williston Basin. URTEC 2169797 Presented at Unconventional Resources Technology Conference in San Antonio, Texas. 20-22 July.

Karimi, S., Saidian, M., Prasad, M., 2015. Reservoir Rock Characterization Using Centrifuge and Nuclear Magnetic Resonance: A laboratory Study of Middle Bakken Cores. SPE 175069 presented at SPE Annual Technical Conference and Exhibition in Houston, Texas. 28-30 September.

Klaver, J., Desbois,G., Littke, R., Urai, J. L.,2016. BIB-SEM pore characterization of mature and post mature Posidonia Shale samples from the Hils area, Germany. Int. J. Coal Geol. 158:78–89.

Klaver, J., Desbois, G., Urai, J. L., Littke, R., 2012. BIB-SEM study of the pore space morphology in early mature Posidonia Shale from the Hils area, Germany. Int. J. Coal Geol. 103, 12–25.

Lash, G.G., Blood, D.R., 2014. Organic matter accumulation, redox, and diagenetic history of the Marcellus Formation, southwestern Pennsylvania, Appalachian basin. Mar. Pet. Geol. 57, 244–263.

Liu, K., Ostadhassan, M., 2017. Quantification of the microstructures of Bakken shale reservoirs using multi-fractal and lacunarity analysis. J. Nat. Gas Sci. Eng. 39, 62–71.

Liu, K., Ostadhassan, M., 2017. Multi-scale fractal analysis of pores in shale rocks. J. Appl. Geophys.140, 1-10.

Loucks, R.G., Reed, R.M., Ruppel, S. C., Hammes, U., 2012. Spectrum of pore types and networks in mudrocks and a descriptive classification for matrix-related mudrock pores. AAPG Bull. 96, 1071–1098.

Loucks, R.G., Reed, R.M., Ruppel, S. C., Jarvie, D. M., 2009. Morphology, Genesis, and Distribution of nanometer-scale pores in siliceous mudstones of the Mississippian Barnett shale. J. Sediment Res. 79, 848–861

Mandelbrot, B.B., 1983. The fractal geometry of nature, first Ed. New York.

Marcon, V., Joseph, C., Carter, K.E., Hedges, S.W., Lopano, C.L., 2017. Experimental insights into geochemical changes in hydraulically fractured Marcellus Shale, Appl.Geochem. 76, 36–50.

Mastalerz, M., Schimmelmann, A., Drobniak, A., Chen, Y., 2013. Porosity of Devonian and Mississippian New Albany Shale across a maturation gradient: insights from organic petrology, gas adsorption, and mercury intrusion. AAPG Bull. 97, 1621–1643.

Milliken, K.L., Rudnicki, M., Awwiller, D. N., Zhang, T., 2013. Organic matter–hosted pore system, Marcellus Formation (Devonian), Pennsylvania. AAPG Bull. 97, 177–200.

Mukhopadhyay, P.K. 1992. Maturation of organic matter as revealed by microscopic methods: Applications and limitations of vitrinite reflectance, and continuous spectral and pulsed laser fluorescence spectroscopy. In: Wolf, K.H., Chilingarian, G.V. (Ed.), Diagenesis II: Developments in Sedimentology, 47, Elsevier Science Publishers, pp.435-510.

Nelson, P.H., 2009. Pore throat sizes in sandstones, tight sandstones, and shales. AAPG Bull. 93, 1–13.

Pitman, J. K., Price, L. C., LeFever, J. A. 2001.Diagenesis and fracture development in the Bakken Formation, Williston Basin: Implications for reservoir quality in the middle member. U.S.G.S.Professional Paper 1653.

Romero-Sarmiento, M.-F., Pillot, D., Letort, G., Lamoureux-Var, V. , Beaumont, V. , Hu A.-Y., Garcia, B., 2015. New Rock-Eval Method for Characterization of Unconventional Shale Resource Systems. Oil Gas Sci. Technol. 71, 1-9.

Sayers, C.M., Dasgupta, S., 2014. Elastic anisotropy of the Middle Bakken formation. Geophysics. 80(1), 23-29.

Schneider,C.A., Rasband,W.S., Eliceiri,K.W., 2012. NIH Image to ImageJ: 25 years of image analysis. Nat. methods. 9(7), 671-675.

Ruhle, W., 2016. Refracturing: Empirical Results in the Bakken Formation. URTEC 2461740 presented at the Unconventional Resources Technology Conference in San Antonio, Texas.1-3 August.

Russell, D.A., Hanson, J.D., Ott, E., 1980. Dimension of Strange Attractors. Phys. Rev. Lett. 45, 1175-1178.

Saraji, S., Piri, M., 2015. The representative sample size in shale oil rocks and nano-scale characterization of transport properties. Int. J. Coal Geol. 146, 42-54.

Shale Industry News and Shale Information, 2013. Investing in Montana's Bakken.http://shalestuff.com/controversy-2/investing-montanas bakken / article 09593 / (accessed 13.10.29).

Shao, X., Pang, X., Li, Q., Wang, P., Chen, D., Shen, W., 2017. Pore structure and fractal characteristics of organic-rich shales: A case study of the lower Silurian Longmaxi shales in the Sichuan Basin, SW China, Mar. Pet. Geol. 80, 192–202.

Smith, M., Bustin, M., 1995. Sedimentology of the Late Devonian Early Mississippian Bakken Formation,Williston Basin. Presented at the the seventh International Williston Basin Symposium.23 July.

Sonnonberg, S.A., Jin, H., Sarg, J.F., 2011. Bakken Mudrocks of the Williston Basin, World Class Source Rocks. AAPG paper 80171 presented at AAPG Annual Convention and Exhibition at Houston, Texas. 10-13 April.

Tang, H.P., Wang, J.Z., Zhu, J.L., 2012. Fractal dimension of pore-structure of porous metal materials made by stainless steel powder. Powder Technol. 217, 383-387.

Wilson, A.,2014. Improved Conductivity and Proppant Applications in the Bakken Formation. JPT. 66(03), 96-100.

Wong, H.S., Head, M.K., Buenfeld, N.R., 2006. Pore segmentation of cement-based materials from backscattered electron images. Cement Concrete Res. 36, 1083-1090.

Zeng, Z., Jiang, A.,2009. Geomechanical study of Bakken Formation for improved oil recovery. SINOROCK 2009-067 presented at the ISRM International Symposium on Rock Mechanics in Hongkong, China. 19-22 May.

CHAPTER 3

QUANTIFICATION OF THE MICROSTRUCTURES OF BAKKEN SHALE RESERVOIRS USING MULTIFRACTAL AND LACUNARITY ANALYSIS

Abstract

Pore structures are one of the most important factors affecting the hydro-mechanical properties of the reservoirs. Unlike the homogeneous pore structures in sandstones, the pores in the shale formations are heterogeneous and more complex to characterize due to the diagenesis and geological processes that they experienced. The heterogeneous rock pore structures can influence not only the flow properties of the oil and gas but also the fracture initiation and propagation characteristics which can impact the hydraulic fracturing performance, a common technique to increase the total production in tight shale formations. Therefore, quantifying the heterogeneities of the pore structures in unconventional shale formations carries a great importance. In this paper, we collected the samples from Bakken formation, which is a typical unconventional oil shale reservoir in North America. We applied image analysis method to study the pore structures. After segmentation of these images, we determined the representative elementary area (REA) of the samples based on the relationships between porosity and magnification ratios. Multifractal theory and lacunarity methods were applied to analyze the pore structures. Multifractal parameters were used to describe the pore probability distributions and the lacunarity value was applied to quantify the heterogeneity of the pores. The impact of the mineral compositions on heterogeneity values is also discussed. Finally, a new REA indicator, which contains the porosity and heterogeneity information, was proposed.

3.1. Introduction

The Bakken shale in the Williston Basin in Montana, North Dakota (USA), is one of the largest unconventional shale oil plays in the world. The Bakken Formation consists of three members with the Middle Bakken Member, which is composed of mixed carbonates and fine-grained clastic, being the primary production zone.

The significant interest in production from unconventional plays including oil and gas shales has called for several studies to better characterize such complex resources. Pore structures which are distributed widely in the shale rocks can influence the hydrocarbon storage capacity and transportation properties (Anovitz and Cole, 2015). The pores existed in the shale may also impact the mechanical properties of the formation which can potentially affect the performance of hydraulic fracturing operations (Boadu,2000; Sanyal et al., 2006; Wang et al., 2012, Yuan et al., 2015a, b). Unlike the homogeneous pore structures in sandstones, the pores in shale formations are always heterogeneous. The heterogeneities which can be identified over the various scales from nanometers to meters will result in different properties of the rocks even at the same porosity (Vasseur, et al., 2015). The impact of the heterogeneity of the pore structures on shale's properties needs to be understood in order for economic production.

In the recent years, several methods have been introduced with some being applied to characterize the pore structures of the shale formation. Mercury Injection Capillary Pressure (MICP), Nuclear Magnetic Resonance (NMR) and image analysis are some of these techniques (Novitz et al., 2015; Somayeh et al., 2015, Deng, et al., 2016). MICP determines the largest entrance to a pore, instead of the actual pore size (Giesc, 2006), and the high injection pressure will distort, compress and damage the pore structures especially for the shale formations which has plenty of clay minerals (Liu et al., 2016a,b). The NMR, as a non-intrusive physical method, can be used to identify the pore structures of tight rocks (Odusina and Sigal, 2011). However, the sample preparation for the

NMR is very cumbersome, and the extraction and injection of the liquid can potentially damage the weak pore structures of the rock which can limit the accuracy of the NMR method, and the variations that occur in surface relaxtivity introduces error in the results (Liu, et al., 2016a, c). Image analysis techniques such as field emission scanning electron microscope (FESEM), transmission electron microscope (TEM) and atomic force microscope (AFM) can be applied to capture the pore structure of shale formation and can be further combined with statistics analysis method to quantify the pore structures such as pore size and pore shape distributions (Loucks et al.,2009; Javadpour, 2009, 2012; Liu, et al., 2016a,c; Bernard, et al., 2011; Klaver et al., 2012,2016). Heterogeneity analysis of the pore structures of shale formations still needs further studies.

Since Mandelbrot introduced the concept of the fractal (Mandelbrot,1977), measuring fractal dimensions has become a common practice for describing the properties of the porous media quantitatively (Jiang, et al., 2016; Chen, et al., 2015). The fractal dimension characterizes the average properties which is very suitable for the homogeneous rocks but is not able to describe the variations from the average (Gould, et al., 2011). The multifractal analysis which decomposes the self-similar measures into intertwined fractal sets, characterized by their singularity strength can provide more information about how the pore distributed than the single fractal dimension (Li, et al., 2012). The multifractal theory has been applied to study the pore structures of different kinds of rocks such as chalk, carbonate and shale gas formations and the results have been promising (Muller and McCauley, 1995,1996; Xie, et al., 2010). Lacunarity, which characterizes the distributions of the pores, has been applied in the study. The main applications of this method are in the medical and agriculture fields (Li, et al., 2012; Utrilla-Coello, et al., 2013; Neves, et al.,

2014). However, Lacunarity analysis has rarely been used to describe the texture properties of rock formations, especially for the unconventional reservoirs such as shale formations.

In this paper, we analyzed the pore structures of the shale rocks from Bakken Formation by using image analysis method. Multifractal dimensions and lacunarity method were applied to quantify the pore probability distributions and the heterogeneities of the pore structures. Based on the study of the magnifications on porosity and heterogeneity, we proposed a new method to determine the representative elementary area of the heterogeneous shale rocks.

3.2. Methodology

3.2.1. Sample description, preparation and SEM imaging.

The detailed procedure of these steps can be seen in section 2.3.3 and section 2.3.5.1.

3.2.2. Multi-fractal theory.

The single fractal dimension which is widely used to study the porous structures cannot describe the complex structures with subsets of regions having various properties. However, the multifractal theory, which considers the amount of mass inside each box, appears to be able to characterize the pore structure properties.

For the measurement of fractal dimension, the number $N(\varepsilon)$ of features of certain size ε scale as (Chhabra and Jensen, 1989, Mendoza, et al., 2010)

$$N(\varepsilon) \sim \varepsilon^{-D_0} \quad , \qquad (3\text{-}1)$$

where D_0 is called the fractal dimension, which is frequently be expressed as:

$$D_0 = \lim_{\varepsilon \to 0} \frac{\log N(\varepsilon)}{\log \frac{1}{\varepsilon}} \quad , \qquad (3\text{-}2)$$

D_0 can be derived by counting the number of boxes with various sizes to cover the object under investigation and then estimating the slope value from the log-log plot.

Then, the following equation will be applied to quantify the local densities by estimating the mass probability in the i^{th} box:

$$p_i(\varepsilon) = N_i(\varepsilon) / N_T \quad , \qquad (3\text{-}3)$$

Where $N_i(\varepsilon)$ is the number of pixels containing mass in the i^{th} box and N_T is the total mass of the system. Thus the probabilities in the i^{th} box $P_i(\varepsilon)$ can be written as the following equation:

$$P_i(\varepsilon) \sim \varepsilon^{\alpha_i} , \qquad (3\text{-}4)$$

where α_i is the singularity strength which can characterize the density in the i^{th} box (Feder, 1988; Halsey et al., 1986).

For multifractal measurements, a probability distribution is measured as:

$$\sum_i [p_i(\varepsilon)]^q \sim \varepsilon^{\tau(q)} \quad , \qquad (3\text{-}5)$$

where q is the exponent expressing the fractal properties in different scales of the object. τ_q can be defined as:

$$\tau(q) = \lim_{r \to 0} [\ln(\sum_i P_i(\varepsilon)^q] / \ln(1/\varepsilon) \quad , \qquad (3\text{-}6)$$

and the generalized dimension D_q which is related with q can be expressed as (Halsey et al., 1986):

$$D_q = \tau(q)/(q-1), \qquad (3\text{-}7)$$

Also, we can use the relationship between parameters of $f(\alpha)$ versus α to calculate the multifractal spectra:

$$N(\alpha) \sim \varepsilon^{-f(\alpha)}, \qquad (3\text{-}8)$$

Where $N(\alpha)$ is the number of boxes for which probability $P_i(\varepsilon)$ has singularity strengths between α and $\alpha+d\alpha$. $f(\alpha)$ contains the same information of generalized dimensions D_q and can be defined as (Halsey et al., 1986, Chhabra and Jensen, 1989):

$$f(\alpha(q)) = q\alpha(q) - \tau(q), \quad (3\text{-}9)$$

Where $\alpha(q)$ can be defined as:

$$\alpha(q) = d\tau(q)/dq. \quad (3\text{-}10)$$

3.2.3. Lacunarity.

In order to quantify the heterogeneities of the pore structures of the sample, lacunarity was introduced to solve this kind of problem. Lacunarity which was introduced by Mandelbrot (1983) is a counterpart of the fractal dimension which can be used to describe the size distributions. Lacunarity measures the deviation of a geometric object that has translational invariance and can be thought as a measure of gapiness of the geometric structure. If the structure has more wide or large gaps, the structure has higher lacunarity value.

The gliding-box counting algorithm was applied to calculate the lacunarity in this paper by utilizing a moving window (Smith et al., 1996; Plotnick et al., 1996). A box of size *r* is positioned at the upper left corner of the image and the number of the occupied sites can be regarded as the box mass. Then the box is moved one column to the right and the box mass is again counted. This process is repeated over all rows and columns of the image producing a frequency distribution, mass *M*, of the region that we studied. The number of the boxes with the size *r* containing a mass (*M*) of the image was designated by *n(M,r)*, with the total number of boxes counted designated by *N(r)*. If the image size is *P*, then:

$$N(r) = (P - r + 1)^2 \quad (3\text{-}11)$$

Then the probability distribution *Q(M, r)* can be calculated by the frequency distribution (Backes, 2013; Plotnick et al., 1993):

$$Q(M,r) = \frac{n(M,r)}{N(r)} \quad (3\text{-}12)$$

The first and second moments of this distribution are defined by:

$$A^{(1)} = \Sigma MQ(M,r) \quad (3\text{-}13)$$

$$A^{(2)} = \Sigma M^2 Q(M,r) \quad (3\text{-}14)$$

Then the lacunarity of this box size is defined as:

$$\Lambda(r) = \frac{A^{(2)}}{(A^{(1)})^2} \quad (3\text{-}15)$$

The statistical behavior of $\Lambda(r)$ can be understood by recognizing that:

$$A^{(1)} = u(r) \quad (3\text{-}16)$$

$$A^{(2)} = u(r)^2 + \sigma^2(r) \quad (3\text{-}17)$$

Finally, we can get (Allain and Cloitre, 1991; Malhi et al., 2008)

$$\Lambda(r) = \frac{\sigma^2(r)}{u(r)^2} + 1 \quad (3\text{-}18)$$

Here $\sigma^2(r)$ is the variance of the number of sites per box and $u(r)$ is the mean value of the number sites per box. Then we can repeat this process with different box size and get the set of the lacunarity values at various box size.

3.3. Results

3.3.1. REA determination.

It is well known that the results of image analysis are closely related to the image resolution or the scale at which the image is looked at. In general, as the scale increases the variation in the properties reduce and beyond a certain scale it remains unchanged. This scale is known as the representative elementary area (REA) in 2D and correspondingly representative elementary volume (REV) in 3D (Saraji and Piri, 2015; Deng, et al. 2016).

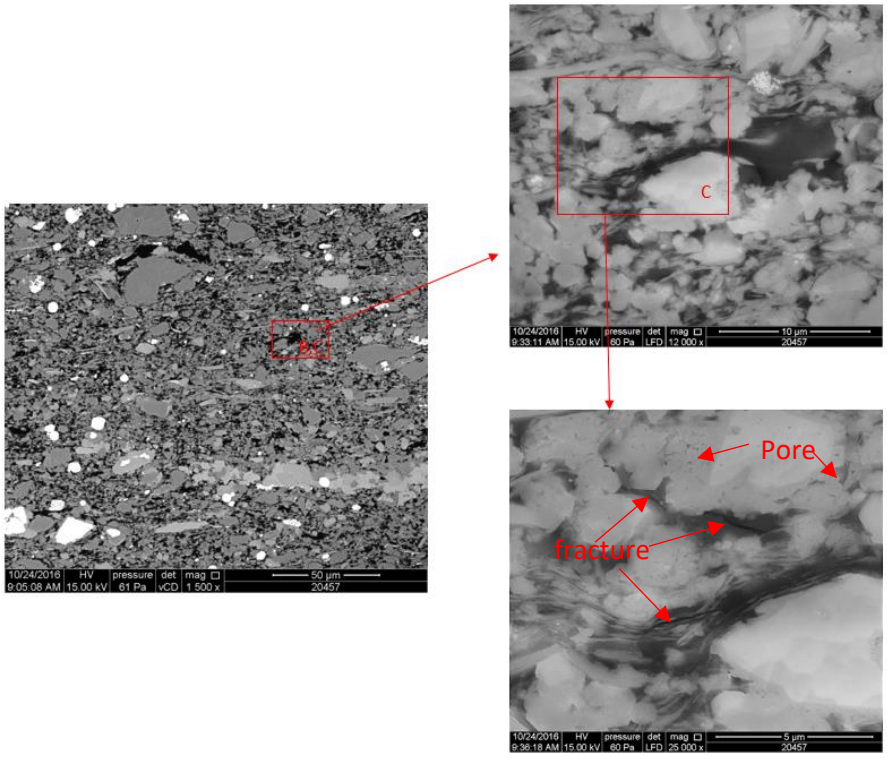

Fig. 3.1. Impact of magnification ratio on pore structures of Sample 12.

Fig. 3.1 illustrates that under the low magnifications, we can find large pores whereas under high magnifications, more of small size pores will appear in the image. We keep the center of the image fixed, change the magnification, and study the impact of the magnifications on the porosity of Sample 12, which is presented in Fig. 3.2a. Looking at Fig. 3.2b, the porosity keeps steady as the magnification increases and varies after the magnification reaches a critical value. The critical point at which the porosity starts to change can be regarded as the indicator for the REA. Therefore, the scan area corresponding to this magnification, i.e. 176um×176 um was chosen as the REA which is comparable with the results from other shales by other researchers (Toarcian shales 200um×200um: Houben et al., 2016; Boom clay 155um×155um: Hemes et al., 2015; Posidonia shale hils area, 140um×140um: Klaver et al., 2016; Opalinus clay 250um ×250um, Houben et al., 2014).

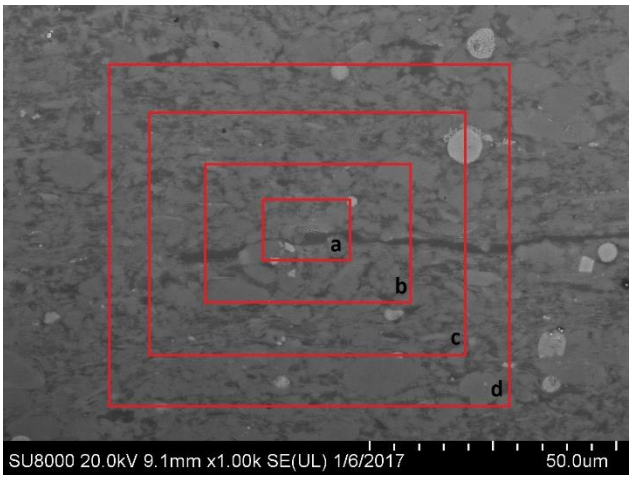

(a) Schematic of the REA analysis method

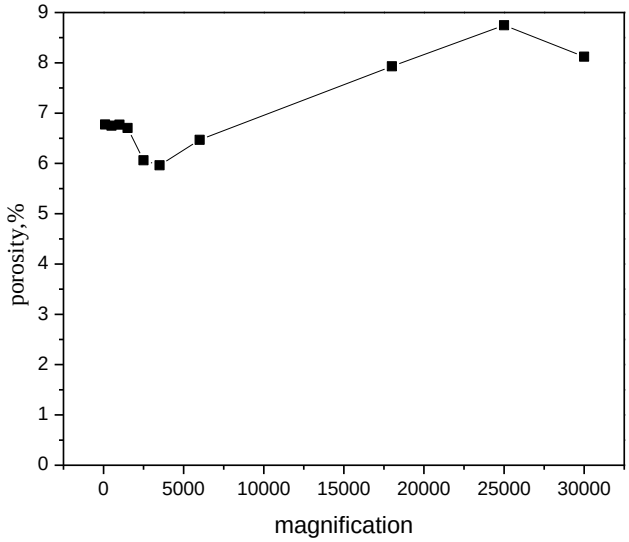

(b) Impact of the magnification ratios on the pore area fractions

Fig. 3.2. REA determination of Sample 12

3.3.2. Multifractal analysis.

Based on the determination of the REA, we segmented all the samples into binary format. Then we did multifractal analysis of all the samples. The mean of generalized dimensions (D_q) versus variable q (between -10 and +10) for the five samples are shown in Fig. 3.3.

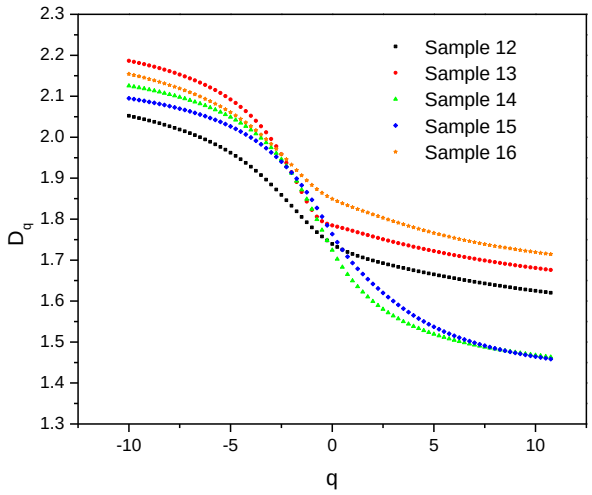

Fig. 3.3. Generalized dimensional spectra for the images of the five samples.

Fig. 3.3 shows that all samples follow a sigmoid fit and exhibit pronounced decreasing D_q values with increasing q. D_0, D_1 and D_2 are the three parameters that are commonly used for the multifractal analysis. D_0 is called the capacity dimension which provides the average values of the analyzed structure distribution, indicating the complexity of the pore structures. D_1 is called the information dimension and D_2 is the correlation dimension (Li et al., 2012). The values of these parameters for the samples tested in this study are listed in Table 3.1.

The parameters in Table 3.1 demonstrate that all the five samples have the same characteristics: $D_0>D_1>D_2$ confirming that the pore distributions of the five samples are multifractal. Sample 16 has the highest D_0 value while Sample 14 showing the smallest demonstrating that Sample 16 has the most complex pore structures as opposed to Sample 14 with the least complex pore structures. The ratio of D_1/D_0 is an indication of the dispersion of the porosity with respect to the pore size since it provides the information of proportional variation instead of the absolute variation (Mendoza et al., 2010). Sample 13 and Sample 14, correspondingly, carry the largest and lowest ratio D_1/D_0 among the five samples tested in this study.

Table 3.1. Values of D_0, D_1 and D_2 for the five samples

	D_0	D_1	D_2	D_1/D_0
Sample 12	1.7394	1.7149	1.6990	0.9859
Sample 13	1.7846	1.7716	1.7576	0.9927
Sample 14	1.7243	1.6495	1.5993	0.9566
Sample 15	1.7637	1.6930	1.6419	0.9599
Sample 16	1.8496	1.8289	1.8115	0.9888

The multifractal spectrum can be plotted to visualize the distribution of the pores of the samples. Fig. 3.4a illustrates the relationship between $\alpha(q)$ and q of the five samples. Similar to D_q, $\alpha(q)$ also decreases as q increases. As $q<0$, $\alpha(q)$ decreases steadily followed by a sudden drop. Fig. 3.4b shows the relationship between $f(\alpha)$ and $\alpha(q)$. Due to the difference of the D_0 values in the five samples tested, a shift is observed in the crest of the spectra from top to the bottom, which corresponds to the apex of the spectrum. Sample 16 has the largest $f(\alpha)_{max}$ value due to its largest D_0 value among all the samples.

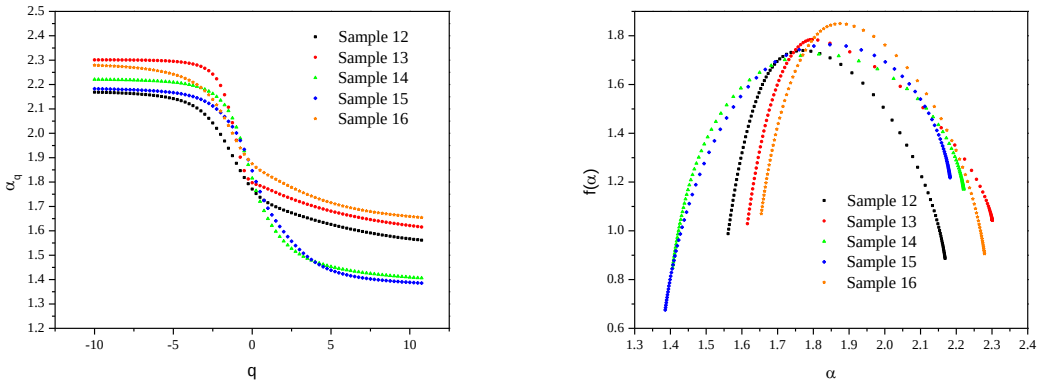

(a) $\alpha(q)$ versus q (b) $f(\alpha)$ versus $\alpha(q)$

Fig. 3.4. The multifractal spectrum of the five samples tested. a) $\alpha(q)$ versus q and b) $f(\alpha)$ versus $\alpha(q)$.

Table 3.2. Values of $\Delta\alpha$ and asymmetry values of singularity spectrum (A) of samples

Sample	α_{max}	α_{min}	α_0	$\Delta\alpha$	A
12	2.1688	1.5615	1.7711	0.6073	0.5270
13	2.3009	1.6157	1.7973	0.6852	0.3606
14	2.2210	1.4062	1.8156	0.8148	1.0099
15	2.1826	1.3855	1.8464	0.7971	1.3709
16	2.2792	1.6544	1.8748	0.6248	0.5450

From the curves in Fig. 3.4a, we can read the values of α_{max} and α_{min}, which indicate the fluctuation of maximum and minimum probability of pixels (Costa and Nogueira, 2015). The related extension of singularity length $\Delta\alpha$ which is defined as $\Delta\alpha = \alpha_{max} - \alpha_{min}$ can be calculated and the curve asymmetry of singularity spectrum (A) can be quantified based on the following equation (Hu et al., 2009; Shi et al., 2009):

$$A = \frac{\alpha_0 - \alpha_{\min}}{\alpha_{\max} - \alpha_0} \qquad (3\text{-}19)$$

The values of A calculated for the samples are shown in Table 3.2. The data in this Table show that Sample 3 has the highest value of the $\Delta\alpha$ whereas Sample 12 experiencing the lowest value. Sample 14 has the largest probability distribution and strongest multifractality. The asymmetry values of Sample 12, 13 and 16 listed in Table 3.2 are less than 1, i.e. the curve is left skewed, indicating the domain of low exponents and slight fluctuation, while the values of Sample 14 and Sample 15 are larger than 1, demonstrating the domain of large exponents and large fluctuation.

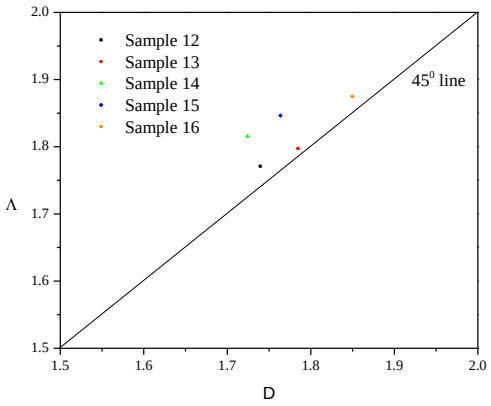

Fig. 3.5. Homogeneity of the five samples.

The magnitude of the difference in the values of α_0 and D_0 is a measure of heterogeneity (Li et al., 2012). Fig. 3.7 shows the plot of α_0 versus D_0 of the five tested samples. The data points of all samples deviate from the 45^0 line indicating that the samples are heterogeneous and should be described by the multifractal spectra rather than the monofractal dimension. From Fig. 3.5, it can also be found that the distance between Sample 14 and the 45^0 line is the largest, indicating that Sample 14 is the most heterogeneous one among all these samples.

3.3.3. Lacunarity analysis.

We changed the window moving size and calculated the related lacunarity. Fig. 3.6 shows the grids of the image at different scales for Sample 12, as an example. Then we plotted lacunarity values against a range of different moving window sizes and the results presented in logarithmic axes. Fig. 3.7 shows that the lacunarity values vary as the box size changes. In all cases, as the box size increases, the lacunarity value decreases. This is because at small spatial scales, the moving window size is much smaller than the size of the dominant textual components of the image, and most boxes are either mostly occupied or left empty. As a result, the variance of the number of occupied sites in a moving window is large, resulting in high lacunarity. As the box size increases, the size of the moving window increases and becomes larger than any repeating spatial pattern in

the image, the variance in the number of the occupied sites in the moving window diminishes and the lacunarity tends to unity (and its logarithm value tends to zero) (Malhi et al., 2008). The plots of Sample 12 and Sample 13 show lower values than those of Sample 14, 15 and 16, showing smaller lacunarity values.

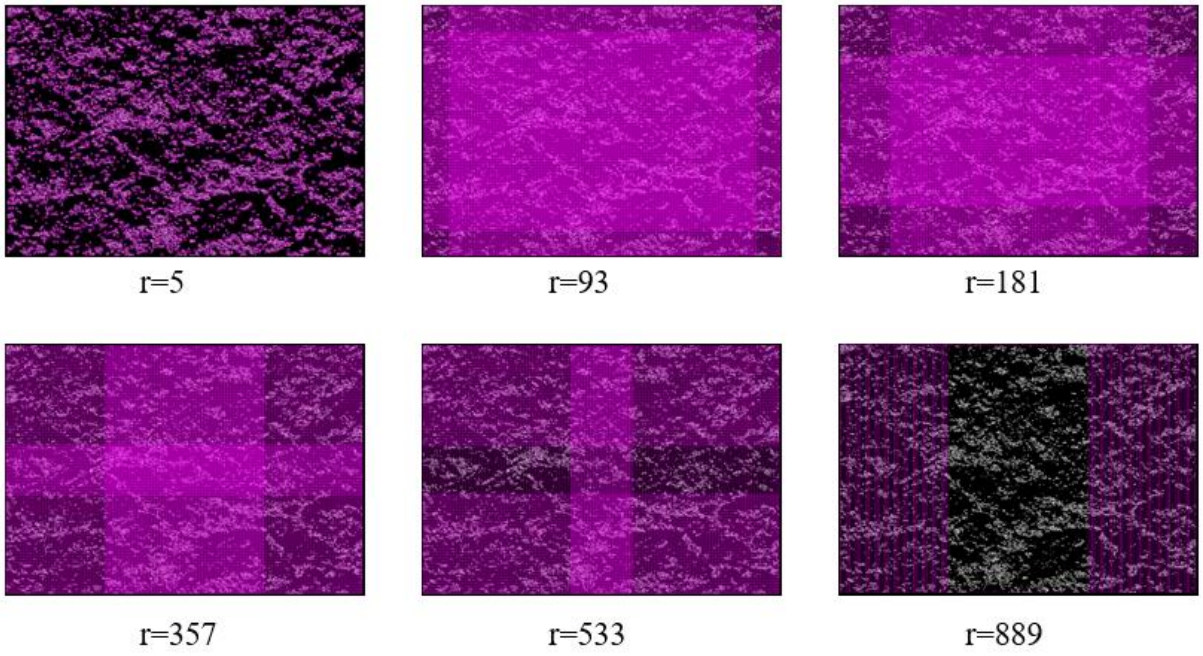

Fig. 3.6. SEM image of Sample 12 divided by grids with different length scale.

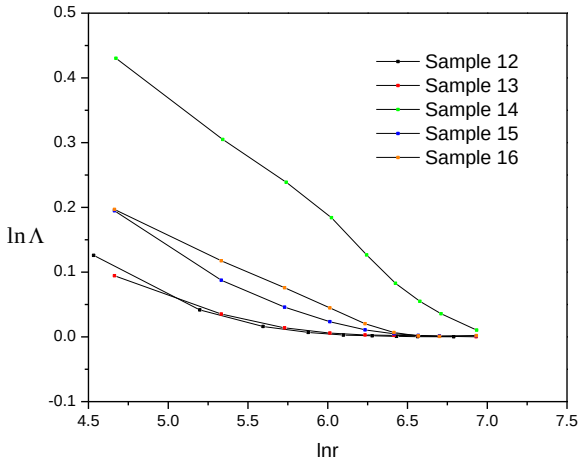

Fig. 3.7. Lacunarity analysis of five samples.

The mean lacunarity, which is to put the heterogeneity from one perspective and one series of grid sizes into an average, was calculated based on the following equation (Costa and Nogueira, 2015):

$$\Lambda = \frac{[\sum_i (1+\sigma(r)/u(r))^2]}{n(M,r)} \qquad (3\text{-}20)$$

The results of the calculations for the five samples are shown in Fig. 3.8.

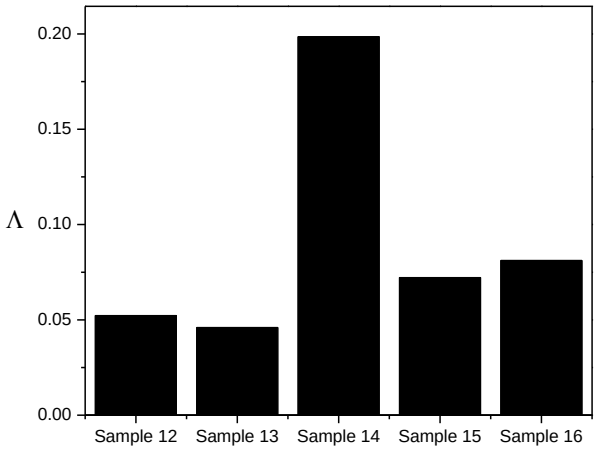

Fig. 3.8. Lacunarity values of five tested samples.

This figure shows that Sample 14 has the highest lacunarity value whereas Sample 13 has the lowest. As it was mentioned earlier, the sample with higher lacunarity exhibits larger gaps in the image, indicating more heterogeneity. Overall, from the lacunarity analysis, Sample 14 exhibits the most heterogeneous pore structure among all samples. We compared the heterogeneity analysis using both lacunarity and multifractal fractal methods. The results showed that we could derive the same results, i.e. Sample 14 is the most heterogeneous and Sample 13 is the most homogeneous among all the testing samples, which demonstrates that multifractal theory and lacunarity method can derive same results regarding the samples' heterogeneity.

One of the important reasons for the existence of the difference in the heterogeneity between the samples is due to the difference in their mineral compositions. Study of the mineral compositions of the five samples was done with an intention to derive some relationships between the mineral compositions and heterogeneities. Fig. 3.9 illustrates the influence of some primary mineral compositions of the samples we analyzed on the heterogeneity values. Based on the data of the five samples we can find that the relationships between the heterogeneity value and quartz and clay minerals can be described using the logarithmic function, while no clear correlation being observed between the heterogeneity and pyrite.

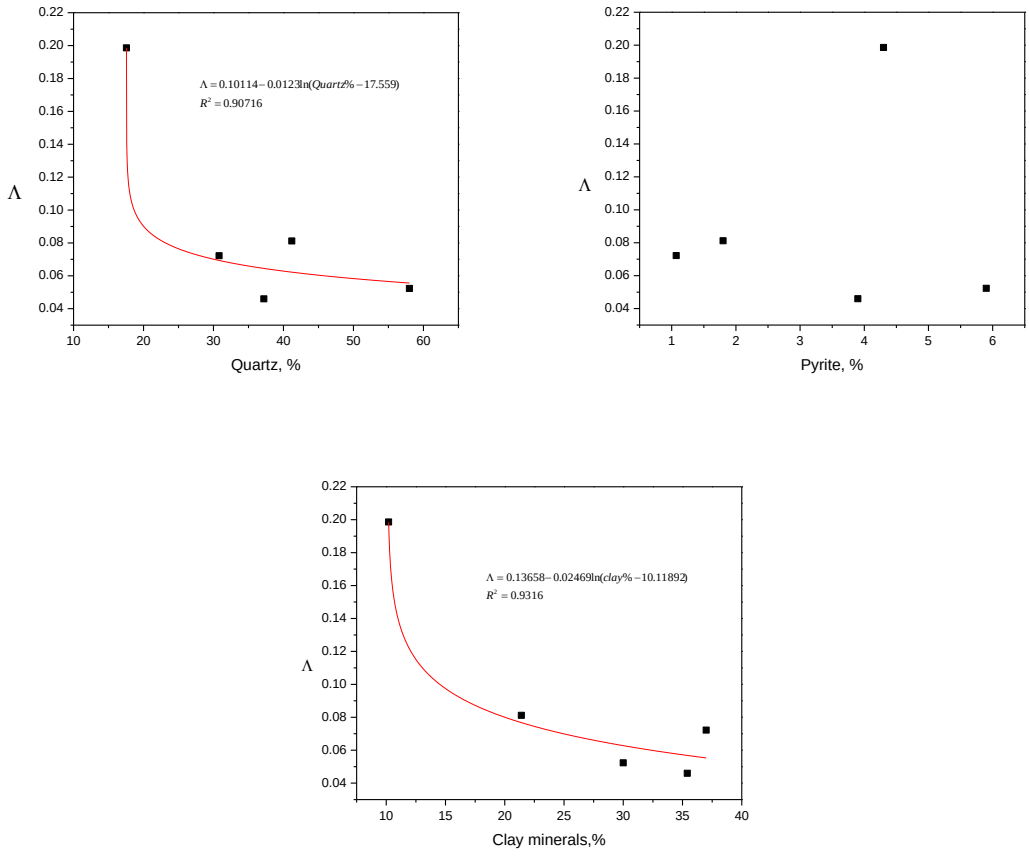

Fig. 3.9. Impact of the mineral compositions on the heterogeneity properties.

3.4. Discussions

The representative elementary area is necessary for the digital rock studies in order to use the properties of the porous rock under nano or micro scale to cover the macro scale properties. Since the introduction of using porosity as the indicator to determine the REA proposed by (Bear and Batchmet, 1990), REA has been applied in the field of soil (Vandenbygaart and Protz, 1990) and recently been used in shale rocks (Saraji and Piri, 2015; Deng et al., 2016). However, the remaining question is if this method is applicable for determining the REA images of the heterogeneous porous medium like shale? To answer this question, we plotted the lacunarity value and porosity value in Fig. 3.10 and found that no obvious correlations between Λ and φ can be established meaning that porosity cannot be used as a parameter to quantify the heterogeneity of the pore structure of these samples. The shortcoming of this method is the lack information about the heterogeneity which is an important parameter in shale pore structures.

We took Sample 12 as an example to further discuss the present REA model. For this sample, we chose 176um×176 um as the REA. Then we randomly moved this scan size across the whole sample surface to capture some images. Fig. 3.11 illustrates that the five images have similar porosity results but have various heterogeneities values, showing that using the porosity indicator to find the REA in shales cannot guarantee that all the images have the same heterogeneous properties. Thus, porosity indicator is not suitable for determination of the REA in shales, which are naturally heterogeneous. A new indicator, which combines the porosity and heterogeneity, should be used to determine the REA in heterogeneous pores such as shales.

We analyzed the impact of the magnification on the heterogeneity of Sample 12 which can be shown in Fig. 3.12. The heterogeneity value varies as the magnification decreases and then under a critical magnification value, the heterogeneity value keeps steady which is similar as the porosity in Fig. 3.4. We find the critical magnification point that the heterogeneity value starts to change as

the $REA_{(heterogeneity)}$, then we compare the scan size of $REA_{porosity}$ and $REA_{(heterogeneity)}$, and choose the larger scan size as the new REA. We also took Sample 12 as an example and found the scan size 600um×600um as the new REA. Then we randomly used this size to capture images through Sample 1 surface and the analysis results are presented in Fig. 3.13. The results showed that all the images have similar porosity and heterogeneity. The new indicator which includes both heterogeneity and porosity information can be a better indicator to describe the REA of heterogeneous samples like shale. In this paper, we focused on using the SEM to determine the REA of the shale porosity which is a 2D approach. For the 3D digital rock images, we should use the REV (representative elementary volume) to study the pore structures. However, similar to the REA determination in this paper, we also need to consider both porosity and heterogeneity information to consider the REV for heterogeneous rocks.

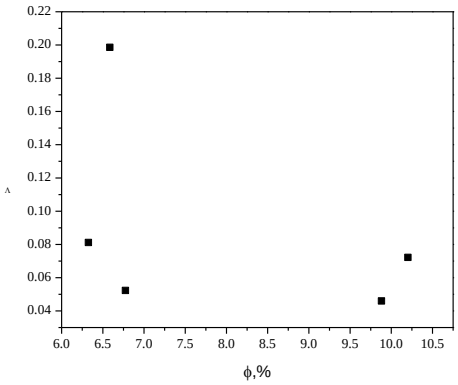

Fig. 3.10. Relationship between Λ and φ.

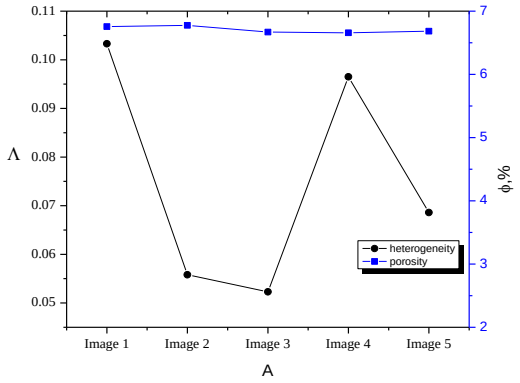

Fig. 3.11. Comparison of the properties of the image at the same scan size (176um× 176.39um).

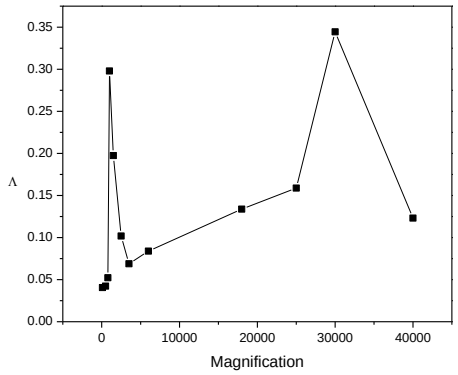

Fig. 3.12. Relationship between heterogeneity and magnification.

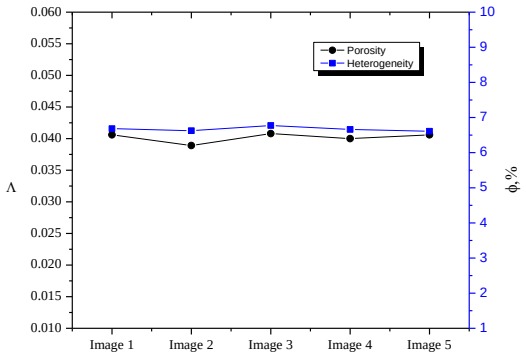

Fig. 3.13. Comparison of the properties of the image at the same scan size (600um× 600um).

3.5. Conclusions

The representative elementary area (REA) of five samples from Bakken Formation estimated from their SEM images based on the porosity indicator. Multifractal theory and lacunarity methods, being newly introduced in Petroleum Engineering applications, were applied to analyze the heterogeneities of pore structures of the shale samples under their REA using the porosity indicator. The variations of D_q with respect to q showed the existence of the multifractal properties of the pore structures. Sample 14 has the largest $\Delta\alpha$ which indicates its most complex probability distributions among all samples. The calculations of the lacunarity value, which can reflect the heterogeneous properties, showed that Sample 14 has the highest lacunarity value demonstrating that this sample has the most heterogeneous pore structure. The results of the heterogeneity analysis from the two indicators, i.e. multifractal value α_0/D_0 and lacunarity value Λ, are consistent with each other. Finally, we proposed a new indicator for REA determination for shale pore structure analysis based on the combination of heterogeneity and porosity.

3.6. References

Allain, C., Cloitre, M., 1991. Characterizing the lacunarity of random and deterministic fractal sets. Phys. Rev. A. 44, 3552-3558.

Anovitz, L.M., Cole, D.R., 2015. Characterization and Analysis of Porosity and Pore Structures. Rev. Mineral Geochem. 80, 61-164.

Backes, A. R., 2013. A new approach to estimate lacunarity of texture images. Pattern Recogn. lett. 34(13),1455–1461.

Bernard, S., Horsfield, B., Schulz, H.M., et al., 2012. Geochemical evolution of organic-rich shales with increasing maturity: A STXM and TEM study of the Posidonia Shale (Lower Toarcian, northern Germany). Mar. Pet. Geol. 31(1),70–89.

Boadu, F.K., 2000. Predicting the transport properties of fractured rocks from seismic information: numerical experiments. J. Appl. Geophys. 44(2–3),103-113.

Chen Y., Zou C., Hu S., et al., 2015. Fractal Characteristics of Shales Across a Maturation Gradient. Acta Geologica Sinica (English Edition). 89, 13-15.

Chhabra, A., Jensen, R.V.,1989. Direction of determination of the f(a) singularity spectrum. Phys. Rev. Lett. 62(12),1327-1330.

Costa, E.V.L., Nogueira, R. A., 2015. Fractal, multifractal and lacunarity analysis applied in retinal regions of diabetic patients with and without nonproliferative diabetic retinopathy. Fractal Geometry and Nonlinear Analysis in Medicine and Biology. 1(3), 112-119.

Deng, H., et al., 2016. Improved pore-structure characterization in shale formations with FESEM technique. J. Nat. Gas Sci. Eng.35(A), 309-319.

Feder, J., 1988. Fractals. Plenum Press, New York.

Giesch, H., 2006. MercuryPorosimetry:AGeneral(Practical)Overview. Part. Part. Syst. Charact. 23, 9–19.

Gould, D.J., Vadakkan, T. J., 2011 . Multifractal and Lacunarity analysis of microvascular morphology and remodeling. Microcirculation. 18(2),136-151.

Halsey, T.C., Hensen, M.H., Kadanoff, L.P., et al., 1986. Fractal measures and their singularities: the characterization of strange sets. Phys. Rev. A. 33(2), 1141-1151.

Hemes, S., Desbois, G., Urai, J.L., Schröppel, B., Schwarz, J.-O., 2015. Multi-scale characterization of porosity in Boom Clay (HADES-lever, Mol, Belgium) using a combination of X-ray μ-CT, 2D BIB-SEM and FIB-SEM tomography. Micropor Mesopor Mat. 208, 1–20.

Houben, M.E., Desbois, G., Urai, J.L., 2014. A comparative study of representative 2D microstructures in Shale and Sandy facies of Opalinus Clay (Mont Terri, Switzerland) inferred from BIB-SEM and MIP methods. Mar. Pet. Geol. 49, 143–161.

Houben, M.E., Barnhoorn, A., Wasch, L., 2016. Microstructures of Early Jurassic (Toarcian) shales of Northern Europe. Int. J. Coal Geol. 165, 76–89.

Hu, M.G., Wang, J.F., and Ge, Y., 2009. Super-Resolution Reconstruction of Remote Sensing Images Using Multifractal Analysis. Sensors. 9(11), 8669-8683.

Javadpour, F., Farshi, M.M., Amrein, M., 2012. Atomic-Force Microscopy: A new Tool for Gas-Shale Characterization. SPE 161015.

Javadpour, F., 2009. Nanopores and Apparent Permeability of GasFlow in Mudrocks (Shales and Siltstone). J. Can. Petrol.Technol. 48 (8),18-21.

Jiang, F., Chen, D., Chen, J., 2016. Fractal Analysis of Shale Pore Structure of Continental Gas Shale Reservoir in the Ordos Basin, NW China. Energy & Fuels. 30 (6), 4676–4689.

Klaver, J., Desbois, G., Urai, J. L., Littke, R., 2012. BIB-SEM study of the pore space morphology in early mature Posidonia Shale from the Hils area, Germany. Int. J. Coal Geol. 103(1), 12–25.

Klaver, J., Desbois,G., Littke, R., Urai, J. L.,2016. BIB-SEM pore characterization of mature and post mature Posidonia Shale samples from the Hils area, Germany. Int. J. Coal Geol. 158, 78–89.

Li, L., Chang L., Le S., and Huang D., 2012. Multifractal analysis and lacunarity analysis: A promising method for the automated assessment of muskmelon (Cucumis melo L.) epidermis netting). Comput. Electron.Agr.. 88, 72-84.

Liu, K., Ostadhassan, M., & Bubach, B., 2016. Pore Structure Analysis by Using Atomic Force Microscopy. URTEC 2448210.

Liu, K., Ostadhassan, M., Jabbari, H. and Bubach, B., 2016. Potential Application of Atomic Force Microscopy in Characterization of Nano-pore Structures of Bakken Formation. Society of Petroleum Engineers.

Liu, K., Ostadhassan, M., 2016. Applications of nano-indentation methods to estimate nanoscale mechanical properties of shale reservoir rocks. J. Nat. Gas Sci. Eng. 35(A), 1310-1319.

Loucks, R. G. et al., 2009. Morphology, Genesis, and Distribution of Nanometer-Scale Pores in Siliceous Mudstones of the Mississippian Barnett Shale. J. Sediment Res. 79(12), 848-861.

Malhi, Y., Román-Cuesta, R. M., 2008. Analysis of lacunarity and scales of spatial homogeneity in IKONOS images of Amazonian tropical forest canopies. Remote Sensing of Environment. 112(5), 2074–2087.

Mandelbrot, B.B., 1977.Fractals: Form, chance, and dimension, W. H. Freeman and Co., New York.

Mandelbrot, B.B., 1983. The fractal geometry of nature. WH Freeman&Co., New York.

Mendoza, F., Verboven,P., Ho, Q.T. , et al., 2010. Multifractal properties of pore-size distribution in apple tissue using X-ray imaging. J. Food Eng. 99(2), 206–215.

Muller, J., Huseby, K.O., Saucier, A., 1995. Influence of multifractal scaling of pore geometry on permeabilities of sedmentary rocks. Chaos, Solitons&Fractals. 5(8), 1485-1492.

Muller, J., 1996.Characterization of pore space in chalk by multifractal analysis. J. hydrol. 187, 215-222

Neves , L.A. , Nascimento, M.Z. , Oliveira, D.L.L., et al., 2014. Multi-scale lacunarity as an alternative to quantify and diagnose the behavior of prostate cancer. Expert Syst. Appl. 41(11), 5017–5029.

Novitz, L.M., Cole, D.R., 2015. Characterization and Analysis of Porosity and Pore Structures. Rev. Mineral. Geochem. 80(1), 61-164.

Odusina, E., Sigal, R.F., 2011.Laboratory NMR Measurements on Methane Saturated Barnett Shale Samples. Petrophysics. 52(01), 32-49.

Plotnick, R.E., Gardner, R. H. , O'Neill, R. V, 1993. Lacunarity indices as measures of landscape texture. Landscape Ecol. 8(3), 201–211.

Sanyal, D., et al., 2006. A fractal description of transport phenomena in dendritic porous network. Chem. Eng. Sci. 61(2), 307-315.

Saraji, S. and Piri, M.,2015. The representative sample size in shale oil rocks and nano-scale characterization of transport properties. Int. J. Coal Geol. 146, 42-54.

Shi, K., Liu, C.Q. , and Ai, N.S., 2009. Monofractal and multifractal approaches in investigating temporal variation of air pollution indexes. Fractals. 17, 513-521.

Smith T.G., Lange, G.D., Marks, W.B. , 1996. Fractal methods and results in cellular morphology — dimensions, lacunarity and multifractals. J. Neurosci. Meth. 69(2), 123–136.

Somayeh K., Milad S., Manika P., 2015. Reservoir Rock Characterization Using Centrifuge and Nuclear Magnetic Resonance: A laboratory Study of Middle Bakken Cores. SPE 175069.

Utrilla-Coello, R.G., Bello-Pérez, L.A. , Vernon-Carter, E.J. , et al., 2013.Microstructure of retrograded starch: Quantification from lacunarity analysis of SEM micrographs. J. Food Eng. 116(4), 775–781.

Vasseur, J., et al., 2015. "Heterogeneity: The key to failure forecasting." Sci Rep-UK. 5: 13259.

Xie, S., Cheng, Q., Ling, Q., et al., 2010. Fractal and multifractal analysis of carbonate pore scale digital images of petroleum reservoirs. Mar. Pet. Geol. 27(2), 476–485.

Yuan, B., Wood, D.A., Yu, W., 2015. Stimulation and hydraulic fracturing technology in natural gas reservoirs: Theory and case studies (2012–2015). J. Nat. Gas Sci. Eng. 26, 1414-1421.

Yuan, B., Wood, D.A., 2015. Production analysis and performance forecasting for natural gas reservoirs: Theory and practice (2011–2015). J. Nat. Gas Sci. Eng. 26, 1433-1438.

Wang, H. et al., 2012. Fractal analysis and its impact factors on pore structure of artificial cores based on the images obtained using magnetic resonance imaging. J. Appl. Geophys. 86, 70-81.

CHAPTER 4

NANOSCALE PORE STRUCTURE CHARACTERIZATION OF THE BAKKEN SHALE IN THE USA-GAS ADSORPTION ANALYSIS

Abstract

Understanding the pore structures of unconventional reservoirs such as shale can assist in estimating their elastic transport and storage properties, thus enhancing the hydrocarbon recovery from such massive resources. Bakken Shale Formation is one of the largest shale oil reserves worldwide located in the Williston Basin, North America. In this paper, we collected a few samples from the Bakken and characterized their properties by using complementary methods including X-ray diffraction (XRD), N_2 and CO_2 adsorption, and Rock-Eval pyrolysis. The results showed that all range of pore sizes: micro (<2 nm), meso (2-50 nm) and macro-pores (>50 nm) exist in the Bakken shale samples. Meso-pores and macro-pores are the main contributors to the porosity for these samples. Compared with the Middle Bakken, samples from Upper and Lower Bakken own more micro pore volumes. Fractal dimension analysis was performed on the pore size distribution data, and the results indicated more complex pore structures for samples taken from the Upper and Lower Bakken shales than the Middle Bakken. Furthermore, the deconvolution of the pore distribution function from the combination of N_2 and CO_2 adsorption results proved that five typical pore size families exist in the Bakken shale samples: one micro-pore, one macro-pore and three meso-pore size families. The studies on the correlations between the compositions and the pore structures showed that mostly feldspar and pyrite affect the total pore volume of samples from Middle Bakken Formation whereas clay dominates the total pore volume of samples from Upper

/Lower Bakken Formation. TOC and clay content are the major contributors to the micro-pore size family in the Upper/ Lower Bakken. Also, it was observed that the increase of hard minerals could increase the percentage of macro-pore family in the Middle Bakken Formation.

4.1. Introduction

The recent advancements in horizontal drilling and hydraulic fracturing have significantly increased the recovery from unconventional shale reservoirs such as Bakken shale. The Bakken "shale", located in the Williston Basin in Montana, North Dakota (USA), and southern Saskatchewan (Canada), is now the second largest hydrocarbon reservoir in the USA. Compared with massive studies of shale gas reservoirs, such as the Barnett (Bowker, 2007), Marcellus (Wang and Reed, 2009), Albany (Strapoc et al., 2010), Long maxi (Cao et al., 2015), Perth (Labani et al., 2013), Toarcian (Houben et al., 2016), Boom clay (Hemes et al., 2015), Posidonia Shale (Klaver et al., 2016), Opalinus clay (Houben et al., 2014), the study of shale oil reservoirs is still limited and in the primary stages. Consequently, the physical properties, especially the porosity and pore size distributions of shale oil formations (i.e. Bakken shale) are still poorly understood. Porosity and pore size distributions are the most important parameters in shale reservoirs which influence the mechanical, storage and transport properties of the porous media (Boadu, 2000; Sanyal et al., 2006; Wang et al., 2012). In comparison to the conventional reservoirs such as sandstone or limestone, the pore structures in shale reservoirs are more complex due to the abundance of the nano-pores.

According to the International Union of Pure and Applied Chemistry (IUPAC) (1994) (Rouquerolb, 1994), pores can be divided into three categories: micro-pores (<2nm), meso-pores (2-50nm) and macro-pores (>50nm). Many researchers have applied this criterion to analyze the pore structures of shale gas formations with various analytical methods. Field emission scanning electron microscopy (FESEM), transmission electron microscopy (TEM) and atomic force

microscopy (AFM) are the image analysis methods to semi-quantify the pores (Klaver et al., 2016; Loucks et al., 2009; Javadpour , 2009; Javadpour et al., Liu and Ostadhassan, 2017; Bernard et al., 2012; Klaver et al., 2012). Low-pressure gas adsorption, mercury injection capillary pressure (MICP), small angle neutron scattering (SANS), nuclear magnetic resonance spectroscopy (NMR) are other common techniques to quantify the pore size distributions (Novitz and Cole, 2015; Somayeh et al., 2015; Deng et al., 2016; Clarkson et al., 2013; Daigle et al., 2016; Zhao et al., 2017; Zhao, 2016). With respect to MICP, the potential shortage is that under high pressure of around 60,000 psia, the injection of mercury will distort, compress and damage the pore structures especially if the sample contains a large amount of compressible clay minerals (Bustin et al., 2008). The theoretical calculation shows that MICP cannot measure the pores with sizes below 3.6 nm, while the practical limit will be higher (Kuila et al., 2013). A significant number of pores in the shale which are less than 3.6 nm is too small to be characterized by the MICP. Regarding nuclear magnetic resonance (NMR), the relaxation time (T_2) increases as the pore size increases, which can be used to characterize the pore size distributions. However, the sample preparation for NMR is complicated and the extraction and injection of the liquid can potentially damage the weak pore structures of the rock. This process can limit the accuracy of NMR, and the variations that would occur in surface relaxation render the results inaccurate (Novitz et al., 2015).

Gas adsorption is of major importance of measuring the pore structures over a wide range of porous materials. Since Dewar (1994) reported the adsorption nitrogen and other gases at liquid air temperature when studying the composition of the atmosphere gases, nitrogen has become a potentially available adsorption material. The monumental work on the monolayer adsorption by Langmuir (1917) attracted a great interest from researchers for the interpretation of adsorption data. In the 1930s, Benton and White (1932) published on the existence of the multilayer

adsorption of nitrogen at the temperature of 77K. Brunauer and Emmett applied gas adsorption to analyze the surface area of samples (Emmett and Brunauer, 1937). In 1938, the publication of the Brunauer-Emmett-Teller (BET) theory, which is the extension of the Langmuir monolayer adsorption model to a multilayer adsorption model, provided researchers the theoretical method to determine the surface area of porous medium (Brunauer et al., 1938). In the late 1940s, by using the Kelvin equation, Barrett, Joyner, and Halenda (BJH) proposed a method (Barrett et al., 1951) to derive the pore size distributions from the appropriate nitrogen isotherm. The BJH method is still one of the most popular methods used to date. In the early 2000s, based on the established principles of statistical mechanics and assuming a model solid structure and pore topology, the DFT method was proposed and has been an important tool in characterizing the pore size distribution of porous samples (Ravikovitch et al., 2000).

For the geological materials, such as rocks, gas adsorption has been applied frequently nowadays to study the shale formations (Cao et al., 2016; Ross and Bustin, 2009; Sun et al., 2016). One limitation of nitrogen, which originates from the gas molecule and pore throat sizes, makes it inaccurate in characterizing the micro-pore size range (less than 2nm). CO_2 adsorption was then used to analyze the micro-pores since it works well in the media containing pores less than 2 nm (Tang et al., 2003). The combination of nitrogen and CO_2 can give us information about the whole pore size distributions less than 200nm.

The purpose of this work is to provide extensive information on the pore size and structure using gas adsorption methods (N_2 and CO_2). In addition, the impacts of the mineral compositions on the pore structures of Bakken shale is investigated.

4.2. Experiments Procedure

4.2.1. Sample preparation.

The Bakken Formation consists of three members (Fig. 4.1): Upper Bakken and Lower Bakken that are dark marine shales with high organic content and serve as both the source and trap for the generated hydrocarbons, whereas the Middle Bakken, composed of mixed carbonates and fine-grained clastics, is the main production unit (Ostadhassan et al., 2013; Sonnenberg et al., 2011). In this study, 12 samples were collected from Upper Bakken (Sample #17, #18, #19, #20, #21), Middle Bakken (Sample #22, #23, #24, #25, #26) and Lower Bakken (#27, #28) to conduct experimental pore structure analysis.

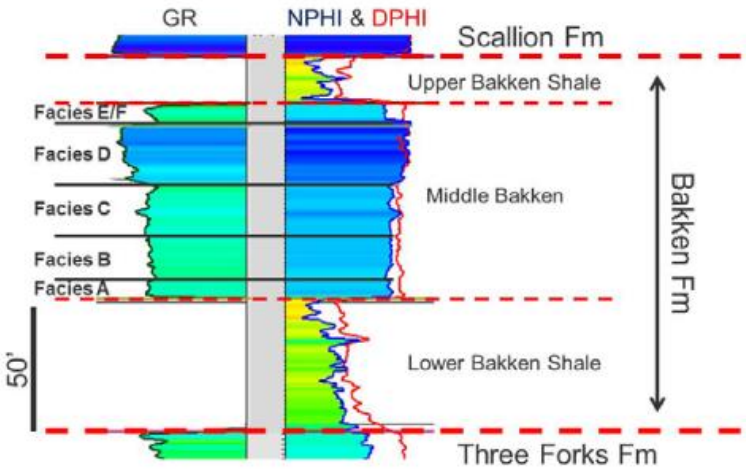

Fig. 4.1. Stratigraphic column of Bakken Formation (Li et al., 2015).

The nano-darcy permeability of the Bakken formation makes the diffusion, penetration, and equilibration of the gas molecules impossible or impractical for the intact samples. In order to solve this problem, the samples were crushed in order to decrease the path length for the gas to access the entire pore structures and acquire the equilibrium within a reasonable time. Based on the study by Kuila and Prasad (2013), the creation of the new surfaces during the crushing process will not affect the pore structure data within the range of investigation. In this paper, samples were crushed to <250 um to be used for gas adsorption analysis (Labani et al., 2013).

4.2.2. Mineral composition analysis.

X-ray diffraction (XRD) was used to analyse the mineralogical compositions of the samples. Sample powders with sizes less than 650 mesh were put in the Bruker D8 Advance X-ray diffractometer. The scanning measurements were performed at the rate of 2°/min in the range of 3-90°. The relative mineral percentages were estimated by calculating the curve of the major peaks of each mineral with correction for Lorentz Polarization (Chen and Xiao, 2014).

4.2.3. Geochemical analysis.

Rock-Eval pyrolysis is applied to quantify the total organic carbon (TOC) and thermal maturity. Following the detailed procedures proposed by Behar et al. (2001) (Behar et al., 2001), 60-70 mg of each sample was used for the analysis. In this study, we applied the shale reservoir method to carry out the Rock-Eval analysis. Shale reservoir method is best-suited for assessing the hydrocarbon potential in these unconventional shale reservoirs compared with other two methods (default method and reservoir method). This is because the shale reservoir method captures the thermos-vaporizable (light) hydrocarbons in the C1-C15 range (Romero-Sarmiento et al., 2015). The initial temperature was 100°C, which was increased to 200°C at 25°C /min steps and held constant for 3 minutes (for Sh0 calculation), then the temperature is increased to 350°C at 25°C /min steps and held steady for 3 minutes (for Sh1 calculation), and finally raised to 650°C at 25°C /min steps. For vitrinite reflectance (R_o) analysis, the whole-rock samples were crushed to 20 mesh (850 um) particles, mixed with the epoxy resin and hardener (ratio of 2:1) and left to harden under vacuum conditions for 24 hours (Hackley et al., 2015). The samples were polished to ensure that the surface is scratch and relief free by using Buehler EcoMet/ AutoMet 250 automated polishing equipment. A Carl Zeiss Axio Imager A2m microscope, equipped with a white light source and a UV light to analyse the reflectance in oil (R_o) and fluorescence, was used for reflectance measurements and visual kerogen analysis.

4.2.4. Gas adsorption.

Prior to adsorption measurement, the samples were degassed for at least 8 hours at 110℃ to remove moisture and volatile in the sample pores. Low-pressure nitrogen was measured on a Micromeritics® Tristar II apparatus at 77K. Carbon dioxide adsorption was measured on a Micromeritics® Tristar II plus apparatus at 273K. Gas adsorption volume was measured over the relative equilibrium adsorption pressure (P/P_0) range of 0.01-0.99, where P is the gas vapor pressure in the system and P_0 is the saturation pressure of nitrogen.

The gas adsorption experimental data was used to quantify the amount of the gas adsorbed at different relative pressures (P/P_0) where P_0 is the saturation pressure of the absorbent and the P is gas vapour pressure in the system.

For the surface area determination, we used the multipoint to calculate the BET. We plotted a straight line $1/v[(P_0/P)-1]$ as the y axis and P/P_0 (range as the 0.05-0.3) as the x axis, which is also called the BET plot according to the requirement of ISO 9277 (2010). The value of the slope and the y intercept of the line were used to calculate the monolayer adsorbed gas quantity and the BET constant. The surface area can then be calculated from the BET (Brunauer, Emmett and Teller) theory (Brunauer et al., 1938).

For nitrogen adsorption, the total volume can be derived from the total amount of vapor adsorbed at the relative pressure (P/P_0) which is close to 1, assuming that the pores are filled with the liquid adsorbate. The average pore radius of the sample can be calculated as:

$$r_p = \frac{2V}{S}, \qquad (4\text{-}1)$$

where V is the total amount of the nitrogen adsorbed, and S is the surface area derived from the.

To calculate the pore size distribution (PSD) from the nitrogen adsorption, BJH and DH model cannot give the realistic description of micro-pore filling which can lead to an underestimation of

pore sizes for micro pores and even the smaller meso-pores (Ravikovitch et al., 1998). In this study, we applied density functional theory (DFT) molecular model due to its applicability in determining the PSD in micro-pore scale as well as meso-pore scale (Do and Do, 2003). The carbon dioxide adsorption data were interpreted using the non-local density functional theory (Amankwah and Schwarz, 1995; Fan and Ziegler, 1992).

4.3. Results

4.3.1. Mineral composition and geochemical properties.

Table 4.1 summarizes the mineral compositions of the samples obtained from the XRD analysis. The results showed that quartz, pyrite, feldspar, and clay minerals are the main minerals that exist in the Bakken samples. Samples from the Upper and Lower Bakken have similar mineral types. The results in Table 4.2 show the data of the geochemical properties where that the samples from the Upper and Lower Bakken have rich organic matters with TOC of more than 10%. The vitrinite reflectance-equivalent (VRo) of the samples (converted from bitumen VBo using the equation: VRo=VBo*0.618+0.4) varied from 0.64% to 1.12%. Sample 17 is the immature sample whereas Sample 21 has the highest maturity value.

Table 4.1. Mineral composition analysis results of the Bakken samples

Samples	Bakken Formation	Quartz, %	Pyrite, %	feldspar, %	clay, %	dolomite, %	calcite, %
#17	Upper Bakken	56.50	23.40	8.90	11.20	0.00	0.00
#18	Upper Bakken	65.20	2.83	3.30	27.00	0.00	0.00
#19	Upper Bakken	16.90	2.80	55.00	24.00	0.00	0.00
#20	Upper Bakken	46.80	2.70	3.90	46.00	0.00	0.00
#21	Upper Bakken	48.10	4.58	15.20	25.30	7.00	0.00
#22	Middle Bakken	42.50	2.76	13.00	15.83	22.50	0.00
#23	Middle Bakken	37.54	0.10	11.10	14.50	11.00	25.70
#24	Middle Bakken	38.25	2.29	13.20	13.60	25.00	7.60
#25	Middle Bakken	24.74	1.09	9.50	42.22	12.40	9.80
#26	Middle Bakken	16.85	0.67	6.39	62.94	5.24	7.50
#27	Lower Bakken	58.00	5.90	2.50	30.00	0.00	0.00
#28	Lower Bakken	44.00	5.20	6.60	33.00	0.00	0.00

Table 4.2. TOC and maturity analysis of the Upper and Lower Bakken samples

Samples	Bakken Formation	VRo-eq, %	TOC, %
#17	Upper Bakken	0.64	14.27
#18	Upper Bakken	0.87	13.54
#19	Upper Bakken	0.89	17.53
#20	Upper Bakken	0.89	13.97
#21	Upper Bakken	1.12	13.00
#27	Lower Bakken	0.94	16.96
#28	Lower Bakken	0.90	10.55

4.3.2. Nitrogen gas adsorption.

4.3.2.1. Nitrogen gas adsorption curve analysis.

Fig. 4.2 represents the nitrogen gas adsorption data for all samples. At the extremely low relative pressure, the pores exhibit micro-pore filling and the amount of the adsorption will depend on the micro-pore volume. Then as the relative pressure increases, the multilayer adsorption will be formed. The knee-bend in Fig. 4.2a in the adsorption isotherm indicates the completion of the monolayer and the beginning of the multilayer, which can reflect the existence of the meso-pores and macro-pores. At the higher relative pressure, the gas in the pores starts to condense. It should be mentioned that gas condensation at various pressures takes place in pores with different sizes. For the desorption part of the Middle Bakken samples (Fig. 4.2b), as the relative pressure decreases, the quantity of gas adsorption decreases. Then, the desorption curve was forced to coincide with the adsorption curve which is caused by the “tensile strength effect” (Groen et al., 2003). The hysteresis loop between the adsorption and desorption can be viewed in Fig. 4.2b due to the existence of the meso-pore pores in the Middle Bakken samples.

The capillary condensation will occur during adsorption and is proceeded by a metastable fluid state while capillary evaporation during desorption occurs via a hemispherical meniscus, separating the vapor and the capillary condensed phase (Groen et al., 2003). The sudden disappearance of the hysteresis loop in Fig. 4.2b around a certain relative pressure can indicate the presence of the small pores less than 4 nm in the Middle Bakken samples. This is due to the

hemispherical meniscus that will collapse during the capillary evaporation in pores with the diameter less than 4 nm. The shape of the hysteresis loop can indicate the pore type of the porous medium. From Fig. 4.2 in the Middle Bakken samples, the desorption part of measurement exhibits an obvious yielding point at the critical relative pressure. When the relative pressure becomes larger than the critical point, the adsorption and desorption both increase steeply, and the hysteresis loop is very narrow which represents the plate type pores in the Middle Bakken Formation. For the Upper and Lower Bakken, the hysteresis loop is very wide, and the adsorption and desorption portion of the curve is flat from the beginning to the end of desorption, which represents the silt type pore. In comparison with Middle Bakken samples, the hysteresis loop in the Upper and Lower Bakken samples does not disappear suddenly and there was no obvious forced closure phenomenon (Fig. 4.2a and Fig. 4.2c). This indicates that the samples from Upper and Lower Bakken Formation contain abundant pores smaller than 4 nm (Cao et al., 2015). The plate-shape pores in the Middle Bakken and the silt-shape pores in Upper and Lower Bakken is advantageous for the flow of the hydrocarbon due to their excellent openness. None of the samples we analysed in this study, showed a horizontal plateau at the relative pressure close to 1, which illustrates that the Bakken shale samples still contain a range of macro-pores which cannot be analysed by the nitrogen gas adsorption method (Cao et al., 2016; Schmitt et al., 2013).

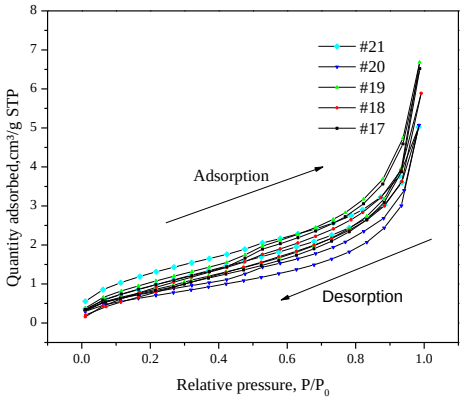

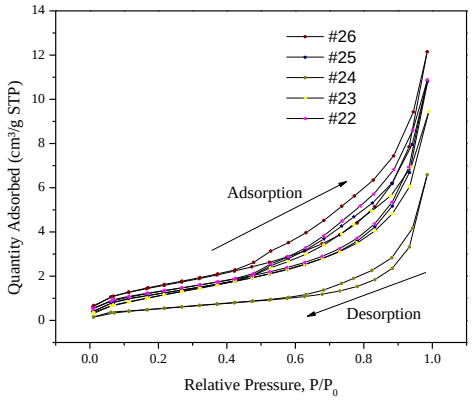

(a) Upper Bakken (b) Middle Bakken

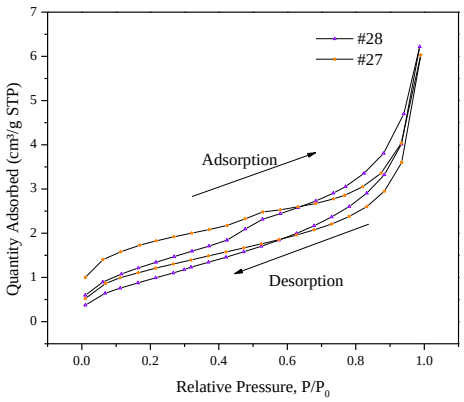

(c) Lower Bakken

Fig. 4.2. Low pressure N_2 isotherms for the Bakken shale samples.

4.3.2.2. PSD analysis from the nitrogen adsorption.

Due to the tensile strength effect, the pore size distribution analysis which can be estimated from the desorption curve, will be limited to 4-5 nm which cannot describe the pore structures accurately. So, in this paper, the adsorption branch will be chosen for the PSD analysis. Fig. 4.3 shows the pore size distribution of the samples based on the DFT theory. The PSD curve of all samples exhibited the multimodal characteristic with several volumetric maxima. The pore structures were analysed, and the following observations were reached:

- Middle Bakken has larger pore volume and average pore size diameter than the Upper and Lower Bakken (Table 4.3).
- Positive relationships exist between macro pore volume and average pore diameter (Fig. 4.4a); total pore volume and pore diameter (Fig. 4.4b).
- An overall inverse correlation exists between the average pore diameter and the BET surface area (Fig. 4.5a). BET shows an increasing trend as the micro-meso pore volume increases (Fig. 4.5b) while no obvious relationship can be seen between the macro-pore volume and BET surface area (Fig. 4.5c).

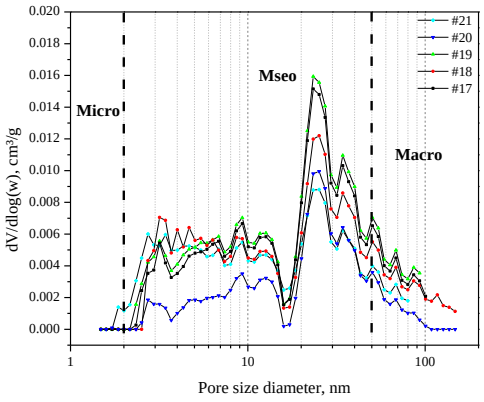

(a) Upper Bakken

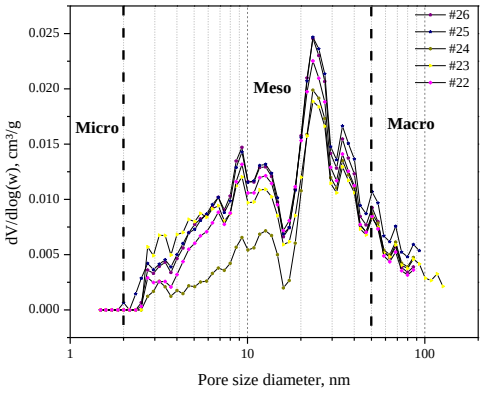

(b) Middle Bakken

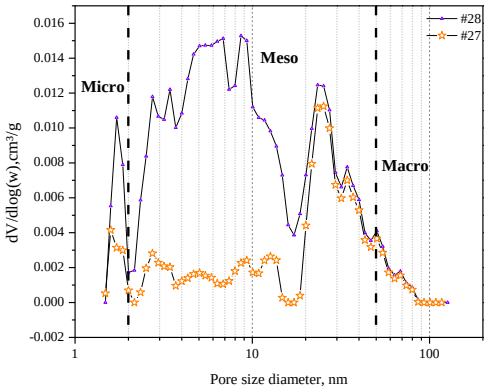

(c) Lower Bakken

Fig. 4.3. PSD analysis of Bakken samples using nitrogen adsorption.

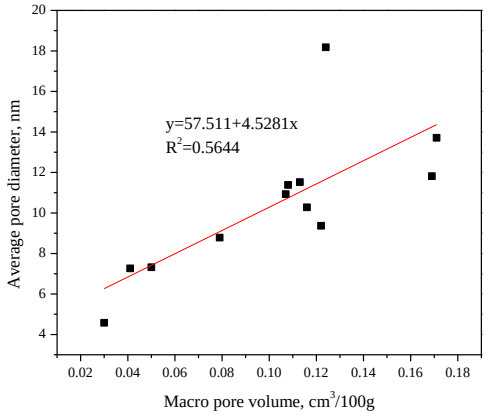

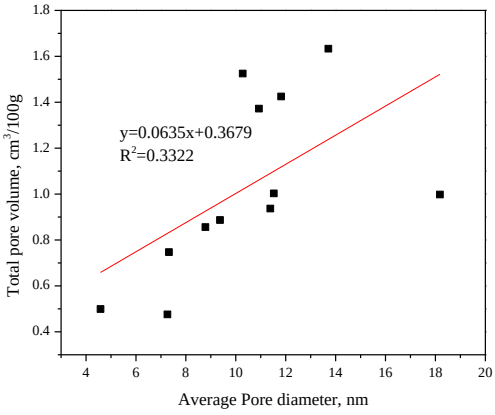

(a) (b)

Fig. 4.4. Average pore diameter versus (a) Macro-pore volume and (b) Total pore volume.

Table 4.3. Low pressure nitrogen adsorption analysis results

Samples	Bakken Formation	BET surface area, m^2/g	Total pore volume, $cm^3/100g$	Micro-Meso pore, $cm^3/100g$	Average pore diameter, nm
#17	Upper Bakken	3.292	0.937	0.829	11.384
#18	Upper Bakken	3.785	0.887	0.765	9.370
#19	Upper Bakken	3.481	1.003	0.890	11.525
#20	Upper Bakken	2.624	0.476	0.435	7.262
#21	Upper Bakken	4.080	0.747	0.697	7.321
#22	Middle Bakken	5.021	1.372	1.265	10.929
#23	Middle Bakken	4.823	1.425	1.256	11.818
#24	Middle Bakken	2.197	0.998	0.874	18.179
#25	Middle Bakken	4.765	1.633	1.462	13.711
#26	Middle Bakken	5.934	1.525	1.409	10.277
#27	Lower Bakken	4.359	0.499	0.469	4.581
#28	Lower Bakken	3.897	0.856	0.777	8.784

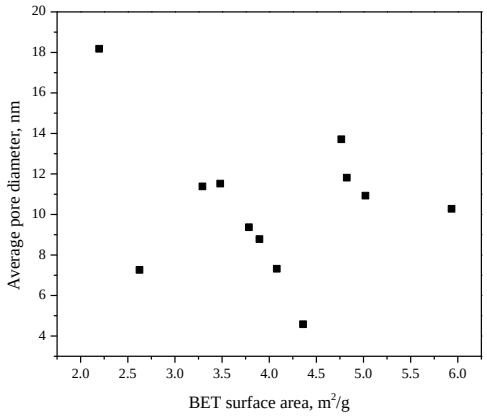

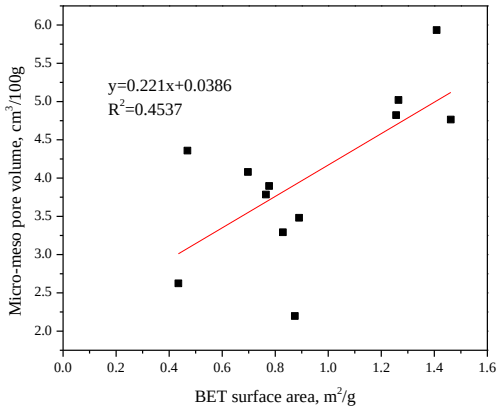

(a) (b)

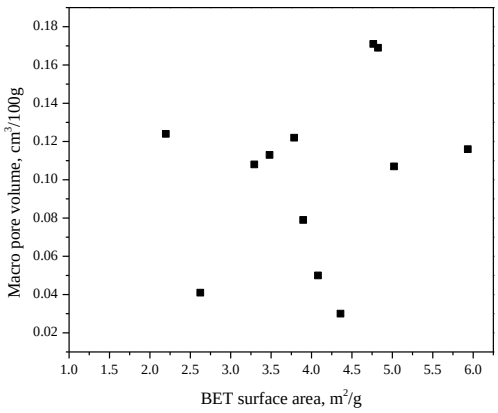

(c)

Fig. 4.5. BET versus (a) Average pore diameter, (b) Micro-meso pore volume and (c) Macro pore volume.

4.3.2.3. Fractal analysis.

Fractal geometry, proposed by the Mandelbrot (1982) (Mandelbrot, 1982), has a strong ability to describe the irregular or fragmented shape of natural features as well as other complex objects that traditional Euclidean geometry fails to characterize (Lopes and Betrouni, 2009). Fractal dimension (*D*) is the key parameter in the fractal geometry, which can offer a systematic approach to quantify irregular patterns. For the gas adsorption theory, several fractal models have been developed such as the BET model, fractal FHH model and the thermodynamic model (Avnir and Jaroniec, 1989; Cai et al., 2011; Yao et al., 2008). The fractal FHH model which focuses on the capillary condensation region of the fractal surface, has been proven to be the most effective method for analyzing the fractal behavior of porous medium (Yao et al., 2008). FHH model can be described using the following equation:

$$\ln V = Cons\tan t + (D-3)\ln(\ln(1/(P/P_0))) \qquad (4\text{-}2)$$

Where V is the total volume of the adsorption, P is the equilibrium pressure, P_0 is the saturated vapour pressure of the adsorption and D is the fractal dimension.

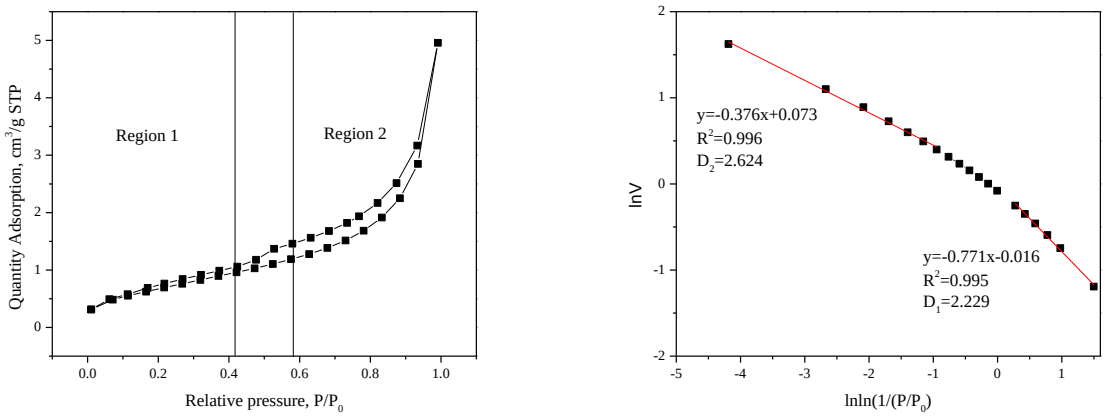

(a) (b)

Fig. 4.6. Fractal analysis of Bakken Sample (#20).

Based on previous studies (Sun et al., 2016), the nitrogen adsorption isotherm can be divided into two main regions (Fig. 4.6a). Region 1 is the monolayer-multilayer adsorption in which the dominant force is van der Waals and Region 2 is the capillary condensation regime with the surface tension being the dominant force (Khalili et al., 2000; Qi et al., 2002). We separated the nitrogen adsorption isotherm and analysed the fractal behaviour of the two regions respectively. D_1 can reflect the fractal behaviour of region 1 with D_2 representing the fractal behaviour of region 2 (Fig. 4.6b). The fractal analysis results for the samples are presented in Table 4.4. The results show that for all the samples, the fractal dimension of region 2 (D_2) is larger than the fractal dimension of region 1 (D_1). This is interpreted as D_2 describes the capillary condensation of gas clumps occurred in the shale pores while D_1 value represents the mono-multilayer adsorption. As more gas was adsorbed, more molecules were available to cover the aggregated outline thus increasing the surface fractal dimension (Sahouli et al., 1997; Tang et al., 2016). D_2 is larger than D_1 can also indicate that the pore structures of the shale samples are more complicated than the pore surface. Samples from the Middle Bakken Formation with higher average D_1 values and lower D_2 values

than samples from the Upper and Lower Bakken Formation corresponds to more irregular pore surface and less complicated pore structures.

Table 4.4. Fractal analysis of the Bakken samples

Samples	Bakken Formation	Slope	D_1	R^2	Slope	D_2	R^2
#17	Upper Bakken	-0.769	2.231	0.998	-0.368	2.632	0.991
#18	Upper Bakken	-1.297	1.703	0.999	-0.269	2.731	0.993
#19	Upper Bakken	-0.885	2.115	0.997	-0.359	2.641	0.995
#20	Upper Bakken	-0.771	2.229	0.995	-0.376	2.624	0.996
#21	Upper Bakken	-0.952	2.048	0.999	-0.270	2.730	0.994
#22	Middle Bakken	-0.632	2.368	0.999	-0.519	2.481	0.998
#23	Middle Bakken	-1.107	1.893	0.996	-0.456	2.544	0.996
#24	Middle Bakken	-0.868	2.132	0.997	-0.602	2.398	0.999
#25	Middle Bakken	-0.724	2.276	0.996	-0.500	2.500	0.997
#26	Middle Bakken	-0.662	2.338	0.999	-0.470	2.530	0.997
#27	Lower Bakken	-0.818	2.182	0.990	-0.298	2.703	0.999
#28	Lower Bakken	-0.895	2.105	0.994	-0.304	2.697	0.994

The correlations between the fractal dimension (D_2) and the pore structures were analysed further. Fig. 4.7 shows that the fractal dimension D_2 has a negative linear relationship between the total pore volume and the average diameter. The shale samples in the Bakken Formation with smaller pore volume and smaller average diameter tends to have higher fractal dimension D_2, demonstrating that those samples have more complex pore structures.

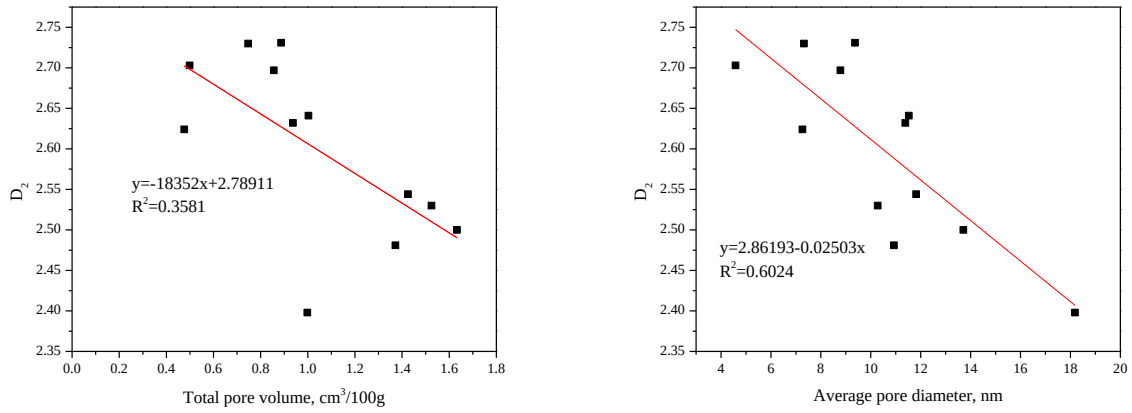

(a) (b)

Fig. 4.7. Correlations between the D_2 and (a) Total pore volume; (b) Average pore diameter.

4.3.3. CO_2 adsorption analysis.

In order to characterize the pores with sizes less than 2 nm, CO_2 gas adsorption was applied. Fig. 4.8 shows the CO_2 adsorption isotherms of all samples tested in this study. The CO_2 adsorption isotherms of the Upper Bakken and Lower Bakken have similar shapes. As the relative pressure increases from 0, the adsorption quantity increases rapidly followed by a slow increase after the relative pressure reaches a critical point. For the Middle Bakken, the adsorption quantity increases with an increasing rate as the relative pressure increases. This is since CO_2 is first adsorbed into the smaller pores and then into the relatively large pores as relative pressure increases. The difference in the CO_2 adsorption isotherms between the Upper/Lower and the Middle Bakken Formation originates from their different pore microstructures.

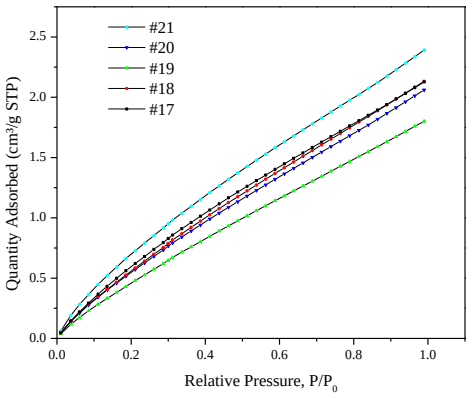

(a) Upper Bakken

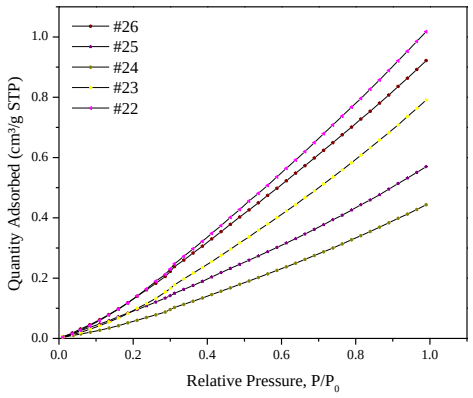

(b) Middle Bakken

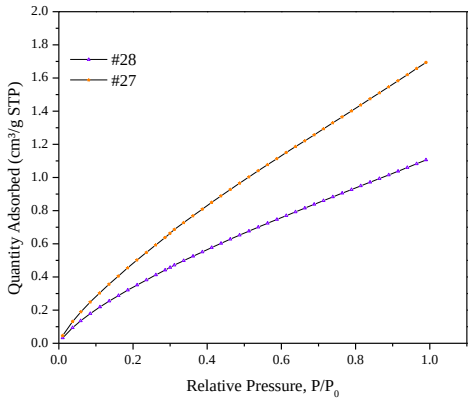

(c) Lower Bakken

Fig. 4.8. CO_2 adsorption isotherms for Bakken samples.

The results in Table 4.5 show that Upper and Lower Bakken formations own more micro-pores (approximately 3 times) than the Middle Bakken. Pores with sizes less than 1 nm exist in the Upper and Lower Bakken. Pores with size range of 1 nm to 2 nm are the main contributors to the total porosity of micro-pores for the Bakken samples.

Table 4.5. Pore size analysis from the CO_2 adsorption

Samples	Bakken Formation	Micro-pore<2nm, cm^3/100g	Micro-pore<1nm, cm^3/100g
#17	Upper Bakken	0.159	0.025
#18	Upper Bakken	0.152	0.025
#19	Upper Bakken	0.126	0.020
#20	Upper Bakken	0.146	0.025
#21	Upper Bakken	0.186	0.039
#22	Middle Bakken	0.048	0.000
#23	Middle Bakken	0.035	0.000
#24	Middle Bakken	0.019	0.000
#25	Middle Bakken	0.028	0.000
#26	Middle Bakken	0.048	0.000
#27	Lower Bakken	0.128	0.024
#28	Lower Bakken	0.090	0.020

4.3.4. Full range pore size analysis.

CO_2 adsorption can characterize the pore sizes less than 2 nm while nitrogen performs well in quantifying the meso-pores and the macro-pores (less than 200 nm). In this section, the pore size distribution results of the two gas adsorption methods were combined in order to analyse the pore structures. The blue curve in Fig. 4.9 shows the pore size distributions (less than 200 nm) of several samples. In order for quantitative measure of the pore size distributions, deconvolution method was applied to determine the mean size and the standard deviation of each pore size family in a given distribution. The pore size family can be quantified by the distinct peaks from the pore size distribution. Gaussian/normal distribution is commonly used to describe the experiments regardless of whatever probability distribution describes an individual experimental result. The detailed deconvolution procedure can be found in Ulm (2007) (Ulm et al., 2007). In this procedure, it can be assumed that the pores can be divided into J=1, n pore size groups with sufficient contrast in pore size distributions. The J_{th} pore group occupies a volume fraction f_J of the total porosity. The theoretical probability density function (PDF) of the single phase, which is assumed to fit a normal distribution is defined as:

$$P_J(x_i, U_J, S_J) = \frac{2}{\sqrt{2\pi(S_J)^2}} \exp\left(\frac{-(x_i - (U_J))^2}{2(S_J)^2}\right), \qquad (4\text{-}3)$$

Where U_J and S_J are the mean value and the standard deviation of pore size distributions of the phase J=1 to n. Minimizing the difference between the data from the weighted model-phase probability distribution function (PDF) and the experimental PDF using the following equation, we can derive the unknowns { f_J, U_J , S_J, }:

$$\min\left[\sum_{i=1}^{m}\sum_{J}^{N}\left(\sum_{J}^{n} f_J P_J(x_i, U_J, S_J) - P_x(x_i)\right)^2\right] \qquad (4\text{-}4)$$

$$\sum_{J=1}^{n} f_J = 1 \qquad (4\text{-}5)$$

In the above equation, $P_x(x_i)$ is the measured value of the normalized frequency of the pore size x_i and m is the number of the intervals (bins).

To ensure that the pore size groups have sufficient contrast, the overlap of successive Gaussian curves representative of the two phases is constrained by the following criterion (Sorelli et al., 2008).

$$U_J + S_J < U_{J+1} + S_{J+1} \qquad (4\text{-}6)$$

The colorful curves in Fig. 4.9 display the deconvolution results of the samples and the red dash curve shows the fit sum of the deconvolution phases. The fitting coefficients of all the samples are above 0.80, which shows that the models fit the experimental data very well. It can be found that the pores in Upper, Middle and Lower Bakken have five typical pore size categories. Table 4.6 shows the deconvolution results for all samples. The deconvolution results of the samples demonstrate that the Bakken samples analysed (Upper, Middle, and Lower Bakken shales) have similar pore size families. One pore size category exists in the micro-pore scale with mean value around 1.5 nm (Family 1), which is defined as the micro-pore size family and one pore size category that is in the macroscale with mean size value larger than 50 nm (Family 5), which is defined as the macro-pore size family. The other three pore families belong to the meso-pore scale with mean size value 9 nm (Family 2), 24 nm (Family 3) and 34 nm (Family 4), respectively, which can be defined as the meso-pore families. Compared with the volume ratios of each pore size family, it was observed that the percentage of micro-pore size family is larger in the samples from the Upper and Lower Bakken than that of the Middle Bakken.

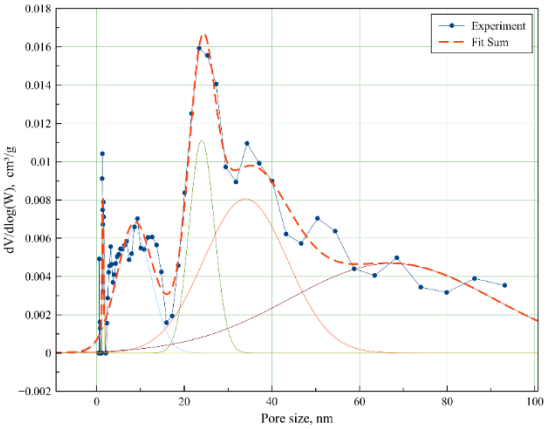

(a) Upper Bakken

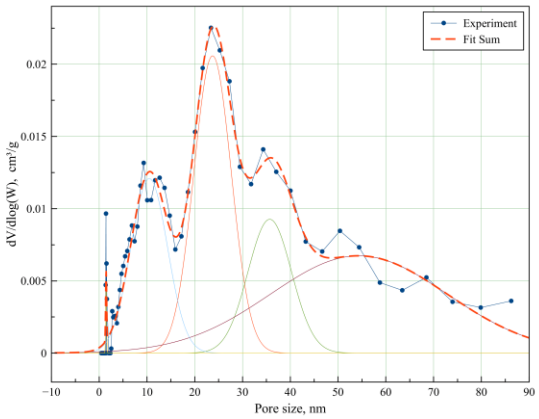

(b) Middle Bakken

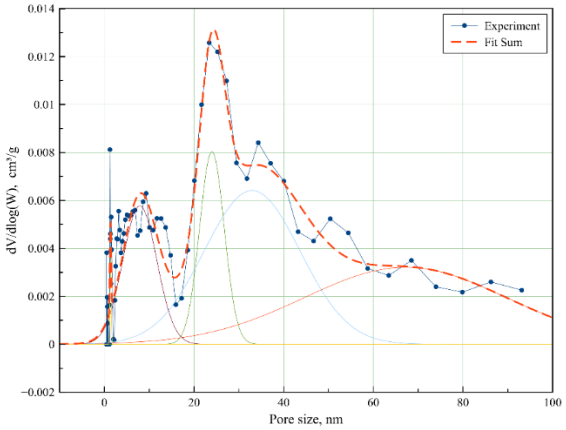

(c) Lower Bakken

Fig. 4.9. Full pore size distribution from gas adsorption and its deconvolution results.

Table 4.6. Deconvolution results of the pore size distributions

Samples	Family 1			Family 2			Family 3		
	mean, nm	SD	Volume, %	Mean, nm	SD	Volume, %	mean, nm	SD	Volume, %
#17	1.386	0.030	0.629	8.772	1.178	10.568	23.977	0.576	13.642
#18	1.399	0.030	0.588	6.964	0.657	8.050	24.402	0.743	8.877
#19	1.393	0.026	0.426	8.558	0.803	10.378	23.977	0.424	13.014
#20	1.409	0.028	2.813	9.685	1.831	10.382	24.319	1.016	22.813
#21	1.388	0.030	1.017	7.685	1.064	16.880	24.399	1.382	23.998
#22	1.454	0.027	0.162	10.473	0.342	15.732	23.729	0.431	27.444
#23	1.544	0.141	0.080	9.378	0.736	12.443	23.716	0.487	11.600
#24	1.384	0.945	0.125	10.814	0.302	7.836	23.991	0.250	20.080
#25	1.544	0.455	0.028	9.988	0.581	12.500	23.625	0.284	12.973
#26	1.528	0.099	0.159	9.976	0.643	15.131	23.431	0.335	16.132
#27	1.391	0.026	1.105	8.516	1.883	9.131	24.374	0.757	27.651
#28	1.367	0.036	0.279	7.899	0.629	11.839	23.986	0.475	11.904

Samples	Family 4			Family 5		
	mean, nm	SD	Volume, %	mean, nm	SD	Volume, %
#17	34.141	4.638	30.201	66.914	21.395	44.961
#18	34.007	3.825	37.732	82.680	24.893	44.753
#19	33.989	3.118	31.495	67.335	15.057	44.688
#20	34.473	6.505	20.938	52.022	24.583	43.056
#21	36.442	2.956	8.542	52.305	23.084	49.564
#22	35.702	1.104	14.365	54.352	6.117	42.296
#23	34.336	4.535	34.969	78.865	12.470	40.907
#24	34.933	0.850	18.030	57.438	2.781	53.929
#25	33.667	2.891	33.927	69.191	8.940	40.572
#26	32.841	3.684	34.826	61.260	14.844	33.752
#27	33.966	3.020	26.620	50.326	18.566	35.493
#28	32.961	3.411	37.000	67.151	30.624	38.977

4.4. Discussion

4.4.1. Sample compositions versus pore structures.

Mineralogical compositions can affect the pore structures of samples. The mineral compositions of the Upper and Lower Bakken shale samples are similar, but they are different compared to the Middle Bakken. To better understand how the compositions, control the pore structures, the Upper and Lower shale samples were treated as one group and the Middle Bakken samples as another

group. In order to avoid eliminating the influence of one parameter on the other based on the bivariate plots, when in fact the parameter may exert a significant influence when it is joined by another independent parameter, PLS (partial least squares regression) was applied. Partial least squares regression (PLS), which is also known as the bilinear factor model, is a statistical method that shows a similarity to the principal components regression. Instead of finding hyperplanes of maximum variance between the response and independent variables, this method finds a linear regression model by projecting the predicted variables and the observable variables to a new space. The governing pore structure parameters (total pore volume, micro-pore volume, meso-pore volume and macro-pore volume) will be input as the dependent parameters while the compositions of the samples are considered as the independent parameters.

Table 4.7. Correlations between the pore structures and the compositions of shale samples (Middle Bakken)

		Dependent variables			
		Total pore volume, $cm^3/100g$	Micro-pore, $cm^3/100g$	Meso-pores, $cm^3/100g$	Macro-pore, $cm^3/100g$
	Intercept	1.751	0.043	1.554	0.154
Independent Variables	Quartz, %	-0.003	0.000	-0.003	0.000
	Pyrite, %	-0.031	-0.001	-0.028	-0.001
	Feldspar, %	-0.015	0.000	-0.014	-0.001
	Clay, %	0.002	0.000	0.002	0.000
	Dolomite, %	-0.006	0.000	-0.005	0.000
	Calcite, %	0.001	0.000	0.001	0.000
	R^2	0.531	0.115	0.529	0.083

Table 4.7 summarizes the PLS fitting model results on the Middle Bakken samples. The results demonstrate that pyrite followed by feldspar affects the total pore volume or meso-pore volumes most. The total (meso) pore volume increases as the clay minerals and the calcite increases. Negative correlations can be found between the total (meso) pore volume and other existing minerals such as quartz, pyrite and feldspar.

Following similar method, the impact of the mineralogical composition on the pore structures of the samples from Upper and Lower Bakken Formation were analysed. Since the Upper and Lower Bakken samples are rich in organic matter (high TOC content), the TOC can be treated as an independent parameter that can potentially affect the pore structures. Table 4.8 shows that clay minerals are the most important parameter that influences the total (meso) pore volume of the Upper and Lower Bakken. The total pore volume/meso-pore volume increases as the clay content decreases. Organic matter has negative influence on the pore volume because the organic matter in the samples analysed, and also based on our previous studies, is non-porous.

Table 4.8. Correlations between the pore structures and the compositions of shale samples (Upper and Lower Bakken)

		Dependent variable			
		Total pore volume, $cm^3/100g$	Micro-pores, $cm^3/100g$	Meso-pores, $cm^3/100g$	Macro-pores $cm^3/100g$
	Intercept	1.175	0.147	0.914	0.114
Independent Variable	Quartz, %	-0.002	0.000	-0.002	0.000
	Pyrite, %	0.007	0.000	0.006	0.001
	Feldspar, %	0.004	0.000	0.004	0.001
	Clay, %	-0.010	0.000	-0.009	-0.001
	TOC, %	-0.001	0.000	-0.001	0.000
	R^2	0.590	0.017	0.561	0.353

4.4.2 Mineral compositions versus pore size families.

Based on the observation from full pore size analysis of integrated gas adsorption, the pores existing in the Bakken samples can be grouped into 5 pore size families. The impact of the compositions of the samples on the pore size families was also analysed. The compositions of the samples were considered as the independent parameter while the volume fractions of the five pore size families were considered as the dependent parameter. Similar to the previous part, the Middle Bakken samples and Upper/Lower samples were analysed separately.

Considering the Middle Bakken samples, Table 4.9 explains that clay minerals and calcite have similar effects on the pore size families. As their content increases within the samples, the percentage of pore size families 2 and 4 increases while the percentage of pore size families 3 and 5 decreases. Regarding pore size family 5 (macro-pore size family), the increase of the hard minerals such as quartz, pyrite, feldspar and dolomite increases its volume fraction, which means that hard minerals are the main contributors to the macro-pore size family distribution and abundance.

Table 4.9. Correlations between the pore size families and the compositions of shale samples (Middle Bakken)

		Dependent Variable				
		Family 1	Family 2	Family 3	Family 4	Family 5
	Intercept	0.088	14.903	9.339	44.261	31.409
Independent variable	Quartz, %	0.000	-0.021	0.082	-0.168	0.107
	Pyrite, %	0.003	-0.262	1.002	-2.055	1.313
	Feldspar, %	0.001	-0.094	0.361	-0.740	0.473
	Clay, %	0.000	0.010	-0.037	0.075	-0.048
	Dolomite, %	0.000	-0.038	0.143	-0.294	0.188
	Calcite, %	0.000	0.013	-0.049	0.101	-0.065
	R^2	0.048	0.147	0.512	0.849	0.670

For the Upper and Lower Bakken, it was found that TOC and clay content are the two governing parameters controlling the pore size family 1 (micro-pore size family) as seen in Table 4.10. As the TOC and clay content increase, the ratio of the pore size family 1 increases, indicating that TOC and clay cause the major abundance of micro-pore size family.

Table 4.10. Correlations between the pore size families and the compositions of shale samples (Upper and Lower Bakken)

		Dependent variables				
		Family 1	Family 2	Family 3	Family 4	Family 5
	Intercept	-1.040	13.172	6.335	31.756	49.778
Independent Variable	Quartz, %	0.007	-0.008	0.040	-0.015	-0.024
	Pyrite, %	-0.022	0.023	-0.119	0.046	0.072
	Feldspar, %	-0.017	0.018	-0.091	0.035	0.055
	Clay, %	0.043	-0.046	0.237	-0.091	-0.143
	TOC, %	0.070	-0.074	0.384	-0.147	-0.232
	R^2	0.472	0.049	0.201	0.015	0.185

4.5. Conclusions

In this study, gas adsorption (N_2 and CO_2) was used to analyse the pore structures of several samples from Bakken Formation. Based on the results, the following conclusions were made:

- Nitrogen gas adsorption showed that the Bakken shale samples have micro-, meso- and macro-pores while the meso-pores are the main pore type. Middle Bakken shale samples have more pore volumes than that of the Upper and Lower Bakken formations.
- Fractal dimension analysis demonstrated that pore structures of the Bakken shale samples exhibit more complexity than the pore surface. The samples from Middle Bakken in comparison to the Upper/Lower Bakken have less complex pore structures. The correlations between the fractal dimension and pore structures revealed that the fractal dimension (D_2) increases as the total pore volume or average pore size decreases, indicating that the pore structures in those samples are becoming more complex.
- CO_2 adsorption quantifies the pore sizes smaller than 2 nm. Upper and Lower Bakken have more micro-pores (by almost 3 times) compared to the Middle Bakken. Upper and Lower Bakken contain pores with sizes smaller than 1 nm while Middle Bakken samples do not

have this range of pore sizes. Pores within the size of 1 nm to 2 nm are the major contributors to the total micro-pores in Bakken samples.

- The deconvolution of the total pore size distribution which is estimated in the gas adsorption (combination of nitrogen and CO_2) experiments provided us with five different distinct pore size families. One family in the micro-pore with mean value 1.5 nm, one family in the macro-pore with mean size value larger than 50 nm and the rest three pore families belong to the meso-pore with mean size values of 9 nm, 24 nm and 34 nm, respectively.
- For the Middle Bakken, feldspar and pyrite are the two major minerals that affect the total pore volume. However, for the Upper and Lower Bakken, clays are the most important parameter that influences the total pore volume. Hard minerals are the main contributors to the volume fraction of the macro pore family in Middle Bakken Formation while TOC and clays are the major contributors for the percentage dominance of the micro-pore size family in the Upper and Lower Bakken.

4.6. References

Amankwah, K.A.G., and Schwarz, J.A.,1995. A modified approach for estimating pseudo-vapor pressures in the application of the Dubinin-Astakhov equation. Carbon 33, 1313-1319.

Avnir, D., Jaroniec, M.,1989. An isotherm equation for adsorption on fractal surfaces of heterogeneous porous materials. Langmuir. 5(6), 1431-1433.

Barrett, E.P., Joyner, L.G., Halenda, P.P.,1951. The Determination of Pore Volume and Area Distributions in Porous Substances. I. Computations from Nitrogen Isotherms. J. Am. Chem. Soc. 73 (1), 373–380.

Behar, F., Beaumont, V., De, B., Penteado, H.L.,2001. Rock-Eval 6 technology: performances and developments. Oil Gas Sci. Technol. 56, 111–134.

Benton, F., White, A.,1932. The sorption of gas by iron. J. Am. Chem. Soc. 54 (5),1820–1830.

Bernard, S., Horsfield, B., Schulz, H.M., 2012. Geochemical evolution of organic-rich shales with increasing maturity: A STXM and TEM study of the Posidonia Shale (Lower Toarcian, northern Germany). Mar. Pet. Geol. 31(1), 70–89.

Boadu, F.K., 2000. Predicting the transport properties of fractured rocks from seismic information: numerical experiments. J. Appl. Geophys. 44(2–3), 103-113.

Bowker, KA., 2007. Barnett Shale gas production, Fort Worth Basin: issues and discussion. AAPG bull. 91(4), 523-533.

Brunauer, S., Emmett, P.H., Teller, E.,1938. Adsorption of Gases in Multimolecular Layers. J. Am. Chem. Soc. 60 (2),309–319.

Bustin, R.M., Bustin, A.M.M., Cui, A., et al., 2008. Impact of shale properties on pore structure and storage characteristics. SPE shale gas production conference. Society of Petroleum Engineers. 2008.

Cai, Y., Liu, D., Yao, Y., et al., 2011. Fractal characteristics of coal pores based on classic geometry and thermodynamics models. Acta Geol. Sin. (English). 85(5), 1150-1162.

Cao, Z., Liu, G., Zhan, H., et al., 2016. Pore structure characterization of Chang-7 tight sandstone using MICP combined with N2GA techniques and its geological control factors. Sci. Rep-UK. 6.

Cao, T.T., Song, Z.G., Wang, S.B., et al.,2015. A comparative study of the specific surface area and pore structure of different shales and their kerogens. Sci. China Earth Sci. 58(4), 510-522.

Chen, J., Xiao, X., 2014. Evolution of nanoporosity in organic-rich shales during thermal maturation. Fuel. 129, 173–181.

Clarkson, C.R., Solano, N., Bustin, R.M., et al., 2013. Pore structure characterization of North American shale gas reservoirs using USANS/SANS, gas adsorption, and mercury intrusion. Fuel. 103, 606-616.

Daigle, H., Johnson, A., 2016. Combining mercury intrusion and nuclear magnetic resonance measurements using percolation theory. Transport Porous Med. 111, 669-679.

Deng, H., Hu, X., Li, H.A., et al.,2016. Improved pore-structure characterization in shale formations with FESEM technique. J. Nat. Gas Sci. Eng. 35, 309-319.

Dewar. J., 1904. The Adsorption and Thermal Evolution of Gases Occuluded in Charcoal at Low Temperatures. Adsorption of Hydrogen, Nitrogen, Oxygen, Argon, Helium, Electrolytic Gas, Carbonic Oxide and Oxygen, Carbonic Oxide, at K and -185 C by Charcoal. Proc. Roy. Soc. 74, 122-127.

Do, D.D., Do, H.D., 2003. Pore characterization of carbonaceous materials by DFT and GCMC simulations: a review. Adsorpt. Sci. Technol. 21(5), 389-423.

Emmett, P.H., Brunauer, S.,1937. The Use of Low Temperature van der Waals Adsorption Isotherms in Determining the Surface Area of Iron Synthetic Ammonia Catalysts. J. Am. Chem. Soc. 59 (8), 1553–1564.

Fan, L., and Ziegler, T., 1992. Nonlocal density functional theory as a practical tool in calculations on transition states and activation energies. Applications to elementary reaction steps in organic chemistry. J. Am. Chem. Soc. 114, 10890-10897.

Groen, J.C., Peffer, L.A.A., Pérez-Ramírez, J.,2003. Pore size determination in modified micro- and mesoporous materials. Pitfalls and limitations in gas adsorption data analysis. Micropor Mesopor Mat. 60(1), 1-17.

Hackley, P.C., Araujo, C.V., Borrego, A.G., et al., 2015. Standarization of reflectance measurements in dispersed organic matter: results of an exercise to improve interlaboratory agreement. Mar. Pet. Geol. 59, 22–34.

Hemes, S., Desbois, G., Urai, J.L., Schröppel, B., Schwarz, J-O., 2015. Multi-scale characterization of porosity in Boom Clay (HADES-lever, Mol, Belgium) using a combination of X-ray μ-CT, 2D BIB-SEM and FIB-SEM tomography. Micropor Mesopor Mat. 208, 1–20.

Houben, M.E., Barnhoorn, A., Wasch, L.,2016. Microstructures of Early Jurassic (Toarcian) shales of Northern Europe. Int. J. Coal Geol. 165, 76–89.

Houben, M.E., Desbois, G., Urai, J.L.,2014. A comparative study of representative 2D microstructures in Shale and Sandy facies of Opalinus Clay (Mont Terri, Switzerland) inferred from BIB-SEM and MIP methods. Mar. Pet. Geol. 49, 143–161.

ISO 9277:2010. Determination of the specific surface area of solids by gas adsorption — BET method.

Javadpour, F.,2009. Nanopores and Apparent Permeability of GasFlow in Mudrocks (Shales and Siltstone). J. Can. Petro. Technol. 48 (8), 18-21.

Javadpour, F., Farshi, M.M., Amrein, M.,2012. Atomic-Force Microscopy: A new Tool for Gas-Shale Characterization. SPE 161015.

Khalili, N.R., Pan, M., Sandi, G., 2000. Determination of fractal dimensions of solid carbons from gas and liquid phase adsorption isotherms. Carbon. 38(4), 573-588.

Klaver, J., Desbois, G., Littke, R., Urai, J.L., 2016. BIB-SEM pore characterization of mature and post mature Posidonia Shale samples from the Hills area, Germany. Int. J. Coal Geol. 158,78–89.

Klaver, J., Desbois, G., Urai, J.L., Littke, R., 2012. BIB-SEM study of the pore space morphology in early mature Posidonia Shale from the Hils area, Germany. Int. J. Coal Geol. 103(1), 12–25.

Kuila, U., Prasad, M.,2013. Specific surface area and pore-size distribution in clays and shales. Geophys.Prospect. 61(2), 341-362.

Labani, M.M., Rezaee, R., Saeedi, A., et al., 2013. Evaluation of pore size spectrum of gas shale reservoirs using low pressure nitrogen adsorption, gas expansion and mercury porosimetry: A case study from the Perth and Canning Basins, Western Australia. J. Petrol. Sci. Eng. 112,7-16.

Langmuir, I.,1917. The constitution and fundmental properties of solids and liquids.II.liquids. J. Am. Chem. Soc. 39 (9). 1848–1906.

Li, H., Hart, B., Dawson, M., & Radjef, E.,2015. Characterizing the Middle Bakken: Laboratory Measurement and Rock Typing of the Middle Bakken Formation. Unconventional Resources Technology Conference.

Liu, K., Ostadhassan, M., 2017. Quantification of the microstructures of Bakken shale reservoirs using multi-fractal and lacunarity analysis. J. Nat. Gas Sci. Eng. 39, 62-71.

Lopes, R., Betrouni, N., 2009. Fractal and multifractal analysis: A review. Med. Image Anal. 13, 634-649.

Loucks, R.G., Reed, R.M., Ruppel, S.C., et al., 2009. Morphology, Genesis, and Distribution of Nanometer-Scale Pores in Siliceous Mudstones of the Mississippian Barnett Shale. J. Sediment Res. 79(12), 848-861.

Mandelbrot, B.B.,1982. The fractal geometry of nature. Freeman, New York.

Novitz, L.M., Cole, D.R., 2015. Characterization and Analysis of Porosity and Pore Structures.Reviews in Mineralogy and Geochemistry. 80(1), 61-164.

Ostadhassan, M., and Benson, S., Zamiran, S.,2013. Stress Analysis and Wellbore Stability in Unconventional Reservoirs. ARMA 2013-150.

Qi, H., Ma, J., Wong, P.,2002. Adsorption isotherms of fractal surfaces. Colloid Surface A. 206(1), 401-407.

Ravikovitch, P.I., Haller, G.L., Neimark, A.V.,1998. Density functional theory model for calculating pore size distributions: pore structure of nanoporous catalysts. Adv. Colloid Interfac. 76, 203-226.

Ravikovitch, P.I., Vishnyakov, A., Russo, R., Neimark, A.V., 2000. Unified Approach to Pore Size Characterization of Microporous Carbonaceous Materials from N2, Ar, and CO2 Adsorption Isotherms. Langmuir. 16 (5), 2311–2320.

Romero-Sarmiento, M-F., Pillot ,D., Letort, G., Lamoureux-Var, V., Beaumont, V., Hu, A-Y., and Garcia, B.,2015. New Rock-Eval Method for Characterization of Unconventional Shale Resource Systems. Oil Gas Sci. Technol. 71, 1-9.

Ross, D.J.K., Bustin, R.M., 2009. The importance of shale composition and pore structure upon gas storage potential of shale gas reservoirs. Mar. Pet. Geol. 26(6), 916-927.

Rouquerolb, J., Avnir, D., Fairbridge, C.W., et al., 1994. Recommendations for the characterization of porous solids (Technical Report). Pure and Applied Chemistry. 66(8), 1739-1758.

Sahouli, B., Blacher, S., Brouers, F.,1997. Applicability of the fractal FHH equation. Langmuir. 13(16), 4391-4394.

Sanyal, D., Ramachandrarao, P., and Gupta, O.P.,2006. A fractal description of transport phenomena in dendritic porous network. Chem. Eng. Sci. 61(2), 307-315.

Schmitt, M., Fernandes, C.P., da Cunha Neto, J.A.B., et al.,2013. Characterization of pore systems in seal rocks using nitrogen gas adsorption combined with mercury injection capillary pressure techniques. Mar. Pet. Geol. 39(1), 138-149.

Somayeh, K., Milad, S., Manika, P..2015. Reservoir Rock Characterization Using Centrifuge and Nuclear Magnetic Resonance: A laboratory Study of Middle Bakken Cores. SPE 175069.

Sonnenberg, S.A., Jin, H., Sarg, J.F., 2011. Bakken Mudrocks of the Williston Basin, World Class Source Rocks. AAPG Annu. Convent. Exhib.

Sorelli, L., Constantinides, G., Ulm, F-J., Toutlemonde, F..2008. The nano-mechanical signature of ultra high performance concrete by statistical nanoindentation techniques. Cem. Concr. Res. 38(12), 1447-1456.

Strapoc, D., Mastalerz, M., Schimmelmann, A., et al., 2010. Geochemical constraints on the origin and volume of gas in the New Albany Shale (Devonian–Mississippian), eastern Illinois Basin. AAPG Bull. 94(11), 1713-1740.

Sun, M., Yu, B., Hu, Q., et al.,2016. Nanoscale pore characteristics of the Lower Cambrian Niutitang Formation Shale: a case study from Well Yuke# 1 in the Southeast of Chongqing, China. Int. J. Coal Geol. 154, 16-29.

Tang, P., Chew, N.Y.K., Chan, H.K., et al., 2003. Limitation of Determination of Surface Fractal Dimension Using N2 Adsorption Isotherms and Modified Frenkel− Halsey− Hill Theory. Langmuir. 19(7), 2632-2638.

Tang, X., Jiang, Z., Jiang, S., et al., 2016. Effect of Organic Matter and Maturity on Pore Size Distribution and Gas Storage Capacity in High-Mature to Post-Mature Shales. Energy & Fuels. 30(11),8985-8996.

Ulm, F.J., Vandamme, M., Bobko, C., et al.,2007. Statistical indentation techniques for hydrated nanocomposites: concrete, bone, and shale. J. Am. Ceram. Soc. 90(9), 2677-2692.

Wang, F.P., Reed, R.M.,2009. Pore networks and fluid flow in gas shales. SPE annual technical conference and exhibition. Society of Petroleum Engineers.

Wang, H., Liu, R., Song, Y.C., et al., 2012. Fractal analysis and its impact factors on pore structure of artificial cores based on the images obtained using magnetic resonance imaging. J. Appl. Geophys. 86, 70-81.

Yao, Y., Liu, D., Tang, D., et al.,2008. Fractal characterization of adsorption-pores of coals from North China: an investigation on CH 4 adsorption capacity of coals. Int. J. Coal Geol. 73(1), 27-42.

Zhao, P., Wang, Z.L., Sun, Z.C., Cai, J.C., Wang, L., 2017. Investigation on the pore structure and multifractal characteristics of tight oil reservoirs using NMR measurements: Permian Lucaogou Formation in Jimusaer Sag, Junggar Basin. Mar. Pet. Geol. 86, 1067-1081.

Zhao, P., 2016. Study on the response mechanisms of nuclear magnetic resonance (NMR) log in tight oil reservoirs. Chinese J. Geophys. 29(5), 1927-1937.

CHAPTER 5

MULTIFRACTAL ANALYSIS OF GAS ADSORPTION ISOTHERMS FRO PORE STRUCTURE CHARACTERIZATION OF THE BAKKEN SHALE

Abstract

Understanding pore heterogeneity can enable us to obtain a deeper insight into the flow and transport processes in any porous medium. In this study, multifractal analysis was employed to analyze gas adsorption isotherms (CO_2 and N_2) for pore structure characterization in both a source (Upper-Lower Bakken) and a reservoir rock (Middle Bakken). For this purpose, detected micropores from CO_2 adsorption isotherms and meso-macropores from N_2 adsorption isotherms were analyzed separately. The results showed that the generalized dimensions derived from CO_2 and the N_2 adsorption isotherms decrease as q increases, demonstrating a multifractal behavior followed by $f(\alpha)$ curves of all pores exhibiting a very strong asymmetry shape. Samples from the Middle Bakken demonstrated the smallest average H value and largest average α_{10-}- α_{10+} for micropores while samples from the Upper Bakken depicted the highest average α_{10-}- α_{10+} for the meso-macropores. This indicated that the Middle Bakken and the Upper Bakken have the largest micropore and meso-macropore heterogeneity, respectively. The impact of rock composition on pore structures showed that organic matter could increase the micropore connectivity and reduce micropore heterogeneity. Also, organic matter will reduce meso-macropore connectivity and increase meso-macropore heterogeneity. We were not able to establish a robust relationship between maturity and pore heterogeneity of the source rock samples from the Bakken.

5.1. Introduction

Oil and gas unconventional shale and conventional hydrocarbon plays contribute a significant amount of petroleum production. Various pore sizes, from nano- to macro- are reported in these reservoirs all around the globe; for example, Second White Speckled Shale (Yin et al., 2016), Dalong Shale (Wei et al., 2018), Perth Shale (Zou et al., 2017), Bakken Shale (Liu et al., 2017a), Barnett Shale (Bowker, 2007), and Marcellus Shale (Wang and Reed, 2009). Therefore, understanding the pore structures can result in a deeper insight about the flow and storage capabilities of any porous medium (Kirchofer et al., 2017; Aljama and Wilcox, 2017).

During the past decade, a wide range of methods have been applied to characterize these pores including: mercury intrusion porosimetry (MIP) (Cao and Hu, 2013), gas adsorption method (Huang and Zhao, 2017), small angle neutron scattering (SANS) and ultra-small angle neutron scattering (USANS) (Clarkson, et al., 2013), nuclear magnetic resonance (NMR) (Zhao et al., 2017), direct observation methods such as: field emission scanning electron microscope (FE-SEM) (Liu and Ostadhassan, 2017; Loucks et al., 2009; Klaver et al., 2012), atomic force microscopy (AFM) (Javadpour, 2009; Liu et al., 2016), microfocus X-ray computed tomography (u-CT) (Li et al., 2017; Su et al., 2018) and transmission electron microscope (TEM) (Bernard et al., 2012). In this regard, each method has advantages and disadvantages. For example, FE-SEM can directly detect size and distribution of larger pores but cannot provide any information about micropores because of limitations in tool resolution (Liu et al., 2017a). MIP determines the largest entrance of mercury into a pore (i.e., pore-throat size) instead of measuring the true pore size (Giesch, 2006). Moreover, a high injection pressure rate will potentially damage the pore structures of the shale with high clay content (Anovitz and Cole, 2015). The methods that mentioned above can provide us with acceptable information about the porosity and pore size distribution (PSD) of rocks. However, in addition to PSD and porosity as a quantity, the complexity of the pore network is

another major parameter that needs to be characterized due to its importance in affecting flow properties and gas storage capacity in different rock samples (Li et al., 2015). Notwithstanding the importance, understanding the complexity of pore structure and pore network in shale formations is still a task that needs further attention.

It is well understood that pore size in shales is not uniformly distributed thus cannot be represented by traditional Euclidean geometry (Li et al., 2015; Tang et al., 2010; Wang et al., 2012). Thus, in order to describe the complexity that exists in pore structures, fractal theory, initially proposed by Mandelbrot (1977), has been widely used instead. A fundamental characteristic of a fractal object is that the measured properties are a function of the scale of measurement (Lopes and Betrouni,2009). So far, several methods have been proposed and used extensively by researchers on methods to define a fractal behavior, such as: box-counting (Russel et al., 1980; Chaudhuri and Sarkar, 1995), fractional Brownian methods (Pentland, 1984) and area measurement methods (Shelberg et al., 1983; Peleg et al., 1984). The box-counting method was defined by Russel et al (1984) and became one of the most popular methods for gas adsorption isotherms data analysis. This method is defined by applying different boxes of various lengths to cover the whole signal spectrum to be analyzed (Russel et al., 1980; Chaudhuri and Sarkar, 1995). In addition to box-counting, fractional Brownian is also another method that has been used for fractal analysis and is based on a non-stationary model to describe random phenomenon. This model is a generalized form of Brownian motion where the expected value of intensity differences between two points should be zero. However, the square of the differences should be proportional to the distance between these two points and fit the power law (Pentland, 1984). Another commonly used method for fractal analysis is the area measurement, which uses structuring elements such as triangle, erosion, or dilation of various scales and then computes the area of the signal intensity surface at

that corresponding scale. Three algorithms: isarithm method, blanket method, and the triangular prism method are the most popular ones in the area measurement methods to calculate the fractal dimensions (Shelberg et al., 1983; Peleg et al., 1984; Clarke et al., 1986).

However, fractal models can only capture a simple fractal behavior that can be described only by one parameter-fractal dimension (D_0). This parameter describes the irregularity within limited size intervals (Li et al., 2015; Martínez et al., 2010; Gould et al., 2011). However, in heterogeneous rocks, the pore size distribution (PSD) curve usually fluctuates randomly, jumps off at different pore size intervals (Li et al., 2015; Martínez et al., 2010) and the pore size intervals may exhibit various types of self-similarity (Li et al., 1999). All these complexities make it difficult to characterize PSD curves with one single fractal dimension.

Considering the above discussion, multifractals can resolve the issue that is a feature of complex pore structures in heterogeneous rocks. Multifractals can be counted as the extension of fractals or the superposition of monofractal structures (Lopes and Betrouni,2009). Multifractal analysis, which decomposes self-similar measures into intertwined fractal sets, is characterized by singularity strength of fractal sets and can provide more accurate information about pore structures. The multifractal theory has recently been applied to study pore structures of different rock types such as chalk, carbonate, and shale gas formations (Muller et al., 1995; Muller, 1996; Xie et al., 2010).

Bakken is one of the largest unconventional shale oil plays in the world. The Bakken Formation consists of three members: organic-rich Upper and Lower Bakken and the Middle member, which is composed of mixed carbonates and fine-grained clastics (Pitman et al., 2001). In previous studies, we analyzed the multifractal behavior of pore structures of the Bakken Formation using SEM images (Liu and Ostadhassan, 2017). However, it was described that SEM imaging technique

was only able to detect pores that are larger than 9 nm. In order to access and evaluate smaller pores, gas adsorption was later acquired. This made it possible to characterize pores beyond SEM resolution. Accordingly, gas adsorption (CO_2 and N_2) was utilized to analyze pore structure of the Bakken in another study (Liu et al., 2017a). In our current research approach, we focused on applying multifractal method to analyze the complexity of pore structures in a wide range of pore sizes, ranging from micro- to macro- that exist in the Bakken both in the reservoir (Middle member) and source section (Upper and Lower member) of the formation.

5.2. Methods and experiments

5.2.1. Samples.

In order to study the heterogeneity of pore structures and compare pore network complexity that may occur in rocks due to the changes in mineralogy and main constituent components, it was decided to study a few samples from each member of the Bakken Formation and compare the results. With respect to the goals of this research attempt, 4 samples were selected from the Upper Bakken (Sample17, 19, 20, 21), 4 samples were selected from the Middle Bakken (Sample 23, 24, 25, 26) and 3 samples were selected from the Lower Bakken (Sample 27, 28 and 29). The numbers were decided based on sample availability. Thus, a total number of 11 samples were crushed to less than 250 μm to be tested by the gas adsorption (CO_2 and N_2) method.

5.2.2. Mineralogy and geochemistry analysis.

A D8 Advance X-ray diffractometer was used to study the mineralogical content of the samples. The scanning measurements were performed at the rate of 2°/min in the range of 3-90°. Then, the mineral percentages were estimated by calculating the curve of major peaks (Chen and Xiao, 2014). In the next step, Rock-Eval 6® was used to quantify the total organic carbon (TOC) of the samples. This part is specifically important for the samples selected from the source section of the Bakken (Upper and Lower members). To evaluate the TOC of the samples, the trademarked Shale Play method by IFP (Institut Françcais du Pétrol) was applied, and the geochemical properties

were derived following the steps suggested by Behar et al (2001). The temperature program for the Shale Play method was set as the following: the initial temperature was 100°C which was increased to 200°C at 25°C /min and was then kept constant for 3 minutes (for Sh0 calculation). In the next step, temperature was increased to 350°C at 25°C /min and held steady for 3 minutes (for Sh1 calculation). Finally, the temperature was raised to 650°C at 25°C /min. The oxidation cycle reached up to 850^{o} C. This procedure resulted in measuring all Rock-Eval parameters along with TOC of the samples.

5.2.3. Gas adsorption.

All samples were degassed for at least 8 hours at 110°C to remove moisture and volatiles that might be present in the samples. Low-pressure nitrogen was measured on a Micromeritics® Tristar II apparatus at 77K while carbon dioxide adsorption was measured on a Micromeritics® Tristar II plus apparatus at 273K. Gas adsorption volume was evaluated over the relative equilibrium adsorption pressure (P/P_0) range of 0.01-0.99, where P is the gas vapor pressure in the system and P_0 is the saturation pressure of nitrogen (Liu et al., 2017a). We utilized the density functional theory (DFT) molecular model to quantify pore size distributions from low temperature N_2 adsorption isotherms (Do and Do, 2003) along with non-local density functional theory to obtain and interpret PSD curves by the CO_2 adsorption method (Amankwah et al., 1995; Fan and Ziegler, 1992). Based on the fundamental principles of statistical mechanics in explaining the molecular behavior of confined fluids in pore spaces, DFT can be used to describe the adsorption and phase behavior of fluids that are confined in the pore structures. Thus, the density functional theory can better define the thermodynamics behavior and density profiles of such fluids in a molecular level compared to other methods such as Brunauer–Emmett–Teller (BET). Based on the reasons explained earlier, DFT, in comparison with other common techniques, can capture the essential features of both micropore and mesopore filling fluids and their hysteresis response. This can result

in a more reliable assessment of pore size distribution curves over a more complete range of values (from micropores to mesopores) (Monson, 2012; Thommes et al., 2015).

5.2.4. Multifractal analysis.

The box-counting method, a frequently used method in other studies (Lopes and Betrouni, 2009, Russel et al., 1980), was applied to our data to study the multifractal behavior believed to exist in our data. In order to execute multifractal analysis in a porous media, a set of different boxes with equal length ε should be used and be laid over the interval in the recorded signal to be analyzed. The boxes are labeled by index *i* where $N(\varepsilon)$ indicates the total number of boxes with size of ε that is needed to cover the interval understudy (the PSD curve). Accordingly, the section of the *i*th box of size ε is denoted as $u_i(\varepsilon)$. For gas adsorption, relative pressure (P/P_0) was taken as the length ε (Ferreiro et al., 2009,2010).

The boxes of length ε were laid over the heterogeneous pattern of the gas adsorption PSD curve. The probability mass function for the *i*th box can be calculated using the following equation:

$$p_i(\varepsilon) = N_i(\varepsilon) / N_T \qquad (5\text{-}1)$$

Where, $N_i(\varepsilon)$ is the volume of adsorbed nitrogen for the *i*th box and N_T is the total volume of gas that is adsorbed in the pores. Likewise, for each interval of size ε, $P_i(\varepsilon)$ can also be defined by an exponential function of the following form for each box of size ε as:

$$P_i(\varepsilon) \sim \varepsilon^{\alpha_i}, \qquad (5\text{-}2)$$

where α_i is the singularity exponent which represents how singularities of the system approach to infinity as ε gets closer to 0 (Feder, 1988; Halsey et al., 1986). For multifractally distributed properties of intervals of size ε, $N(\varepsilon)$ increases when ε decreases following a power law function of the form:

$$N_\alpha(\varepsilon) \sim \varepsilon^{-f(\alpha)} \qquad (5\text{-}3)$$

where $N_\alpha(\varepsilon)$ is the number of boxes for which probability mass function of the *i*th box, $P_i(\varepsilon)$, has singularity strength between α and $\alpha+d\alpha$. Then, $f(\alpha)$ represents the spectrum of the fractal dimensions that characterizes the abundance in the set with α singularity. Subsequently, $\alpha(q)$ and $f(\alpha)$ can be calculated based on the equations that are proposed by Chhabra and Jensen (1989):

$$\alpha(q) \propto [\sum_{i=1}^{N(\varepsilon)} (u_i(q,\varepsilon) \times \ln p_i(\varepsilon))] / \ln(\varepsilon) \quad (5\text{-}4)$$

$$f(\alpha) \propto [\sum_{i=1}^{N(\varepsilon)} (u_i(q,\varepsilon) \times \ln u_i(q,\varepsilon))] / \ln(\varepsilon) \quad (5\text{-}5)$$

where

$$u_i(q,\varepsilon) = \frac{p_i(\varepsilon)^q}{\sum_{i=1}^{N(\varepsilon)} p_i(\varepsilon)^q} \quad (5\text{-}6)$$

Here, q is the exponent expressing the fractal properties in different scales of the object. In this study, α and $f(\alpha)$ were calculated through a linear regression using Eq. 4 and Eq. 5 with q varying from -10 to 10 for successive unit steps. For multifractal applications, a probability distribution function is defined as:

$$u(q,\varepsilon) = \sum_{i=1}^{N(\varepsilon)} P_i(\varepsilon)^q \sim \varepsilon^{\tau(q)} \quad (5\text{-}7)$$

Where τ_q is the mass scaling function of order q which can be defined as:

$$\tau(q) = \lim_{\varepsilon \to 0} [\ln \sum_i P_i(\varepsilon)^q / \ln(1/\varepsilon)] \quad (5\text{-}8)$$

thus, the generalized dimension (D_q) which is related to q can be expressed as (Halsey, et al., 1986):

$$D_q = \tau(q)/(q-1) \quad (5\text{-}9)$$

While for q=1, D_q will become:

$$D_1 = \lim_{\varepsilon \to 0} \left(\sum_{i=1}^{N(\varepsilon)} p_i(\varepsilon) \ln p_i(\varepsilon) / \ln(\varepsilon) \right) \quad (5\text{-}10)$$

5.3. Results and discussion

5.3.1. Multifractal analysis of CO2 adsorption.

The log-log plot of the partition function $u(q, \varepsilon)$ versus the length scale ε for the interval of q= -10 to q=10 at successive intervals of q=1 was created and is shown for the representative samples of each member of the Bakken Formation in Fig. 5.1. The plots demonstrated that a linear relationship exists between log$u(q,\varepsilon)$ and logε of these representative samples from the Upper, Middle and Lower Bakken. This shows the existence of a multifractal behavior for pore size distributions (PSD) curves in our samples. The results show a clear distinction between the partition function of q>0 and q<0 with negative and positive slopes, respectively. In addition, the regression lines are found very close to one another, indicating that most of the measured data can be concentrated in a small size domain of the study scale (Ferreiro et al., 2009).

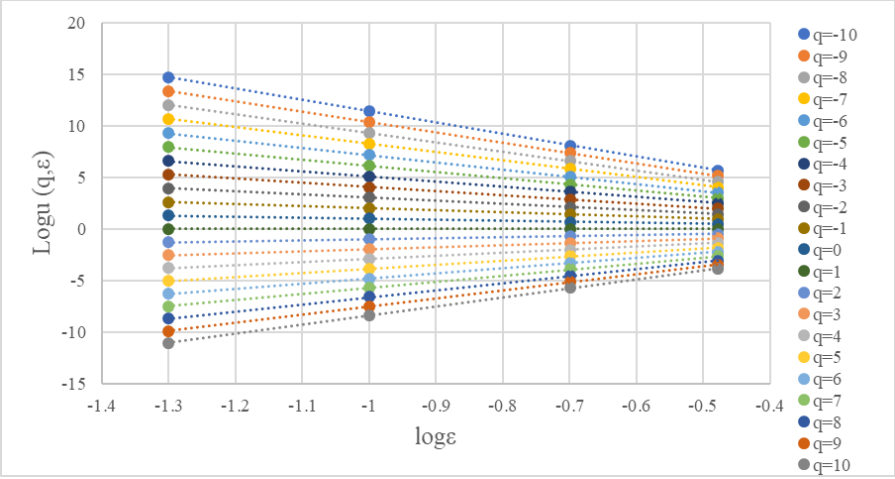

(a) Sample 17(Upper Bakken)

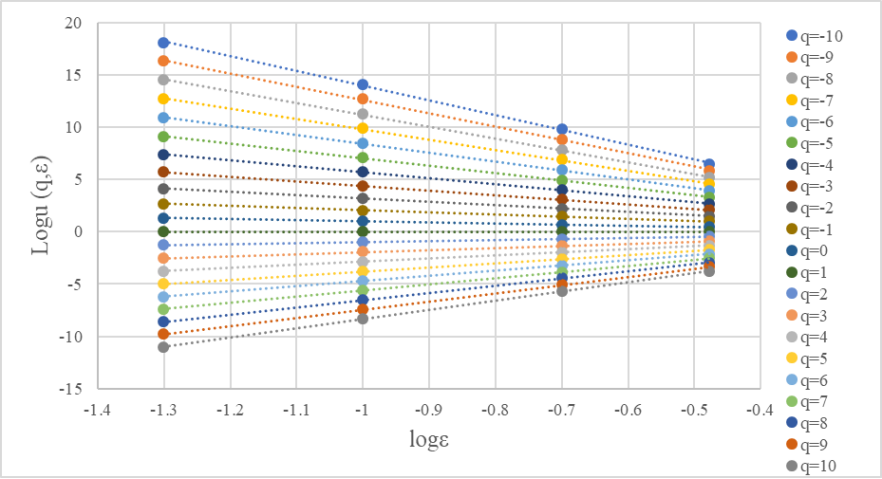

(b) Sample 23 (Middle Bakken)

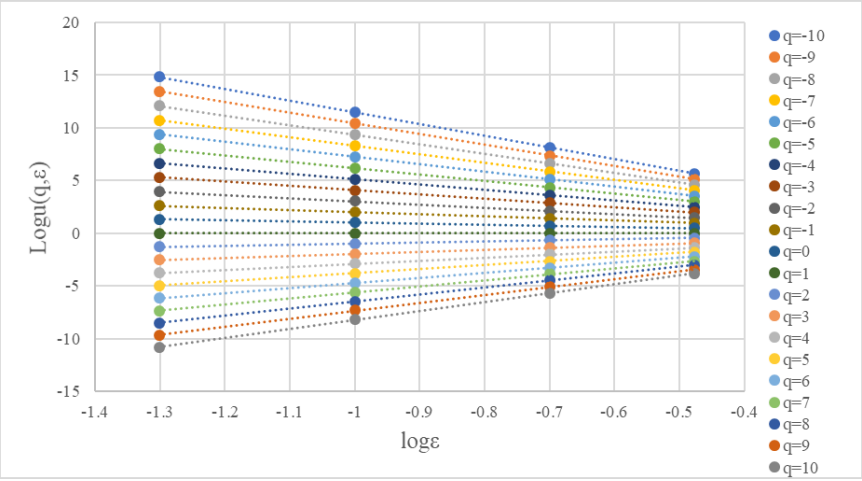

(c) Sample 27 (Lower Bakken)

Fig. 5.1. Log-log plots of the partition function versus box scale of samples from different members of the Bakken from CO_2 adsorption isotherms.

Combining Eq. 9 and Eq. 10, the generalized dimensions D_q from CO_2 adsorption of all studied samples were calculated and are presented in Fig. 5.2. The curves for all samples followed a monotonic decrease as q increased. The data, summarized in Table 5.1, represents $D_0>D_1>D_2$, and demonstrates that the distributions of pore size fit a multifractal behavior, in agreement with the results derived from Fig. 5.1(Ferreiro et al., 2009).

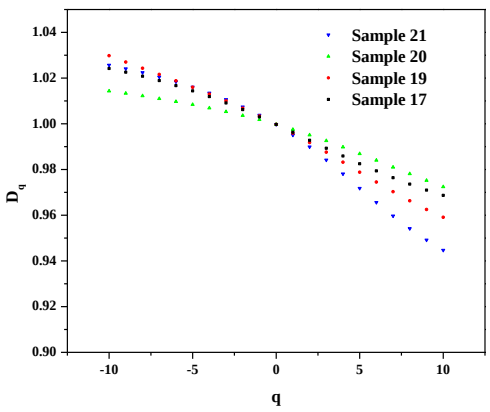

(a) Upper Bakken

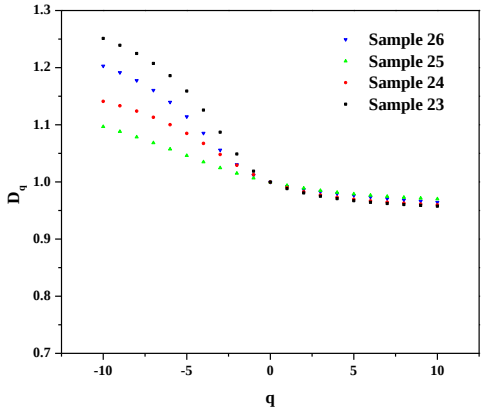

(b) Middle Bakken

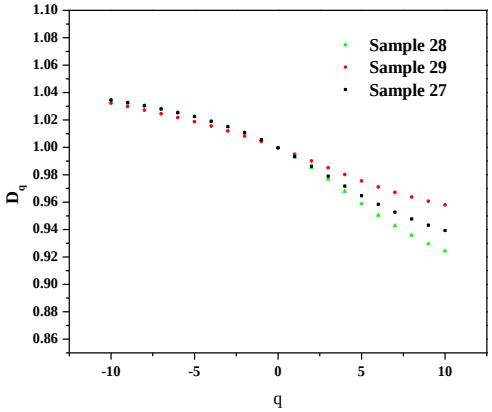

(c) Lower Bakken

Fig. 5.2. The relationships between D_q and q of the samples from CO_2 adsorption isotherms.

D_0 represents singularity of non-empty boxes containing some value of porosity under successive finer partitions, which is independent of the probability of the porosity in that box. From Table 5.1 it can be found that the capacity D_0 of all samples is the same and equal to 1. D_1, the entropy information can characterize the concentration degree of the pore size distribution along the pore size intervals. The indicator D_0-D_1 can be used to describe the degree of uniform distributions across a specific range of pore sizes (Li et al., 2015; Song et al., 2018). The results in Table 5.1

illustrate that the Middle Bakken has higher D_0-D_1 values (0.0087 on average) compared to the D_0-D_1 values calculated from the Upper (0.0035 on average) and Lower Bakken (0.0060 on average). This verifies that the Middle Bakken has the most clustered style of pore size distribution. Thus, we can conclude that the pore size distribution (PSD) in the Upper and Lower Bakken is more homogeneous. Fig. 5.3 shows the pore size distributions of the samples based on CO_2 adsorption. While comparing the pore size distributions of the Eagle Ford Formation, which is a calcareous shale that produces both oil and gas in Texas with our samples from the Bakken Formation, smaller pore volumes with sizes less than 1 nm were detected (Psarras et al., 2017). In this regard, pore size from the Upper Bakken and the Lower Bakken varies from 0.4 nm to 1.8 nm while the pore size from the Middle Bakken is measured between 1.2 nm to 1.8 nm. Fig. 5.3 depicts that the Middle Bakken with the narrowest pore size range has the most grouped pore size distribution, confirming that D_0-D_1 can be a good indicator to describe the concentration degree of pore size distributions.

D_2 is defined as the correlation dimension, which accounts for the behavior of the second sampling moments. Table 5.1 shows that samples from the Middle Bakken have smaller D_2 values than the Upper and Lower Bakken. *H*, which is (D_2+1)/2, and is known as the Hurst exponent (Holmes et al., 2017). *H* can vary from 0.5 to 1 and indicates the degree of the positive autocorrelation. A smaller (1-*H*) value is corresponding to a stronger autocorrelation in size-dependent distribution of any property, porosity in this case. The Middle Bakken has the largest value of (1- *H*) with the average of 0.0076 compared to the samples from the Upper Bakken (0.0038 on average) and Lower Bakken (0.0064 on average). This is a representative of the lowest autocorrelation in the size dependent distribution of porosity, which agrees with pore size distributions that were found in Fig. 5.3. *H* can also be used to specify the pore connectivity across the pore size network of various

sizes, which can affect the permeability or flow through the sample (Martínez et al., 2010). A smaller *H* value represents poor pore connectivity, which was calculated to be the smallest for the Middle Bakken.

Table 5.1. Characteristics of the generalized dimension from all the samples from CO_2 adsorption

	D_{10+}	D_{10-}	D_0	D_1	D_2	D_0-D_1	H	D_{10-}-D_{10+}
Sample 17	0.9687	1.0242	0.9997	0.9963	0.9928	0.0034	0.9964	0.0555
Sample 19	0.9591	1.0298	0.9997	0.9959	0.9918	0.0038	0.9959	0.0707
Sample 20	0.9724	1.0143	0.9997	0.9975	0.9951	0.0022	0.9976	0.0419
Sample 21	0.9447	1.0257	0.9997	0.9951	0.9899	0.0046	0.9950	0.0810
Sample 23	0.9576	1.2511	0.9997	0.9882	0.9806	0.0115	0.9903	0.2935
Sample 24	0.9599	1.1410	0.9997	0.9900	0.9827	0.0097	0.9914	0.1811
Sample 25	0.9701	1.0968	0.9997	0.9938	0.9890	0.0059	0.9945	0.1267
Sample 26	0.9644	1.2029	0.9997	0.9920	0.9867	0.0077	0.9934	0.2385
Sample 27	0.9393	1.0345	0.9997	0.9932	0.9862	0.0065	0.9931	0.0952
Sample 28	0.9243	1.0346	0.9997	0.9930	0.9853	0.0067	0.9927	0.1103
Sample 29	0.9580	1.0323	0.9997	0.9950	0.9901	0.0047	0.9951	0.0743

The difference between D_{10-}-D_{10+} of the D_q spectrum is that it can characterize the heterogeneity of the porosity distribution over the entire pore size range (0-2 nm that was measured by CO_2 adsorption). Table 5.2 shows that samples from the Middle Bakken have the highest D_{10-}-D_{10+} value with an average of 0.2100 compared to the samples from the Upper Bakken (0.062 in average) and Lower Bakken (0.0933 in average). Overall, considering the micropores that exist in the samples, the Middle Bakken has the highest level of heterogeneity in porosity distribution while samples from the Upper Bakken have the least degree of heterogeneity in the distribution of pore sizes.

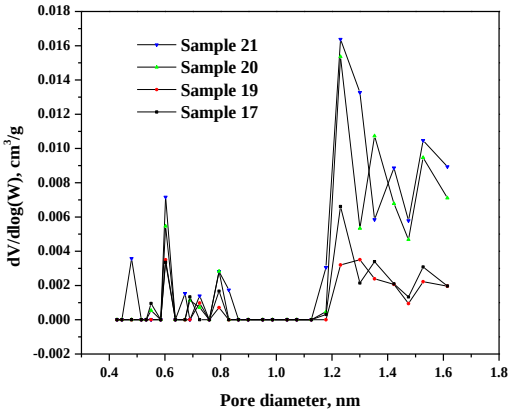

(a) Upper Bakken

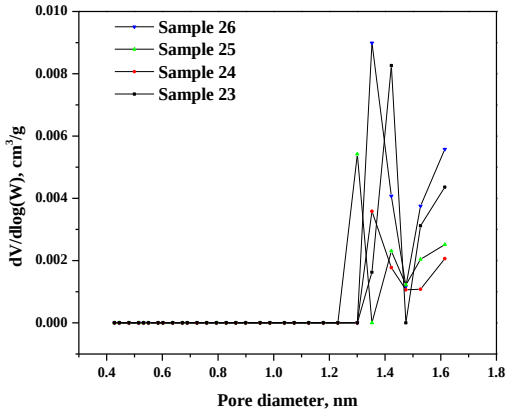

(b) Middle Bakken

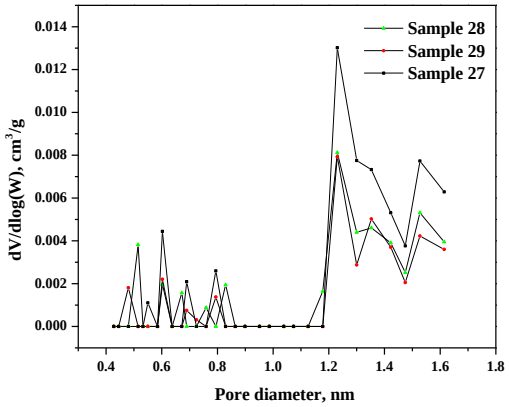

(c) Lower Bakken

Fig. 5.3. Pore size distributions of the sample from the CO_2 adsorption.

The *f(α)* curves versus *α* for all samples are shown in Fig. 5.4, which demonstrates a strong asymmetric (around *α* equal to 1) convex parabolic shape. For the samples from the Upper and Lower Bakken, the portion of the curve with the negative slope is wider and extends longer than the portion of the curve with the positive slope. In other words, the absolute value of the curve tangent on the left side of the symmetry line (around *α* equal to 1) is larger than the right portion of the curve. In contrast, for the samples from the Middle Bakken, the portion of the curve with

the positive slope is wider compared with the left portion with the negative slope. All of these behaviors explain that pore size distributions (PSD) of all samples exhibit a multifractal behavior. The results in Table 5.2 show that the samples from the Middle Bakken have a higher α_0 value (1.0102 on average) than the samples from the Upper (1.0031 on average) and Lower Bakken (1.0054 on average), meaning that the Middle Bakken has a higher degree of pore size distribution concentrations over a specific range of pore size. This conclusion verifies the results from Fig. 5.3 and the Hurst exponent (*H*).

The value of $\alpha_{10-} - \alpha_{10+}$ is used to describe the degree of heterogeneity of the pore size distribution. Larger $\alpha_{10-} - \alpha_{10+}$ can be translated to a more heterogeneous pore size distribution within the sample. The calculation revealed that the samples from the Middle Bakken have a larger $\alpha_{10-} - \alpha_{10+}$ value with 0.3240 on average than the samples retrieved from the Upper Bakken (0.1089 on average) and Lower Bakken (0.1497 on average). This indicates that the pore size distribution in the Middle Bakken has a more internal difference from the multifractal analysis perspective (Do and Do, 2003). Thus, pore size distribution in the Middle Bakken is more heterogeneous than in the Upper and Lower Bakken. The left side of the $f(\alpha)$ curve with respect to the symmetry line represents areas with higher probability density of the pore volume distribution while the right portion corresponds to areas with lower probability density (Song et al., 2018). We used a parameter known as R_d, which is defined as $((\alpha_0 - \alpha_{10+}) - (\alpha_{10-} - \alpha_0))$, to show the departure degree of the $f(\alpha)$ spectrum from the center or the symmetry line. The results in Table 5.2 display that samples from the Middle Bakken all have negative R_d values, indicating that pore size distributions in these samples are dominated mostly by areas with higher probability (concentrated areas). In contrast, the samples from the Upper and Lower Bakken Formation all have positive R_d values,

inferring that pore size distributions of these samples are dominated by areas with lower probability (sparse areas).

Table 5.2. Characteristics of the multifractal singularity spectra from CO_2 adsorption

	α_0	α_{10+}	α_{10-}	α_0- α_{10+}	α_{10-}-α_0	α_{10-}-α_{10+}	R_d
Sample 17	1.0031	0.9483	1.0412	0.0548	0.0381	0.0929	0.0167
Sample 19	1.0035	0.9295	1.0597	0.0740	0.0562	0.1302	0.0178
Sample 20	1.0018	0.9484	1.0252	0.0534	0.0234	0.0768	0.0300
Sample 21	1.0041	0.9063	1.0419	0.0978	0.0378	0.1356	0.0600
Sample 23	1.0143	0.9475	1.3715	0.0668	0.3572	0.4240	-0.2904
Sample 24	1.0110	0.9486	1.2207	0.0624	0.2097	0.2721	-0.1473
Sample 25	1.0062	0.9589	1.1869	0.0473	0.1807	0.2280	-0.1334
Sample 26	1.0092	0.9469	1.3186	0.0623	0.3094	0.3717	-0.2471
Sample 27	1.0059	0.9061	1.0554	0.0998	0.0495	0.1493	0.0503
Sample 28	1.0060	0.8789	1.0542	0.1271	0.0482	0.1753	0.0789
Sample 29	1.0043	0.9354	1.0598	0.0689	0.0555	0.1244	0.0134

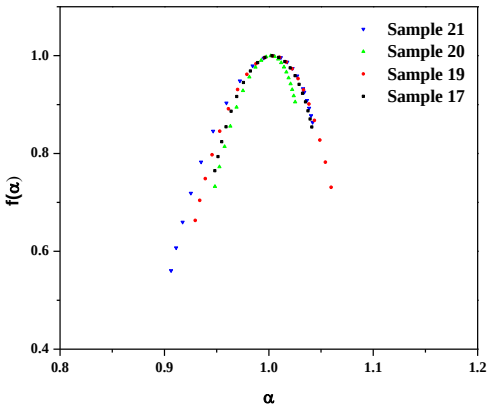

(a) Upper Bakken

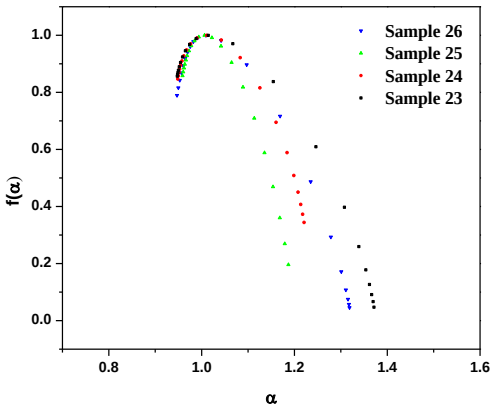

(b) Middle Bakken

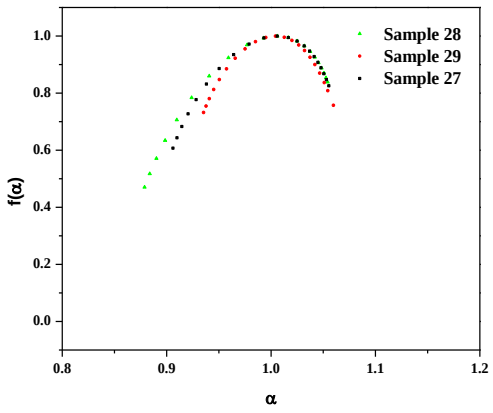

(c) Lower Bakken

Fig. 5.4. Multifractal singularity spectra *f(α)* for the Bakken samples from CO_2 adsorption isotherms.

5.3.2. Multifractal analysis of N_2 adsorption.

The N_2 adsorption method can access the pores in the range of meso- to macro-scale which CO_2 adsorption is incapable of detecting since it measures only the distribution of micropores. In this part, we will analyze the multifractal behavior of the pore size distribution by nitrogen adsorption. For this purpose, the log-log plots of the partition function $u(q, \varepsilon)$ versus the length scale ε between q=-10 to q=10 at successive intervals of q=1 were made based on nitrogen adsorption isotherms and are displayed for representative samples of each member of the Bakken in Fig. 5.5. The curves show that pore size distributions from the nitrogen adsorption exhibit a multifractal behavior. Similar to the curves in Fig. 5.1, the partition function has a notable difference between q>0 and q<0 with negative and positive slopes, respectively. Also, the regression lines are very close to each other, indicating that the majority of pore size distributions are concentrated in a small size domain of the study scale that was measured by nitrogen adsorption isotherms.

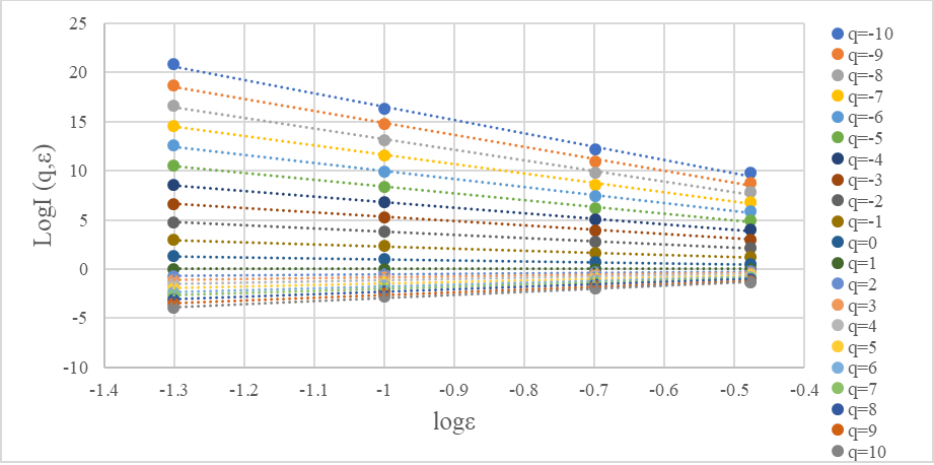

(a) Sample 17 (Upper Bakken)

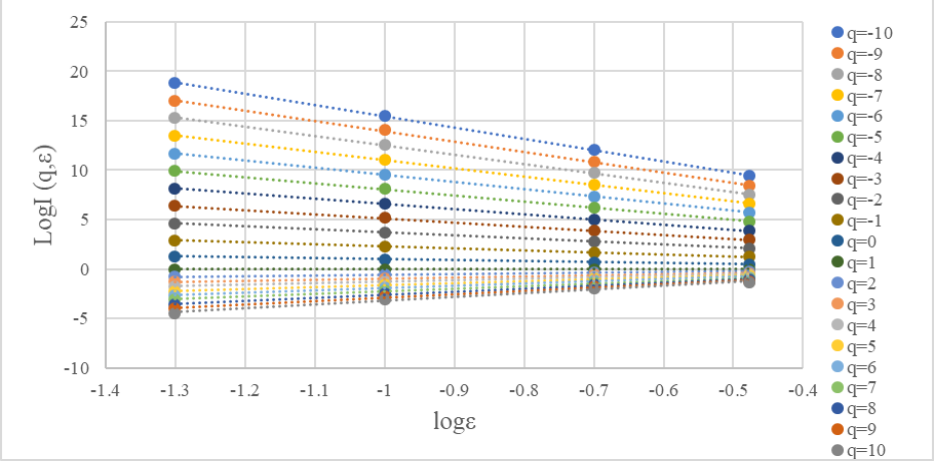

(b) Sample 23 (Middle Bakken)

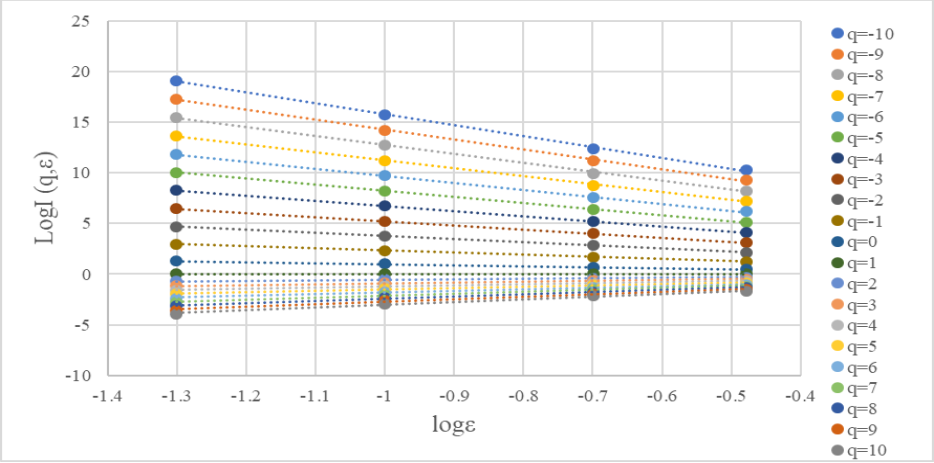

(c) Sample 27 (Lower Bakken)

Fig. 5.5. Log-log plots of the partition function versus box scale of the representative samples from different members of the Bakken from N_2 adsorption isotherms.

The generalized dimensions from the nitrogen adsorption were calculated and are shown in Fig. 5.6. Considering all of the samples from the Bakken Formation, D_q decreases as q increases. Table 5.3 shows the characteristics of the generalized dimension from our samples derived from nitrogen adsorption. D_0 that was calculated from the nitrogen adsorption isotherms are similar with the results obtained by other researchers in the soil science field (Ferreiro et al., 2009;2010). It was realized that the Middle Bakken has a larger D_0-D_1 value (with an average value of 0.2133) in comparison to the Upper and Lower Bakken with average D_0-D_1 values of 0.1964 and 0.1582, respectively. This illustrated that the samples from the Middle Bakken have more clustered pore size data while samples from the Lower Bakken has a more uniform pore size distribution. Sample 10 and Sample 6 had the smallest and the largest D_0-D_1 values, respectively, indicating the most and the least uniformity of pore size distributions. This conclusion was also confirmed by the pore size distribution curves of each sample shown in Fig. 5.7.

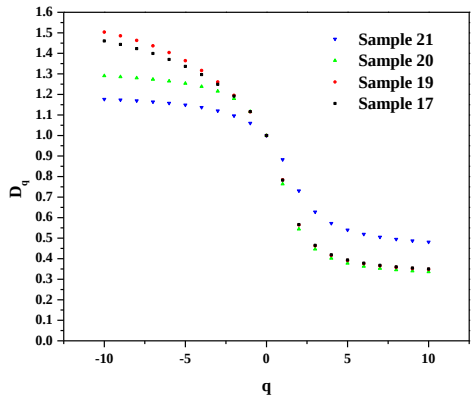

(a) Upper Bakken

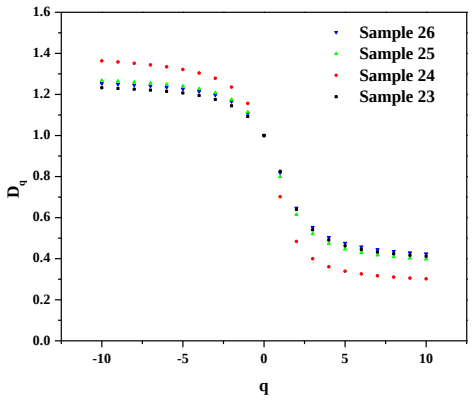

(b) Middle Bakken

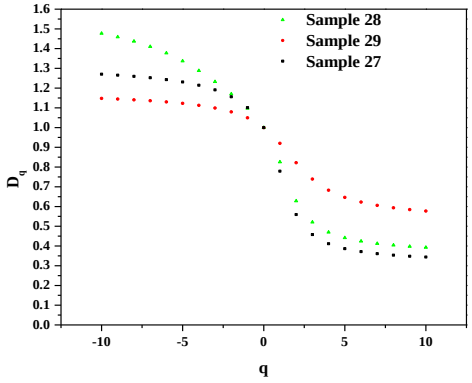

(c) Lower Bakken

Fig. 5.6. Generalized dimensions of the samples from the N_2 adsorption.

Table 5.3. Characteristics of the generalized dimension from all the samples from nitrogen adsorption

	D_{10+}	D_{10-}	D_0	D_1	D_2	D_0-D_1	D_{10-}-D_{10+}	H
Sample 17	0.3501	1.4604	0.9997	0.7826	0.5661	0.2171	1.1103	0.7831
Sample 19	0.3480	1.5033	0.9997	0.7841	0.5648	0.2156	1.1553	0.7824
Sample 20	0.3359	1.2904	0.9997	0.7638	0.5440	0.2359	0.9545	0.7720
Sample 21	0.4815	1.1767	0.9997	0.8826	0.7307	0.1171	0.6952	0.8654
Sample 23	0.4119	1.2322	0.9997	0.8253	0.6400	0.1744	0.8203	0.8200
Sample 24	0.3015	1.3633	0.9997	0.7018	0.4842	0.2979	1.0618	0.7421
Sample 25	0.3975	1.2675	0.9997	0.7997	0.6147	0.2000	0.8700	0.8074
Sample 26	0.4240	1.2534	0.9997	0.8190	0.6472	0.1807	0.8294	0.8236
Sample 27	0.3438	1.2705	0.9997	0.7790	0.5593	0.2207	0.9267	0.7797
Sample 28	0.3928	1.4772	0.9997	0.8253	0.6279	0.1744	1.0844	0.8140
Sample 29	0.5769	1.1476	0.9997	0.9202	0.8220	0.0795	0.5707	0.9110

Fig. 5.7 shows the pore size distribution from the nitrogen gas adsorption. Comparing pore size distributions of our samples with other major shale formations such as the Eagle Ford or the Barnett, it was found that our samples from the Bakken Formation exhibited much lower pore volumes (Holmes et al., 2017). D_2 of the samples from the Upper and the Middle Bakken found very close in values and smaller than the D_2 of the samples from the Lower Bakken. The Hurst exponent of the samples from the Lower Bakken found to be the largest, demonstrating that the

pore connectivity of the Lower Bakken is the best among these three members. The (1-*H*) value of the samples from the Lower Bakken was calculated to be the smallest, meaning that the Lower Bakken samples have the highest autocorrelation degree in a size dependent distribution of porosity.

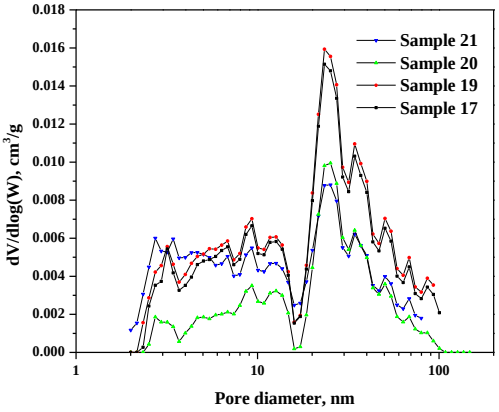

(a) Upper Bakken

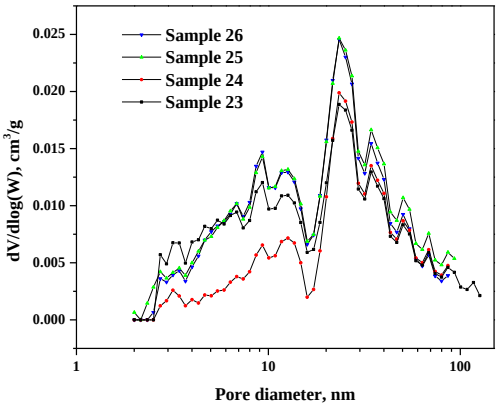

(b) Middle Bakken

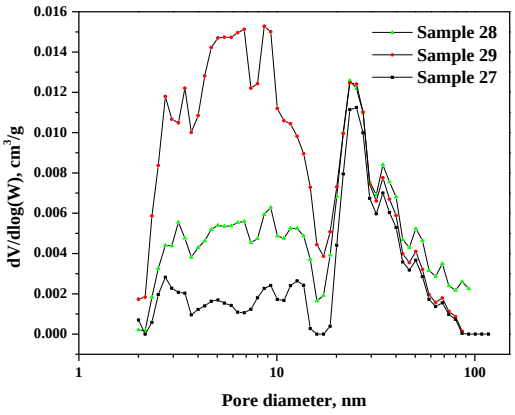

(c) Lower Bakken

Fig. 5.7. Pore size distributions of the samples from the N_2 adsorption.

The difference between D_{10-} and D_{10+}, which is shown as (D_{10-}-D_{10+}) of the D_q spectrum, can characterize the heterogeneity of the porosity distribution over complete collected pore size distribution data. Nitrogen adsorption was capable to detect pore sizes in a range of 2-200 nm in

our samples. We found that the Upper Bakken has the highest D_{10-}-D_{10+}value with an average of 0.9788, compared to the Middle and Lower Bakken with average values of 0.8954 and 0.8606, respectively. This is interpreted to mean that the Upper Bakken has the most heterogeneous pore distribution while the Lower Bakken has the least.

The $f(\alpha)$ curve of the samples, plotted in Fig. 5.8, expresses a convex parabolic shape, indicating that pore size distributions (2-200nm) of our samples exhibit a multifractal behavior. The results in Table 5.4 indicate that samples from the Middle Bakken have a higher α_0 value (average of 1.1407) compared to the samples from the Upper and the Lower Bakken with average α_0 values of 1.1389 and 1.1123, respectively. This is explained by the fact that the Middle Bakken has a slight higher concentrative degree of pore size distributions, which also confirms the results in Fig. 5.7 and the Hurst exponent. Regarding α_{10-}-α_{10+}, the Upper Bakken exhibits the largest value followed by the Lower and then by the Middle Bakken with average values of 1.1253, 0.9927, and 0.9721, respectively. In terms of the internal difference for multifractal analysis of pore size distributions, the Upper Bakken with the largest α_{10-}-α_{10+} value and the highest degree of internal difference. Consequently, samples from the Upper Bakken are found to be the most heterogeneous ones with respect to pore size distributions while the Middle Bakken is the most homogeneous. The R_d of all samples were calculated to be positive, presenting that pore size distributions of these samples are dominated mostly by the areas with lower probability (sparse areas).

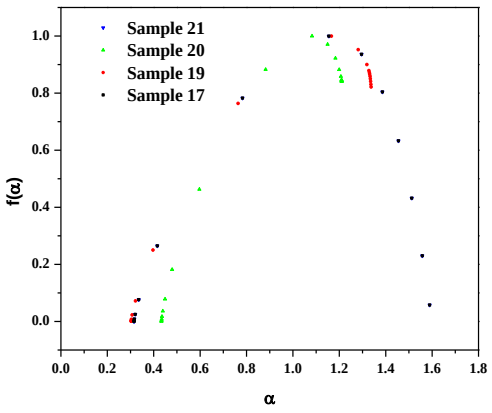

(a) Upper Bakken

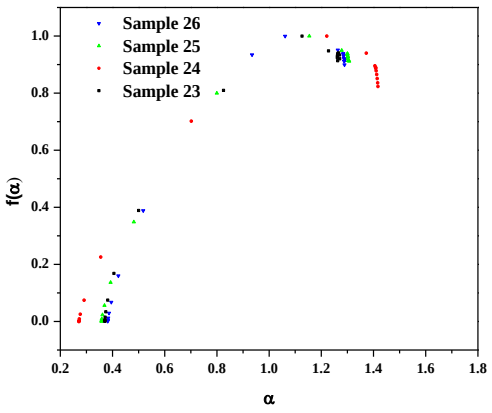

(b) Middle Bakken

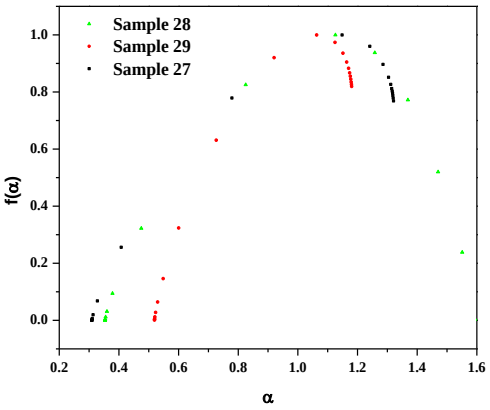

(c) Lower Bakken

Fig. 5.8. Multifractal singularity spectra, f(α) for the Bakken samples from N_2 adsorption isotherms.

Table 5.4. Characteristics of the multifractal singularity spectra from N_2 adsorption

	α_0	α_{10+}	α_{10-}	α_0- α_{10+}	α_{10-}-α_0	α_{10-}-α_{10+}	R_d
Sample 17	1.1550	0.3151	1.6321	0.8399	0.4771	1.3170	0.3628
Sample 19	1.1524	0.3132	1.6858	0.8392	0.5334	1.3726	0.3058
Sample 20	1.1660	0.3023	1.3373	0.8637	0.1713	1.0350	0.6924
Sample 21	1.0823	0.4334	1.2099	0.6489	0.1276	0.7765	0.5213
Sample 23	1.1262	0.3707	1.2613	0.7555	0.1351	0.8906	0.6204
Sample 24	1.2211	0.2714	1.4173	0.9497	0.1962	1.1459	0.7535
Sample 25	1.1540	0.3578	1.3029	0.7962	0.1489	0.9451	0.6473
Sample 26	1.0613	0.3817	1.2888	0.6796	0.2275	0.9071	0.4521
Sample 27	1.1482	0.3094	1.3207	0.8388	0.1725	1.0113	0.6663
Sample 28	1.1257	0.3535	1.6591	0.7722	0.5334	1.3056	0.2388
Sample 29	1.0631	0.5193	1.1804	0.5438	0.1173	0.6611	0.4265

It is well understood that CO_2 adsorption can be used to analyze pore structures in the microscale (<2 nm) while N_2 is suitable to detect and characterize the pores in a meso- to macro-scale (2-200 nm) level (Liu et al., 2017a). The integration of the two methods can help to better understand pore size information for pores less than 200 nm. In this study, we acquired multifractal analysis results from CO_2 adsorption to represent the heterogeneity information of the micropores and then combined that with the results from nitrogen adsorption as the heterogeneity information of meso- and macropores (2-200 nm). Thus, this will provide us with comprehensive heterogeneity information over a wide range of pore sizes. Based on the analysis and results that were presented in sections 3.1 and 3.2, it can be concluded that, regarding micropores, the Middle Bakken is the most heterogeneous while considering meso- and macropores, the Upper Bakken is the most heterogeneous in terms of pore size distributions.

Figure 5.9 shows the comparison results of micropores and meso-macropores of the samples that were analyzed in this study. It can be found that micropores in the Bakken samples are less heterogeneous (Fig. 5.9a) and show a larger Hurst exponent (Fig. 5.9b) compared to the meso-

macropores. This is a good representation that micropores in the Bakken Formation have a better connectivity and more homogeneity regarding their distribution. Samples with the largest meso-macro pore heterogeneity do not have the highest micropore heterogeneity. No clear relationship can be found between the micro-pore heterogeneity and meso-macro-pore heterogeneity (Fig. 5.9c), indicating that the micropore heterogeneity and the meso-macro pore heterogeneity needs to be analyzed separately.

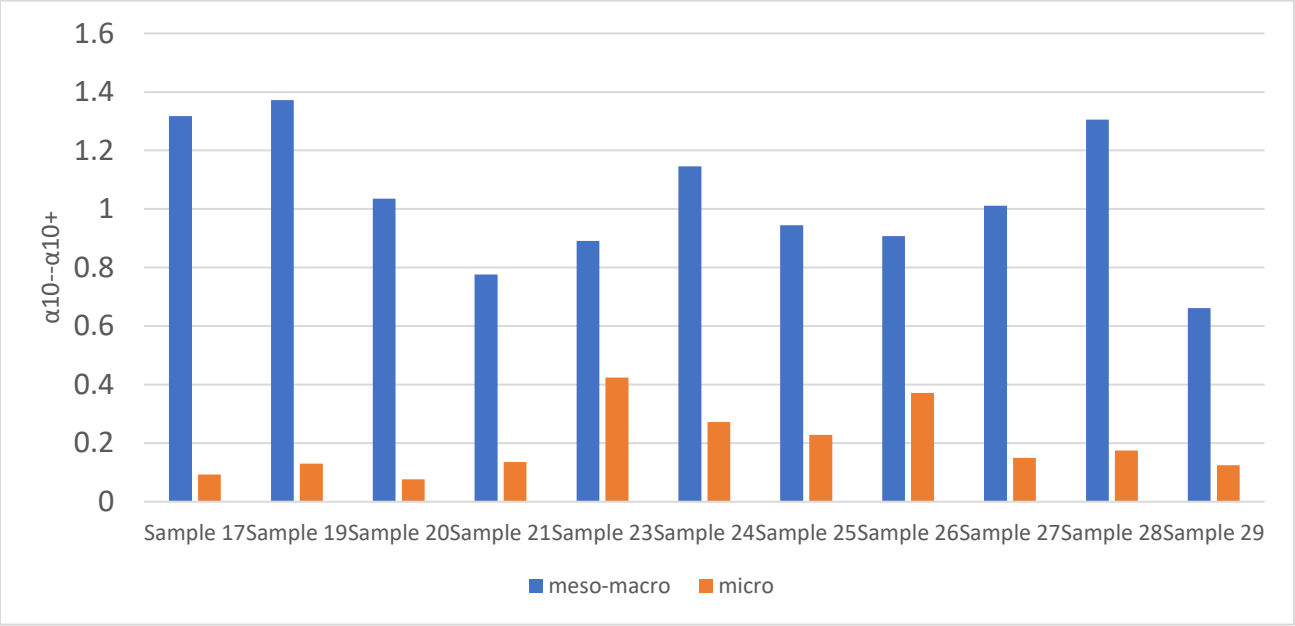

(a) Heterogeneity

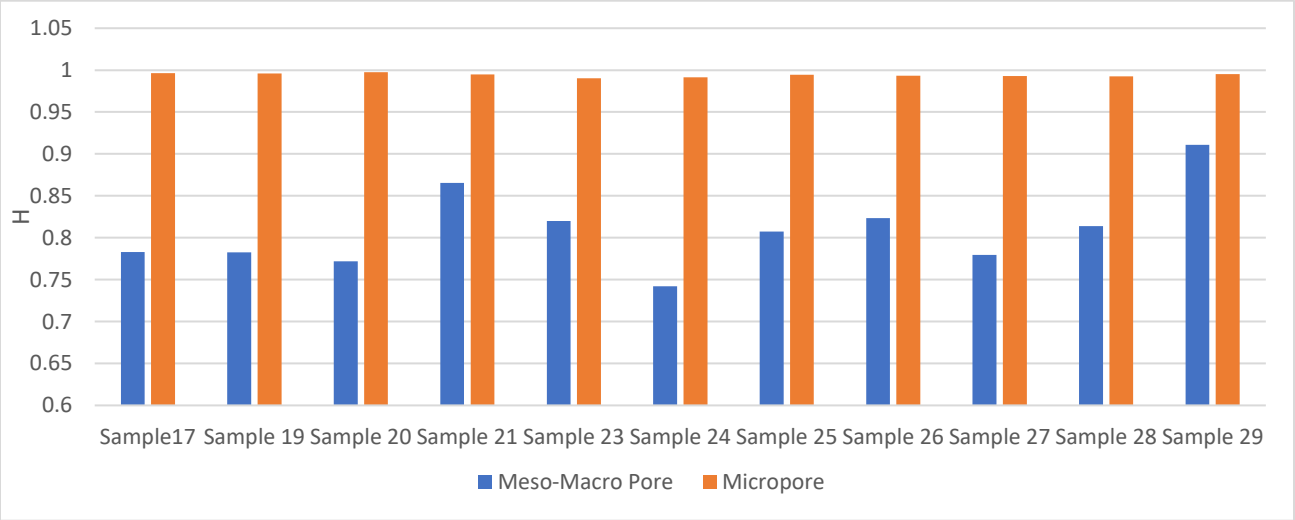

(b) Hurst exponent

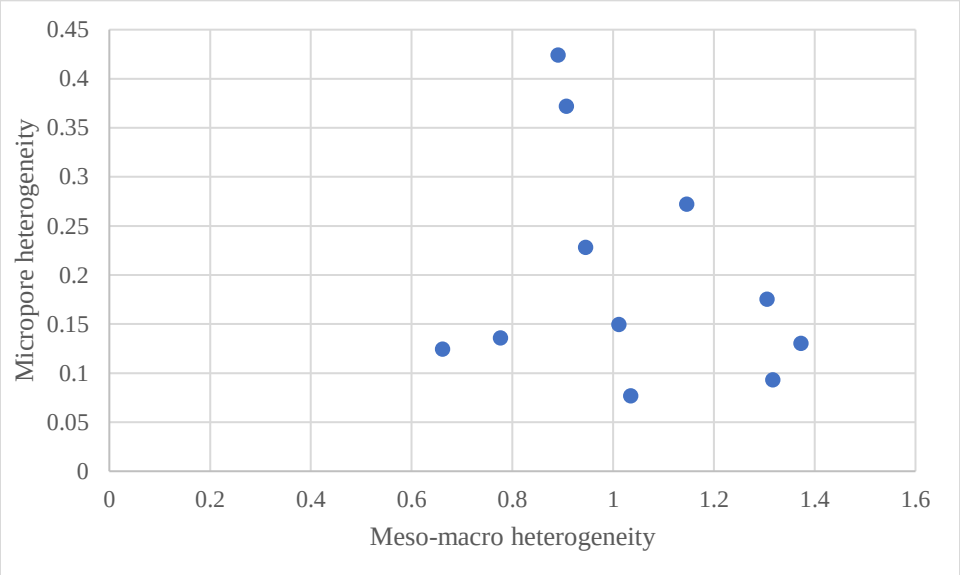

(c) Correlation between the micropore heterogeneity and meso-macropore heterogeneity

Fig. 5.9. Comparison of the pore structure information of the samples.

5.3.3. Potential factors affecting heterogeneity of pore structures.

In order to analyze the factors that could potentially affect the heterogeneity of pore structures, it was decided to investigate these factors for micro- and meso-macro size range of pores, separately.

5.3.3.1. The impact of pore volume.

We plotted pore volume on the x-axis versus the heterogeneity index (α_{10}-α_{10+}) on the y-axis to find whether pore volume has any effect on pore heterogeneity. Based on the results in Fig. 5.10, we were not able to establish any strong correlation between pore volume and heterogeneity. Therefore, we may conclude that pore volume or porosity as a quantity is not a valid constraint on the heterogeneity of the meso-macro pores, which agrees with our previous study that related heterogeneity index and porosity using SEM images (Liu and Ostadhassan, 2017). For micropores, we can deduce that as pore volume increases, pore heterogeneity appears to have a decreasing tendency.

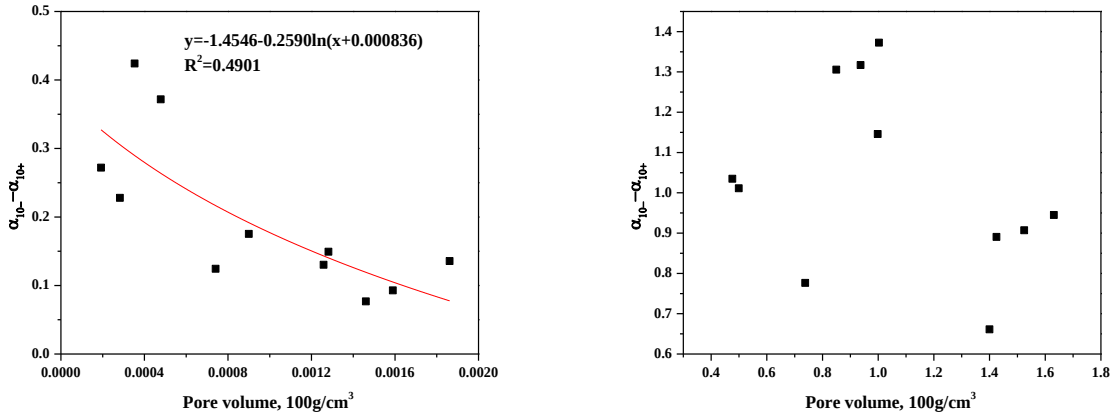

(a) micropores (<2 nm) (b) meso-macro pores (2-200 nm)

Fig. 5.10. Correlations between the pore volume and the heterogeneity of the pores.

5.3.4.2. The impact of the rock compositions.

Among our samples, the ones chosen from the Upper and the Lower Bakken are organic-rich while the Middle Bakken samples are composed of mostly mixed carbonates and fine-grained clastics. Considering this difference in constituent components, we categorized the Upper and Lower Bakken under group I and the Middle Bakken as group II in order to study them separately. To illustrate if mineralogy can control pore heterogeneity, partial least-squares regression (PLS), which is a measure of how one parameter can impact the other one, was employed (Liu et al., 2017a, b). To apply PLS to our data, rock compositions were taken as the independent variable while the pore heterogeneity index (α_{10-}-α_{10+}) and the Hurst parameter as the dependent components. Table 5.5 and Table 5.6 summarize rock compositions of the samples in group I and group II, respectively. In addition, Table 5.7 and Table 5.8 show the PLS results from the samples in group I and group II, respectively. Table 5.5 and Table 5.6 show that quartz is the dominant mineral in these samples. The TOC (total organic carbon) of the samples from the Upper and the Lower Bakken was recorded more than 10 %wt., reflecting the organic-rich nature of the studied

samples with the kerogen been mostly type II marine (Liu et al., 2017b). In addition, the main clay mineral in these samples was found to be illite.

Table 5.7 shows that for micropores within the Upper and Lower Bakken, quartz and clay will slightly reduce the pore connectivity and increase the pore heterogeneity whereas pyrite and feldspar increase pore connectivity and reduce pore heterogeneity. For meso-macro pores of these samples, quartz and clay were found to increase pore connectivity and lower pore heterogeneity while pyrite and feldspar have an opposite effect. Among all constituent components, organic matter was found to impact both pore connectivity and heterogeneity the most, and for all ranges of pore sizes. We realized that organic matter could increase the micropore connectivity and decrease the micropore heterogeneity. This finding can also be an indication of the existence of micropores associated with the organic matter.

Table 5.8 data, which summarize the impact of rock composition on pore heterogeneity of the samples from the Middle Bakken, exhibit a slight difference in values than the previous group (upper and lower members). The results demonstrate that quartz and pyrite have a negative effect on pore connectivity both in micro and meso-macro scale while feldspar, clay, and calcite can increase pore network connectivity in micro to macro scale. Dolomite enhances micropore connectivity while it deteriorates the connectivity of meso-macro pores. Regarding pore heterogeneity, clay, feldspar, and calcite reduce the heterogeneity of both micropores and meso-macro pores whereas, quartz, and pyrite increase micro to macro pore heterogeneity.

Table 5.5. Rock compositions of the samples from the Upper and Lower Bakken[4]

		Quartz, %	Pyrite, %	Feldspar, %	Clay, %	Dolomite, %	TOC, %
Upper Bakken	Sample 17	48.44	20.06	7.63	9.60	0.00	14.27
	Sample 19	13.94	2.31	45.36	19.79	0.00	17.53
	Sample 20	40.26	2.32	3.36	39.57	0.00	13.97
	Sample 21	41.85	3.98	13.22	22.01	6.09	13.00

	Sample 27	48.16	4.90	2.08	24.91	0.00	16.96
Lower Bakken	Sample 28	39.36	4.65	5.90	29.52	0.00	10.55
	Sample 29	44.36	2.69	2.78	33.22	0.00	10.21

Table 5.6. Rock compositions of the samples from the Middle Bakken[4]

	Quartz, %	Pyrite, %	Feldspar, %	Clay, %	Dolomite, %	Calcite, %
Sample 23	37.54	0.10	11.10	14.50	11.00	25.70
Sample 24	38.25	2.29	13.20	13.60	25.00	7.60
Sample 25	24.74	1.09	9.50	42.22	12.40	9.80
Sample 26	16.85	0.67	6.39	62.94	5.24	7.50

Table 5.7. PLS results of the Upper and the Lower Bakken

Variable	Micropore H	Micropore Index	Meso-macro Pore H	Meso-macro Pore Index
Intercept	0.994668	0.130531	0.846872	0.874269
Quartz	-0.000009	0.000086	0.000651	-0.004013
Pyrite	0.000019	-0.000176	-0.001332	0.008209
feldspar	0.000007	-0.000069	-0.000520	0.003203
clay	-0.000010	0.000096	0.000721	-0.004444
Organic matter	0.000064	-0.000595	-0.004487	0.027658

Table 5.8. PLS results of the Middle Bakken

Variable	Micropore H	Micropore Index	Meso-macro Pore H	Meso-macro Pore Index
Intercept	0.983958	0.957752	0.796001	1.018137
Quartz	-0.000711	0.038123	-0.003635	0.012458
Pyrite	-0.001817	0.085394	-0.024920	0.084494
feldspar	0.002570	-0.152274	0.010655	-0.039664
clay	0.000073	-0.003296	0.000416	-0.001281
dolomite	0.000146	-0.010848	-0.000629	0.001610
Calcite	0.000077	-0.004418	0.001765	-0.006293

5.3.4.3. The impact of maturity.

Besides total organic content, which could affect the heterogeneity of the pore structures, the maturity of source rocks can be another parameter that could significantly influence pore structures (Liu et al., 2017b; Löhr et al., 2015). Thus, it is important to investigate if the samples in group I are affected by different maturity levels with respect to their pore structures and corresponding

heterogeneity. Thermal maturity of the organic matter in source rocks can be evaluated by vitrinite reflectance or equivalent reflectance of other macerals, such as solid bitumen in the absence of vitrinite (Kuila et al., 2014). To carry out this analysis, the maturity of the samples was plotted on the x-axis versus H and α_{10-}-α_{10+} in two separate plots on the y-axis. Hence, the effect of maturity on pore connectivity and pore heterogeneity on the pores at different size scales can be concluded from Fig. 5.11. As a result of the plots and for the samples that were analyzed for this study, we were not able to establish any strong correlation between maturity and pore connectivity (Fig. 5.11a, c) and heterogeneity (Fig. 5.11b, d).

In this study, we attempted to relate different parameters that represent the multifractal behavior of PSD curves to pore connectivity of the samples. Additionally, we investigated the impact of various components on pore network and relevant heterogeneities. We also made conclusions on how major constituent components may affect heterogeneity and what each multifractal parameter may disclose about pore network connectivity. Considering the importance that the existence of different pore sizes and their connectivity have on permeability, especially in unconventional reservoirs, and in order to validate our conclusions, the use of microcomputed tomography (μCT) imaging is necessary. This would be a valuable tool and its use would be highly recommended in future studies in order to examine the connectivity of pores in similar samples.

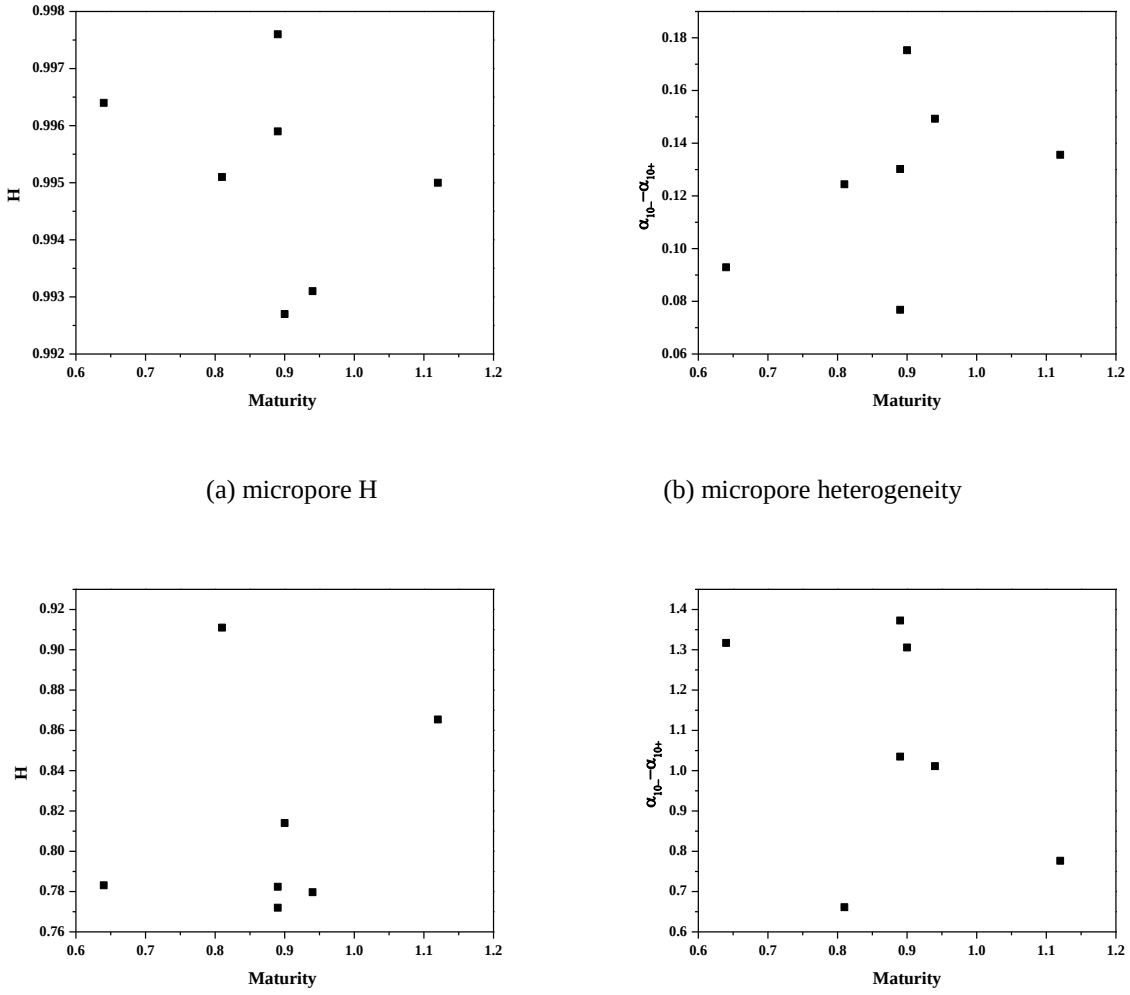

(a) micropore H (b) micropore heterogeneity

(c) meso-macro pore H (d) Meso-macro pore heterogeneity

Fig. 5.11. Impact of the maturity on the pore connectivity and heterogeneity.

5.4. Conclusions

In the presented research, we collected several samples from the Bakken Formation and applied multifractal analysis method to characterize the heterogeneity of pore structures on a wide range of pore sizes. In order to do so, CO_2 and N_2 adsorption were employed to detect micro and meso-macro pores, respectively. Based on this study, the following conclusions were made:

1. Both CO_2 and N_2 adsorption isotherms revealed the multifractal nature of different pore sizes that were detected in our samples.

2. Middle Bakken was found to have the most bundled (concentration) pore size distribution in both micropore (<2 nm) and meso-macropore range (2-200 nm). Additionally, the samples from the Middle Bakken showed the worst micropore connectivity.
3. Samples from the Middle Bakken exhibited the most heterogeneous characteristic in micropores while the Upper Bakken the most heterogeneous nature of meso and macro pores.
4. We were not able to establish a clear correlation between pore volume and heterogeneity, also maturity and heterogeneity and maturity and pore connectivity.
5. For samples taken from the Upper and the Lower Bakken, quartz and clay were found to reduce micropore connectivity and increase micropore heterogeneity while enhancing meso-macro pore connectivity and reducing meso-macro pore heterogeneity. Considering major constituent components of the samples, organic matter showed to have the most influence on pore heterogeneity and connectivity.
6. For samples taken from the Middle Bakken, quartz and pyrite were found to decrease pore connectivity and increase pore heterogeneity of all range of pore sizes whereas clay minerals were found to have an opposite effect on pore connectivity and pore heterogeneity.

5.5. References

Aljama, H., & Wilcox, J.,2017. Microscopic diffusion of CO2 in clay nanopores. Chem.Phys. Lett. 677,162-166.

Amankwah, K.A.G., and Schwarz, J.A., 1995. A modified approach for estimating pseudo-vapor pressures in the application of the Dubinin-Astakhov equation. Carbon. 33, 1313-1319.

Anovitz, L.M., Cole, D.R.,2015. Characterization and Analysis of Porosity and Pore Structures. Rev. Mineral. Geochem. 80(1), 61-164.

Behar, F., Beaμmont, V., De, B., Penteado, H.L., 2001. Rock-Eval 6 technology: performances and developments. Oil Gas Sci. Technol. 56, 111–134.

Bernard, S., Horsfield, B., Schulz, H.M., 2012. Geochemical evolution of organic-rich shales with increasing maturity: A STXM and TEM study of the Posidonia Shale (Lower Toarcian, northern Germany). Mar. Pet. Geol. 31(1), 70–89.

Bowker, K.A., 2007. Barnett Shale gas production, Fort Worth Basin: issues and discussion. AAPG Bull. 91(4), 523-533.

Chaudhuri, B., Sarkar, N., 1995. Texture Segmentation Using Fractal Dimension. IEEE T. Pattern Anal. 17 (1), 72–77.

Chen, J., Xiao, X., 2014. Evolution of nanoporosity in organic-rich shales during thermal maturation. Fuel. 129, 173–181.

Chhabra, A., and Jensen, R.V., 1989. Direct Determination of the $f(\alpha)$ singularity spectrμm. Phys. Rev. Lett. 62, 1327.

Clarke, K.,1986. Computation of the fractal dimension of topographic surfaces using the triangular prism surface area method. Comput. Geosci. 12 (5),713–722.

Clarkson, C.R., Solano, N., Bustin, R.M., et al., 2013. Pore structure characterization of North American shale gas reservoirs using USANS/SANS, gas adsorption, and mercury intrusion. Fuel. 103, 606-616.

Do, D.D., Do, H.D., 2003. Pore characterization of carbonaceous materials by DFT and GCMC simulations: a review. Adsorpt. Sci. Technol. 21(5), 389-423.

Fan, L., and Ziegler, T., 1992. Nonlocal density functional theory as a practical tool in calculations on transition states and activation energies. Applications to elementary reaction steps in organic chemistry. J. Am. Chem. Soc. 114, 10890-10897.

Feder J., 1988. Fractals. Plenμm Press, New York.

Ferreiro, J.P., Miranda, J.G.V., and Vázquez, E.V., 2010. Multifractal analysis of soil porosity based on mercury injection and nitrogen adsorption. Vadose Zone J. 9, 325-335.

Ferreiro, J.P., Wilson, M., and Vázquez, E.V., 2009. Multifractal description of nitrogen adsorption isotherms. Vadose Zone J. 8, 209-219.

Gao, Z.Y., and Hu, Q.H.,2013. Estimating permeability using median pore-throat radius obtained from mercury intrusion porosimetry. J. Geophys. Eng. 10(2), 025014.

Giesch, H., 2006. MercuryPorosimetry: A General (Practical) Overview. Part. Part. Syst. Charact. 23, 9–19.

Gould, D.J., Vadakkan, T.J., 2011. Multifractal and Lacunarity analysis of microvascular morphology and remodeling. Microcirculation. 18(2), 136-151.

Halsey, T.C., Hensen, M.H., Kadanoff, L.P., et al., 1986. Fractal measures and their singularities: the characterization of strange sets. Phys. R. A. 33(2), 1141-1151.

Holmes, R., Rupp, E.C., Vishal, V., & Wilcox, J., 2017. Selection of shale preparation protocol and outgas procedures for applications in low-pressure analysis. Energy & Fuels. 31(9), 9043-9051.

Huang, X.F., and Zhao, Y.P.,2017. Characterization of pore structure, gas adsorption, and spontaneous imbibition in shale gas reservoirs. J. Petrol. Sci. Eng. 159, 197-204.

Javadpour, F., 2009. Nanopores and Apparent Permeability of GasFlow in Mudrocks (Shales and Siltstone). J. Can. Petro. Technol. 48 (8),18-21.

Kirchofer, A., Firouzi, M., Psarras, P., & Wilcox, J.,2017. Modeling CO2 Transport and Sorption in Carbon Slit Pores. J. Phys. Chem. C. 121(38), 21018-21028.

Klaver, J., Desbois, G., Urai, J.L., Littke, R., 2012. BIB-SEM study of the pore space morphology in early mature Posidonia Shale from the Hils area, Germany. Int. J. Coal Geol. 103(1), 12–25.

Kuila, U., McCarty, D.K., Derkowski, A., Fischer, T.B., Topór,T., & Prasad, M.,2014. Nano-scale texture and porosity of organic matter and clay minerals in organic-rich mudrocks. Fuel. 135:359-373.

Li, W., Liu, H.F., and Song, X.X., 2015. Multifractal analysis of Hg pore size distributions of tectonically deformed coals. Int. J. Coal Geol. 144, 138-152.

Li, Y.H., Gao, Q.L., and Victor, R., 1999. Compressibility and fractal dimension of fine coal particles in relation to pore structure characterization using mercury porosimetry. Particle & particle systems characterization. 16, 25-31.

Li, Z.T., Liu, D.M., Cai, Y.D., et al., 2017. Multi-scale quantitative characterization of 3-D pore-fracture networks in bitμminous and anthracite coals using FIB-SEM tomography and X-ray mu-CT. Fuel. 209, 43-53.

Liu, K., Ostadhassan, M., & Bubach, B., 2016. Pore Structure Analysis by Using Atomic Force Microscopy. URTEC 2448210.

Liu, K., Ostadhassan, M., 2017. Quantification of the microstructures of Bakken shale reservoirs using multi-fractal and lacunarity analysis. J. Nat. Gas Sci. Eng. 39, 62-71.

Liu, K., Ostadhassan, M., Zhou, J., et al., 2017a. Nanoscale pore structure characterization of the Bakken shale in the USA. Fuel. 209, 567-578.

Liu, K., Ostadhassan, M., Gentzis, T. et al., 2017b. Characterization of geochemical properties and microstructures of the Bakken Shale in North Dakota. Int. J. Coal Geol. Accept, in press.

Löhr, S.C., Baruch, E.T., Hall, P.A., 2015. Is organic pore development in gas shales influenced by the primary porosity and structure of thermally immature organic matter? Org. Geochem. 87, 119-132.

Lopes, R., and Betrouni, N., 2009. Fractal and multifractal analysis: a review. Med. Image Anal. 13, 634-649.

Loucks, R.G., Reed, R.M., Ruppel, S.C., et al., 2009. Morphology, Genesis, and Distribution of Nanometer-Scale Pores in Siliceous Mudstones of the Mississippian Barnett Shale. J. Sediment Res. 79(12), 848-861.

Mandelbrot, B.B., 1977.Fractals: Form, chance, and dimension, W. H. Freeman and Co., New York.

Martínez, F.S., Martin, M.A., Caniego, F.J., et al.,2010. Multifractal analysis of discretized X-ray CT images for the characterization of soil macropore structures. Geoderma. 156, 32-42.

Monson, P.A., 2012. Understanding adsorption/desorption hysteresis for fluids in mesoporous materials using simple molecular models and classical density functional theory. Micropor Mesopor Mat. 160,47-66.

Muller, J., 1996. Characterization of pore space in chalk by multifractal analysis. J. Hydrol. 187, 215-222.

Muller, J., Huseby, K.O., Saucier, A., 1995. Influence of multifractal scaling of pore geometry on permeabilities of sedimentary rocks. Chaos, Solitons & Fractals. 5(8), 1485-1492.

Peleg, S., Naor, J., Hartley, R., Avnir, D.,1984. Multiple resolution texture analysis and classification. IEEE T. Pattern Anal. 6 (6), 661–674.

Pentland, A., 1984. Fractal-based description of natural scenes. IEEE T. Pattern Anal. 6 (6), 661–674.

Pitman, J.K., Price, L.C., LeFever, J.A., 2001. Diagenesis and fracture development in the Bakken Formation, Williston Basin; implications for reservoir quality in the middle member.

Psarras, P., Holmes, R., Vishal, V., & Wilcox, J., 2017. Methane and CO2 adsorption capacities of kerogen in the Eagle Ford shale from molecular simulation. Accounts Chem. Res. 50(8), 1818-1828.

Russel, D.A., Hanson, J., Ott, E., 1980. Dimension of strange attractors. Phys. Rev. Lett. 45 (14), 1175–1178.

Shelberg, M., Lam, N., Moellering, H.,1983. Measuring the fractal dimension of surfaces. Proceedings of the Sixth International Symposiμm on Computer-Assisted Cartography Auto-Carto. 6, 319–328.

Song, Y., Jiang, B., Shao, P., Wu, J., 2018. Matrix compression and multifractal characterization for tectonically deformed coals by Hg porosimetry. Fuel. 211, 661-675.

Su, Y., Zha, M., Ding, X.J., et al., 2018. Pore type and pore size distribution of tight reservoirs in the Permian Lucaogou Formation of the Jimsar Sag, Junggar Basin, NW China. Mar. Pet. Geol. 89, 761-774.

Tang, H., et al., 2010. Impact factors of fractal analysis of porous structure. Sci. China Technol. Sc. 53(2), 348-351.

Thommes, M., Kaneko, K., Neimark, A.V., et al., 2015. Physisorption of gases, with special reference to the evaluation of surface area and pore size distribution (IUPAC Technical Report). Pure Appl. Chem. 87(9-10), 1051-1069.

Wang, F.P., Reed, R.M., 2009. Pore networks and fluid flow in gas shales. SPE annual technical conference and exhibition. Society of Petroleμm Engineers.

Wang, H.M., Liu, Y., Song, Y., et al., 2012. Fractal analysis and its impact factors on pore structure of artificial cores based on the images obtained using magnetic resonance imaging. J. Appl. Geophys. 86, 70-81.

Wei, Z., Wang, Y., Wang, G, et al., 2018. Pore characterization of organic-rich Late Permian Da-long Formation shale in the Sichuan Basin, southwestern China. Fuel. 211, 507-516.

Xie, S., Cheng, Q., Ling, Q., et al., 2010. Fractal and multifractal analysis of carbonate pore scale digital images of petroleμm reservoirs. Mar. Pet. Geol. 27(2), 476–485.

Yin, M., Huang, H., and Ma, J., 2016. Pore size constrains on hydrocarbon biodegradation in shales from the Second White Speckled Shale Formation of the Western Canada Sedimentary Basin. Fuel. 185, 639-648.

Zhao, P.Q., et al., 2017. Investigation on the pore structure and multifractal characteristics of tight oil reservoirs using NMR measurements: Permian Lucaogou Formation in Jimusaer Sag, Junggar Basin. Mar. Pet. Geol. 86, 1067-1081.

Zou, J., Rezaee, R., and Liu, K., 2017. The effect of temperature on methane adsorption in shale gas reservoirs. Energy & Fuels. 31, 12081-12092.

CHAPTER 6

APPLICATION OF NANOINDENTATION METHODS TO ESTIMATE NANOSCALE MECHANICAL PROPERTIES OF RESERVOIR ROCKS

Abstract

In order to study the mechanical properties of shale samples from Bakken Formation, nanoindentation method, an imaging technique borrowed from other engineering disciplines, was used. Different types of nanoindentation curves were analyzed and the applicability of the nanoindentation theories to study mechanical properties of shale samples at nanoscale was demonstrated. Elastic modulus and Hardness of different samples were calculated, compared and related to their mineral compositions and microstructures which are detected by 2D XRD and FESEM methods, respectively. Results showed that samples with more clay minerals (mainly composed of illite) and larger pore structures have less Young's modulus. In addition, based on the energy analysis method, the fracture toughness at nanoscale was estimated and its relationships with Young's modulus was quantified. It was observed that fracture toughness increases linearly with Young's modulus. This paper presents the results and major findings of this study.

6.1. Introduction

As the first commercially successful application in 1950, hydraulic fracturing has been performed worldwide in oil and gas wells (King, 2012). Especially in the past decade, hydraulic fracturing has been an essential technique to enhance the production of the hydrocarbon from unconventional reservoirs such as shale gas, tight gas, shale oil and coal methane. Fracturing increases not only the production but also the total reserves that can be produced (Montgomery and Smith, 2010).

Rock's elastic and mechanical properties such as elastic modulus, fracture toughness and Poisson's ratio are critical design parameters in hydraulic fracturing. Elastic modulus can influence the stability of fractures while fracture toughness – a generic term for analyzing material resistance to extension of a crack – can affect the geometry of the fractures (Thiercelin et al., 1989). Characterizing and quantifying these parameters has already been studied by many researchers in the past (Ghamgosar et al., 2015; Park et al., 2004; Senseny and Pfeifle, 1984; Thiercelin, 1987; Too et al., 2015; Zoback, 1978). However, due to the mineralogical variability, mechanically and chemically unstable properties of the shale formations, it is very expensive and sometimes even impossible to obtain suitable size samples for standard mechanical testing. Nanoindentation, which only requires a small sample volume, is a technique to detect the local mechanical properties such as Young's modulus and hardness of the materials. This method has been widely used in material science research such as films, biological tissues and other cement-based materials (Naderi et al., 2016; Tanguy et al., 2016; Xiao et al., 2015). In recent years, researchers began to use this method in studying the mechanical properties of shale formations (Kumar et al., 2012; Mason et al., 2014; Shukla et al., 2013), however, they limited their studies only in measuring Young's modulus and hardness. In this paper, we report the results of using nanoindentation to study Bakken Formation samples from the Williston Basin, which is an unconventional reservoir. Estimation of mechanical properties such as Young's modulus, hardness and fracture toughness of the Bakken Formation demonstrates the applicability of the nanoindentation technique in studying shale formations geomechanical properties.

6.2. Theory and Background

6.2.1. Nanoindentation curve.

Nanoindentation is a technique whereby an indenter tip is used to contact the test sample surface under a certain mode and the penetration depth along with the related applied load are recorded (Hu and Li, 2015).

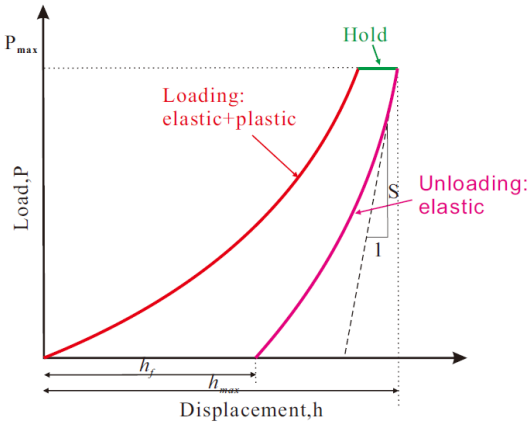

Fig. 6.1. Schematic illustration of indentation load–displacement curve (Hu and Li, 2015).

Fig. 6.1 shows the typical indentation curve which consists of three stages of loading, holding and unloading. In the loading stage, the applied load increases as the penetration depth increase. This stage can be regarded as the combination of elastic and plastic deformation, whereas during the unloading stage we can assume that only elastic deformation can be recovered, and this is used to calculate the mechanical properties.

6.2.2. Young's modulus and hardness.

In order to estimate Young's modulus and hardness values, several parameters derived from Fig. 6.1 was analyzed. For instance, contact stiffness S, defined as $S = \frac{dP}{dh}/_{h_{max}}$, which quantifies the slope of the upper portion of the unloading part (h_{max}) is one that can provide us with valuable information regarding the mechanical response of the material. In order to eliminate the influence

of the bluntness of the indenter on the test results, energy-based analysis was used to calculate the initial contact stiffness (Kaushal K. Jha and Arvind, 2012):

$$S = 0.75*(2\nu_E - 1)\frac{P_{\max}}{h_{\max}}, \qquad (6\text{-}1)$$

Where V_E is called elastic energy ratios which can be defined as the ratio of the absolute work and the elastic work (Fig. 6.2):

$$\nu_E = \frac{U_s}{U_e} \qquad (6\text{-}2)$$

Where U_s is the absolute work from nanoindentation determined by the area OAh_LO whereas U_{ir} is the irreversible energy work determined from the area $OABh_{max}$ and U_e can be calculated from the area $h_fBh_{max}h_f$.

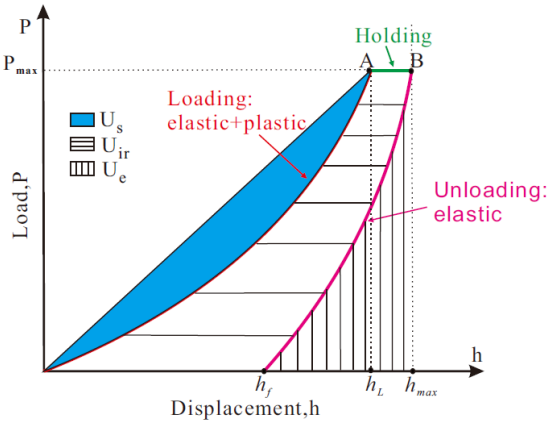

Fig. 6.2. Schematic illustration of the energy analysis for calculation purposes(Kaushal K. Jha and Arvind, 2012).

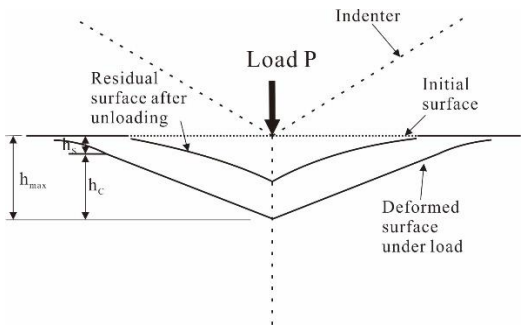

Fig. 6.3. Schematic illustration of the unloading process (Oliver and Pharr, 1992).

Fig. 6.3 illustrates the unloading process during a typical nanoindentation test, from which it is concluded that

$$h_{\max} = h_s + h_c , \qquad (6\text{-}3)$$

Where h_s is the vertical surface deflection at the perimeter of the contact and h_c is the contact depth. h_s and h_c can be derived using the following equation separately(Hu and Li, 2015; Oliver and Pharr, 1992):

$$h_s = \varepsilon \frac{P_{\max}}{S} \quad \varepsilon = 0.75 \qquad (6\text{-}4)$$

$$h_c = \frac{2(\nu_E - 1)}{(2\nu_E - 1)} h_{\max} \qquad (6\text{-}5)$$

Once initial contact stiffness and contact depth were derived, the reduced Young's modulus can be calculated as (Oliver and Pharr, 1992):

$$E_r = \frac{\sqrt{\pi} S}{2\sqrt{A_c}}, \qquad (6\text{-}6)$$

Where $A_c = 24.5 h_c^2$. (6-7)

Finally, the Young's modulus and hardness parameters can be obtained as:

$$\frac{1}{E_r} = \frac{1-\nu^2}{E} + \frac{1-\nu_i^2}{E_i} \qquad (6\text{-}8)$$

$$H = \frac{P_{\max}}{A} / {}_{h_{\max}} \qquad (6\text{-}9)$$

6.2.3. Toughness measurement using nanoindentation.

There is a significant growth in the number of researchers who are using nanoindentation methods to study fracture toughness for its accurate and repeatable measurement (Kruzic et al., 2009; Scholz et al., 2004; Sebastiani et al., 2015; Wang et al., 2015), whereas using nanoindentation method to

study the fracture toughness of rocks is very scarce to date. In this paper, we acquired nanoindentation technique to study the fracture toughness of shale samples from the Bakken Formation. Due to the inhomogeneous nature of the samples and the difficulty in measuring the crack length during the nanoindentation process, we applied energy analysis method in this study. The theoretical concept behind the energy analysis method is that the irreversible energy (U_{ir}) can be defined as the difference of the total energy (U_t) and the elastic energy (U_e) (Cheng et al., 2002). Then fracture energy (U_{crack}) can be described using the following equation:

$$U_{crack} = U_{ir} - U_{pp}. \qquad (6\text{-}10)$$

In this equation U_{pp} is the energy cost due to the pure plasticity which can be calculated using the following mathematical relationship:

$$\frac{U_{pp}}{U_t} = 1 - \left[\frac{1 - 3\left(\frac{h_f}{h_{\max}}\right)^2 + 2\left(\frac{h_f}{h_{\max}}\right)^3}{1 - \left(\frac{h_f}{h_m}\right)^2}\right]. \qquad (6\text{-}11)$$

Therefore, the critical energy release rate G_c can then be determined as

$$G_c = \frac{\partial U_{crack}}{\partial A} = \frac{U_{crack}}{A_m}, \qquad (6\text{-}12)$$

Where A_m is the maximum crack area. For Berkovich indenter, the area can be calculated as

$$A_{\max} = 24.5 h_{\max}^2 . \qquad (6\text{-}13)$$

Finally, the fracture stress intensity factor K_c can be computed as:

$$K_c = \sqrt{G_c E_r} . \qquad (6\text{-}14)$$

6.3. Geological Setting and Experiments

6.3.1. Geological setting.

All the samples that are tested are retrieved from the wells drilled through the Bakken Formation in the State of North Dakota, USA. The Bakken Formation is located in the Williston Basin in Montana, North Dakota, and southern Saskatchewan (shown in Fig. 6.4), has become one of the largest shale plays in the world. In this paper, we analyzed samples from the Well CHARLIE SORENSON 17-8 3TFH. The target Bakken Formation of this well consists of three members: Upper, Middle and Lower Bakken. In this well, the upper Bakken is composed of distinctive black, blocky, carbonaceous shale with an instant milky cut. Then as ROP decreased with the increasing drilling depth, the samples changed from the black Upper Bakken Shale to silty Dolomite, indicating the appearance of Middle Bakken Formation. For this well, the Middle Bakken Formation has light gray, off white dolomitic siltstone, finely crystalline, with fair intercrystalline porosity. And for the lower Bakken Formation, samples were collected as the ROP increased again. Samples of the Lower Bakken were typical shale, brownish black in color, fissile, gritty, with bright fluorescence and streaming bright yellow cut. Overall, Upper and Lower Bakken is composed of shale with an abundance of clay minerals whereas the Middle Member varies in lithology and consists of interbedded siltstones and sandstones with lesser amounts of clay minerals (Pitman et al., 2001).

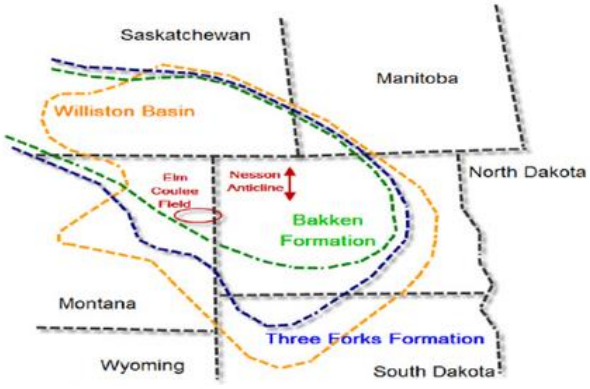

Fig. 6.4. Schematic of the area and the well we studied in this paper

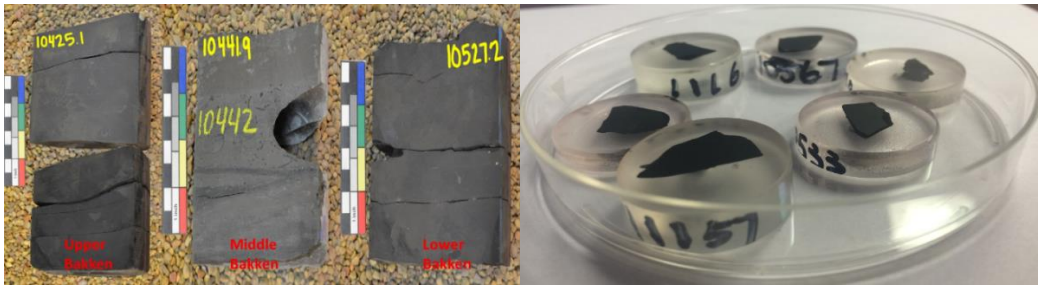

(a) Raw core samples (b) Prepared samples for tests

Fig. 6.5. Shale samples used in this study.

6.3.2. Experiments.

To get the most accurate results sample, preparation plays a crucial role. The surface of the smoothness of the sample specimens is very crucial for the accuracy of the results. Based on the combination of log and core photo image analysis, we collected the rock fragments from the original cores extracted from the Bakken Formation available at the North Dakota Core Library. The samples were broken into small pieces and then put in the resin liquid until the resin becomes solid under vacuum conditions. Sand papers of different grit sizes from 600 to 1200 was used to polish the sample surface followed by the different grain size of diamond polishers of 5, 3 and 1 microns. Fig. 6.5a shows the raw samples and Fig. 6.5b represents the prepared samples ready for the tests.

MTS Nanoindenter XP with Berkovich-type indenter (see Fig. 6.6) was used to test the samples. Indentation experiments were conducted at room temperature and ambient pressure. The instrument operates in a displacement-controlled mode with a loading rate of 20 nm/s. Scores of data were collected as the indenter approaches and retracts from the test point. Then data analysis was carried to calculate the mechanical properties of the sample.

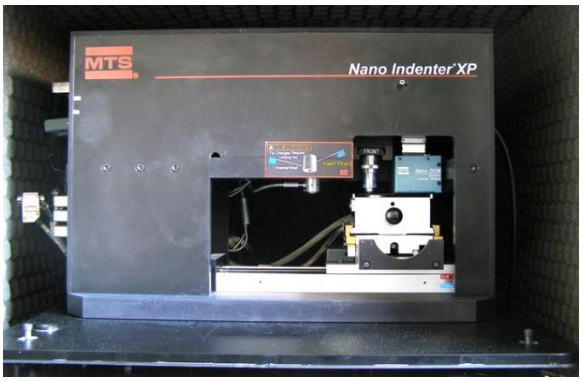

Fig. 6.6. MTS Nano-indenter (Agilent Company) used in this study.

6.4. Results and Discussions

6.4.1. Nano-indentation curves analysis.

All the curves in Fig. 6.7 show the elastic-plastic deformation during the loading process. Fig. 6.7 a illustrates the typical indentation curve without any abnormal phenomenon. From Fig. 6.7b, it is evident that the loading curve shows a normal pattern, however, the unloading curve follows an elbow pattern. The pressure beneath the indenter is very high and always increases as the indentation depth increases. Once the hydrostatic pressure is larger than the critical point, phase transformation occurs (Tabor, 1978). The gradual change of the unloading curve is the result of the material expansion during the slow transformation to the amorphous phase, which contributes to the indenter uplift (Domnich et al., 2000). Fig. 6.7c shows the "pop in" phenomena in the loading curve. This is interpreted due to the cracks forming during the nanoindentation process. When the indenter contacts the material, the work by the indenter will change the elastic energy of the material once the elastic energy increases to a critical value at some point in the contact field, plastic deformation occurs with the increasing load. For the elastic–plastic materials such as rocks, their elastic energy is almost invariant within the localized plastic deformation zones. However, rocks which are just exterior to this zone and in a state of incipient plastic deformation have less elastic energy and the elastic energy decreases significantly as the distance from the contact zone increases. The large energy difference in different zones can lead to the formation of the cracks

(Cook and Pharr, 1990; Lawn et al., 1980; Oyen and Cook, 2009). Fig. 6.7d shows combinations of "pop in" and "elbow" phenomena.

The parameters of curve fitting to the loading and unloading stages of Fig. 6.7a, b, c and d are calculated respectively and reported in Table 6.1. The results explain that the loading and unloading curves fit the power law functions listed below very well:

$$P = Kh^n \,(loading),$$
$$P = \alpha(h - h_f)^m \,(unloading) \qquad (6\text{-}15)$$

Where P and h are the loading force and displacement, respectively. h_f is the residual displacement. K, n, α and m are constants which can be calculated based on the experiments.

This is a similar behavior observed in other materials(Lawn et al., 1980), proving that the theory of nanoindentation may be used for the calculation of rock mechanical properties.

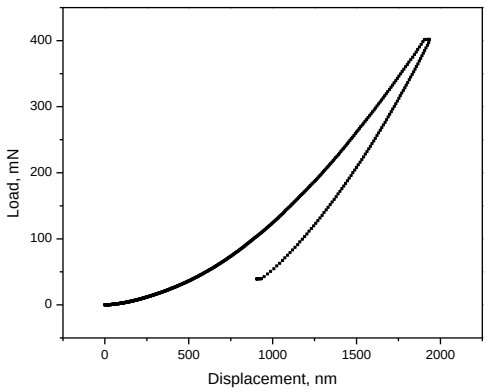

(a) Normal

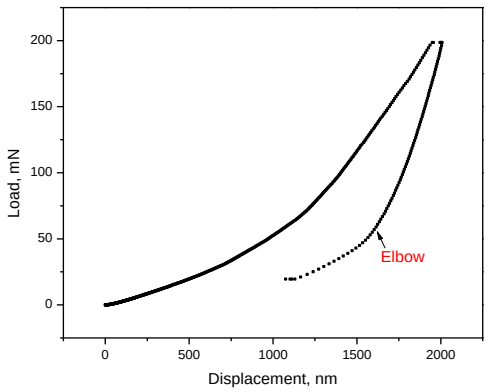

(b)Elbow

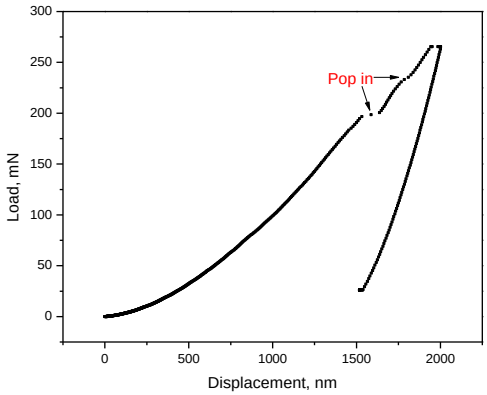

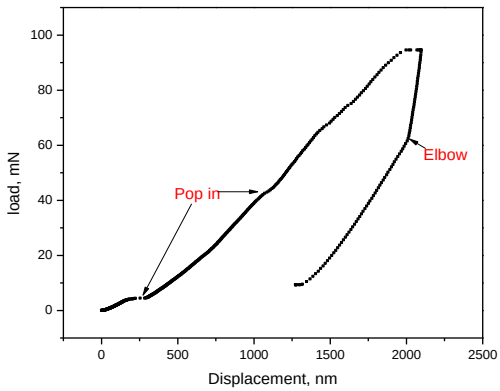

(c) Pop in (d) Pop in and Elbow

Fig. 6.7. Typical nanoindentation curves identified during testing the Bakken Shale samples.

Table 6.1. Curve fitting analysis of the loading and unloading processes, respectively

		K	r_1	R^2
Loading process	a	0.00048	1.80591	0.99992
	b	0.00013	1.87968	0.99586
	c	0.00265	1.52325	0.99848
	d	0.02687	1.15039	0.96086
		α	m	R^2
Unloading process	a	0.07906	1.22777	0.99450
	b	0.00490	1.50995	0.99044
	c	0.14466	1.21886	0.99238
	d	0.00597	1.62741	0.98771

6.4.2. Elastic modulus and hardness.

Young's modulus and hardness of the samples were derived, and their values were plotted versus the penetration depth as shown in Fig. 6.8.

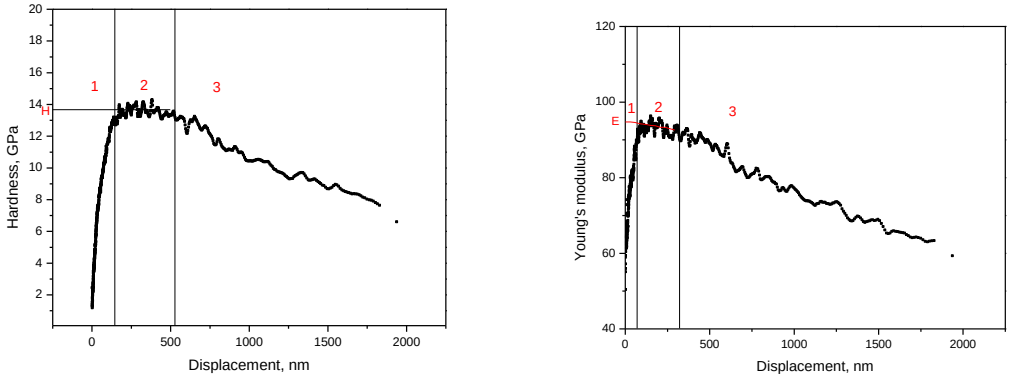

(a) Hardness value (b) Young's modulus

Fig. 6.8. Changes of elastic modulus and Hardness versus penetration depth. Both plots show three distinguished stages: 1. Initial rising; 2. Plateau; 3. falling off.

Fig. 6.8 represents the results of a sample for calculating Young's modulus. From this figure, it is concluded that both plots adhere three distinguished stages. During the initial stage, we can assume that the contact is elastic, which means that the values of this stage are the mean values and less than the real mechanical value of the materials. At larger penetration depth, the influence of the substrate on the test values will become more pronounced as is visible from the third stage in the figure, so the hardness value extracted from the plateau stage will be considered as the real hardness value of the sample. For the Young's modulus we use the extrapolation technique (see Fig. 6.8b). We extended the plot from the second stage to the sample surface (i.e. when displacement equals to 0), and where the vertical axis intercept the graph, Young's modulus of the samples is read (Fischer-Cripps, 2006). Following this procedure, for this test point in this sample, its hardness value is obtained to be 13.8 GPa and Young's modulus equal to 95 GPa .

Fig. 6.9 shows the elastic modulus and hardness values of the four samples we tested. Sample 30 is from Upper Bakken Formation while Sample 31, 32 and Sample 33 are from Middle Bakken Formation. The data shows that sample 33 has the highest elastic modulus while sample 32 has

the lowest values. More research about the properties of the four samples can be seen in the following section.

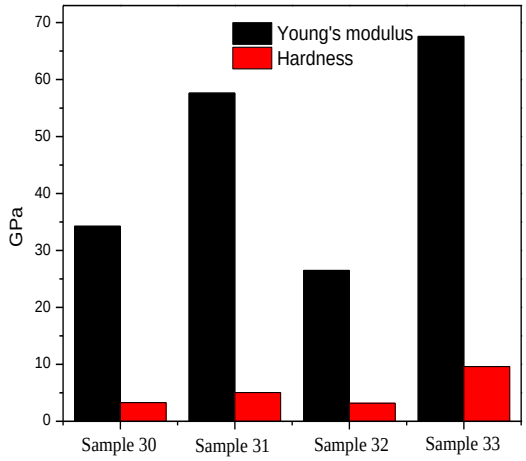

Fig. 6.9. Elastic properties of different samples.

6.4.3. Young's modulus, hardness, mineral compositions and microstructures.

In order to study the relationship between the elastic properties, mineral compositions and microstructures, the four samples with quite different elastic properties derived from nanoindentation test were analyzed by XRD, FESEM.

6.4.3.1. Mineral compositions.

X-Ray Diffraction (XRD) was performed on the flat surface of the samples using Bruker D8 Discover 2D apparatus. For the rock such as shale, having preferred orientation, the percent crystallinity measured with the conventional diffractometer is not consistent. While the sample orientation has no effect on the full circle integrated diffraction profile from a 2D frame, 2D XRD system can measure percent crystallinity more accurately with consistent results(He, 2003).

Fig. 6.10 presents the images of 3 frames of the 2D XRD scanning for Sample 30. Combining the three frames and the relevant signals for 25-115-degree scan angle produces Fig. 6.11. Quantitative

measurement of the mineral composition can be obtained by analyzing the signal peaks. The results showed this particular sample contained 51.3% clay minerals (mainly illite) and 31.9% quartz. Following a similar procedure, we derived the mineralogical compositions for the rest of the samples (see Table 6.2).

Table 6.2. Composition analysis by XRD

	Sample 30	Sample 31	Sample 32	Sample 33
Quartz, %	31.9	35.8	37.9	49.4
Calcite, %	0.0	2.5	2.6	1.7
Dolomite, %	12.0	0.1	0.3	2.0
Ankerite, %	0.0	4.0	6.3	3.4
Pyrite, %	0.0	3.6	5.0	4.8
K-feldspar, %	4.7	11.2	8.7	9.8
Albite, %	0.0	7.6	5.1	3.7
clay minerals, %	51.3	35.2	34.0	25.2

Results show that the two major minerals components of the samples are quartz and clay minerals (mainly composed of illite). Due to the small percentage of other minerals, so in this paper, we neglect their influence on the mechanical properties. Results show that Sample 30 has the most clay minerals (51.3%) and the least amount of quartz (31.3%) whereas Sample 33 has the least clay minerals (25.2%) with the highest amount of quartz content (49.4%). Sample 31 and Sample 32 has similar mineral compositions (Sample 31 has 35.8% quartz and 35.2% clay minerals while sample 32 has 37.3% quartz and 34% clay minerals). These results will be cross-validated by the SEM analysis of the samples presented in the following subsection.

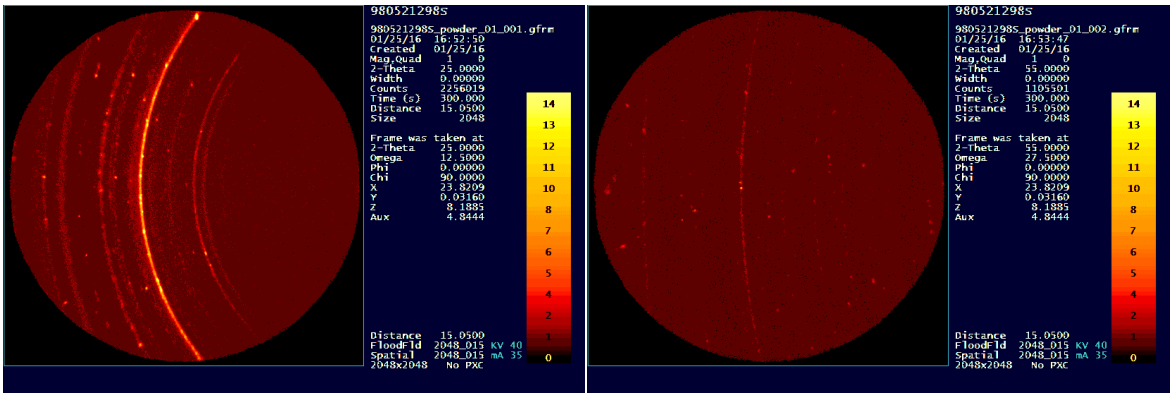

(a) (b)

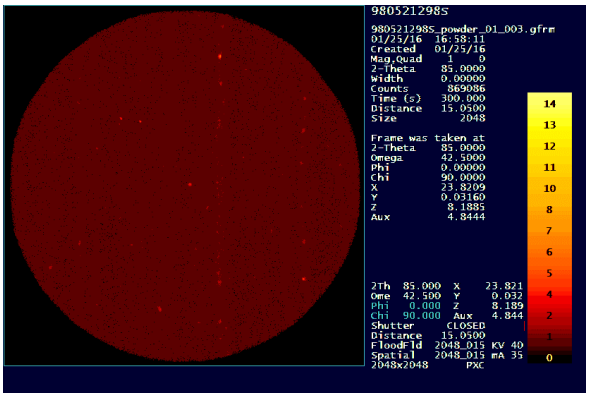

(c)

Fig. 6.10. Image of 3 Frames of 2D XRD scanning for angles of (a) of 25-55°, (b) 55-85° and (c) 85-115° representing one sample.

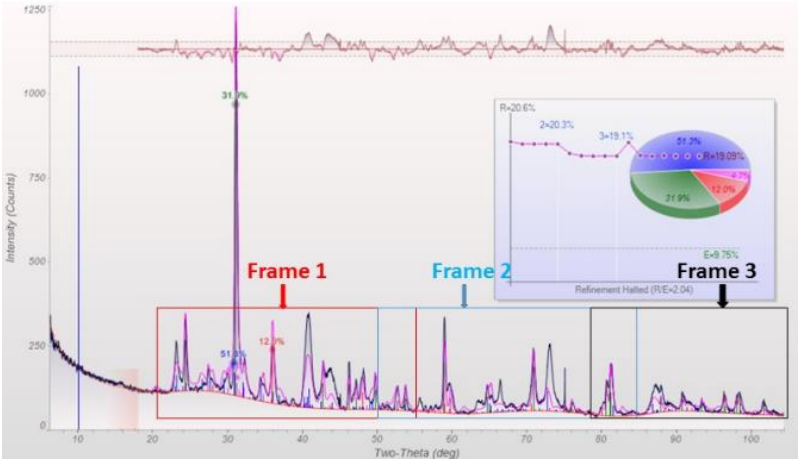

Fig. 6.11. XRD signal of one sample obtained by combining the three frames from Fig. 10.

6.4.3.2. Microstructures.

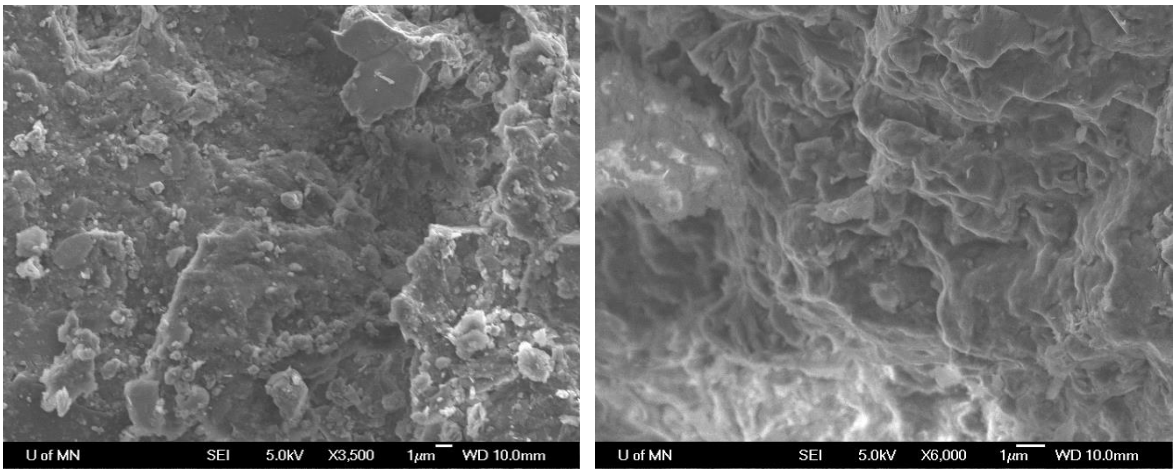

(a) Sample 30 (b) Sample 31

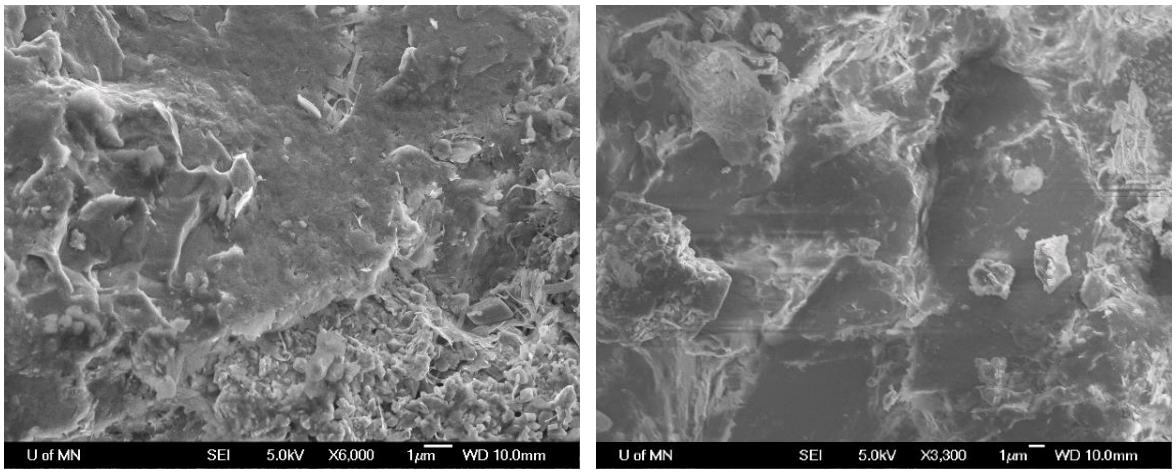

(c) Sample 32 (d) Sample 33

Fig. 6.12. SEM images of few shale samples from different members of the Bakken Formation.

Field Emission Gun Scanning Electron Microscope JEOL 6500 apparatus (JEOL Company) was used to study the microstructures of the four samples. The results are shown in Fig. 6.12. From this figure, it is observed that samples 30, 31 and 33 have, in order, the highest to the least clay minerals which are in agreement with the XRD analysis results presented earlier. The results also represent that Sample 32 has more pores and fractures than the rest. Comparing the values of Young's modulus and hardness for four different samples which were presented in Fig. 6.9 with the SEM and XRD data, it's concluded that Sample 33 that has the highest Young's modulus and

hardness values, and Sample 32 with the lowest values exhibit more pore structures and fewer clay minerals respectively.

6.4.4. Fracture toughness test

Based on the energy analysis method, 20 nanoindentation tests were performed on four different samples from three members of the Bakken Formation.

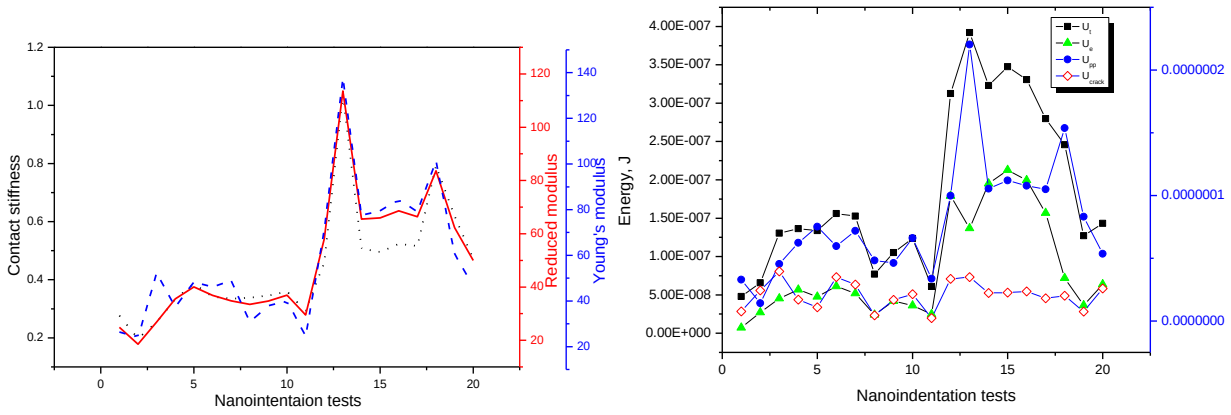

(a) (b)

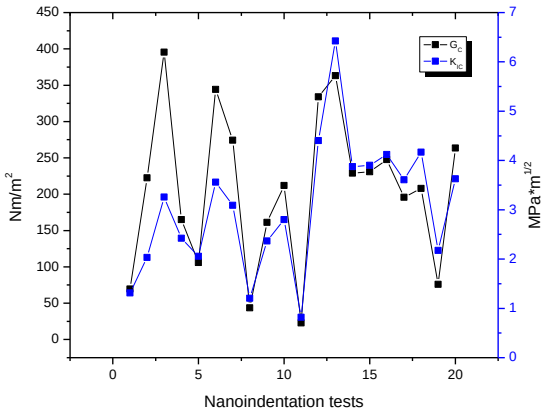

(c)

Fig. 6.13. Energy analysis results from nanoindentation. (a) contact stiffness, reduced modulus and Young's modulus; (b) total energy, plastic energy, elastic energy and crack energy; (c) energy release rate and fracture intensity factor.

Fig. 6.13a depicts the results of the contact stiffness, reduced modulus and Young's modulus. From this figure, it is seen that the higher contact stiffness, the higher the Young's modulus is.

This is because the contact stiffness is the value of the slope of the nanoindentation curve at h_{max}. Elastic energy increases as the *S* increases. So, Young's modulus which can reflect the elastic properties of rocks also increases as shown in Fig. 6.14. Fig. 6.13b presents the energy distribution corresponding to each nanoindentation test. Fig. 6.13c depicts the results of the energy release rate and fracture intensity factor of the nanoindentation tests, showing the fracture toughness increases and the energy release rate increases.

The average value of K_{IC} from Fig. 6.13c for the samples from the Bakken in nanoscale is around $3.06\,MPa\sqrt{m}$. Plotting the Young's modulus versus the toughness values for the samples, a linear relationship is developed at the nanoscale as shown in Fig. 6.15. The following equation allows us to estimate the fracture toughness from Young's modulus at nanoscale:

$$K_{IC} = 0.7288 + 0.04048E \qquad (6\text{-}16)$$

From literature and database, the values of fracture toughness of Bakken formation rocks are rarely to be found while the information of elastic modulus is abundant and easily to be derived. Eq.6-16 gives us a potential estimation of the fracture toughness of Bakken Formation without doing many experiments, saving a lot of time and making more profits.

In this paper, all the mechanical properties such as Young's modulus, Hardness and fracture toughness were calculated under the ambient temperature and pressure which can be a little different from the value of the rocks under the real reservoir conditions. Under the reservoir conditions, the pore structures will change, and rocks become more plastic due to the high temperature and high pressure. Also, in this paper, we only studied the mechanical properties of the rock sample in nanoscale, which is not suitable to estimate the rocks in large scale directly due to the heterogeneous properties of the rock. In the near future, we will use project nanoindentation and phase characterization method to upscale the mechanical properties of the rocks from

nanoscale to a large scale and then we will compare the results from true triaxial test and logs to confirm the validity of this method, however, at this stage, these results provide a good insight in order to understand some nanoscale behavior of these samples, showing the great potential of the application of this method to study rock mechanical properties.

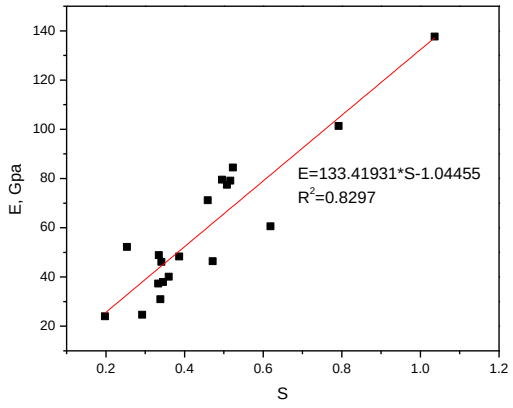

Fig. 6.14. Relationships between contact stiffness and Young's modulus.

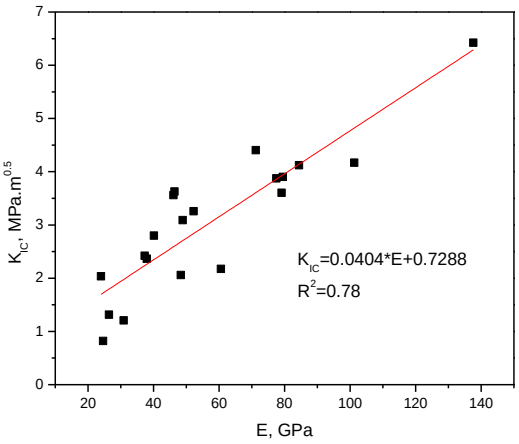

Fig. 6.15. Relationships between Young's modulus and fracture toughness.

6.5. Conclusions

In this study, we applied the nanoindentation method to study the mechanical properties of shale samples from Bakken Formation. The analysis of the nanoindentation indicated some abnormal phenomenon such as pop in and elbow. The results of this study showed that the theory of

nanoindentation can be applied for studying the mechanical properties of rocks at nano-scale. Young's modulus and hardness values were calculated and compared with their mineral compositions and microstructures. The results suggested that the more clay minerals and pore microstructures present in the samples, the less the elastic Young's modulus and hardness values will be. Based on the energy analysis, fracture toughness of different samples at nanoscale was calculated and compared and the relationship with Young's modulus is developed. The results stated that toughness of the samples tested in this study increases linearly with the Young's modulus. The results of this study provide a great potential application of nanoindentation method in analyzing the rock mechanical properties and predicting fracture properties required in a successful hydraulic fracturing operation in unconventional shale plays (shale gas and shale oil formation). Future work is focused to upscale the mechanical properties in nanoscale to macro and reservoir scale.

Nomenclature

$h_{\max}$	Maximum displacement, nm
$P_{\max}$	Maximum indentation load, mN
S	Contact stiffness
ν_E	Elastic energy ratio
h_s	Vertical surface deflection, nm
h_c	Contact depth, nm
h_f	Residual displacement, nm
E_r	Reduced modulus, GPa
U_t	Total energy, J

U_{ir} Irreversible energy, J

U_{pp} Energy cost by plastic deformation, J

U_{e} Energy cost by elastic deformation, J

U_{crack} Energy cost by cracks, J

G_{c} Energy release rate, Nm/m^2

K_{IC} Fracture stress intensity factor, $MPa\sqrt{m}$

6.6. References

Cheng, Y.-T., Li, Z. and Cheng, C.-M., 2002. Scaling relationships for indentation measurements. Philos. Mag. A. 82(10), 1821-1829.

Cook, R.F. and Pharr, G.M., 1990. Direct Observation and Analysis of Indentation Cracking in Glasses and Ceramics. J. Am. Ceram.Soc. 73(4), 787-817.

Domnich, V., Gogotsi, Y. and Dub, S., 2000. Effect of phase transformations on the shape of the unloading curve in the nanoindentation of silicon. Appl. Phys. Lett. 76(16), 2214-2216.

Fischer-Cripps, A.C., 2006. Critical review of analysis and interpretation of nanoindentation test data. Surf. Coat Tech. 200(14–15), 4153-4165.

Ghamgosar, M., Williams, D.J. and Erarslan, N., 2015. Effect of Anisotropy on Fracture Toughness and Fracturing of Rocks. American Rock Mechanics Association.

He, B.B., 2003. Introduction to two-dimensional X-ray diffraction. Powder Diffr. 18(02), 71-85.

Hu, C. and Li, Z., 2015. A review on the mechanical properties of cement-based materials measured by nanoindentation. Constr. Build Mater. 90, 80-90.

Kaushal K. Jha, N.S.D.L. and Arvind, A., 2012. Energy-Based Analysis of Nanoindentation Curves for Cementitious Materials. Mater. J.109(1).

King, G.E., 2012. Hydraulic Fracturing 101: What Every Representative, Environmentalist, Regulator, Reporter, Investor, University Researcher, Neighbor and Engineer Should Know About Estimating Frac Risk and Improving Frac Performance in Unconventional Gas and Oil Wells. Society of Petroleum Engineers.

Kruzic, J.J., Kim, D.K., Koester, K.J. and Ritchie, R.O., 2009. Indentation techniques for evaluating the fracture toughness of biomaterials and hard tissues. J.Mech.Behav.Biomed. 2(4), 384-395.

Kumar, V., Curtis, M.E., Gupta, N., Sondergeld, C.H. and Rai, C.S., 2012. Estimation of Elastic Properties of Organic Matter in Woodford Shale Through Nanoindentation Measurements. Society of Petroleum Engineers.

Lawn, B.R., Evans, A.G. and Marshall, D.B., 1980. Elastic/Plastic Indentation Damage in Ceramics: The Median/Radial Crack System. J. Am. Ceram.Soc. 63(9-10), 574-581.

Mason, J., Carloni, J., Zehnder, A., Baker, S.P. and Jordan, T., 2014. Dependence of Micro-Mechanical Properties on Lithofacies: Indentation Experiments on Marcellus Shale. Society of Petroleum Engineers.

Montgomery, C.T. and Smith, M.B., 2010. Hydraulic Fracturing: History of an Enduring Technology.

Naderi, S. et al., 2016. Modeling of porosity in hydroxyapatite for finite element simulation of nanoindentation test. Ceram. Int. 42(6), 7543-7550.

Oliver, W.C. and Pharr, G.M., 1992. An improved technique for determining hardness and elastic modulus using load and displacement sensing indentation experiments. J. Mater.Res. 7(06), 1564-1583.

Oyen, M.L. and Cook, R.F., 2009. A practical guide for analysis of nanoindentation data. J.Mech.Behav.Biomed.. 2(4), 396-407.

Park, N., Holder, J. and Olson, J.E., 2004. Discrete Element Modeling Of Fracture Toughness Tests In Weakly Cemented Sandstone. American Rock Mechanics Association.

Pitman, J.K., Price, L.C. and LeFever, J.A., 2001. Diagenesis and fracture development in the Bakken Formation, Williston Basin; implications for reservoir quality in the middle member. 1653.

Scholz, T., Schneider, G.A., Muñoz-Saldaña, J. and Swain, M.V., 2004. Fracture toughness from submicron derived indentation cracks.Appl. Phys. Lett. 84(16), 3055-3057.

Sebastiani, M., Johanns, K.E., Herbert, E.G. and Pharr, G.M., 2015. Measurement of fracture toughness by nanoindentation methods: Recent advances and future challenges.Curr. Opin. Solid St. M.. 19(6), 324-333.

Senseny, P.E. and Pfeifle, T.W., 1984. Fracture Toughness of Sandstones And Shales. American Rock Mechanics Association.

Shukla, P., Kumar, V., Curtis, M., Sondergeld, C.H. and Rai, C.S., 2013. Nanoindentation Studies on Shales. American Rock Mechanics Association.

Tabor, D., 1978. Phase transitions and indentation hardness of Ge and diamond. Nature. 273(5661), 406-406.

Tanguy, M., Bourmaud, A. and Baley, C., 2016. Plant cell walls to reinforce composite materials: Relationship between nanoindentation and tensile modulus. Mater. Lett. 167, 161-164.

Thiercelin, M., 1987. Fracture Toughness Under Confining Pressure Using the Modified Ting Test. American Rock Mechanics Association.

Thiercelin, M., Jeffrey, R.G. and Naceur, K.B., 1989. Influence of Fracture Toughness on the Geometry of Hydraulic Fractures. Society of Petroleum Engineers.

Too, J.L. et al., 2015. An Experimental Method to Determine the Fracture Toughness of Brittle and Heterogeneous Material by Hydraulic Fracturing. Society of Petroleum Engineers.

Wang, X. et al., 2015. High damage tolerance of electrochemically lithiated silicon. Nat Commun, 6.

Xiao, G., Yang, X., Yuan, G., Li, Z. and Shu, X., 2015. Mechanical properties of intermetallic compounds at the Sn–3.0Ag–0.5Cu/Cu joint interface using nanoindentation. Materials & Design. 88, 520-527.

Zoback, M.D., 1978. A Simple Hydraulic Fracturing Technique For Determining Fracture Toughness. American Rock Mechanics Association.

CHAPTER 7

STATISTICAL GRID NANOINDENTATION ANALYSIS TO ESTIMATE MACRO-MECHANICAL PROPERTIES OF THE BAKKEN SHALE

Abstract

Retrieving standard sized core plugs to perform conventional geomechanical testing on organic rich shale samples can be very challenging. This is due to unavailability of inch-size core plugs or difficulties in the coring process. In order to overcome these issues, statistical grid nanoindentation method was applied to analyze mechanical properties of the Bakken. Then the Mori-Tanaka scheme was carried out to homogenize the elastic properties of the samples and upscale the nanoindentation data to the macroscale. To verify these procedures, the results were compared with unconfined compression test data. The results showed that the surveyed surface which was 300 um x300 um is larger than the representative elementary area (REA) and can be used safely as the nanoindentation grid area. Three different mechanical phases and the corresponding percentages can be derived from the grid nanoindentation through deconvolution of the data. It was found that the mechanical phase which has the smallest mean Young's modulus represents soft materials (mainly clay and organic matter) while the mechanical phases with the largest mean Young's modulus denote hard minerals. The mechanical properties (Young's modulus and hardness) of the samples in X-1 direction (perpendicular to the bedding line) was measured smaller than X-3 direction (parallel to the bedding line) which reflected mechanical anisotropy. The discrepancy between the macromechanical modulus from the homogenization and unconfined compression test was less than 15% which was acceptable. Finally, we showed that

homogenization provides more accurate upscaling results compared to the common averaging method.

7.1. Introduction

The Bakken Formation is one of the largest unconventional shale oil plays in the world. The average recovery factor of the Bakken Formation is approximately 7% which is much lower than the national average level of 30%. This is due to its low porosity and extremely low permeability (Clark, 2009) thus horizontal drilling, combined with hydraulic fracturing, are the two commonly used technologies that are employed to increase the production from the Bakken Formation. Having a good knowledge of the formation's mechanical properties is very important in the placement and design of horizontal drilling and hydraulic fracturing. Reliable estimation of the mechanical properties can improve the success rate of the drilling and production and, eventually, enhance the overall recovery factor. In a routine laboratory analysis, standard static tri-axial lab experiments or dynamic field-scale analysis using sonic logs are normally performed to obtain the necessary rock properties (Shukla et al., 2013). However, obtaining standard sized core plugs from downhole cores would be challenging and, thus, not considered to be ideal for conducting conventional geomechanics testing (Liu et al., 2016). On the other hand, nanoindentation tests, which only need a small volume of rock sample, have proven to be a great success in petroleum engineering applications to investigate the mechanical properties of shale samples (Shukla et al., 2013; Kumar et al., 2012; Mason et al., 2014).

An indentation test is a surface testing method that provides data on the bulk properties of the sample using the tools of continuum indentation analysis. In 1901, Brinell was the first to use indentation methods by applying a small ball of hardened steel or tungsten carbide against the surface of samples to measure their material properties (Brinell, 1901). In the 1950s, Tabor suggested the use of empirical relations to transform indentation data into meaningful mechanical

properties (Tabor, 2000). Following this, researchers from the former Soviet Union implemented the idea of depth sensing techniques to the nanoscale level (Bobko, 2008). In the late 1980s and early 1990s, Doerner and Nix (1986) and Oliver and Pharr (1992) expanded the theory to quantify the mechanical properties of samples using nanoindentation methods, which have since received world-wide attention.

For homogeneous samples, a single indent or a few indents can provide an estimate of the sample's mechanical properties whereas for a heterogeneous material (i.e., shale) a single indent or a few indents cannot provide sufficient information about the properties of the material (Randall et al., 2009). Shale is composed of different minerals (hard and soft). The limited number of idents on the hard or soft minerals can overestimate or underestimate the true mechanical properties of the sample. In order to solve this problem, a grid indentation method was developed by Ulm and colleagues and was applied to analyze mechanical properties of composites (Constantinides et al., 2003, 2006a). The principle of grid nanoindentation is to apply a large number of indents on a material surface with specific requirements. First, the number of indents that are carried out on the surface should be larger than the representative elementary area (REA). Second, if each indent is characterized by the length scale D and depth h, then indentation depth h should be much smaller than D. The distance between the grids should be larger than the characteristic size of the indentation impression. This is mandatory to avoid interference between the neighboring indents and each mechanical phase. Under these conditions, the locus of the indentation has no statistical bias concerning the spatial distribution of these phases. Additionally, this will certify that the probability of encountering different phases can be equal to the surface fraction which is occupied by several phases on the indentation surface (Constantinides et al., 2003, 2006a).

Due to its strong ability, researchers have used grid indentation to analyze the mechanical properties of cementitious materials (Constantinides, 2006b; Němeček et al., 2011), bone (Ulm, et al., 2007), batteries (de Vasconcelos et al., 2016), and steel (Nohava et al., 2010). Grid indentation has become an important method to characterize material properties. In the petroleum engineering industry, Vialle and Lebedev (2015) applied grid nanoindentation to analyze the heterogeneities of carbonate rocks. In shale studies, most researchers are focused on the analysis of indentation data at the nanoscale-level, such as the creep characterization (Mighani et al., 2015), understanding the mechanical properties of organic matter (Kumar et al., 2012b), or analyzing fluid- shale interactions (Yang et al., 2016).

Nanoindentation can reflect the mechanical properties of the samples in nanoscale. Some researchers have used this data to estimate mechanical properties in macroscale. Averaging the nanoindentation data from large number of indents is the conventional method that researchers have utilized to predict the macroscale properties (Shukla, et al., 2013; Kumar et al., 2012; Alstadt et al., 2015; Yang et al., 2016; Zhang et al., 2017). However, sometimes, the discrepancy between the averaged data from nanoindentation and the results from macroscale testing such as unconfined compression test are obvious. This shows that averaging is not the most suitable method for upscaling and better techniques should be proposed to characterize the macroscale properties of the materials based on the nanoindentation data.

The first part of this study is dedicated to the determination of the nanoindentation area based on the EDX mineral mapping of samples. The box counting method was applied to analyze the impact of the box length on the mineral fractions and to identify the REA (representative elementary area) of the sample. This was followed by the statistical analysis of the nanoindentation data. Several different mechanical phases were distinguished based on the nanoindentation results. This was

followed by homogenization of the elastic properties to the macroscale-level. Finally, the results from the homogenization scheme were compared to the results from the macro-scale laboratory mechanical tests on core plugs in order to verify the accuracy of the method.

7.2. Materials and methods

7.2.1. Materials.

Four samples from the Bakken Formation were collected for the analysis. Quartz, feldspar, dolomite and clay minerals (mainly illite–smectite) were identified as the main mineral components in the samples (Liu and Ostadhassan, 2017a). Small pieces of rock (chips), parallel and perpendicular to the bedding plane, were taken from the cores and placed into resin for 24 hours. The roughness of the surface can add length scale to the nanoindentation upscaling problem, which can break the self- similarity of the problem (Miller et al., 2008). In order to reduce the surface roughness, sand paper of different grit sizes from 600 to 1200 was used to polish the sample surface followed by a series of diamond polishers of 5, 3 and 1 microns to ensure that the desired surface roughness had been reached.

7.2.2. Grid nanoindentation.

Nanoindentation can reflect the bulk properties of a sample using the continuum indentation analysis. Fig. 7.1 shows the schematic of a typical nanoindentation curve. The nanoindentation curve starts with an initial loading stage followed by the unloading stage. The loading stage can be regarded as the combination of elastic and plastic deformation while the unloading stage can be viewed as the recovery of the pure elastic deformation that can be used to calculate the hardness and Young's modulus of the indent (Oliver and Pharr, 1992). The detailed calculation about the Young's modulus and hardness can be seen in section 6.2.2.

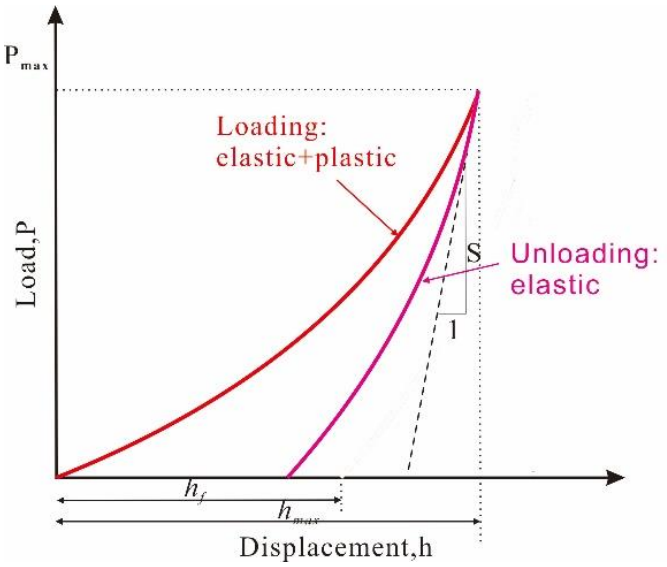

Fig. 7.1. Schematic of the typical nanoindentation curve (Modified from Hu and Li, 2015).

Shales are highly heterogeneous rocks at the nano- and micro-scale levels (Ulm et al., 2007). In order to analyze the mechanical properties of shales, grid indentation analysis was applied in this study (Constantinides et al., 2006a). A large number of indents was performed on the sample surface and each indent was considered as an independent event.

7.2.3. Statistical deconvolution.

Statistical deconvolution was first applied in deconvoluting two signals with little prior knowledge about either of them (Eisenstein, 1976). In this study, this method was applied to analyze the results from grid nanoindentation in order to separate the mechanical phases. Let N be the number of the total indents performed on the shale sample. Then, Young's modulus and hardness $\{M_i\}$ and $\{H_i\}$ (i=1, N) can be derived by assuming that shale is composed of J=1, n material phases with sufficient contrast in mechanical properties. The following equations are obtained:

$$f_J = \frac{N_J}{N}; \qquad \sum_{J=1}^{n} N_J = N \qquad (7\text{-}1)$$

Where N_J is the number of indents on the mechanical material phase and f_J is the volume fraction of the material phase.

The phase distribution function is very important in the deconvolution process. In order to keep the deconvolution process as automated as possible, a single form distribution with zero skewness is most appropriate (Constantinides et al., 2006a). The appropriate probability density function of the single phase, which is assumed to fit a normal distribution, is:

$$P_J(x) = \frac{2}{\sqrt{2\pi(S_J^x)^2}} \exp\left(\frac{-(x-(U_J^x))^2}{2(S_J^x)^2}\right) \qquad x= (M, H) \qquad (7\text{-}2)$$

where U_J^x and S_J^x are the mean value and the standard deviation of $x= (M, H)$ of all N_J values of each phase.

To ensure that the phases have sufficient contrast in properties, the overlap of successive Gaussian curves representative of the two phases is constrained by the following criterion (Sorelli et al., 2008):

$$U_J^x + S_J^x < U_{J+1}^x + S_{J+1}^x \qquad x= (M, H) \qquad (7\text{-}3)$$

Based on the assumption that each material phase is normally distributed and does not mechanically interact with another phase, one could obtain the overall frequency distribution of the mechanical properties, X= (M, H), using the following equation:

$$P_x = \sum_{J=1}^{n} f_J P_J(x) \qquad (7\text{-}4)$$

Where P_J is the normal distribution of the material phase and f_J is the volume fraction of the material phase which subjects the constraint:

$$\sum_{J=1}^{n} f_J = 1 \qquad (7\text{-}5)$$

From Eq. (7), one can obtain n×5 unknowns { f_J, U_J^M , S_J^M , U_J^H , S_J^H }, J=1, n. These unknowns can be determined by minimizing the difference between the data from the weighted model-phase

probability distribution function (PDF) and the experimental PDF using the following equation (Constantinides et al., 2006a):

$$\min[\sum_{k=1}^{m} \frac{\sum_{x=M,H} \sum_{i=1}^{N} (\sum_{J}^{n} f_J P_J(x) - P_x^{\,i})^2}{m}] \qquad (7\text{-}6)$$

Here, $P_x^{\,i}$ is the observed value of the experimental frequency density of *x (M, H)* and *m* is the number of the intervals (bins).

In this study, Matlab was used to write the code program and perform the statistical deconvolution on the data set.

7.2.4. Analytical elastic homogenization.

Elastic homogenization is a technique used to upscale mechanical properties from the microscale level to a larger scale. The Mori-Tanaka method is one of the most popular methods for the homogenization of multiphase elastic composites because it approximates the interaction between the different phases assuming that each inclusion is embedded. The average strain in the inclusion is related to the average strain by a fourth order tensor (Mori and Tanaka, 1973). The homogenized bulk and shear modulus of an *n* phase material can be calculated by using the following equations:

$$K_{\text{hom}} = \frac{\sum_{J=1}^{n} f_J . K_J (1 + \alpha_0 . (K_J / K_0 - 1))^{-1}}{\sum_{J=1}^{n} f_J . (1 + \alpha_0 . (K_J / K_0 - 1))^{-1}} \qquad (7\text{-}7)$$

$$G_{\text{hom}} = \frac{\sum_{J=1}^{n} f_J . G_J (1 + \beta_0 . (G_J / G_0 - 1))^{-1}}{\sum_{J=1}^{n} f_J . (1 + \beta_0 . (G_J / G_0 - 1))^{-1}} \qquad (7\text{-}8)$$

$$\alpha_0 = \frac{3K_0}{3K_0 + 4G_0} \qquad (7\text{-}9)$$

$$\beta_0 = \frac{6K_0 + 12G_0}{15K_0 + 20G_0} \quad (7\text{-}10)$$

Here, K_0 and G_0 are the bulk modulus and shear modulus of the reference medium, respectively while K_J and G_J are the moduli of the inclusion phases. f_J is the volume fraction of the J_{th} phase. Finally, the elastic properties can be homogenized (Young's modulus and Poison's ratio) using these set of equations (Mori and Tanaka, 1973):

$$E_{\text{hom}} = \frac{9K_{\text{hom}}G_{\text{hom}}}{3K_{\text{hom}} + G_{\text{hom}}} \quad (7\text{-}11)$$

$$V_{\text{hom}} = \frac{3K_{\text{hom}} - 2G_{\text{hom}}}{6K_{\text{hom}} + 2G_{\text{hom}}} \quad (7\text{-}12)$$

7.3. Results and Discussion

7.3.1. Determination of grid Nanoindentation area.

For the grid nanoindentation test, the indentation area was determined initially. In order to upscale the mechanical properties of the shale samples, the area over which the indents were performed should be larger than the REA (representative elementary area). The REA is the smallest area that can yield a value that can represent the whole sample property which is going to be measured. The box-counting method was applied to investigate the REA for the mineral fraction in this study (Houben et al., 2016). Fig. 7.2 shows the schematic of the REA determination on the base of mineral mapping of Sample 34. First, one box size was chosen, and the mineral compositions under this box size were quantified by using the Nanomin software developed by the FEI Company. When the center of the box was accurately determined, the box size and quantified mineral compositions within larger box sizes was increased. The changes of the mineral compositions due to the variation of the box size were analyzed and the right REA was determined. Fig. 7.3a shows that as the box size increases, the fraction of the main minerals and organic matter varies until the box size of 250 um is reached, at which stage the mineral compositions become

constant. Using this approach, the REA of Sample 34 was found to be 250 um×250 um, which is comparable to the REA determined using the porosity indicator (Liu and Ostadhassan, 2017b). The influence of the box length on the sample density and hardness (Mohs scale) is shown in Fig. 7.3b. If the box length is larger than 250 um, the density and the hardness values of Sample 34 become constant, which shows that one can use the mechanical properties of an area larger than the REA to represent the mechanical properties of the whole sample at the macro-scale level. Using the same approach, the REA of other three samples were determined. Based on these REA values, it was decided to use 300 um×300 um as the nanoindentation area for the samples to ensure that the correct box size was used.

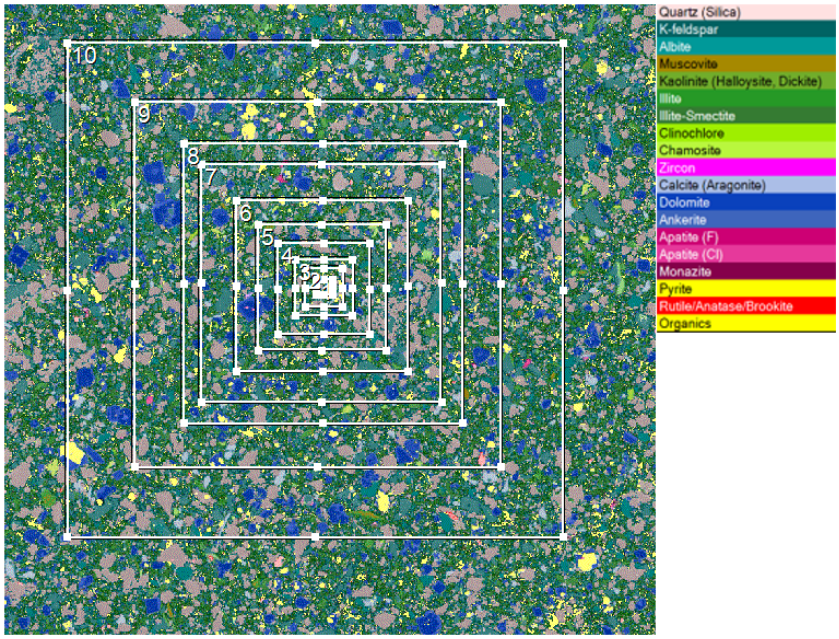

Fig. 7.2. Schematic of determining the REA of Sample 34 for mineral fractions.

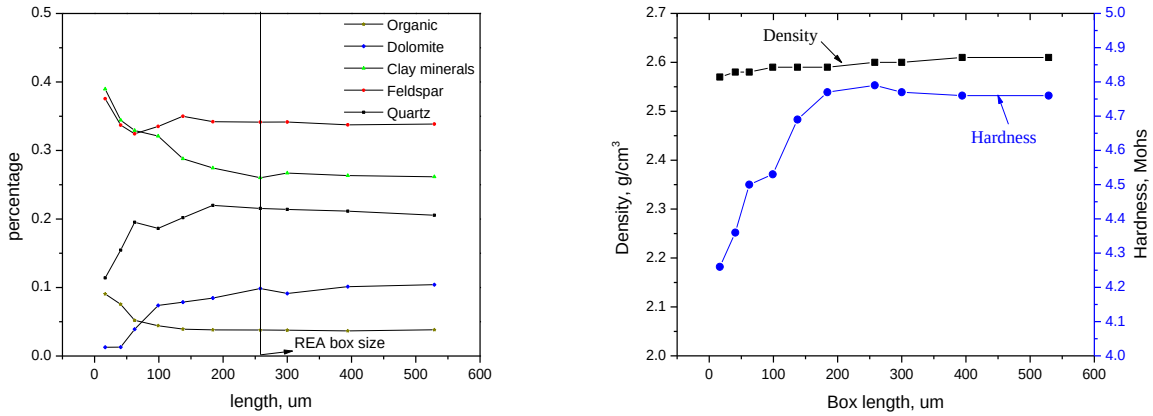

(a) Mineral fractions (b) Density and Hardness (Mohs)

Fig. 7.3. Influence of the box length on properties of Sample 34.

7.3.2. Grid Nanoindentation.

A Hysitron Triboindenter with a Berkovich indenter was used for the indentation analysis of the shale samples. Based on the combination of the image taken under the optical microscope and the scaled separability condition (Bobko, 2008), a matrix of 225 indents covering 300 um × 300 um of the sample surface (which is larger than the REA) was chosen. After considering the surface roughness and the impact of the neighboring idents, the distance between the neighboring indents was selected to be 20um.

The grid nanoindentation modeling was applied on the samples both perpendicular (X-1 direction) and parallel (X-3 direction) to the bedding planes. Fig. 7.4 and Fig. 7.5 show the mechanical properties maps of the nanoindentation areas of Sample 34 along the X-1 and X-3 directions, respectively. These images show that the Young's modulus and the hardness map correlate very well; for example, the points with the higher Young's modulus compare to the higher hardness values. The correlation between the two property maps was found to be linear with a positive slope (Fig. 7.6) (Liu et al., 2016, 2017a). In addition, from Fig. 7.4 and Fig. 7.5 it is seen that the shale

is composed of different mechanical phases. The points with the higher Young's modulus represent stiffer minerals such as feldspar and quartz whereas the points with lower Young's modulus values represent clay minerals and organic matter (Zhu et al., 2007). The histogram of Young's modulus and hardness shown in Fig. 7.7 displays more than one peak, which indicates the composite behavior of Sample 34.

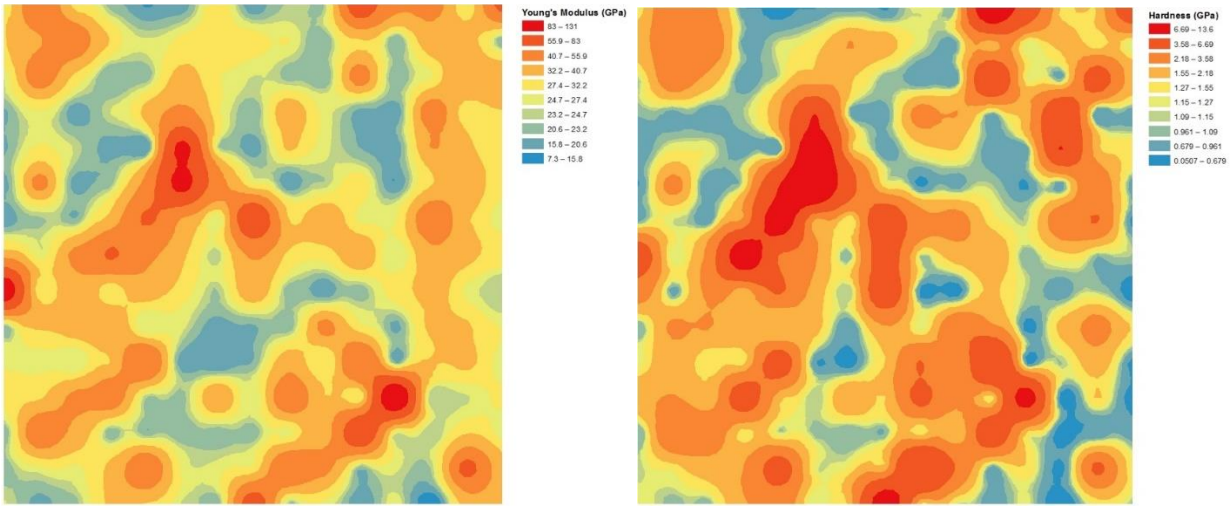

(a) Young's modulus (b) Hardness

Fig. 7.4. Mechanical mapping of Sample 1 along the X-1 direction.

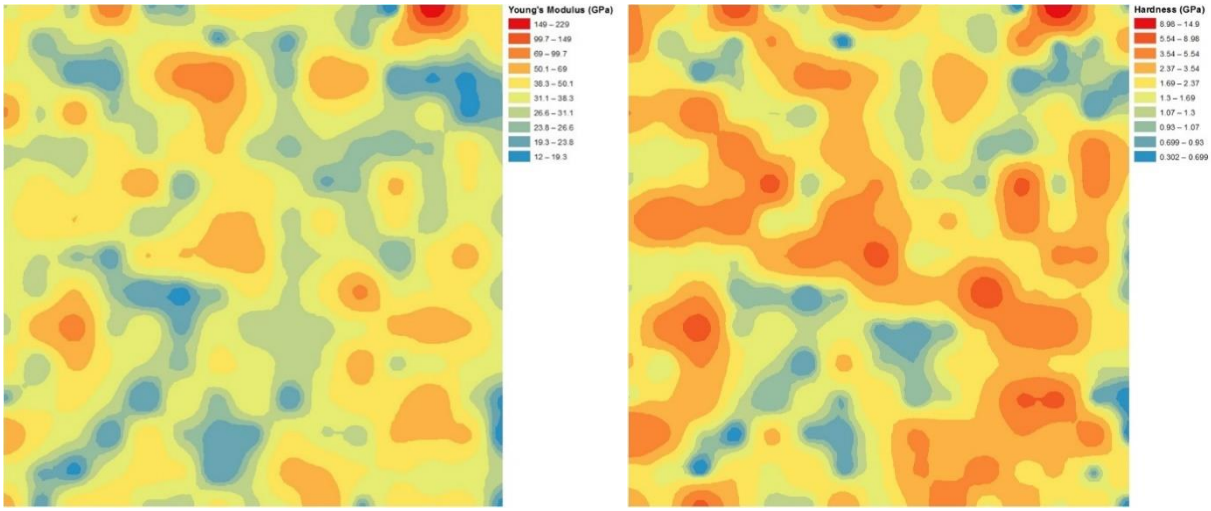

(a) Young's modulus (b) Hardness

Fig. 7.5. Mechanical mapping of Sample 34 along the X-3 direction.

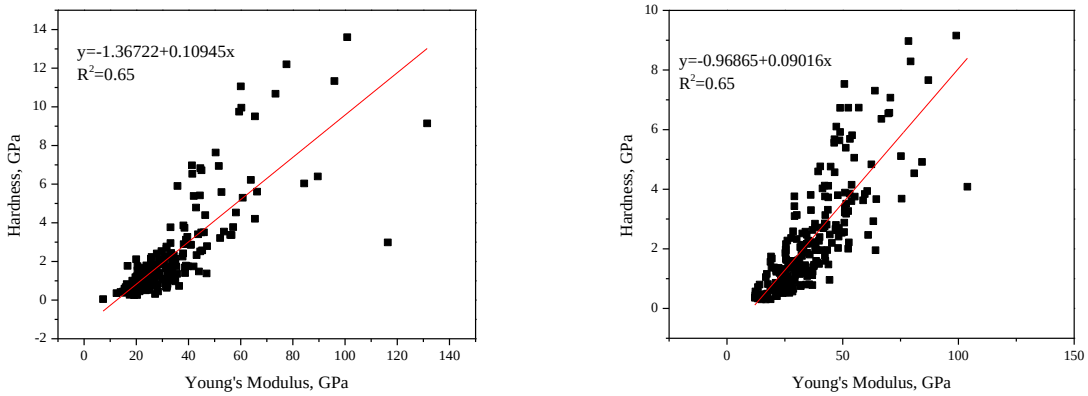

(a) X-1 direction (b) X-3 direction

Fig. 7.6. Correlations between Young's Modulus and Hardness of Sample 34.

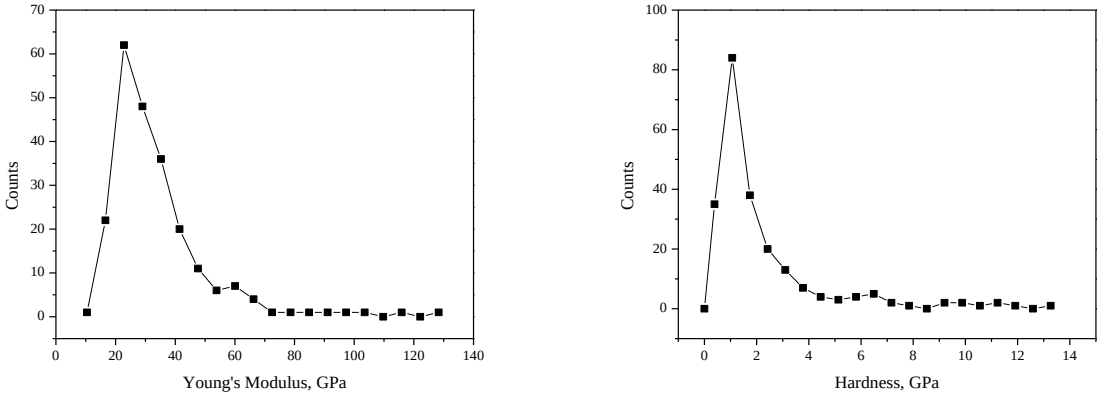

(a) Young's Modulus (b) Hardness

Fig. 7.7. Histograms of Young's Modulus and Hardness of Sample 34.

Table 7.1 summarizes the results of the mean mechanical properties of the samples based on the grid nanoindentation method. The samples along the X-3 direction display larger values than the ones taken along the X-1 direction. The difference between the responses in the two different directions shows the anisotropic characteristics of the shale samples.

Table 7.1. Nanoindentation results for different samples

	Direction	E_{mean}, Gpa	H_{mean}, Gpa
Sample 34	X-1	32.31	2.16
	X-3	37.83	2.42
Sample 35	X-1	22.92	1.32
	X-3	32.71	1.96
Sample 36	X-1	32.67	2.72
	X-3	44.66	3.08
Sample 37	X-1	29.61	1.91
	X-3	37.54	2.44

7.3.3. Deconvolution.

Fig. 7.8 and Fig. 7.9 illustrate the deconvolution results of Sample 34 along the X-1 and X-3 directions, respectively. Both nanoindentation curves can be deconvoluted into three different mechanical phases. For Fig. 7.8 a, the indentation response with the first phase (mean value of 22.34 *GPa*) likely represents clay minerals and organic matter whereas the third phase with the mean of value of 52.53 *GPa* could be due to the presence of silt inclusions composed mainly of quartz, feldspar and dolomite. The third phase with the largest standard deviation indicates the largest experimental variabilities. The second phase with a mean Young's modulus value of approximately 31.64 *GPa* (between 22.34 *GPa* and 52.53 *GPa*) can be regarded as the composite behavior of clay minerals and silt inclusions. This is because the grid nanoindentation leads to random placements of the indentations and some indents occur on the boundary of clay minerals and silt inclusions (Bobko, 2008).

The area below each histogram divided by the area under the combined curve can be considered as the measure of the surface fraction of each mechanical phase. Surface fractions can be identical to the volume fractions of a perfectly-disordered material, which is known as the Delesse principle (1847). Thus, one can derive the volume fractions of each mechanical phase from the

deconvolution process. Table 7.2 shows the deconvolution results for all samples. Although all the samples, which are along the X-1 direction and X-3 direction, can be deconvoluted into 3 stages, the deconvolute data is different. Even with the same mineral composition for the same sample, the mean value of mechanical phases 1, 2 and 3 along the X-3 direction is larger than the mean value of phases 1, 2, 3 along the X-1 direction, respectively. This proves the mechanical anisotropy that is expected from shales. In this regard, a few potential factors can cause shale to represent anisotropic behavior which can be summarized as: the stacking of platy shaped clay minerals that produces planes of weaknesses in a specific direction, thus preferred orientations are created (Sone and Zoback, 2013); the huge amount of organic content in the rock can increase anisotropic characteristics of shales (Vernik and Liu, 1997; Ahmadov, 2011). This is interpreted as organic material to be anomalously compliant compared to the surrounding minerals (Kumar et al., 2012; Ahmadov, 2011) and can become a strong source of mechanical anisotropy if they are distributed in a specific direction; finally, the orientation of various minerals such as quartz and feldspar during deformation, compaction and crystallization can become a source of anisotropy.

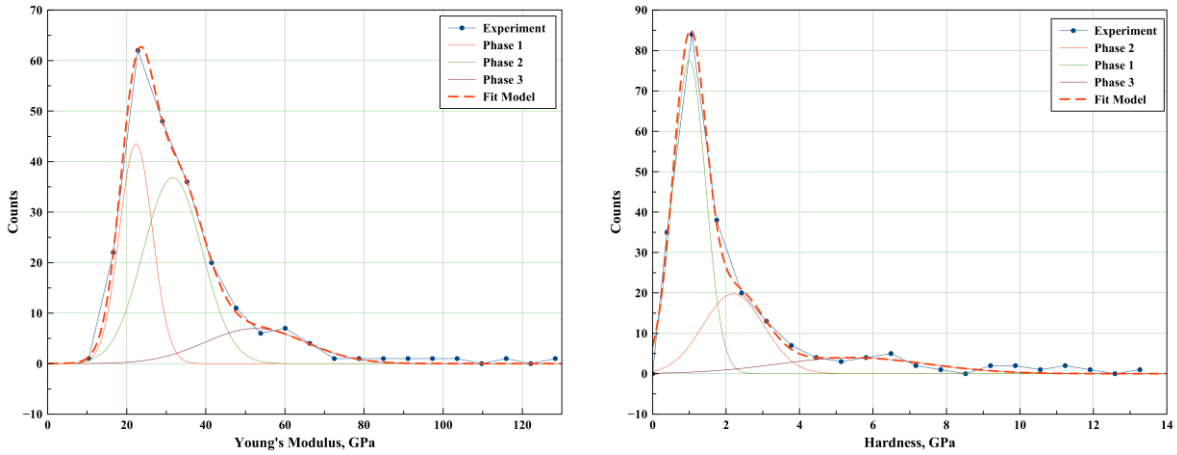

(a) Young's Modulus (b) Hardness

Fig. 7.8. The deconvolution results of Sample 34 at X-1 direction.

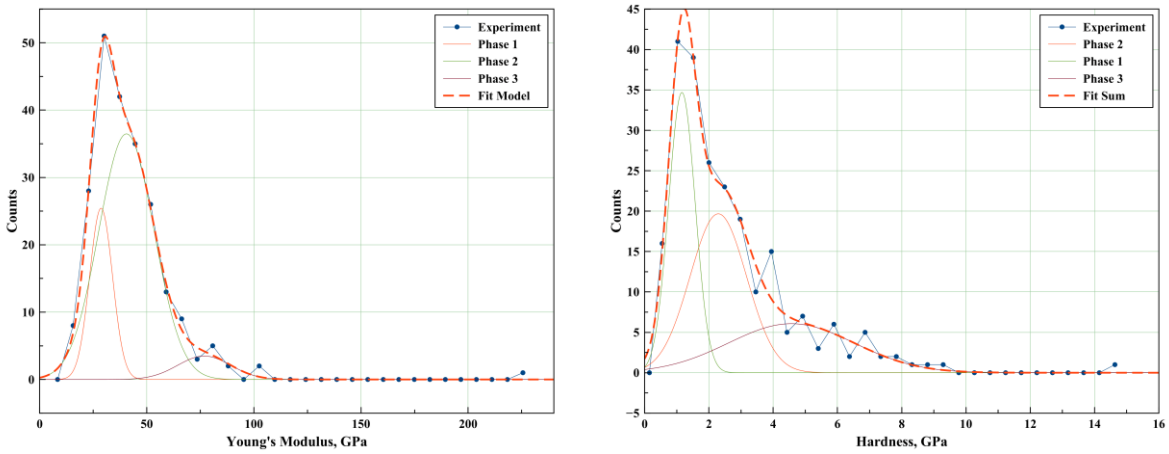

(a)Young's Modulus (b) Hardness

Fig. 7.9. The deconvolution results of Sample 34 at X-3 direction.

Table 7.2. The deconvolution results of Young's modulus for all samples

Sample	Direction	Phase1			Phase 2			Phase 3		
		mean, GPa	SD, GPa	V, %	mean, GPa	SD, GPa	V, %	mean, GPa	SD, GPa	V, %
Sample 34	X-1	22.34	0.52	0.33	31.64	2.74	0.50	52.53	7.67	0.16
	X-3	28.69	0.41	0.21	40.54	1.17	0.73	76.80	6.13	0.07
Sample 35	X-1	14.38	0.25	0.26	23.14	1.03	0.61	43.50	3.80	0.14
	X-3	20.06	0.74	0.31	31.19	0.58	0.33	44.95	8.68	0.36
Sample 36	X-1	16.96	1.15	0.20	26.76	0.46	0.29	37.00	1.69	0.51
	X-3	21.27	0.68	0.24	33.45	0.73	0.20	50.38	5.17	0.56
Sample 37	X-1	19.49	0.50	0.11	26.23	0.91	0.67	50.20	18.69	0.23
	X-3	28.17	0.20	0.69	46.56	0.62	0.14	72.72	1.17	0.17

7.3.4. Homogenization.

Homogenization is a very important step when upscaling the mechanical properties from the nano- or micro-scale to a larger scale level. Based on the discussion in Section 3.1, the mechanical properties that are measured within the nanoindentation area can be utilized to represent the mechanical properties of the sample at the macro-scale (whole sample). Pores with various sizes and shapes are widely distributed in the Bakken Shale, which can affect its mechanical properties. For the Berkovich indenter, the indentation measures the elastic response of a material volume 3-

5 times of the depth of indentation (Larsson et al., 1996). In this study, the mean indent size (depth of penetration *h*) is around 500nm; consequently, the volume under the indenter is estimated as 1.5 um. Hence, pores smaller than 1.5 um will be included in the nanoindentation analysis (Da Silva et al., 2014). However, some pores with sizes larger than 1.5 um may not be detected by the nanoindentation tests, which needs to be considered in the homogenization scheme. In order to quantify the pores larger than the size limit, the image analysis method was applied to analyze the pore size distributions (de Vasconcelos et al., 2016) and derive the pore size distributions of Sample 1 with a scan area of 300 um×300 um. Following this, the pores that were beyond the nanoindentation detection level, were considered in the homogenization process. The Poisson's ratio of the Bakken Shale ranges from 0.2-0.4 (Havens, 2012) and the value of 0.25 for the Mori-Tanaka homogenization was chosen for this study. The results of the homogenization of all four samples (Table 7.3) shows that all samples have larger Young's modulus along the X-3 direction than those taken with respect to the X-1 direction, which is consistent with the results shown in Table 7.1.

Table 7.3. Homogenization results of all samples

Samples	Direction	Large Pores, %	E_{hom}, GPa	V_{hom}
Sample 34	X-1	1.26	29.81	0.25
	X-3	3.41	36.75	0.25
Sample 35	X-1	1.60	21.64	0.25
	X-3	2.44	29.51	0.25
Sample 36	X-1	4.30	26.30	0.25
	X-3	2.90	34.65	0.25
Sample 37	X-1	2.86	28.05	0.25
	X-3	1.96	34.38	0.25

7.3.5. Homogenization value VS. macroscale.

In order to verify the accuracy of this upscaling approach, we compared the results from the homogenization scheme and the data that have been measured in macroscale elastic experiments. Considering the importance of the elastic properties of the materials, a large number of

experimental techniques have been developed such as the static method (Radovic et al., 2004; Dvorak et al., 1973) (i.e. tensile, torsion and bedding tests) or the dynamic methods (i.e. resonant frequency method (Christaras et al., 1994) and ultrasonic echo-pulse method (Kobelev et al., 1998)). In this paper, the non-destructive static tests (samples were not taken to failure) to measure Young's modulus were performed using the MTS 816 Rock testing system (Fig. 7.10). Cores with the size of 2-inch in length and 1-inch in diameter were taken perpendicular to the bedding planes (X-1 direction) and LVDT displacement transducers were mounted on the rock outer surface (Fig. 7.11). The non-destructive test started with increasing the load axially followed by removing the load to make sure the displacement follows the same path before the sample reaches its maximum strength and fails. The stress- strain curve is plotted in Fig. 7.12 and Young's modulus was estimated from the linear part of the curve. The following figure on the left shows the MTS 816 rock testing system equipment that was used for the static geomechanics analysis on the samples that are prepared and shown on the right.

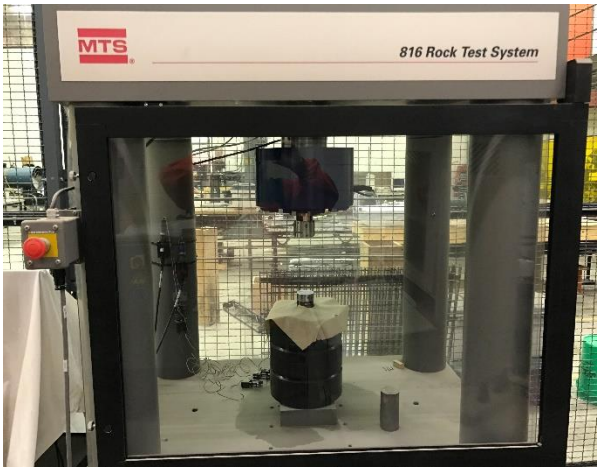

Fig. 7.10. Macroscale test equipment.

Fig. 7.11. Prepared samples for the macroscale test.

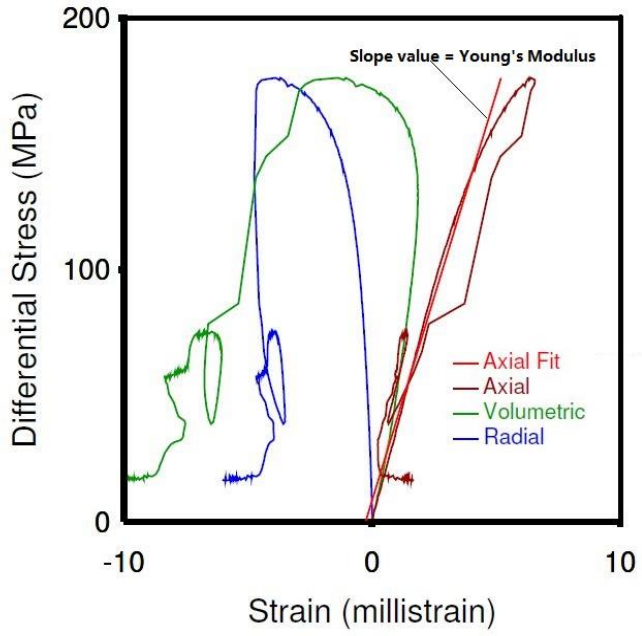

Fig. 7.12. Estimation of Young's modulus from macroscale test.

The estimated values of the elastic modulus of all four samples are summarized in Table 7.4 along with the data obtained from the homogenization scheme. The results show that the Young's modulus of the Bakken Shale samples tested were all below 30 GPa and the difference between the two different testing methods is less than 4 GPa or 14.5%. This demonstrates that the results of the homogenization scheme are reliable and can be used to estimate the mechanical properties of the Bakken Shale at the macro-scale level.

Table 7.4. Comparison of the elastic modulus: Homogenization vs. Macroscale test

Samples	Direction	Macroscale, GPa	E_{hom}, GPa	Difference, GPa	Error, %
Sample 34	X-1	26.07	29.81	3.74	14.35
Sample 35	X-1	25.01	21.64	3.37	13.47
Sample 36	X-1	25.55	26.30	0.75	2.94
Sample 37	X-1	25.09	28.05	2.96	11.80

However, the application of the nanoindentation method is not free of uncertainty. The accurate displacement of the indents can help find the limit of pore size that cannot be detected by the

nanoindentation tests. In this study, the load control mode for the nanoindentation test (peak load value is the same for all indents) was applied. However, the displacement of the indents varies from point to point due to the heterogeneous properties of the shale. The average displacement of the indenter was utilized as the input value to find the limit of the pore sizes, which can cause some minor errors. Another source of uncertainty in the measured values is due to the roughness of the sample surface. The standard mechanical polishing method applied in this study still provides surface roughness, at least on the order of several tens of nanometers. This can cause scattering in the measured indentation modulus and indentation hardness.

It is noteworthy that to quantify mechanical properties in macro scale by nanoindentation is more complicated compared to conventional methods such as unconfined compressive strength and triaxial compression testing which can derive the mechanical properties in macroscale directly. Despite these limitations, the grid nanoindentation tests still showed strong ability to characterize mechanical properties of the Bakken samples. The method allowed us to study the mechanical properties at the nano-scale level, which is beyond the standard scale of laboratory testing. Nevertheless, the small volume of the samples that was used for the grid nanoindentation test is the most useful characteristic of this proposed method.

7.3.6. Homogenization value vs. Average value.

The mean Young's modulus measured by the nanoindentation (E_{mean}) method is one of the parameters that many researchers have used to represent the true value of the specimens' elastic property (Shukla, et al., 2013; Kumar et al., 2012; Alstadt et al., 2015; Yang et al., 2016; Zhang et al., 2017). In order to assess the validity of this approach, the values obtained at a macro-scale level and at the nanoindentation level (E_{mean}) were compared. The results shown in Table 7.5 represent the values of Sample 34, 36 and 37 and indicate that the discrepancy between Young's modulus values from the macro-scale testing and the E_{mean} is significant. This means that using

E_{mean} cannot represent the true elastic properties of the samples. The values from the homogenization scheme (E_{hom}) and the mean value (E_{mean}) were further compared. It was found that E_{hom} is closer to the true Young's modulus value than E_{mean}, which may infer that E_{hom} is a better representative than the E_{mean} when characterizing the mechanical properties of the Bakken Shale at the macro-scale level.

Table 7.5. Comparison of the elastic moduli: Average value vs. Macro-scale tests

Samples	Direction	E_{mean}, GPa	Macroscale, GPa	Difference, GPa	Error, %
Sample 34	X-1	32.31	26.07	6.24	23.94
Sample 35	X-1	22.92	25.01	2.09	8.36
Sample 36	X-1	32.67	25.55	7.12	27.87
Sample 37	X-1	29.61	25.09	4.52	18.01

7.4. Conclusion

In this study, grid nanoindentation was applied to analyze the mechanical properties of a selected number of samples from the Bakken Shale Formation. It was shown that the elastic properties of the individual mechanical phases could be assessed through the statistical evaluation and deconvolution from grid nanoindentation data. By using the analytical elastic homogenization method (Mori-Tanaka scheme), the macro-scale elastic modulus of the Bakken Shale samples was estimated and compared to the values measured from the standard macro-scale core plug rock mechanical testing. The results showed that the values obtained from the homogenization scheme are close to those obtained through macro-scale measurements. This indicates that statistical grid nanoindentation methods can provide a reliable estimation of the mechanical properties of heterogeneous shale rock samples. Statistical grid nanoindentation tests not only are useful for evaluating the mechanical properties of rock specimens at the nano/micro-scale level but also can be applied to estimate the properties at the macro-scale level. This study provides a great potential for the geomechanical investigation of heterogeneous and anisotropic rocks in the petroleum industry when core plugs are not available.

7.5. References

Alstadt, K. N., Katti, K. S., Katti, D. R., 2015. Nanoscale morphology of kerogen and in situ nanomechanical properties of green river oil shale. J. Nanomech. Micromech. 1-10.

Ahmadov, R., 2011. Micro-textural, elastic and transport properties of source rocks: Ph.D. thesis, Stanford University.

Bobko, C. P., 2008. Assessing the Mechanical Microstructure of Shale by Nanoindentation: The Link Between Mineral Composition and Mechanical Properties. PhD thesis. Massachusetts Institute of Technology.

Brinell, J.A., 1901. Congrrs Intemational des Mrthodes d'Essai des Matrriaux de Construction. Paris, Tome, 83-94.

Christaras, B., Auger, F., Mosse, E., 1994. Determination of the moduli of elasticity of rocks. Comparison of the ultrasonic velocity and mechanical resonance frequency methods with direct static methods. Mater.Struct. 27(4), 222-228.

Clark, A. J., 2009. Determination of Recovery Factor in the Bakken Formation, Mountrail County, ND. Society of Petroleum Engineers.

Constantinides, G., Ulm, F.-J., & Van Vliet, K., 2003. On the use of nanoindentation for cementitious materials. Mater. Struct. 36 (257), 191-196.

Constantinides, G., Ravi Chandran, K.S., Ulm, F.-J. & Van Vliet, K.J., 2006a. Grid indentation analysis of composite microstructure and mechanics: Principles and validation. Mat. Sc. Eng. A. 430(1-2), 189-202.

Constantinides, G., 2006b. Invariant Mechanical Properties of Calcium-Silicate-Hydrates (C-S-H) in Cement-Based Materials: Instrumented Nanoindentation and Microporomechanical Modeling. Ph.D. Thesis, Department of Civil and Environmental Engineering, MIT, Cambridge, MA.

Da Silva, W. R. L., Němeček, J., Štemberk, P., 2014. Methodology for nanoindentation-assisted prediction of macroscale elastic properties of high performance cementitious composites, Cem. Concr. Compos. 45, 57-68.

de Vasconcelos, L.S., Xu, R., Li, J., et al., 2016. Grid indentation analysis of mechanical properties of composite electrodes in Li-ion batteries. E.M.L. 9, 495-502.

Delesse, M., 1847. 'Procede mecanique pour determiner la composition des roches.' Comptes Rendus de l'Acadamie des Sciences. 25, 544-547.

Doerner, M.F. & Nix, W.D., 1986. A method for interpreting the data from depth-sensing indentation instruments. J. Mater. Res. 1, 601-609.

Dvorak,G.J., Rao, M.S.M., Tarn, J.Q., 1973. Yielding in unidirectional composites under external loads and temperature changes. J. Compos. Mater. 7, 194-216.

Eisenstein, B. A., Cerrato, L. R., 1976. Statistical deconvolution. Journal of the Franklin Institute. 302(2), 147–157.

Havens, J. 2012.Mechanical Properties of the Bakken Formation. MS thesis. Colorado School of Mines.

Hu, C. and Li, Z., 2015. A review on the mechanical properties of cement-based materials measured by nanoindentation. Constr. Build Mater. 90, 80-90.

Houben, M. E., Barnhoorn, A., Wasch, L., 2016. Microstructures of Early Jurassic (Toarcian) shales of Northern Europe. Int. J. Coal Geol. 165, 76–89.

Kobelev, N. P., Nikolaev, R.K., Soifer, Y.M., et al., 1998. Elastic moduli of single-crystal C60. Phys. Solid State. 40(1), 154-156.

Kumar, V., Curtis, M. E., Gupta, N., Sondergeld, C. H., and Rai, C. S., 2012. Estimation of Elastic Properties of Organic Matter in Woodford Shale Through Nanoindentation Measurements. Society of Petroleum Engineers.

Larsson, P. L., Giannakopoulos, A., Soderlund, E., Rowcliffe, D. & Vestergaard, R., 1996. Analysis of Berkovich indentation. Int. J. Solids Struct. 33 (2), 221-248.

Liu, K., Ostadhassan, M., Bubach, B., 2016. Applications of nanoindentation methods to estimate nanoscale mechanical properties of shale reservoir rocks. J. Nat. Gas Sci. Eng. 35,1310–1319.

Liu, K., Ostadhassan, M., 2017a. Microstructural and geomechanical analysis of Bakken shale at nanoscale. J. Pet. Sci. Eng. 153, 133-144.

Liu, K., Ostadhassan, M., 2017b. Quantification of the microstructures of Bakken shale reservoirs using multi-fractal and lacunarity analysis. J. Nat. Gas Sci. Eng. 39, 62-71.

Mason, J., Carloni, J., Zehnder, A., Baker, S. P., and Jordan, T., 2014. Dependence of Micro-Mechanical Properties on Lithofacies: Indentation Experiments on Marcellus Shale. Society of Petroleum Engineers.

Mighani, S., Taneja, S., Sondergeld, C.H., et al., 2015. Nanoindentation Creep Measurements on Shale. 49th US Rock Mechanics/Geomechanics Symposium. American Rock Mechanics Association.

Miller, M., Bobko, C., Vandamme, M., Ulm, F-J., 2008. Surface roughness criteria for cement paste nanoindentation. Cem. Concr. Res. 38(4), 467-476.

Mori, T., and Tanaka, K., 1973. Average stress in matrix and average elastic energy of materials with misfitting inclusions. Acta Metall. 21(5), 571-574.

Němeček, J., Lehmann, C., Fontana, P., 2011. Nanoindentation on ultra high performance concrete system. Chem. Listy**.** 105(17), 656-659.

Nohava, J., Hausild, P., Randall, N.X., et al., 2010. Grid nanoindentation on multiphase materials for mapping the mechanical properties of complex microstructures. IMEKO 2010 TC3, TC5 and TC22 Conferences Metrology in Modern Context. 22-25.

Oliver, W.C. & Pharr, G.M., 1992. An improved technique for determining hardness and elastic modulus using load and displacement sensing indentation experiments. J. Mater. Res. 7 (6), 1564-1583.

Radovic, M., Lara-Curzio, E., Riester, L., 2004. Comparison of different experimental techniques for determination of elastic properties of solids. Mater.Sci.Eng. 368(1), 56-70.

Randall, N.X., Vandamme, M., and Ulm, F-J., 2009. Nanoindentation analysis as a two-dimensional tool for mapping the mechanical properties of complex surfaces.Journal of materials research . 24, 679-690.

Shukla, P., Kuma, V., Curtis, M., 2013. Nanoindentation studies on shales. ARMA 13-578.

Sone, H., Zoback, M.D., 2013. Mechanical properties of shale-gas reservoir rocks—Part 1: Static and dynamic elastic properties and anisotropy. Geophysics. 78(5), 381-392.

Sorelli, L., Constantinides, G., Ulm, F-J., Toutlemonde, F., 2008. The nano-mechanical signature of ultra high performance concrete by statistical nanoindentation techniques. Cem. Concr. Res. 38(12), 1447-1456.

Tabor, D., 2000. The Hardness of Metals. Oxford university press.

Ulm, F-J., Vandamme, M., Bobko, C., et al., 2007. Statistical indentation techniques for hydrated nanocomposites: concrete, bone, and shale. J. Am. Ceram. Soc. 90(9), 2677-2692.

Vernik, L., Liu, X., 1997. Velocity anisotropy in shales: A petrophysical study. Geophysics. 62(2), 521-532.

Vernik, L., Milovac, J., 2011. Rock physics of organic shales. The Leading Edge. 30(3), 318-323.

Vialle, S., Lebedev, M., 2015. Heterogeneities in the elastic properties of microporous carbonate rocks at the microscale from nanoindentation tests. SEG Technical Program Expanded Abstracts 2015. Society of Exploration Geophysicists. 3279-3284.

Yang, Z., Wang, L., Zhang, G., et al., 2016. Micromechanical Characterization of Fluid-Shale Interactions via Nanoindentation. SPE Asia Pacific Hydraulic Fracturing Conference. Society of Petroleum Engineers.

Zhang, Y. H., Zhang, Z. K., Sarmadivaleh, M., 2017. Micro-scale fracturing mechanisms in coal induced by adsorption of supercritical $CO_{2..}$ Int. J. Coal Geol. 175, 40-50.

Zhu, W., Hughes, J. J., Bicanic, N., Pearce, C. J., 2007. Nanoindentation mapping of mechanical properties of cement paste and natural rocks. Mater. Charact. 58 (11-12), 1189-1198.

CHAPTER 8

NANO-DYNAMIC MECHANICAL ANALYSIS(NANO-DMA) OF CREEP BEHAVIOR OF SHALES

Abstract

Understanding the time-dependent mechanical behavior of rocks is important from various aspects such as: predicting reservoir subsidence that can take place in different scales from depletion induced compaction to proppant embedment. Instead of using the conventional creep tests, nano-dynamic mechanical analysis (nano-DMA) was applied in this study to quantify the displacement and mechanical changes of shale samples over its creep time at a very fine scale. The results showed that the minerals with various mechanical properties exhibit different creep behavior. It was found that under the same constant load and time conditions, the creep displacement of hard minerals would be smaller than the soft ones. On the contrary, the changes in mechanical properties (storage modulus, loss modulus, complex modulus, and hardness) of hard minerals are larger than soft minerals. The results from curve fitting showed that the changes in creep displacement, storage modulus, complex modulus and hardness over creep time follow a logarithmic function. We further analyzed the mechanical changes in every single phase during the creep time based on the deconvolution method to realize each phase's response independently. Two distinct mechanical phases can be derived from the related histograms. As the creep time increases, the volume percentage of the hard-mechanical phase decreases, while this shows an increase for the soft phases. The results suggest that nano-DMA can be a strong advocate to study the creep behavior of shale rocks with complex mineralogy.

8.1. Introduction

Failure to taking into account the creep behavior of shale when modeling its mechanical behavior may lead to an inaccurate operational design. Examples of these include incorrect predictions of depletion due to reservoir compaction, or overestimating the permeability increase as a result of hydraulic fracturing while the proppant embedment into the formation has not enhanced permeability in reality. The embedment of proppant into the rock is a direct result of creep behavior of the formation (Alramahi and Sundberg, 2012; Almasoodi et al., 2014; Bybee, 2007; Li and Ghassemi, 2012; Sone and Zoback, 2011). Creep is a term to describe the time dependent behavior of the rocks under constant but long-time exposure to the stress which is still below its yield strength. Creep happens due to the viscoelastic properties of rocks. Based on the study by Heap et al. (2009), the creep in rocks can be divided into three stages: 1) primary or decelerating stage; 2) secondary or stationary stage; 3) tertiary or accelerating stage. Uniaxial creep test and multi-stage triaxial creep experiments are the common lab testing methods that researchers perform to study the creep behavior (Li and Ghassemi, 2012; Sone and Zoback, 2014). These types of studies are limited in analyzing the creep behavior at macroscale and need large sample volumes which are sometimes not practical to obtain especially from shale formations due to coring issues. Shale is known to be a fine-grained sedimentary rock consisting of a mixture of clay, quartz, feldspar, pyrite, carbonate, and organic matters forming a highly heterogeneous nanocomposite (Ulm et al., 2007) and each of these components show different creep behavior. Understanding the deformation that occurs while shale undergoes creep at nanoscale can provide an insight into the fundamental processes governing on this phenomenon at the larger scale such as properly functioning as a cap rock.

Nanoindentation tests, which only require a small sample volume, are a widely-used method for characterizing the mechanical properties of different materials at nanoscale (Naderi et al., 2016;

Tanguy et al., 2016; Xiao et al., 2015; Kobelev et al., 1998; Alstadt et al., 2015; Yang et al., 2016; Zhang et al., 2017; Kumar et al., 2012; Yang et al., 2016). Analyzing the load-displacement curve which is extracted from a nanoindentation experiment, Young's modulus and the hardness can be derived (Oliver and Pharr, 1992). In recent years, nanoindentation has been applied to analyze the viscoelastic behavior of various types of materials by applying a constant load and subsequently measuring the creep depth as a function of time. Past studies have shown that the creep behavior of the samples determined from the nanoindentation at nanoscale in a short time period are identical to the behavior from the macro scale tests which are carried out over an extended time period. This shows that the nanoindentation creep test can be a reliable representation of the creep behavior while it is much less time consuming compared to the tests that are done on a larger scale (Vandamme and Ulm, 2009, 2013). It is noteworthy that conventional nanoindentation creep tests can only generate Young's modulus and hardness at the maximum penetration depth and are limited in describing the changes in mechanical properties during the creep.

Since Poynting attempted to use oscillatory experiments in 1902 for analyzing the elastic properties of different materials (Menard, 2008), dynamic mechanical analysis (DMA) has been used to analyze the properties of metals (Elomari et al., 1995), polymers (Kararli, 1990), bone (Yamashita et al., 2001), and concrete (Yan et al., 1999). DMA can be simply described as applying an oscillating force to a sample and analyzing the response to that force. For the creep analysis, DMA tests can evaluate the mechanical properties under the constant load over the creep time continuously. Nano dynamic mechanical analysis (Nano-DMA), a recently developed mode in nanoindentation studies which not only characterizes the properties of the sample in nanoscale but also measures the mechanical properties continuously during the creep time has proven to have a great potential in analyzing the mechanical changes of shales (Herbert et al., 2008).

In this paper, we carried out a Nano-DMA test to study the creep behavior of shales. We applied the statistical grids method to do the creep data and quantified how the associated creep displacement and mechanical properties can change over time.

8.2. Methods and experiments

8.2.1. Sample Preparation.

In order to analyze the creep behavior of shale, we collected one sample (Sample 38) from the Bakken Formation, a typical unconventional shale oil reservoir in Williston Basin, North Dakota. Small pieces of rocks were taken from cores that were retrieved from a few wells drilled into the formation. The samples were taken perpendicular to the bedding plane and then were palced in a resin liquid for 24 hours under vacuum conditions, until they became solid. To ensure that the sample surface is flat (roughness less than 200 nm), they were polished with successive grades of sand paper and were finished with a 0.05 μm alumina suspension diamond polisher.

8.2.2. Statistical grid nanoindentation.

It is well understood that shales exhibit phase heterogeneity. This will lead to a mechanical response that would vary on different measurement scales (nanometers to meters). In order to fully understand the mechanical properties of the shale, the grid nanoindentation method was applied to remove the mechanical heterogeneity. This technique is based on the repeated indentation in the form of a rectangular matrix with a total indentation count up to several hundred. Each indent can be regarded independently to be used to calculate Young's modulus, hardness and other mechanical properties (Bobko, 2008). When mechanical properties of each indent were calculated, statistical methods were applied to analyze the driven data set. The benefit of this approach is that we can use less number of indents to determine the single-phase properties and by increasing the number of indents the properties of the homogenized medium can be estimated (Constantinides et al., 2006).

8.2.3. Nano-DMA.

A conventional (quasi-static) nanoindentation test involves applying a load to force an indenter into the sample surface. The applied load is held over a time period and then withdrawn. In the next step, the contact area is determined based on the indenter displacement, thus contact stiffness can be calculated. Finally, hardness and modulus values of this test point could also be quantified (Oliver and Pharr, 1992). Fig. 8.1 shows the schematic of a conventional nanoindentation or quasi-static creep test. The main shortage of this method is that one can only get the hardness and modulus values at the maximum contact depth (end of the creep test) while the change in these properties during the creep test will remain unknown.

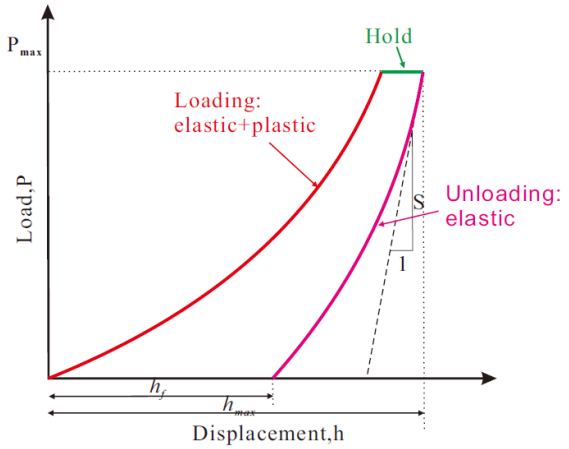

Fig. 8.1. Schematic of the typical nanoindentation curve (Hu and Li., 2015)

In the nano-DMA creep test, the quasi-static force is kept constant while a small oscillation is superimposed to allow for the continuous measurement of the contact stiffness (Fig. 8.2). Since modulus is derived at the beginning of the hold segment, the thermal drift error is negligible due to the minimal temperature changes on the tip of the indenter. The measured modulus is then used to calculate the contact area continuously for the remainder of the test, allowing for a continuous and accurate measurement of mean contact pressure and penetration depth over time (Bruker company).

In this study, the TI 950 TriboIndenter® equipped with a diamond Berkovich probe was used to perform dynamic nanoindentation tests on a few shale samples. The probe was oscillated at the constant reference frequency of 220HZ in order to measure the contact area. This will enable an accurate calculation of the modulus despite the relatively long test time which is normally required at low frequencies.[31] The creep time in our experiment was set to 60s.

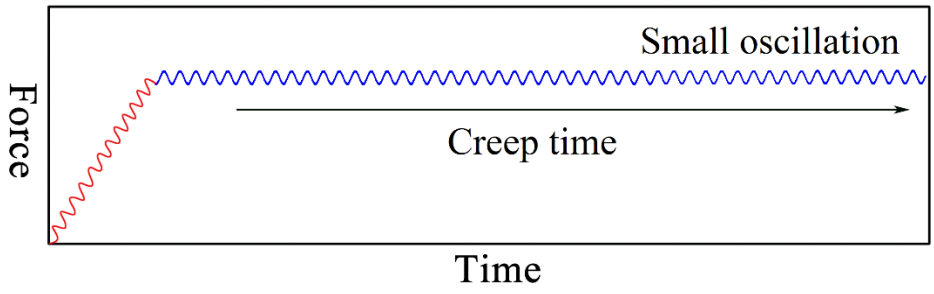

Fig. 8.2. Schematic representation of a nano-DMA creep test.

8.2.4. DMA parameter analysis.

Dynamic mechanical analysis is used to characterize the response of different materials under a sinusoidal stress or strain oscillation. The following few parameters can be derived from the DMA test (Herbert [et al.], 2008; Yamashita et al., 2001; Les et al., 2004): (1) Storage modulus (E') and loss modulus (E''). The storage modulus (E') represents the stiffness of a viscoelastic material and is proportional to the energy stored during a loading cycle. The loss modulus is related to the energy which is dissipated during one loading cycle. The loss modulus is often associated with internal friction and is very sensitive to various ways of molecular motion. (2) Complex modulus (E*) which is a combination of the storage modulus (the real part) and loss modulus (the imaginary part), reflecting the viscoelastic properties of the material. Complex modulus is defined as the ratio of the stress amplitude to the strain amplitude and represents the stiffness of the material; (3) Phase angle (δ) which represents the phase difference between the dynamic stress and the dynamic strain

in a viscoelastic material that is subjected to a sinusoidal oscillation. If the phase angle is 0°, then the material is pure elastic and if the phase angle is 90° then the material is defined to be pure plastic. The phase angle between 0-90° shows that the material is viscoelastic; (4) Hardness (H). Hardness is a measure of how resistant the material is to various types of permanent changes in shape when a certain compression load is applied. (5) Loss factor (tan δ). This is defined as the ratio of loss modulus to storage modulus. It is a measure of the energy loss, expressed in recoverable energy, and represents mechanical damping or internal friction in a viscoelastic system. The lower the loss factor is, the higher the elastic properties of the material would be. The relevant equations to calculate these parameters can be found as follows:

$$E' = \frac{K_s \sqrt{\pi}}{2\sqrt{A_c}} \qquad (8\text{-}1)$$

$$E'' = \frac{wC_s \sqrt{\pi}}{2\sqrt{A_c}} \qquad (8\text{-}2)$$

$$E^* = E' + iE'' \qquad (8\text{-}3)$$

$$H = \frac{P}{A_c} \qquad (8\text{-}4)$$

$$\tan\delta = \frac{E''}{E'} \qquad (8\text{-}5)$$

In these equations, *E'* is the storage modulus and *E''* is the loss modulus; *H*, *P*, A_c and tan δ refer to the hardness, contact load, contact area and the loss factor, respectively. *w* is the frequency, K_s and C_s are the stiffness and the damping coefficients of the contact which can be calculated using the following equations:

$$K_c = \frac{F_0}{Z_0}\cos\delta + mw^2 - K_i \qquad (8\text{-}6)$$

$$wC_s = \frac{F_0}{Z_0}\sin\delta - wC_i \qquad (8\text{-}7)$$

Here, F_0 and Z_0 are the force and displacement amplitude; respectively; m, K_i, C_i are the mass of the indenter, stiffness of the indenter and damping coefficients of the indenter, respectively and are known parameters.

8.3. Results and discussions

8.3.1. Data analysis at the beginning of creep.

In order to study the creep behavior of our shale samples, an area covering 300 μm ×300 μm surface was chosen based on previous studies (Liu and Ostadhassan, 2017). A total of 225 indents were performed with 20 μm distance between the neighboring indents. Fig. 8.3 shows the schematic of the nanoindentation matrix.

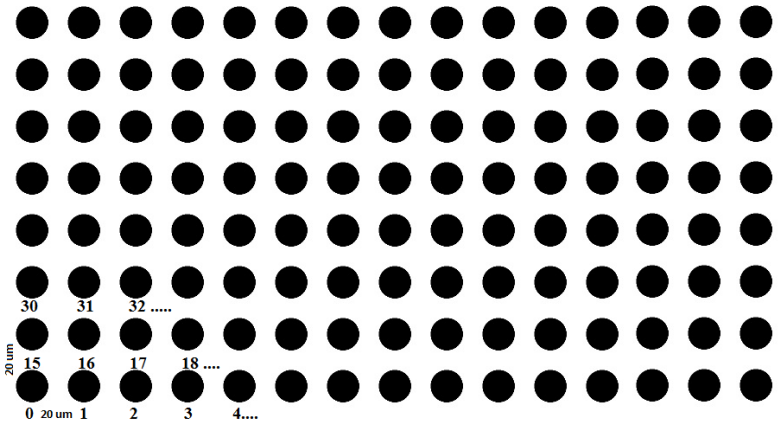

Fig. 8.3. Schematic of the nanoindentation grid.

Fig. 8.4a and Fig. 8.4b show, respectively, the maps of storage and Loss modulus at the beginning of the creep test. It can be easily found that various test points exhibit different storage and loss modulus values, revealing the heterogeneous nature of the tested sample. The points with higher storage modulus values (red regions in Fig. 8.4a) perfectly matched with areas of higher loss modulus values (red areas in Fig. 8.4b). Fig. 8.5 shows that a good linear relationship exists between the storage modulus and loss modulus. In addition, it was found that our shale samples

have a larger storage modulus value than the loss modulus (with slope value less than 0.5), demonstrating their elastic behavior.

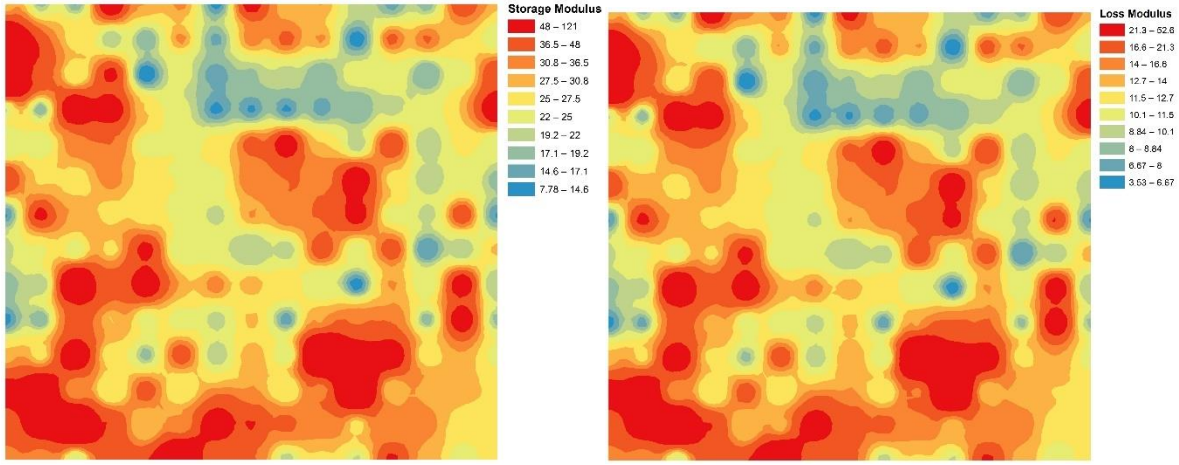

(a) Storage modulus (b) Loss modulus

Fig. 8.4. The storage modulus and the loss modulus map of the nanoindentation area (at the beginning of creep).

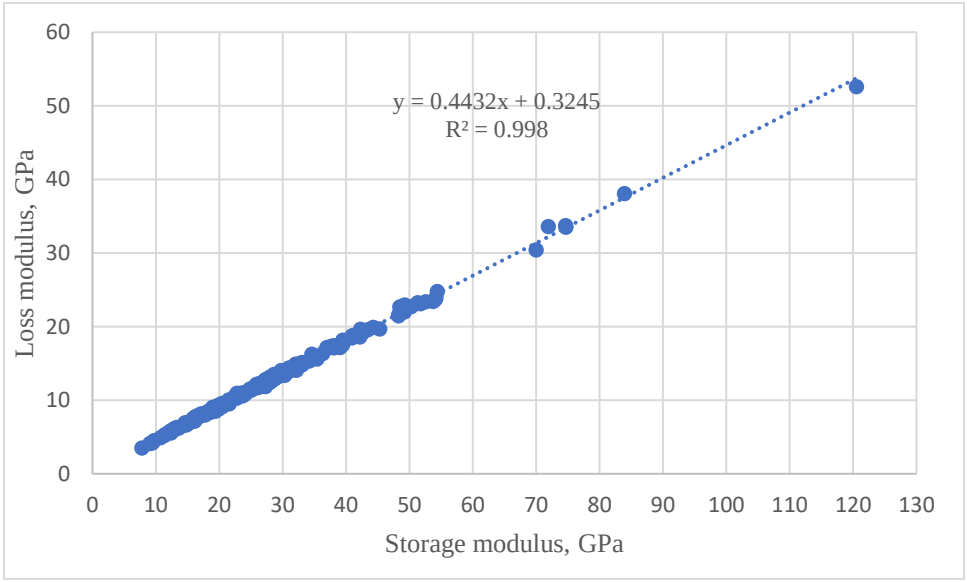

Fig. 8.5. Correlations between the loss modulus and storage modulus.

Complex modulus can be used to determine the viscoelastic properties of the samples. The map of the complex modulus of a tested sample covering the nanoindentation area at the beginning of the creep is displayed in Fig. 8.6. Similar to the storage modulus, complex modulus varies significantly

which reflects the viscoelastic behavior of the sample. Linear relationships exist between the complex modulus and storage modulus shown in Fig. 8.7a, and between the complex modulus and loss modulus represented in Fig. 8.7b.

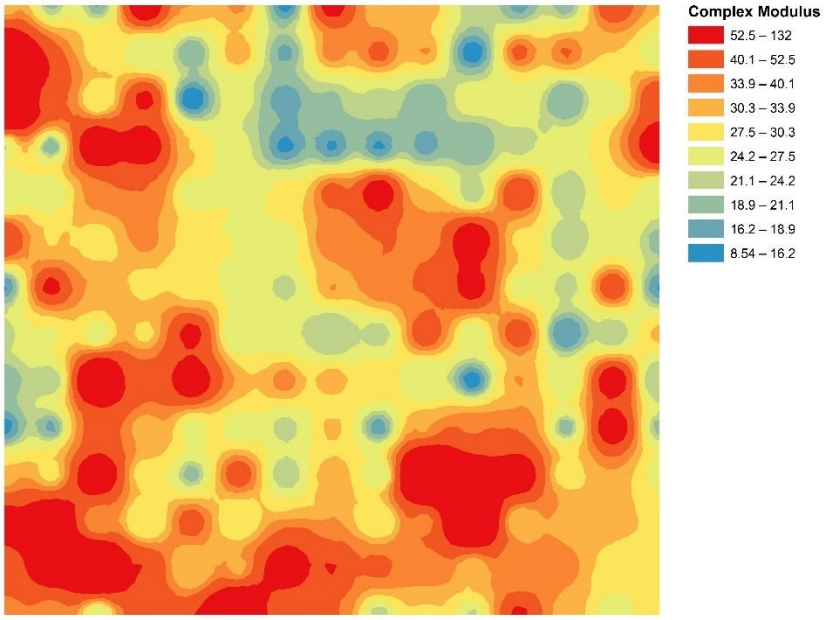

Fig. 8.6. Complex modulus map covering the nanoindentation area at the beginning of creep.

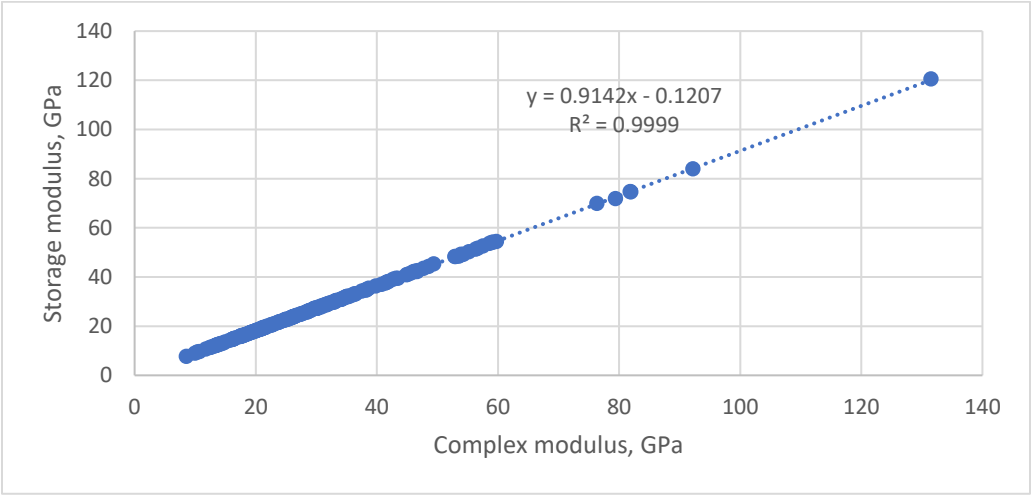

(a) storage modulus

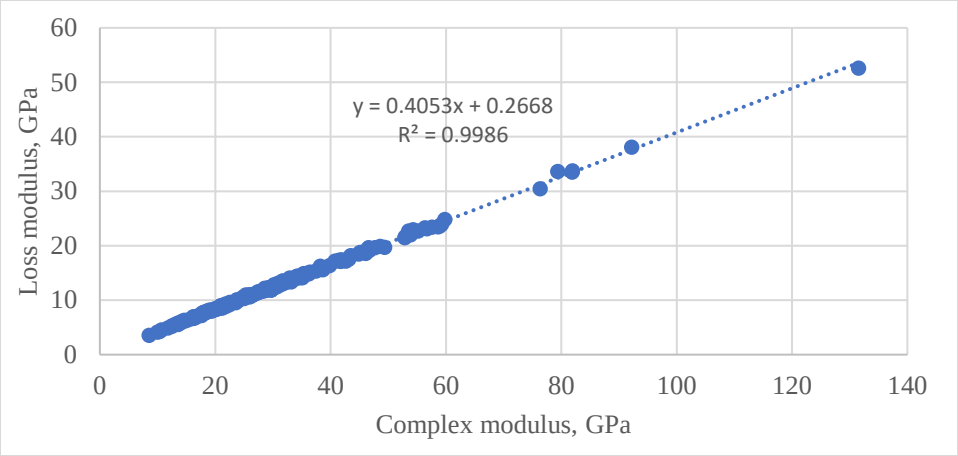

(b) complex modulus

Fig. 8.7. Correlations between the complex modulus and storage modulus (a) and loss modulus (b).

Compared with Young's modulus which can reflect the elastic properties of the rock, hardness can reveal more information about the deformation that has taken place in the sample. This makes H to be an important parameter which should be analyzed precisely. The hardness map over the nanoindentation area is shown in Fig. 8.8 and the positive linear correlations between the complex modulus and hardness exists which is displayed in Fig .8.9.

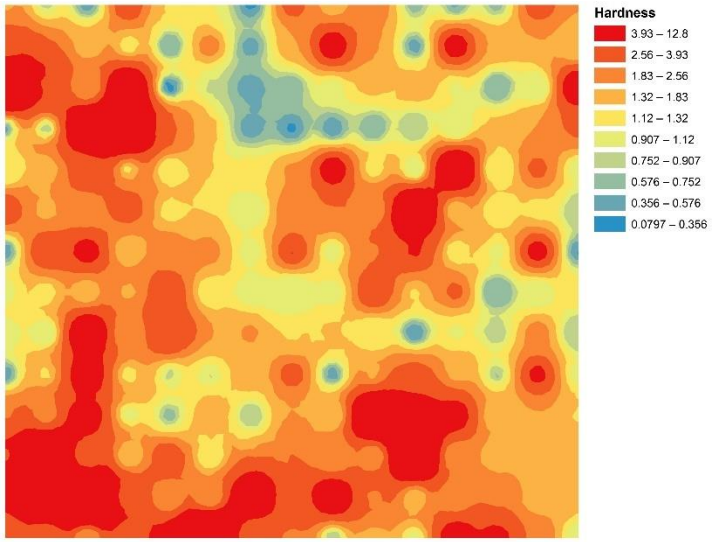

Fig. 8.8. Hardness map covering the nanoindentation area at the beginning of creep.

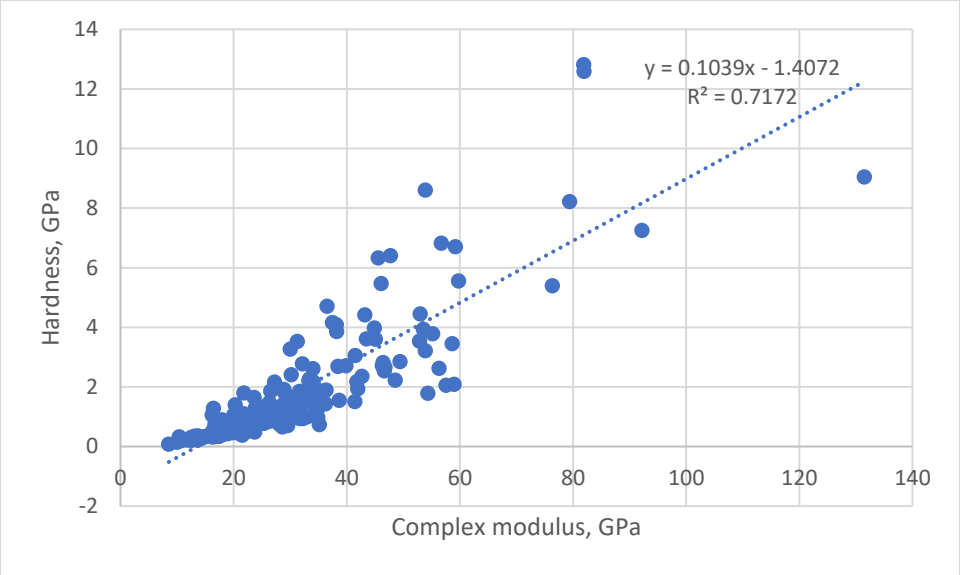

Fig. 8.9. Correlations between the complex modulus and hardness.

8.3.2. Impact of creep on the properties.

Shales are composed of various minerals with different mechanical properties, thus the creep behavior of each mechanical phase might be different under the same stress conditions and creep time. In order to better investigate and attain a deeper insight into the creep behavior of shales at nanoscale, we chose three points from the grid indents for more detailed analysis. Table 8.1 summarizes the information about these three data points where Points 1, 2, and 3, respectively represent soft minerals, medium hard minerals and hard minerals. These data points are chosen based on their complex modulus and Hardness values.

Table 8.1. Summary of the mechanical properties of the three points

Points	Complex modulus, GPa	Hardness, GPa
Point 1	16.714	0.766
Point 2	38.451	2.692
Point 3	56.704	6.819

Plotting the displacement recorded for these three data points as a function of creep time, it can be seen that the curve follows a similar trend in all data points (Fig. 8.10). At the beginning, the creep

displacement is rapidly increasing and then slows down over time. Under the same creep time, the mineral with larger complex modulus and hardness showed less creep displacement. Curve fitting technique was used to quantify the changes in displacement while the sample is under creep. The results are summarized in Table 8.2, indicating that all three creep curves follow a logarithmic function which is similar to conclusions in previous studies (Vandamme and Ulm, 2009; Wu et al., 2011). The equation for the logarithmic function was found in the following format:

$$y = a\ln(t+b)+c, \qquad (8\text{-}8)$$

where y is the creep displacement (nm); t is the creep time (s); a, b, c are the constants derived from curve fitting. a is an important parameter that can be used to characterize the creep behavior. The curve with higher a value would express a larger creep displacement.

Table 8.2. The constants and regression coefficients corresponding to the three points logarithmic functions

	a	b	c	R^2
Point 1	8.7913	0.7797	-0.5695	0.9919
Point 2	7.4478	1.8052	-4.5319	0.9990
Point 3	1.9998	0.4221	0.9926	0.9898

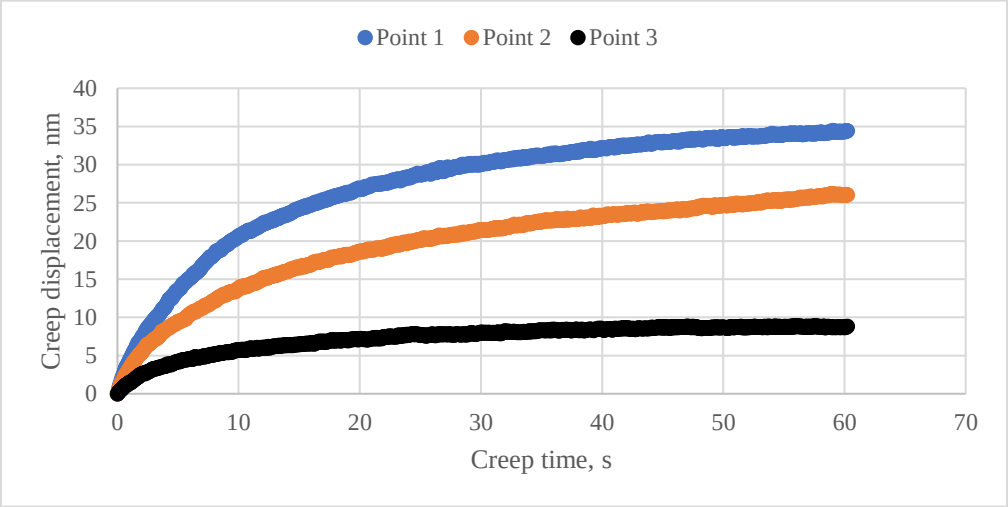

Fig. 8.10. The correlations between the creep displacement and creep time.

We further analyzed the impact of the creep time on the mechanical and viscoelastic properties of these chosen data points. As the creep time increases, loss modulus fluctuates around 0 without any distinguishable relationship between the loss modulus and creep time (Fig. 8.11). However, considering other properties such as the storage modulus, complex modulus and hardness, as the creep time evolves, the changes in these values increases (Fig. 8.12-8.14). Fig. 8.12 explains that variations in Point 1 which is measurements on a soft mineral is smaller compared to Point 2 and Point 3 from medium hard and hard minerals, respectively. We followed the similar curve fitting method that we earlier proposed for the displacement, to quantify the changes of mechanical properties during the creep time. Table 8.3 illustrates that Eq. 8 can also describe the effects of the creep time on mechanical properties.

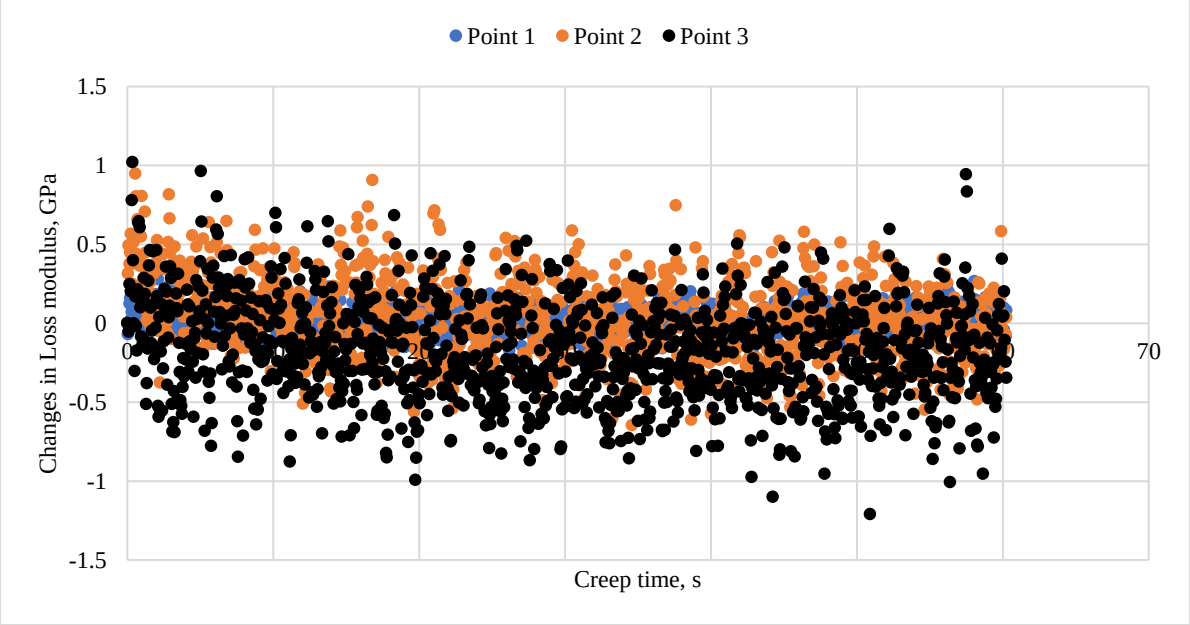

Fig. 8.11: Changes of the loss modulus as a function of creep time.

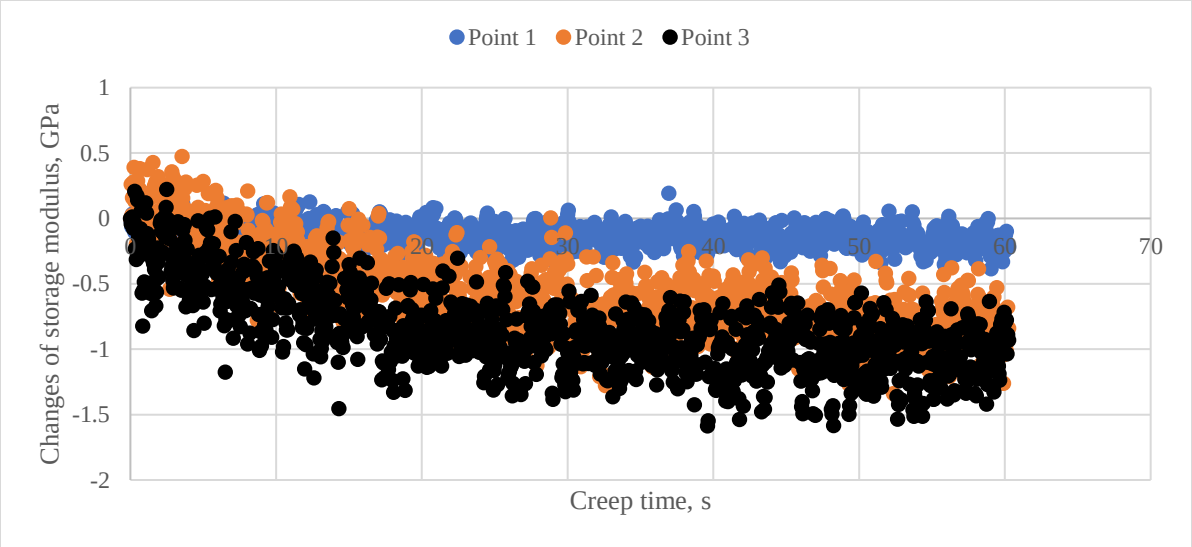

Fig. 8.12: Changes of the storage modulus as a function of creep time.

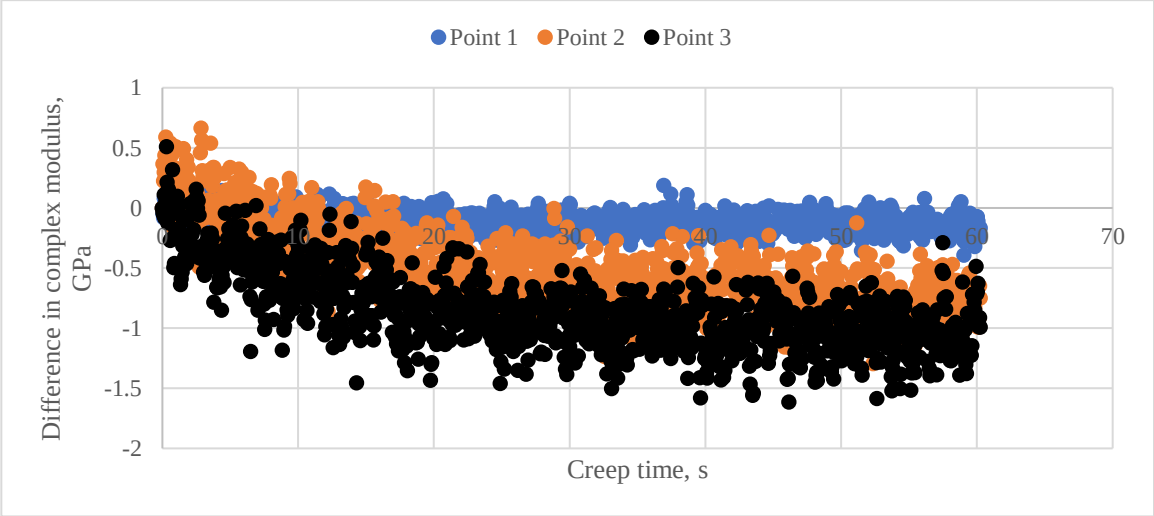

Fig. 8.13: Changes of the complex modulus as a function of creep time.

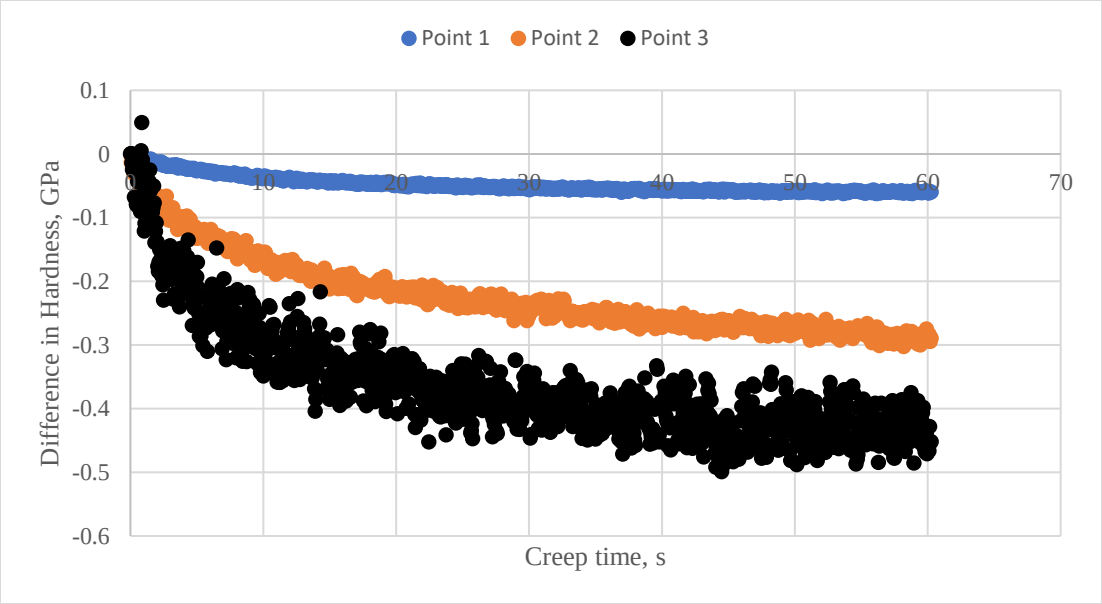

Fig. 8.14. Changes of the hardness as a function of creep time.

Table 8.3. Curve fitting results of the storage modulus, complex modulus and hardness

Properties	Points	a	b	c	R^2
storage modulus	Point 1	-0.0564	4.1846	0.0632	0.1897
	Point 2	-0.4052	4.0786	0.7970	0.6508
	Point 3	-0.2797	1.1977	0.0431	0.5404
Complex modulus	Point 1	-0.0465	1.4891	0.0420	0.1966
	Point 2	-0.3936	2.9837	0.8041	0.6829
	Point 3	-0.2807	0.8335	0.0398	0.5587
Hardness	Point 1	-0.0148	0.5906	-0.0016	0.9834
	Point 2	-0.0724	1.1333	0.0077	0.9864
	Point 3	-0.0907	0.1919	-0.0782	0.8775

8.3.3. Nanoindentation analysis of entire sample.

We attempted to estimate the overall mechanical properties of the entire nanoindentation area as one value. Based on the statistical design of the grid indents, first, we defined the creep behavior of each indent, and then used the average value of the measured indents as an estimation for the whole surveyed area. Fig. 8.15 shows the displacement curve of the entire nanoindentation area. The average displacement value increases as the creep time increases which is similar to Fig. 8.10.

Regarding the impact of creep time on mechanical properties, we can find that the initial loss modulus decreases as the creep time increases followed by an increase (Fig. 8.16). The other mechanical parameters, such as storage modulus, complex modulus, and hardness, demonstrate a sharp increase followed by a steady decrease as creep time proceeds (Fig. 8.17-8.19). The decrease of the storage modulus indicates that some structures are broken in the rocks during the creep. The decline of the hardness value can demonstrate that the resistant ability of the shale to the change in shape is decreasing under certain stress intervals. Relating this phenomenon to field operations, we can understand one of the reasons for proppant embedment into the fractures, leading to a reduction in fracture conductivity and the overall performance of hydraulic fracturing. Analyzing the curve fitting results from Table 8.4 indicates as the creep time increases, displacement, storage modulus, loss modulus and hardness follow a logarithmic function expressed in Eq. (8).

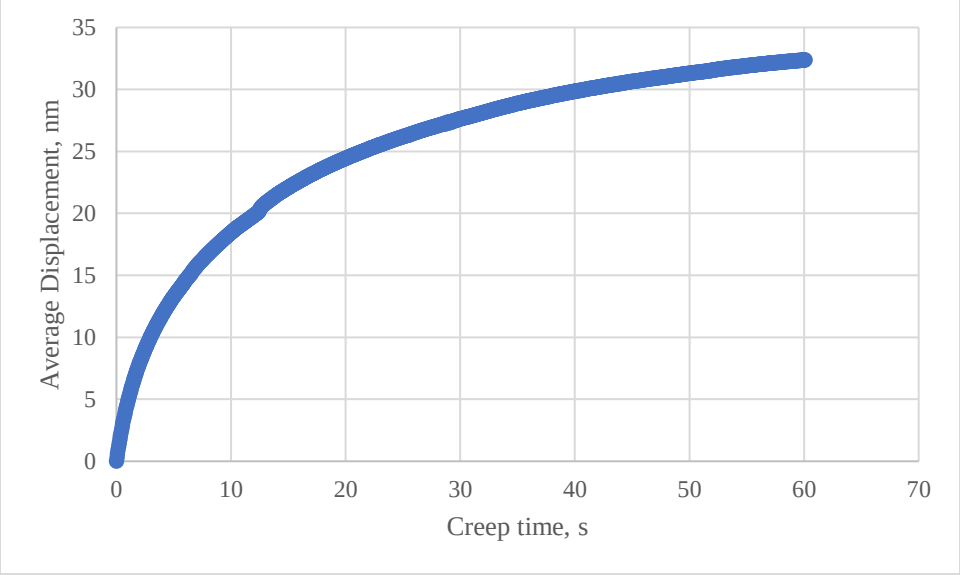

Fig. 8.15. The correlations between the creep displacement and creep time (Whole nanoindentation area).

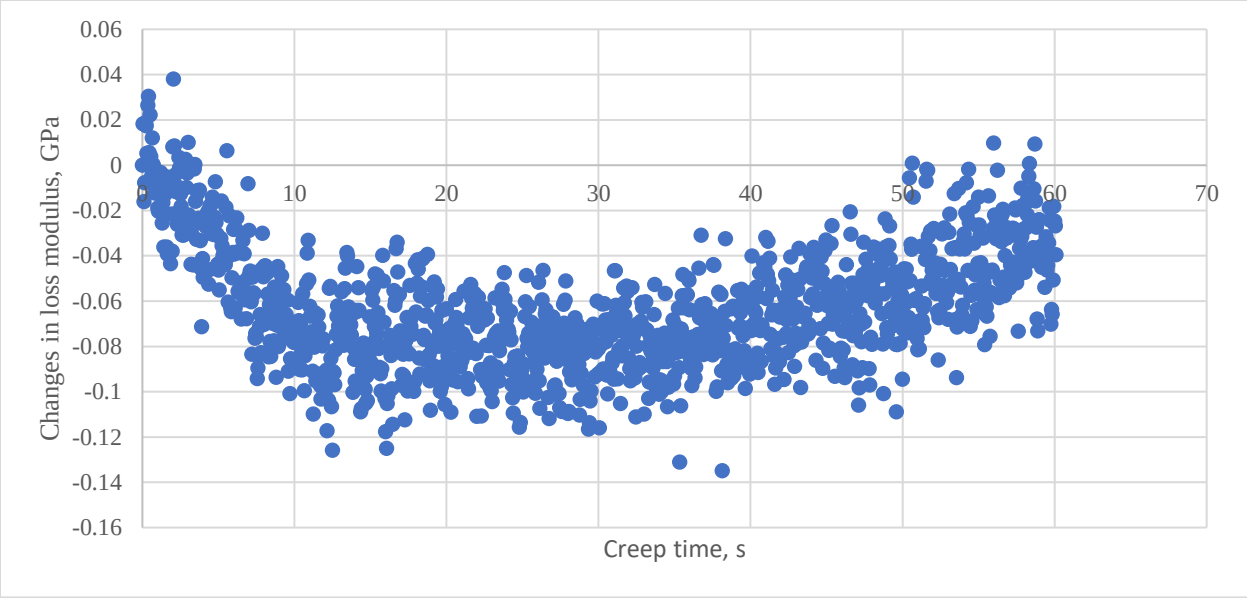

Fig. 8.16. Correlations between the loss modulus and creep time (Whole nanoindentation area).

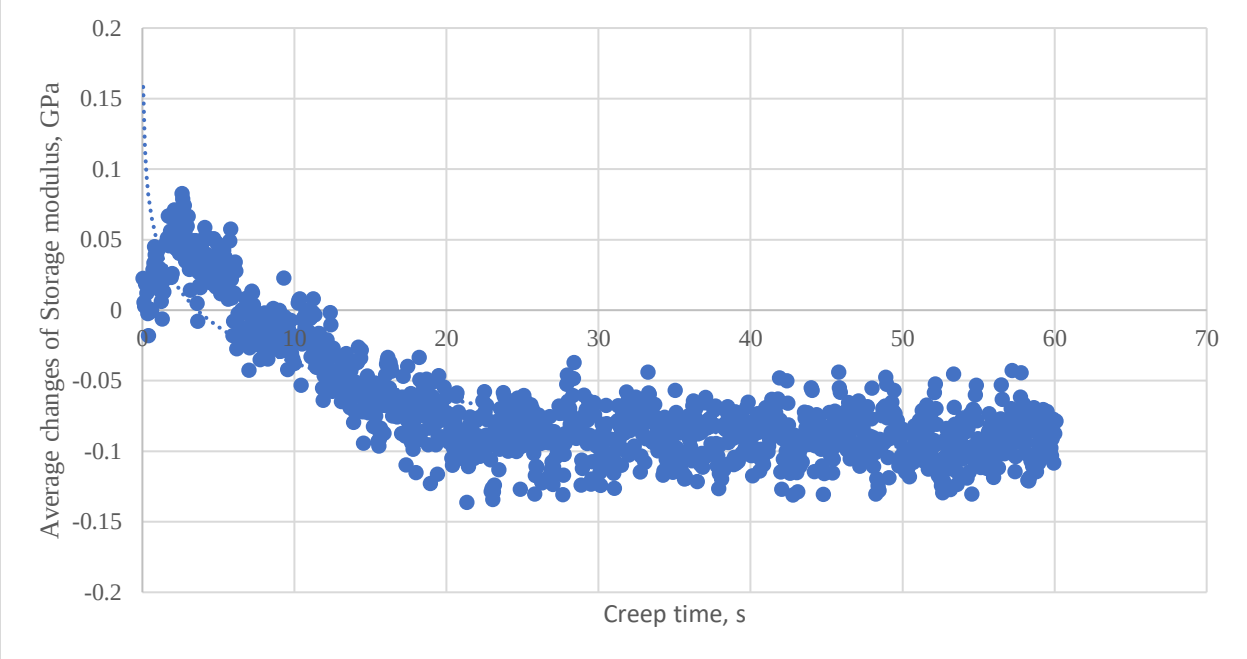

Fig. 8.17. Correlations between the storage modulus and creep time (Whole nanoindentation area).

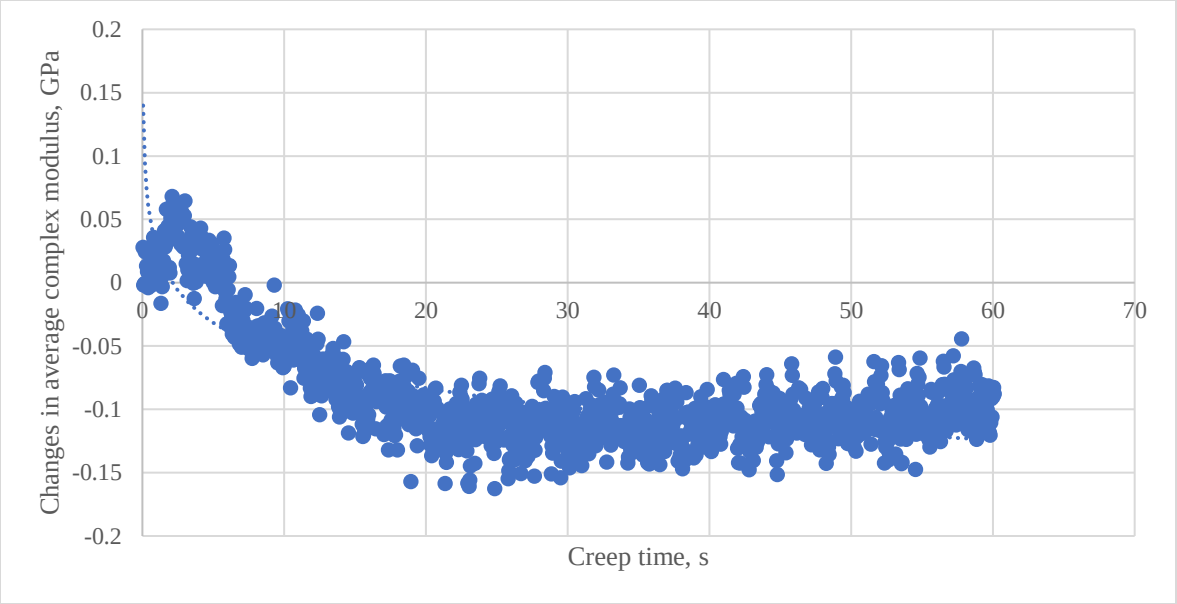

Fig. 8.18. Correlations between the complex modulus and creep time (Whole nanoindentation area).

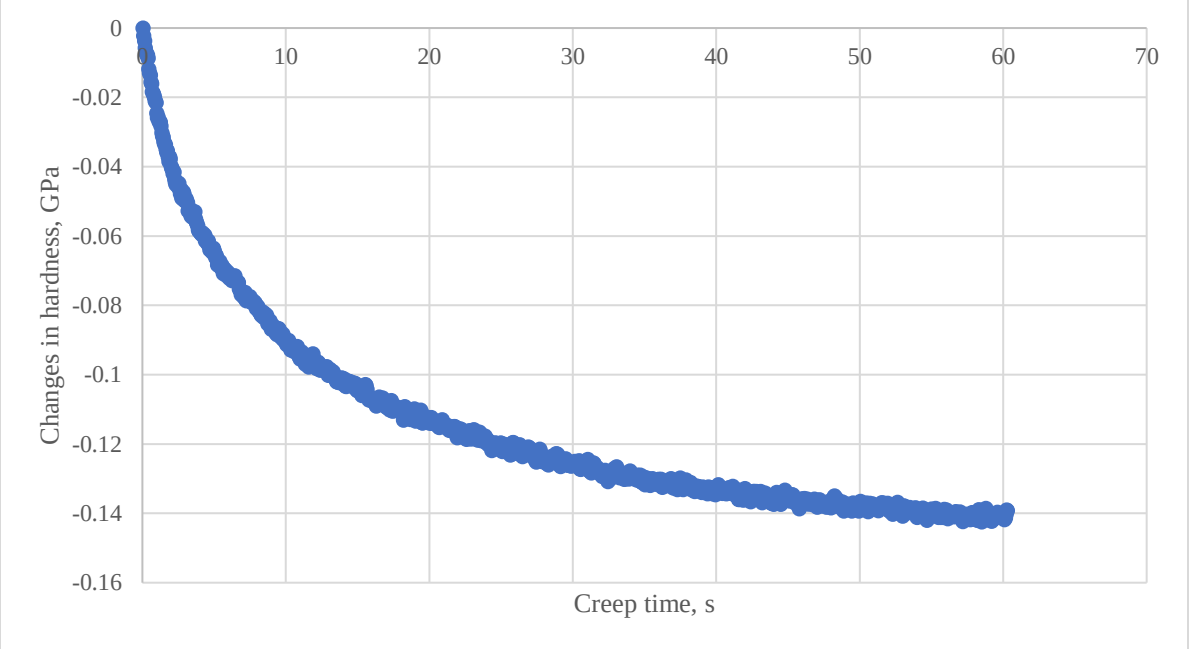

Fig. 8.19. Correlations between the hardness and creep time (Whole nanoindentation area).

Table 8.4. Curve fitting results of the average value over the entire sample

Properties	a	b	c	R^2
Displacement	7.4970	0.6038	1.3779	0.9922
Storage modulus	0.0465	1.4537	0.0823	0.7264
Complex modulus	0.0420	0.5813	0.0452	0.6761
Hardness	0.0318	0.4023	0.0150	0.9925

8.3.4. The impact of the creep time on the shale structures.

In the following section, we studied the changes in rock properties as a function of creep time.

Fig. 8.20 displays the hardness map of the sample at three different creep time periods.

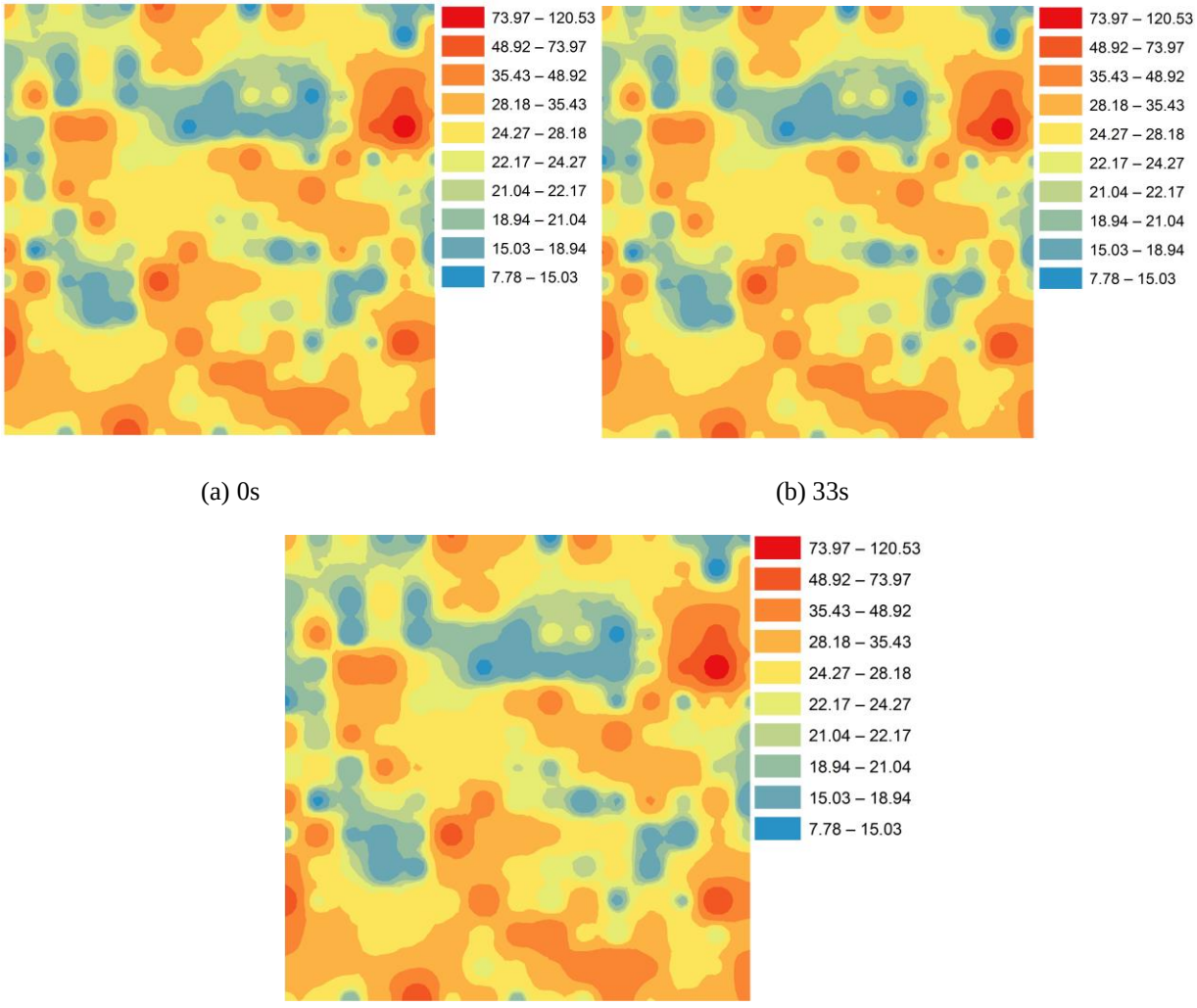

(a) 0s

(b) 33s

(c) 58s

Fig. 8.20. Storage modulus map covering the nanoindentation area as creep time evolves.

In order to accurately quantify the variations that are associated with the creep time, we applied deconvolution discrimination method to create the histogram of the data set. This method divides the data set into different categories that are presented in Fig. 8.21. The deconvolution method was proposed by Ulm and his co-authors (Ulm et al., 2007; Bobko et al., 2008) which is used to analyze the grid indentation data statistically. Fig. 8.21 shows the deconvolution results from the storage modulus map at different creep times. The results are also summarized in Table 8.5. The outcome of the deconvolution discrimination explains that the nanoindentation area of our sample can be separated into two distinct mechanical phases. One phase with the smaller mean value which can represent softer materials whereas the second one expressing higher mean value corresponding to harder minerals. The area underneath each histogram, divided by the area under the combined curve can be considered as the surface fraction for each mechanical phase. Moreover, based on the Delesse principle (Delesse, 1847), we can derive the volume fractions of each mechanical phase from the deconvolution process. Table 8.5 illustrates as the creep time increases, the volume percentage of mechanical phase 2 (hard mineral phase) decreases while the volume percentage of l phase 1 (soft mineral phase) increases. This is caused by the dislocation creep phenomenon. Dislocation is defined as the propagation front line of a slip which is characterized by two components 1) the slip plane and 2) slip direction. A collective motion of atoms such as migration of crystal dislocations can cause a plastic deformation. The deformation by the dislocation creep can result in dynamic recrystallization which can further reduce the grain size. Consequently, smaller grains will be formed along the pre-existing grain boundaries making such areas softer prior to the dislocation (Karato, 2013). As a result, the volume of hard mechanical phase will decrease, and the volume of the soft mechanical phase will increase.

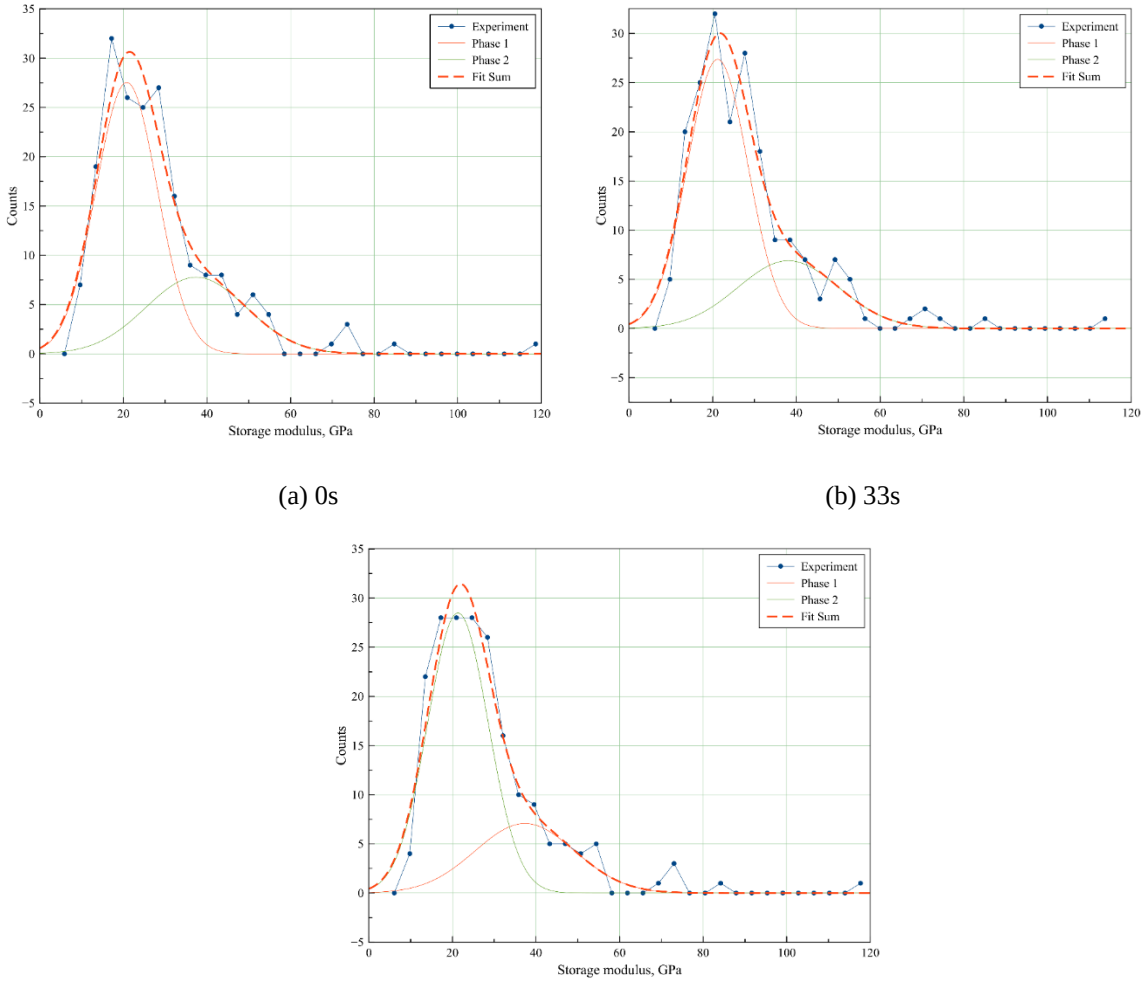

(a) 0s

(b) 33s

(c) 58s

Fig. 8.21. Histogram of the storage modulus covering the nanoindentation area under different creep time.

Table 8.5. Comparison of deconvolution results of the sample under different creep time

	Phase 1, Gpa	percentage, %	Phase 2, Gpa	percentage, %	Fitting coefficient
0s	20.80	68.47	37.41	31.53	0.94
33s	21.19	70.54	38.07	29.46	0.92
58s	21.33	71.06	37.35	28.94	0.95

8.4. Conclusions

In this paper, we applied the new NanoDMA on a few shale samples from the Bakken Formation to examine their creep behavior at nanoscale. The following conclusions were drawn from this study:

1) Shale is a heterogeneous material, but linear correlations can be found between storage modulus and loss modulus, complex modulus and storage modulus, and finally between complex modulus and hardness.

2) Under the same stress and creep conditions, hard minerals expressed less creep displacement compared to soft minerals. The changes of properties such as storage modulus, complex modulus and hardness of hard minerals are larger than the soft ones.

3) We averaged the data of the nanoindentation area to represent the entire surveyed shale sample and then analyzed its overall creep behavior. The results showed that the creep displacement, storage modulus, complex modulus and hardness follow a logarithmic function with respect to the creep time.

4) Two distinct mechanical phases (hard mechanical phase and soft mechanical phase) can be derived from the deconvolution of storage modulus histograms. As the creep time proceeds, the volume percentage of hard mechanical phase decreases while the percentage volume of soft mechanical phase will increase.

8.5. References

Almasoodi, M.M., Abousleiman,Y.N., Hoang, S.K., 2014. Viscoelastic Creep of Eagle Ford Shale: Investigating Fluid-Shale Interaction. Presented at the SPE/CSUR Unconventional Resources Conference–Canada. Society of Petroleum Engineers.

Alramahi, B., Sundberg, M.I., 2012. Proppant embedment and conductivity of hydraulic fractures in shales. Presented at the 46th US Rock Mechanics/Geomechanics Symposium. American Rock Mechanics Association.

Alstadt, K. N., Katti, K. S., Katti, D. R., 2015. Nanoscale morphology of kerogen and in situ nanomechanical properties of green river oil shale. J. Nanomech. Micromech. 1-10.

Bobko, C. P., 2008. Assessing the Mechanical Microstructure of Shale by Nanoindentation: The Link Between Mineral Composition and Mechanical Properties. PhD thesis. Massachusetts Institute of Technology.

Bruker company. Quantitative nanoscale depth-profiling and viscoelastic property measurements. https://www.bruker.com/nc/products/surface-and-dimensional-analysis/nanomechanical-test-instruments/nanomechanical-upgrade-options/nanodma-iii.html

Bybee, K., 2007. Rock-mechanics considerations in fracturing a carbonate formation. JPT. 59(07), 50-53.

Constantinides, G., Ravi Chandran, K.S., Ulm, F.-J. & Van Vliet, K.J., 2006. Grid indentation analysis of composite microstructure and mechanics: Principles and validation. Mat. Sc. Eng. A. 430(1-2), 189-202.

Delesse, M. 'Procede mecanique pour determiner la composition des roches.' Comptes Rendus de l'Acadamie des Sciences 1847, 25, 544-547.

Elomari, S., Boukhili, R., Skibo, M.D, et al., 1995. Dynamic mechanical analysis of prestrained Al2O3/Al metal-matrix composite. J. Mater. Sci. 30(12), 3037-3044.

Heap, M.J., Baud, P., Meredith, P.G., et al., 2009. Time-dependent brittle creep in Darley Dale sandstone. J.Geophys. Res-Sol.Ea. 114(B7).

Herbert, E.G., Oliver, W.C., Pharr, G.M.,2008. Nanoindentation and the dynamic characterization of viscoelastic solids. J. Phys. D. Appl. Phys. 41(7), 074021.

Hu, C. and Li, Z., 2015. A review on the mechanical properties of cement-based materials measured by nanoindentation. Constr. Build Mater. 90, 80-90.

Kararli, T.T., Hurlbut, J.B., Needham, T.E., 1990. Glass–rubber transitions of cellulosic polymers by dynamic mechanical analysis. J. Pharm. SCI. 79(9), 845-848.

Karato, S.I., 2013. Rheological properties of minerals and rocks. Physics and Chemistry of the Deep Earth. 94-144.

Kobelev, N. P., Nikolaev, R.K., Soifer, Y.M., et al., 1998. Elastic moduli of single-crystal C 60. Phys. Solid State. 40(1), 154-156.

Kumar, V., Curtis, M.E, Gupta, N., et al., 2012. Estimation of elastic properties of organic matter in Woodford Shale through nanoindentation measurements. SPE Canadian Unconventional Resources Conference. Society of Petroleum Engineers.

Les, C.M., Spence, C.A., Vance, J. L., et al., 2004. Determinants of ovine compact bone viscoelastic properties: effects of architecture, mineralization, and remodeling. Bone. 35(3), 729-738.

Li,Y., Ghassemi, A., 2012. Creep behavior of Barnett, Haynesville, and Marcellus shale. Presented at the 46th US Rock Mechanics/Geomechanics Symposium. American Rock Mechanics Association.

Liu, K., Ostadhassan, M., 2017. Quantification of the microstructures of Bakken shale reservoirs using multi-fractal and lacunarity analysis. J. Nat. Gas Sci. Eng. 39, 62-71.

Menard, K.P., 2008. Dynamic mechanical analysis: a practical introduction. CRC press.

Naderi, S., Dabbagh, A., Hassan, M.A., et al., 2016. Modeling of porosity in hydroxyapatite for finite element simulation of nanoindentation test. Ceram. Int. 42(6), 7543-7550.

Oliver, W.C. & Pharr, G.M.,1992. An improved technique for determining hardness and elastic modulus using load and displacement sensing indentation experiments. J. Mater. Res. 7 (6), 1564-1583.

Sone, H., Zoback, M.D., 2011. Visco-plastic properties of shale gas reservoir rocks. Presented at the 45th US Rock Mechanics/Geomechanics Symposium. American Rock Mechanics Association.

Sone, H., Zoback, M.D., 2014. Time-dependent deformation of shale gas reservoir rocks and its long-term effect on the in situ state of stress. Int. J. Rock. Mech. Min. 69, 120-132.

Tanguy, M., Bourmaud, A., and Baley, C., 2016. Plant cell walls to reinforce composite materials: Relationship between nanoindentation and tensile modulus. Mater. Lett. 167, 161-164.

Ulm, F-J., Vandamme, M., Bobko, C., et al., 2007. Statistical indentation techniques for hydrated nanocomposites: concrete, bone, and shale. J. Am. Ceram. Soc. 90(9), 2677-2692.

Vandamme, M., Ulm, F-J., 2009. Nanogranular origin of concrete creep. PNAS.106(26),10552-10557.

Vandamme, M., Ulm, F-J., 2013. Nanoindentation investigation of creep properties of calcium silicate hydrates. Cement Concrete Res. 52, 38-52.

Vieregge, J., Schier, J. Continuous Nanoscale Dynamic Mechanical Analysis of PMMA. https://www.hysitron.com/media/1520/pol11an-r1f.pdf.

Wu, Z., Baker, T.A., Ovaert, T.C., et al., 2011. The effect of holding time on nanoindentation measurements of creep in bone. J. Biomech. 44(6), 1066-1072.

Xiao, G., Yang, X., Yuan, G., Li, Z. and Shu, X., 2015. Mechanical properties of intermetallic compounds at the Sn–3.0Ag–0.5Cu/Cu joint interface using nanoindentation. Mater. Design. 88, 520-527.

Yamashita, J., Furman, B.R., Rawls, H.R., et al., 2001. The use of dynamic mechanical analysis to assess the viscoelastic properties of human cortical bone. J. Biomed. Mater. Res. A. 58(1): 47-53.

Yan, H., Sun, W., Chen, H., 1999. The effect of silica fume and steel fiber on the dynamic mechanical performance of high-strength concrete. Cement Concrete Res. 29(3), 423-426.

Yang, Z., Wang, L., Zhang, G., et al., 2016. Micromechanical Characterization of Fluid-Shale Interactions via Nanoindentation. SPE Asia Pacific Hydraulic Fracturing Conference. Society of Petroleum Engineers.

Zhang, Y. H., Zhang, Z. K., Sarmadivaleh, M., 2017. Micro-scale fracturing mechanisms in coal induced by adsorption of supercritical CO2. Int. J. Coal Geol.175, 40-50.